CONTRIBUTIONS TO THE MECHANISM OF RANEY NICKEL DSK ELECTRODES

Eduard W. Justi and Adolf W. Kalberlah

Institute of Technical Physics, University of Braunschweig, Braunschweig, Germany

1. Introduction

A decade ago Justi et al. (1) have disclosed the DSK (double skeleton katalyst) system of gas diffusion electrodes consisting of a supporting homeoporous macroskeleton with embedded homogenized grains of catalytically active microskeletons of Raney metal type. A primary goal of this system has been to avoid platinum metal catalysts and to improve hitherto less powerful electrocatalysts such as Raney nickel. This is the main reason why the DSK system does not meet the requirements of space technology but continues being of actual importance for terrestrial applications such as electrotraction. Apart from its abundance nickel has the peculiar advantage to store great amounts of hydrogen and to facilitate in this way the operation of hydrogen nickel anodes even under overload and as accumulator electrode. In fact, our own group (2) and Russian (3) and Czechoslowackian (4) laboratories have made remarkable progress already in the preparation of new Raney nickel catalysts which are not pyrophoric despite of increased activity. For optimum construction and operation of DSK electrodes with nickel macroskeleton and microskeleton a detailed knowledge of reversible and irreversible oxidation and corrosion processes seems to be necessary.

From the work of formation of nickelhydroxide $Ni(OH)_2$ -105.6 kcal/mole and of water -56.69 kcal/mole the enthalpy of formation of the reaction $Ni(OH)_2 + H_2 \longrightarrow Ni + H_2O$ may be calculated as -7.78 kcal/mole. Hence the potential of the reversible $Ni(OH)_2$ electrode vs H_2 electrode in the same electrolyte is +168 mv. This means that Ni in this anode will be oxidized already at a polarization of 170 mv. Moreover it is known that nickel in alkaline electrolyte is coated by a passivating layer. Therefore, the question was how these layers will influence the porosity of the DSK anodes and the catalytic activity of the Raney Ni. In Raney Ni with its large inner surface about one out of four atoms belongs to the surface and, therefore, if only the surface atoms will be oxidized this would mean a considerable increase of volume and decrease of porosity, a change of surface structure and perhaps of the electronic structure of the catalyst grains. Such changes should be investigated by measurements of porosity, of weight, catalytic activity including gas consumption and of electric resistance vs state of oxidation. Such measurements are described below and their teachings for construction and operation of DSK anodes are discussed.

2. Influence of oxidation on porosity of DSK nickel anodes

If one places an electrode disk A as separating diaphragm between two electrolyte spaces the liquid may flow through the electrode and the pressure drop Δp at said electrode may be measured. As shown by fig. 1 two additional electrodes B are placed on each side permitting to send a direct current I through the middle electrode and to measure the potential drop $\Delta\varphi$ at two more reference electrodes C in the vicinity of electrode A. In this configuration the Ni DSK electrode was gradually oxidized anodically departing fromthe hydrogen

potential and in this way both the flow resistance and electric diaphragm resistance are measured as function of the state of oxidation of the electrode A (5). Fig. 2 shows both resistances vs electrode potential against hydrogen in the same electrolyte. Both resistances are increased suddenly at about +150 mv what may be explained as filling up the pores by nickel hydroxide layers at its potential of formation. Corresponding experiments with carbonylnickel electrodes without Raney nickel failed to show such resistance changes and therefore, it is concluded that the Raney nickel alone is responsible for the darning of electrode pores.

3. Inactivation of catalyst by $Ni(OH)_2$ coating layers

3.1 Overloading a Raney Ni DSK anode

Together with the formation of the $Ni(OH)_2$ coating layer the catalytic activity of Raney nickel is lost as shown by experiment 1 in fig. 3. In this diagram is shown the potentiostatically controlled electric current I and the hydrogen flow $\dot{Q}$ consumed by the anode and expressed by its ampere equivalent vs time in minutes. In this experiment the electrode was discharged with a polarization of +930 mv. In the beginning there is a rather high current of 6 amp corresponding to 240 ma/cm^2 at 20°C which is fed nearly completely by the hydrogen consumption of the electrode. But the hydrogen influx remains always somewhat smaller than the electric current and the difference is supplied from the electrochemical capacity causing a gradual oxidation of the catalyst. From the decrease of electric current and the hydrogen resorption per unit time one may see the gradual deterioration of the anode.

3.2 The process of recovery of the DSK Raney Ni anode

If one waits until there flows but a little portion of the initial electric current and if one interrupts thereupon the current the hydrogen consumption will first decrease considerably, then remain constant some time and will pass afterwards a steep maximum, cf. fig. 4.

In this diagram is also shown the electric potential φ as function of time during this recovery period. At the left hand nadir of the maximum this is at the beginning of the strong hydrogen consumption the potential has reached the value of +170 mv against reversible hydrogen potential. Therefore, it is plausible to explain this peak as consequence of an autocatalytic reduction of the $Ni(OH)_2$ layer by gaseous molecular hydrogen. At some single germs of the surface there is activated the hydrogen and dissolved anodically. The $Ni(OH)_2$ layer is reduced cathodically at the same velocity next to the germs caused by local element effect. The autocatalysis consists in the ability of the nickel atoms formed by the reduction to accelerate subsequent hydrogen resorption from the gas phase. Therefore, at the beginning of the expansion of the above mentioned active areas the hydrogen supply will be accelerated until the nickel hydroxide areas are diminished considerably. There will remain a small residual hydrogen influx caused by diffusion of hydrogen into remote regions far off the surface (6). If one extends this recovery process over several days the electrode may reach the same performance as before. But under certain circumstances one observes a deterioration of the electrochemical performance which may be understood as the formation of another "aged" phase of nickelhydroxide, as in the corresponding case of Cd (7).

4. Ageing of nickel hydroxide layers

4.1 Recovery processes after potentiostatic anodic oxidation

During the experiments described above the state of the catalyst inside the electrode was not homogenous for it was under gas pressure during overloading and was divided in an area accessible to oxidation and an unaccessible one. To reach well defined conditions we have flooded the whole electrode with electrolyte and subsequently discharged potentiostatically at a potential of +350 mv against hydrogen during 15 hours. Then the electrode was pressurized again with hydrogen and both hydrogen consumption and potential was measured during 9 hours, cf. fig. 5. The experiment was repeated on 4 following days. From the curves 2, 3, 4 and 5 it may be seen that the maxima of subsequent experiments are setting in respectively later and are decreasing each time. Integration of the $\dot{Q}$ curves shows that charge Q received decreases from one experiment to the following one. If one compares the hydrogen amount consumed during one experiment with the oxidation charge withdrawn previously one will state that it amounts to about 70 % only. This means that during each experiment a part of the $Ni(OH)_2$ it not reduced. Whereas most of the $Ni(OH)_2$ is reduced spontaneously as soon as the nickel hydroxide potential is reached, the remainder is tranformed in a less reducible phase the reduction of which needs several days. This is what we call "aged" nickel hydroxide.

4.2 Electronic conductivity of Raney Ni as function of state of oxidation

All details of the reaction process at Raney Ni catalysts should be disclosed if one investigates various physical properties during oxidation and subsequent reduction. In connection with the electronic state of catalyst it will be important to measure the electronic conductivity. Therefore, we have pressed under water Raney nickel powder with a pressure of 1 to/cm^2 at room temperature and cut from the sheet thus produced a specimen of 37.3 x 6.1 x 3.3 mm^3. This rod St was provided with two current and potential wires (I and P) and suspended in 6n KOH solution on one beam of a balance, as shown by fig. 6. The experiment was performed in this way: starting from the hydrogen potential we have drained anodic charges in subsequent little portions and have measured simultaneously the electric resistance, weight and potential of the specimen after having reached a steady state. Fig. 7 shows the results. From the shape of the potential curve φ vs charge L one takes cognizance of the beginning hydroxide formation after 11 amp. min discharge. Before hydroxide formation only hydrogen was withdrawn at negative potentials, the region 1 in fig. 7. During this period the resistance R of the Raney Ni specimen drops from about 7.4 to 5.3 mohms, and simultaneously the weight decreases proportional to the charge L withdrawn. This part of the phenomena observed is understandable as caused by the removal of hydrogen built in the nickel lattice during activation, and the reduction of weight is caused in this way. The process is supported by additional removal of aluminum. Now one may expect that according to the well known experiments of Suhrmann (8) the removal of hydrogen as donor is connected with a resistance increase. Surprisingly that is not the case but we observe a considerable decrease of resistance understandable as removal of scattering centres.

During the formation of nickel hydroxide both electric resistance and weight is increasing nearly proportional to the charge, see region 2 in fig. 7 . The increase of resistance is explained by the depletion of conductivity electrons which are consumed by the oxidation process. The weight increase is due to the augmentation of the specimen. But the increase of volume must also be considered because the increase of buoyancy causes a appearent decrease in weight. The change of weight observed is the difference of the real change Δg minus the change of buoyancy $\Delta V.\rho$. For the reaction $Ni + Ni(OH)_2$ is $\Delta g = 17$ g/val, $V = 8.01$ cm^3/val and $\rho = 1.257$ g/cm^3. The expected weight change $\Delta g = 17 - 10 = 7$ g/val is in good agreement with the measured value of 6.85 .

Until complete oxidation the resistance increases by nearly 300 % , but continues behaving metallic as proved by its always positive coefficient of temperature. If one tries to reduce the specimen electrochemically one reaches very soon the hydrogen potential without an appreciable reduction of the catalyst. Accordingly the resistance remains relatively high, about 200 % above the lowest resistance value. Also evolution of hydrogen at higher polarization changes the resistance hardly. Even here appears a hysteresis showing that nickel hydroxide reduction may be a slow process.

4.3 Interpretation of ageing

Certainly the reduction of nickel hydroxide may be accelerated by raising the temperature. To measure this effect we have reduced cathodically the specimen at different temperatures at a potential of + 80 mv against reversible hydrogen or else - 88 mv against nickel hydroxide potential t. At this potential we have measured the currents I dependent on temperature. Fig. 8 shows log I vs 1/T. The linear character proves that the speed controlling process is a purely chemical reaction with an activation energy of 15.9 kcal/mole and occurs prior to the electrochemical process. If one assumes that the cathodic reduction of $Ni(OH)_2$ proceeds according to $Ni(OH)_2 + e^- \longrightarrow NiOH + OH^-$, the speed limiting chemical process should be the transformation of aged $Ni(OH)_2$ into a phase appropriate for the electrochemical discharge process. One plausible explanation is that during the ageing nickelhydroxide forms NiO by splitting off water (9), which must reformed in hydroxide again by absorption of water. The maximum work of the water splitting reaction is $\Delta G = G_{NiO} + G_{H_2O} - G_{Ni(OH)_2} = 2.79$ kcal/mole and hence rather little, but according to the above mentioned high energy of activation there is a high energy peak in the course of reaction, as shown by fig. 9 . Another explanation of the strong temperature dependence but little potential dependence of the cathodic reduction of Raney Ni is a polymorphism of nickel hydroxide as discussed by Bode (10). Similar observations on $Cd(OH)_2$ of Gottlieb (7) have been mentioned already.

5. Discussion of results and outlook

The experiments described have given the teaching for the operation of anodes with nickel catalyst that one should avoid the formation of nickelhydroxide layers. Nevertheless this does not mean one must not operate such hydrogen anodes at polarizations exceeding 170 mv, for the ohmic I.R drop and concentra-

tion polarization are not included and, moreover, hydroxide formation will insert at more positive potentials in dilute KOH solution. In fact, the electrode will supply at polarizations of about 150 mv such great current densities that the electrolyte inside the pores will be diluted and the current will be limited by lack of OH^- ions. Therefore, under normal conditions the current is not limited by hydroxide formation but by concentration polarization and we have developed a method to increase the limiting current density and to decrease the polarization by continous or intermittant rinsing with small amounts of concentrated KOH(11).

In conclusion it should be mentioned that the stationary polarization current performance of a Raney nickel anode may be improved considerably by a transient positivation of electrode potential. As example fig. 10 presents two curves of the same electrode, which was oxidized anodically one hour at 350 mv against hydrogen and then dried in air. After reduction with molecular hydrogen the electrode showed an improved performance with a polarization resistance of 1.2 ohm. cm^2.

Although the present investigations into the mechanism of Raney catalyst electrodes have contributed interesting informations about construction and operation of electrodes avoiding rare metal catalysts the authors feel we are only at the beginning of a fully utilizing the possibilities of such electrodes both in fuel cells and accumulators.

REFERENCES

1. E. W. Justi and A. W. Winsel, "Cold Combustion - Fuel Cells", Fr. Steiner Publ., Wiesbaden, Germany, 1962; J. Electrochem. Soc., vol. 108, p. 1073, 1961.
2. H. v. Doehren, H. Grüne and M. Jung, VARTA Res. Center, Kelkheim, private communication.
3. A. G. Pschenichnikov and R. Ch. Burstein, Pat. UdSSR 147617/21b, 14/01, 1961.
4. F. P. Dousek, J. Jansta and J. Riha, Coll. Czech. Chem. Comm. 31, 457, 1966.
5. B. Köhler and A. W. Winsel, Z. Naturforsch. 19a, 602, 1964.
6. A. W. Kalberlah and A. W. Winsel, Z. Elektrochem., Ber. Bunsenges. physik. Chem. 68, 250, 1964.
7. M. H. Gottlieb, Electrochem. Techn. 5, 12, 1967.
8. R. Suhrmann and K. Schulz, Naturwiss. 42, 340, 1955; R. Suhrmann, Z. Elektrochem. 60, 804, 1956.
9. M. A. Aia, J. Electrochem. Soc. 113, 1045, 1966.
10. H. Bode, K. Dehmelt and J. Witte, Elechtrochim. Acta 11, 1079, 1966.
11. R. Wendtland, Doctor Thesis Braunschweig 1966.

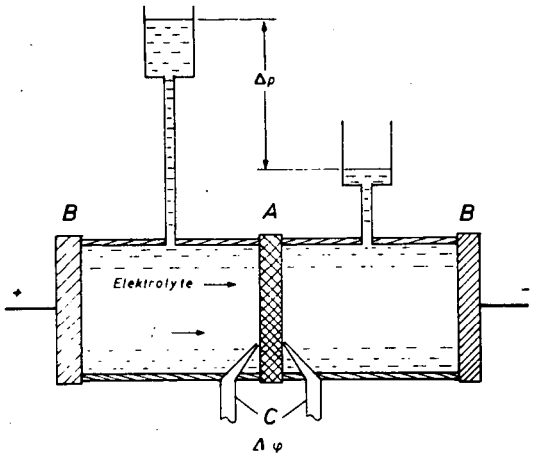

Fig. 1. Schematic arrangement for the simultaneous measurement of liquid flow resistance and electric diaphragm resistance of a porous electrode A. B outer electrodes, C Luggin capillaries.

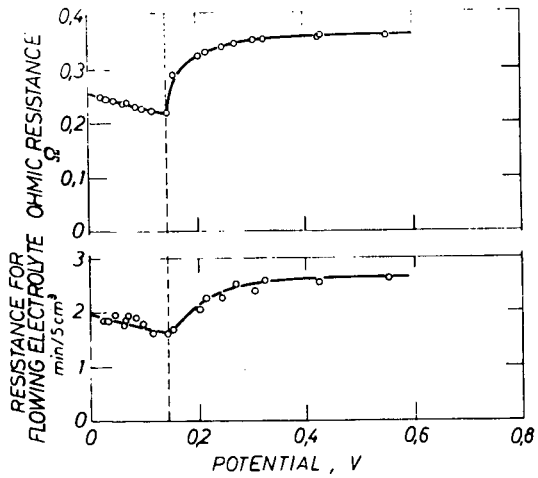

Fig. 2. Diaphragm resistance (upper curve) and liquid flow resistance (lower curve) of a Raney nickel DSK anode vs electrode potential against hydrogen reference electrode in the same 6 n KOH.

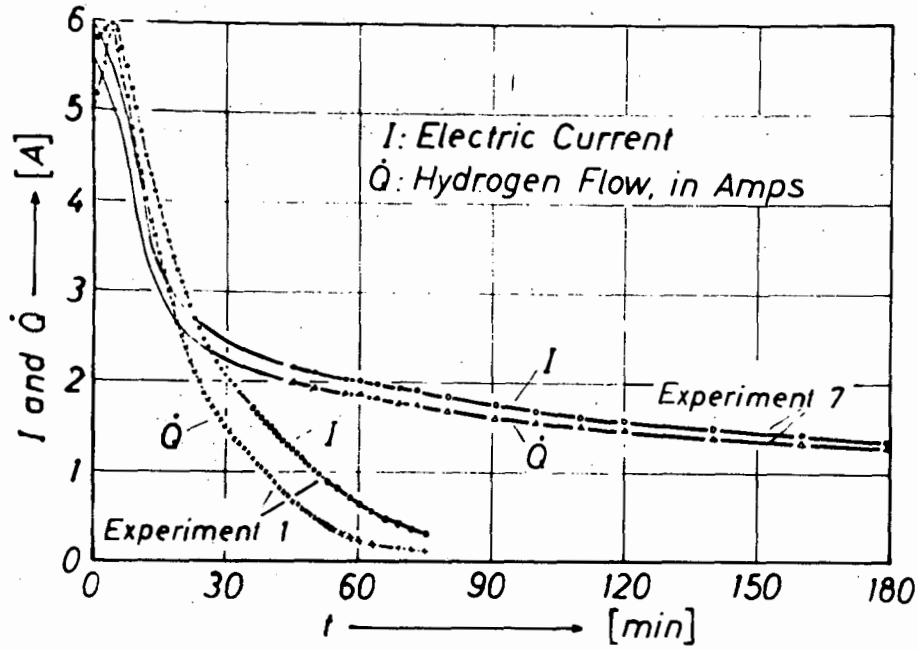

Fig. 3. Potentiostatic discharging of a Raney nickel DSK anode at a polarization of +942 mv. Experiments no. 1 and 7. Current I surpassing the equivalent hydrogen influx Q̇ is plotted vs. time in min.

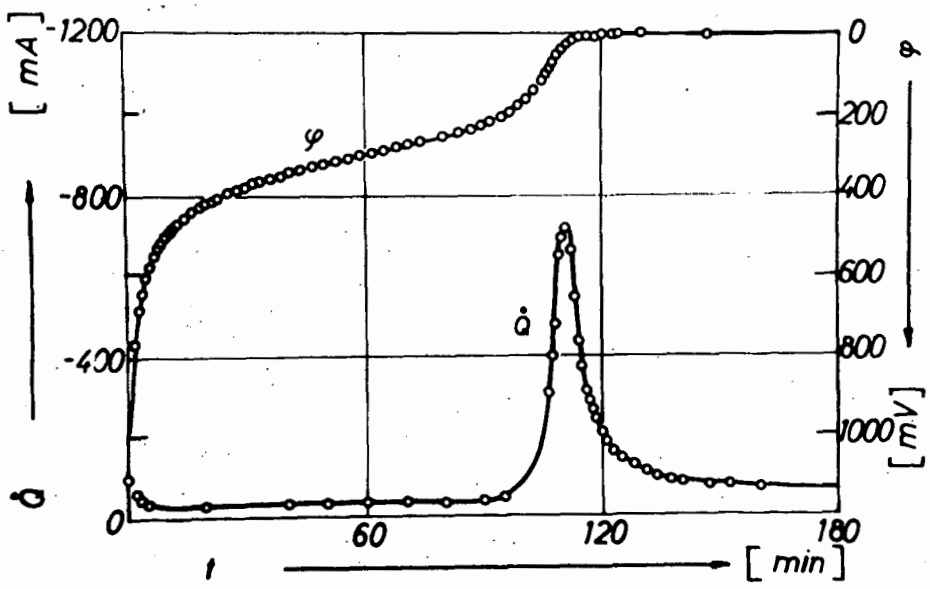

Fig. 4. Electrode potential φ against hydrogen reference electrode in the same electrolyte and influx Q̇ of hydrogen vs. time after switching off the potentiostatic loading of experiment 1 in fig. 3.

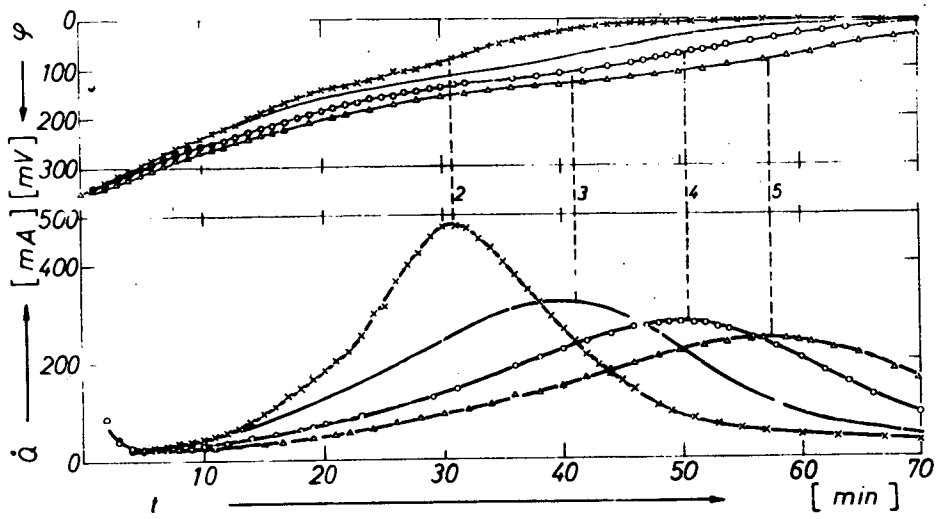

Fig. 5. Four recovering processes, showing the aging of $Ni(OH)_2$. (Meaning of the symbols cf. fig. 4). Before each experiment the hydrogen electrode was potentiostatically discharged without hydrogen pressure to +350 mv vs. hydrogen potential.

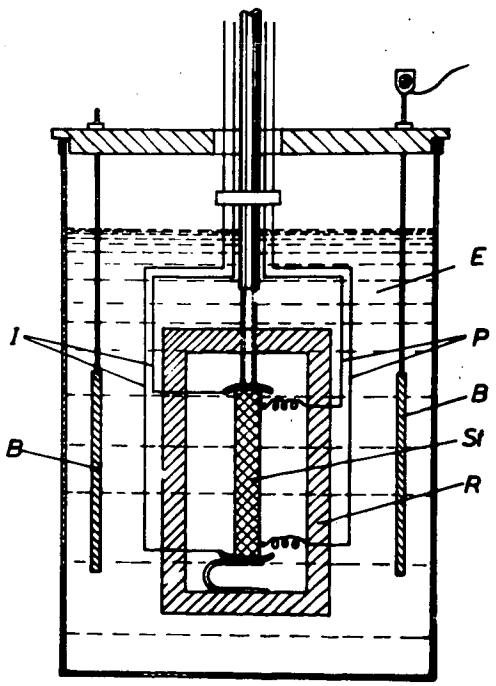

Fig. 6.
Schematic arrangement for simultaneous measurement of electrical resistance, potential and weight of a Raney nickel specimen St as function of state of oxidation.
I current contacts,
P potential contacts,
E electrolyte 6 n KOH,
B cylindrical counter electrode.

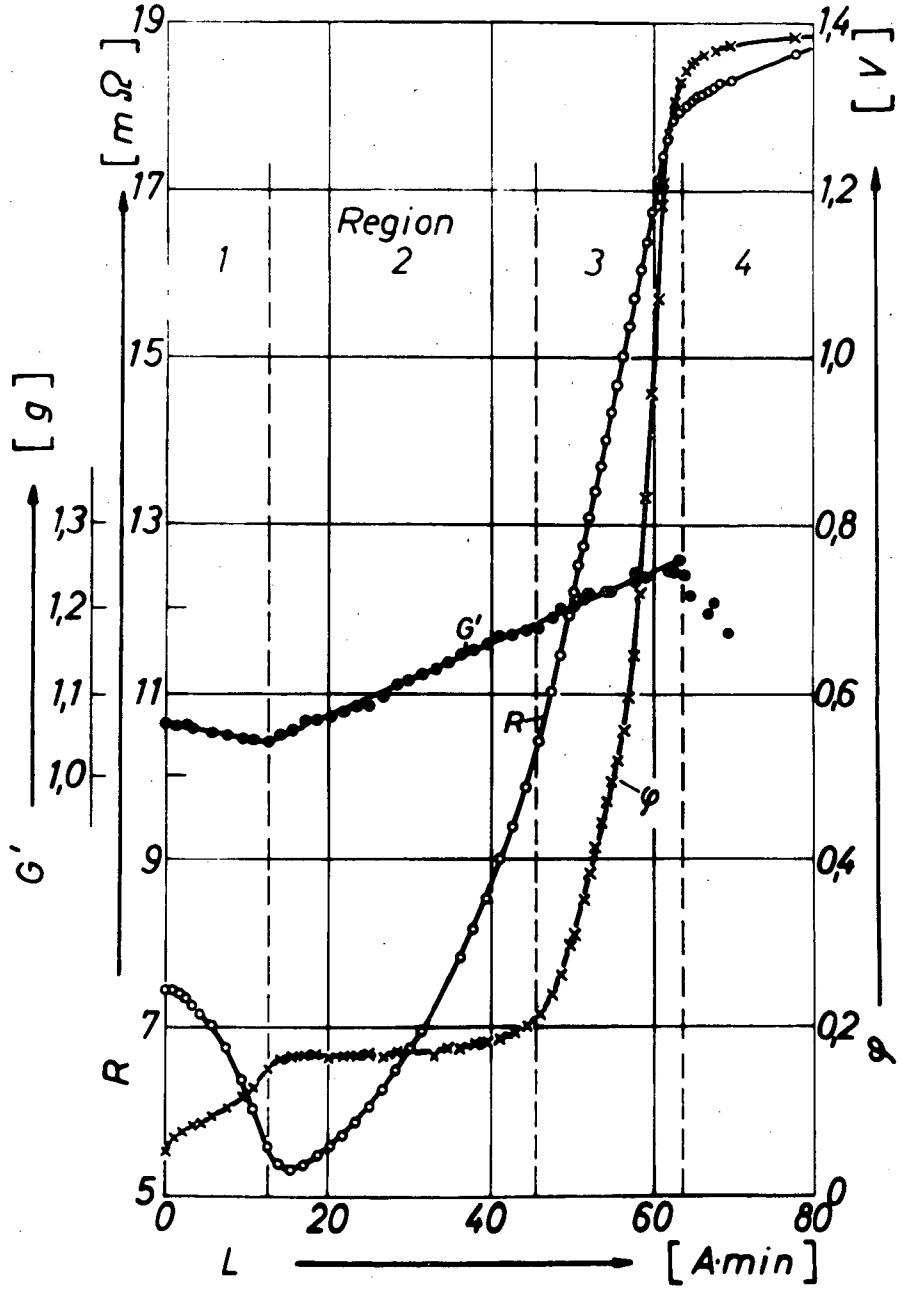

Fig. 7. Electric resistance R, potential φ in 6 n KOH against hydrogen reference electrode in the same electrolyte and apparent weight G' of a Raney nickel specimen St vs. its anodic charge L.

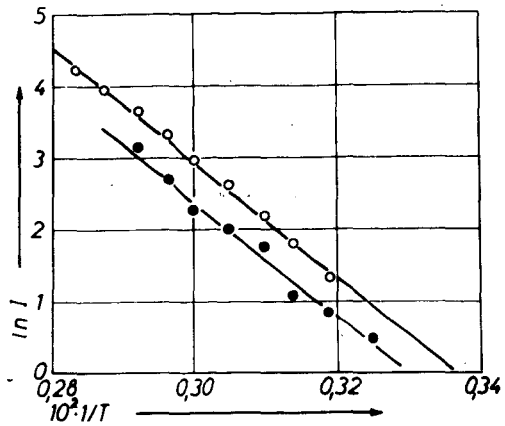

Fig. 8. Electrochemical reduction of oxidized Raney nickel as a function of the temperature T °K of electrolyte. I potentiostatic reduction current.

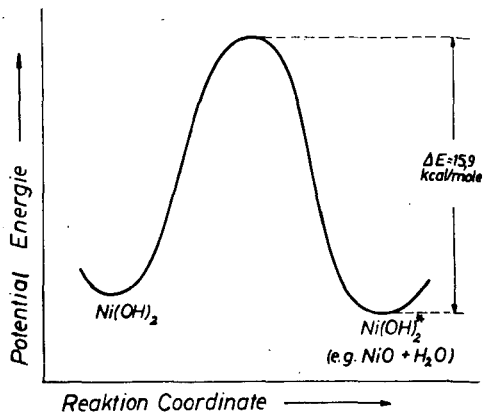

Fig. 9. Schematic of transformation of primary nickelhydroxide into the aged phase. Potential energy E vs. reaction course.

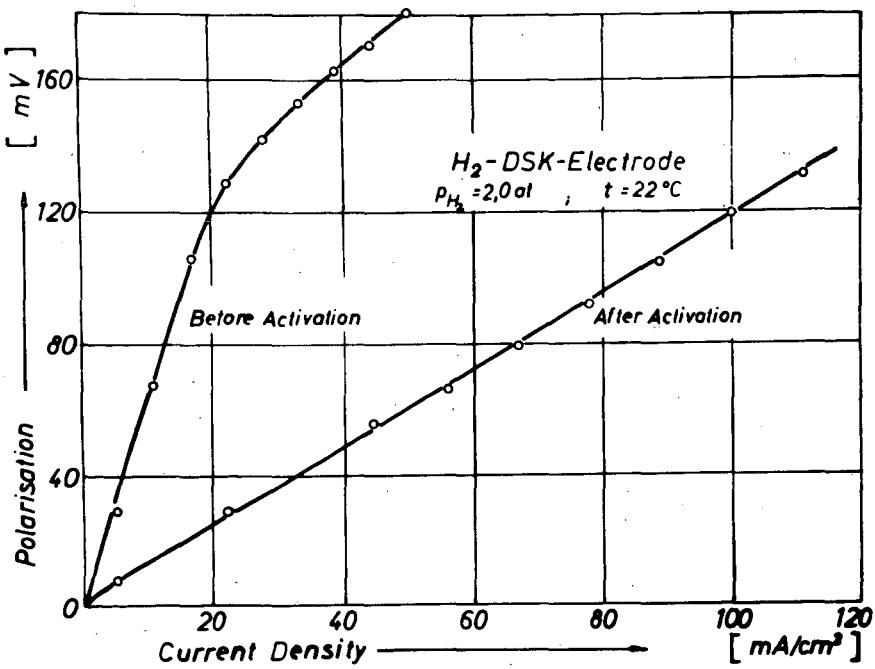

Fig. 10. Performance of a Raney nickel DSK anode showing the improvement after transient oxidation. Upper curve before, lower curve after transient oxidation and reduction.

THE FUEL CELL AIR ELECTRODE

Henri J. R. Maget

Direct Energy Conversion Operation
General Electric Company
930 Western Avenue
West Lynn, Massachusetts

ABSTRACT

The development of fuel cells for ground power applications requires detailed analysis of the dynamic behavior of air cathodes operating at atmospheric pressure and variable conditions (temperature, relative humidity). For low power levels, systems considerations such as simplicity of operation, low parasitic power requirements, safety, etc.. are to a large extent related to the air electrode. Immobilized and poly-electrolytes (ion exchange membranes) offer advantages such as: support for electrodes and barrier between reactant gases, no special requirements for well-defined electrode pore geometries and population, mechanical integrity, etc.

The ion exchange membrane air electrode is rather well suited for operation under conditions of natural convection. This approach results in a complete system without moving parts, thus in absence of parasitic power requirements. Recent work in these air electrodes has been directed towards solutions of simultaneous heat and mass transfer problems to achieve proper water management and yield quasi-uniform electrode surface conditions.

A NOVEL AIR ELECTRODE

H. P. Landi, J. D. Voorhies, W. A. Barber

Stamford Research Laboratories
American Cyanamid Company
Stamford, Connecticut

Gas diffusion electrodes suitable for use as air cathodes are a necessary component for most practical fuel cells and metal-air batteries. The general requirements of air cathodes are similar to those for other gas diffusion electrodes, namely, an optimum contact of reactant gas, electrolyte and electrode reaction sites for minimum electrode polarization. The cathodic reduction of oxygen in air, however, is impaired by the initial dilution of reactant oxygen with inert nitrogen and the tendency for nitrogen to remain in the electrode structure and thereby increase the dilution effect during cathodic discharge.

In practice, air electrodes are used in contact with free liquid electrolyte or with electrolyte confined within a solid or semisolid matrix. Electrodes designed for matrix use such as thin screen supported electrodes (1,2) are generally not applicable to free liquid electrolyte cells because of excessive macroporosity. They can, however, be adapted to such use by application of a microporous, hydrophobic backing.

Several gas electrode structures have been described (1-6) which satisfy most of the requirements for air. Clark, Darland and Kordesch (3) have described a multilayer, graded porosity electrode based on carbon which is suitable as an air cathode in alkaline electrolyte. Paper fuel cell electrodes (6), while simple, flexible and strong, are too grossly porous to use in a free electrolyte cell.

The air cathode described in this paper has a combination of pore structure and controlled hydrophobicity which make it suitable for use in free liquid electrolyte or matrix-electrolyte cells. The basic carbon filled sheet is thin, strong, flexible and conductive and can be manufactured uniformly and economically on a large scale.

Description of Electrodes

The new electrode, designated Type E, is fabricated with conventional plastics processing equipment. A thermoplastic molding compound is blended vigorously with polytetrafluoroethylene (PTFE) latex and a graphitic carbon or metallized, graphitic carbon filler. During the blending process, long fibers of PTFE are drawn throughout the plastic mass to form an interconnected network which enmeshes the filler particles. This blend is molded into a flat sheet, and the thermoplastic is then extracted leaving a cohesive sheet of graphitic carbon catalyst bonded by PTFE fibers. This process is versatile and allows for variations in temperature, filler type, PTFE level and the addition of other ingredients to add special properties to the finished sheet. Figure 1 shows a surface replica photomicrograph of the Type E sheet.

Most PTFE bonded gas electrodes contain 10 to 30% PTFE for the combined function of mechanical bonding and "wetproofing" or gas-electrolyte interface control. A novel feature of the Type E electrode is the very low level, in the range of 2 to 8% PTFE, which is capable of performing this dual function effectively. An obvious advantage of this low PTFE level is the very high percentage of conductive and catalytic components which can be incorporated into a highly porous structure.

The physical properties of typical Type E electrode sheets made in this manner are shown below.

Table I

Properties of Type E Sheet

Composition	95% graphitic carbon, 5% PTFE
Thickness	0.02 inch
Pore Volume	65%
Pore Distribution*	67% (0.1-1 μ) 15% (1-10 μ) 10% (> 10 μ)
Tensile Strength	100 psi
Tensile Modulus of Elasticity	9000 psi
Resistivity (Dry)**	50 ohms per square
Air Permeability	1.1 $\frac{cc}{cm^2 \times min \times mm\ Hg}$

* By mercury porosimeter (volume % distribution).
** Measured with contacts along opposite sides of a one-inch square (50 pounds on contact).

A highly effective convected air cathode is fabricated by laminating two thin (0.005 to 0.010 inch) sheets of Type E electrode onto both sides of an open mesh expanded nickel screen with moderate heat and pressure. The sheet facing the electrolyte in a cell is catalyzed while the side facing the ambient air is an uncatalyzed, highly porous, graphitic carbon layer of the same type. This structure is referred to as ESE (S for screen).

Catalyzation of the Electrode

The carbon-PTFE sheet functions well as an oxygen or air electrode in alkaline electrolyte without additional catalyst, but in most cases it will be desirable to incorporate a catalyst metal in the structure. This can be done by blending a precatalyzed carbon into the structure instead of the uncatalyzed carbons. Catalysts such as platinum, silver and silver-palladium alloy will be described. Or, the catalyst can be applied after fabrication of the Type E sheet by any of several chemical or thermal-chemical means.

An example of a post platinization technique is impregnation with chloroplatinic acid followed by reduction with dry hydrogen at 200-225°C. High temperatures should be avoided, however, to prevent distortion of the sheet near the softening point of PTFE.

Electrochemical Measurements

Two kinds of current-potential measurement have been made on Type E air cathodes: (1) hydrogen-air matrix cell measurements in acid and alkaline electrolyte with a standardized hydrogen counter electrode and (2) half cell measurements on the ESE structure in free 6N KOH with naturally convected air. The hydrogen-air matrix cell shown in Figure 2 is used for terminal voltage-current density measurements which reflect the air cathode activity. In this test, Type E electrodes are compared with Cyanamid PTFE bonded, thin screen electrodes (1) designated Type B for graphitic carbon supported platinum and Type A for platinum black.

The half cell air cathode measurements are made in a cell shown in Figure 3. The electrodes are vertically oriented and exposed to the ambient air. A controlled current is applied to the cell such that the counter anode, which can be another ESE electrode, evolves oxygen, and air is reduced at the working cathode. The cathode potential is measured with respect to an Hg/HgO/6 N KOH reference electrode through

a Luggin capillary. The reference is calibrated occasionally with respect to the hydrogen-platinum black electrode in the same solution. The measured potential of H_2(Pt)/6N KOH/HgO/Hg is 0.93 V at 25°C.

Because of a rather slow attainment of the steady state cathode polarization at a given current density with naturally convected air at room temperature, a cathodic preconditioning is required for meaningful results. The procedure used is to predischarge the air cathode for about 25 minutes at 50 mA/cm² before measuring the polarization curve. The polarization values are then measured after three-minute equilibration at each current density. The details of the transient response of dry, untested electrodes will be discussed further in the RESULTS section.

RESULTS AND DISCUSSION

Matrix Cell-Acid and Alkaline Electrolyte

The polarization of Types A, B and E air cathodes at room temperature and 70°C in 5N H_2SO_4 is shown in Figure 4. The Type E cathode containing 1.9 mg/cm² platinum is essentially equivalent to a Type B screen electrode at 2.5 mg/cm² platinum. For comparison, air data obtained with a Type A cathode at 9 mg/cm² platinum black are also shown.

In Figure 5 is shown the matrix fuel cell air performance of the same Type E cathode compared with a similar Type B on nickel screen in 5N KOH. Again the results are about equivalent. A limiting current region is apparent for these electrodes in base, but Type E is no worse than Type B in this respect. Neither type shows a limiting current in acid electrolyte over the same current range investigated in base.

Convected Air - 6N KOH, 25°C

The average steady state electrochemical performance in a free electrolyte cell of ESE type air cathodes with various metal catalysts supported on graphitic carbons is shown in Table II. The cited half cell measurements were obtained in the free electrolyte cell described previously. Low level platinum is an excellent catalyst and is stable in alkaline electrolyte for long periods under various load conditions. Silver is known to be a good catalyst for oxygen reduction but is slightly soluble in alkaline electrolyte and is degraded by repetitive changes in current density. The silver-palladium alloy is an example of a group of binary alloys with silver which represent improvements over silver in steady state performance and stability to cyclic current changes.

Platinum catalysts have been applied at several loadings by chemical or thermal-chemical deposition before or after fabrication of the Type E sheet. The results in Table III show an apparent insensitivity to catalyst loading and a slight bias to post-platinization as the best method of catalyst application. It is possible that the real utilization of catalyst surface is relatively poor and that concentration and ohmic polarization within the electrode structure dominate the cathodic activity of these electrodes.

The two structural features of ESE electrodes which are most important for convected air cathode performance are the thickness of the catalyzed E layer and the distribution of polyfluorocarbon throughout the electrode. These effects are seen in Table IV. As one would expect, polarization is decreased by reducing the thickness of the catalyst layer thereby concentrating the electrocatalyst in the current producing regions of the cathode. The lower limit of thickness is controlled primarily by fabrication considerations particularly the low cohesive strength of thin Type E layers.

Table II

Convected Air Electrode Polarization

Electrode	Catalyst Loading	$-E_{c(air)}$ (Volts vs. Hg/HgO/6N KOH) 25°C			
	(mg/cm^2)	10	20	50	100 mA/cm^2
95% Pre-Platinized ACCO* Graphite	1.1 Pt	.03	.06	.12	.21
95% ACCO Graphite Post-Silverized	9 Ag	.12	.17	.25	.35
95% ACCO Graphite Post-Catalyzed 75-25, Ag-Pd	13 Ag-Pd	.04	.08	.17	.23
95% ACCO Graphite Uncatalyzed	0	.20	.28	.40	.50
92% Darco G-60 Carbon Uncatalyzed	0	.15	.17	.22	.28

Table III

Platinum Level and Method of Catalyzation

Catalyst	Loading	$-E_{air}$ (V. vs. Hg/HgO/6N KOH)		No. of Measurements
	(mg/cm^2)	@ 50	100 mA/cm^2 (25°C)	
Post-Platinized (Method 1)	0.60	.13	.21	1
Post-Platinized (Method 2)	0.65	.13	.21	1
Post-Platinized (Method 3)	0.6	.13	.21	3
Pre-Platinized	1.1	.12	.21	6 (3 electrodes)
Pre-Platinized	2.5	.11	.19	5 (3 electrodes)

* A graphitized carbon from American Cyanamid Company (1).

Table IV

Effects of Thickness and Composition -
Pre-Platinized ESE Electrodes (2.5 mg/cm² Pt)

	$-E_{air}$ (V. vs. Hg/HgO/6N KOH)	
	50	100 mA/cm²
1. Thickness of platinized E layer		
.017 inch	.23	.38
.007 inch	.11	.19
2. Polyhalocarbon content of platinized E layer. (E backing layer - 2.5% PTFE, 2.5% Kel-F)		
4% PTFE	.14	.37
4% PTFE, 4% Kel-F	.11	.19
15% PTFE	.18	.37
3. Polyhalocarbon content of E backing layer (platinized E layer - 4% PTFE, 4% Kel F)		
25% PTFE, 25% Kel-F	.11	.36
20% PTFE	.17	.28
13% PTFE	.12	.22
2.5% PTFE, 2.5% Kel-F	.11	.19

The distribution of polyfluorocarbon in both the catalyst and backing layers is also of critical importance. In the platinized E layer this is probably a matter of a critical balance between the amounts of air and electrolyte in the structure. The sensitivity of ESE air cathodes to the polyfluorocarbon level in the backing layer is somewhat unexpected. It would appear that a relatively low level of wetproofing is necessary in the backing to bring the cathode reaction zone closer to the centrally located screen by virtue of deep electrolyte penetration. This in turn reduces the electronic conductive path to the collector screen thereby decreasing the measured half cell cathode polarization.

Transient Response

The ESE air cathode operating on convected air at room temperature with alkaline electrolyte exhibits large transients in cathode potential after instantaneous changes in current density under certain conditions. The most dramatic transient is that observed upon changing the current density from zero to a value in the range 50 to 200 mA/cm² for a cathode which has not been tested previously or preconditioned in any way. Such a transient for a 0 to 50 mA/cm² change is shown in Figure 6. Similar transients are observed for platinum-carbon, silver-carbon and carbon catalysts.

The total transient for platinum-carbon is characterized by a short term (1 to 2 minutes) and long term (2 to 20 minutes) portion. The largest part of the total transient is apparently associated with optimal wetting of the electrode structure. This occurs at open circuit and perhaps in a more significant way after application of the current. It is also likely that some of the transient is caused by cathodic catalyst activation and perhaps by rearrangement of sorbed oxygen. In the case of silver on graphitic carbon, the increase in cathode potential with time is more gradual and the time to achieve a steady state value is longer than for platinum.

There are three pretreatments which can alone or in combinations remove most of the transient for platinum-carbon: (1) presoaking in water or electrolyte for more than one hour, (2) a 25 minute precathodization in 6N KOH at 50 mA/cm^2 with air (O_2 reduction region) and (3) one or more polarization tests followed by rinsing and air drying the cathode. The fact that treatment (3) is effective in reducing the transient by up to 50% for a period of at least several days suggests the possibility of a short term irreversible activation of the catalyst.

The transient response appears to be partly associated with the cell design but independent of the feed of oxygen (air). Type E electrodes assembled in matrix fuel cells show almost no transient with flowing air, room temperature, 6N KOH. The same electrodes show a pronounced transient when assembled in a free electrolyte cell under the same conditions and with flowing air.

SUMMARY

A novel air cathode for matrix and free electrolyte type fuel cells and metal-air batteries has been described. The basic and novel component of this electrode is a thin, strong, flexible, electrically conductive sheet containing interconnected polytetrafluoroethylene fibers which bind the conductive and catalytic components into a cohesive structure. This structure is particularly suitable for use with convected air. The problem of large cathode potential transients upon first application of a moderate discharge current arises from a combination of slow wetting and catalyst activation.

ACKNOWLEDGMENT

The authors wish to acknowledge the contributions of H. P. Ledden, S. Arcano, J. Durkin and E. A. Battistelli to the experimental phase of this work and of R. G. Haldeman in useful discussions on the fabrication and mechanism of air cathodes.

REFERENCES

1. R. G. Haldeman, W. P. Colman, S. H. Langer and W. A. Barber, "Advances in Chemistry," Vol. 47, "Fuel Cell Systems," p. 106 American Chemical Society, Washington, D. C. (1965).

2. L. W. Niedrach and H. R. Alford, J. Electrochem. Soc., 112, 117 (1965).

3. M. B. Clark, W. G. Darland and K. V. Kordesch, Electrochem. Tech., 3, 166 (1965).

4. E. W. Justi and A. W. Winsel, "Kalte Verbrennung" Fuel Cells, Steiner Verlag, Weisbaden (1962).

5. A. M. Adams, F. T. Bacon and R. G. H. Watson in "Fuel Cells," Chemical Technology, Vol. 1, Will Mitchell ed. p. 129 (1963).

6. W. A. Barber and N. T. Woodberry, Electrochem. Tech., 3, 194 (1965).

Fig. 1. SURFACE REPLICA PHOTOMICROGRAPH OF TYPE E ELECTRODE

A: PTFE FIBERS
B: ACCO GRAPHITIC CARBON PARTICLES

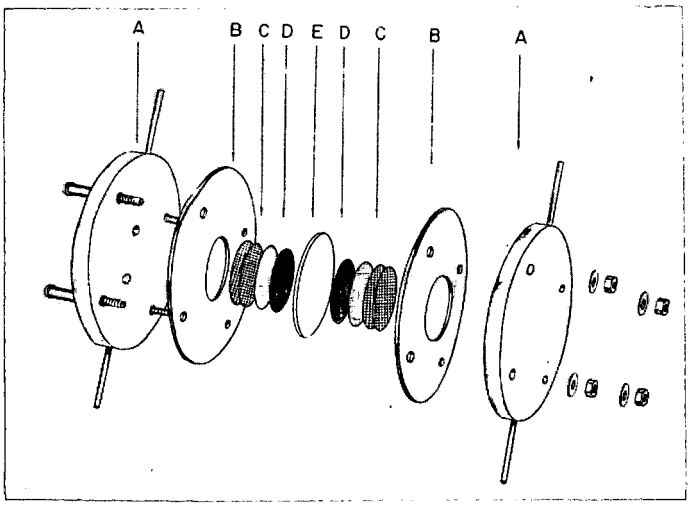

Fig. 2. MATRIX CELL

A. FACE PLATES
B. GASKETS
C. COLLECTOR SCREENS
D. ELECTRODES
E. MATRIX

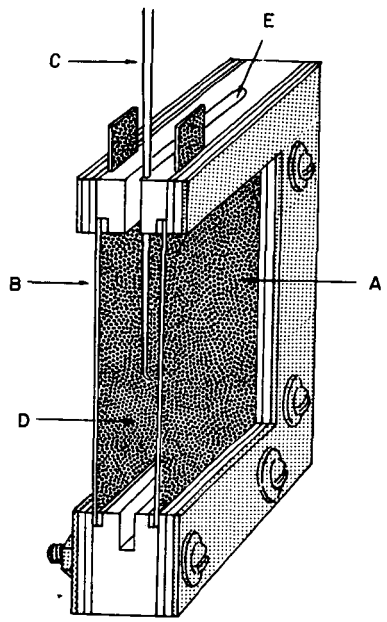

Fig: 3. AIR ELECTRODE TEST CELL

A: CONVECTED AIR ELECTRODE
B: COUNTER ELECTRODE
C: REFERENCE PROBE (6 N KOH)
D: FREE ELECTROLYTE CHAMBER
E: SLOT FOR ZINC ANODE

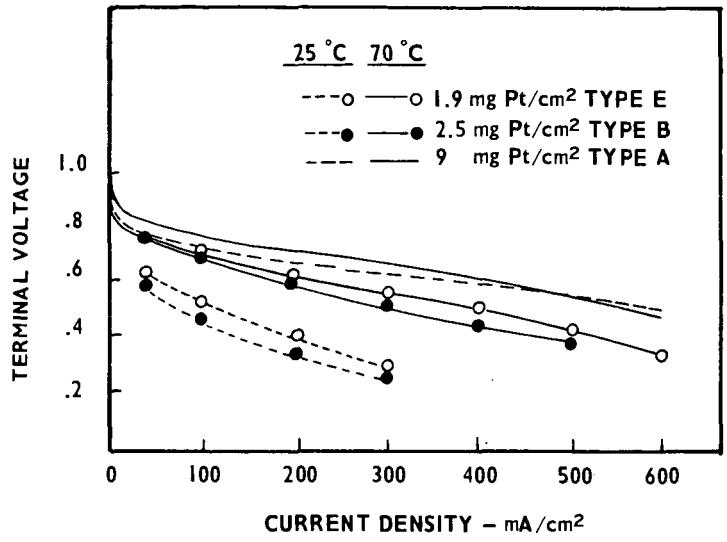

FIG. 4: CURRENT–VOLTAGE CURVES – HYDROGEN/5 N H_2SO_4/ AIR, @ 25°C AND 70°C

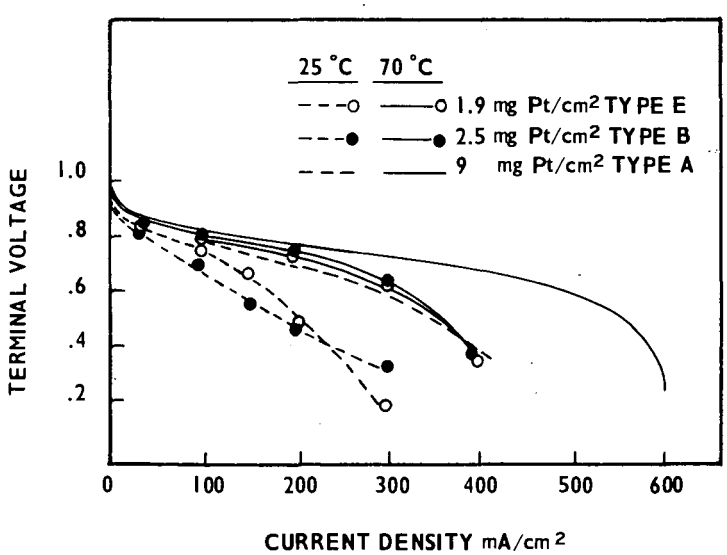

FIG. 5: CURRENT–VOLTAGE CURVES – HYDROGEN/5 N KOH/AIR @ 25°C AND 70° C

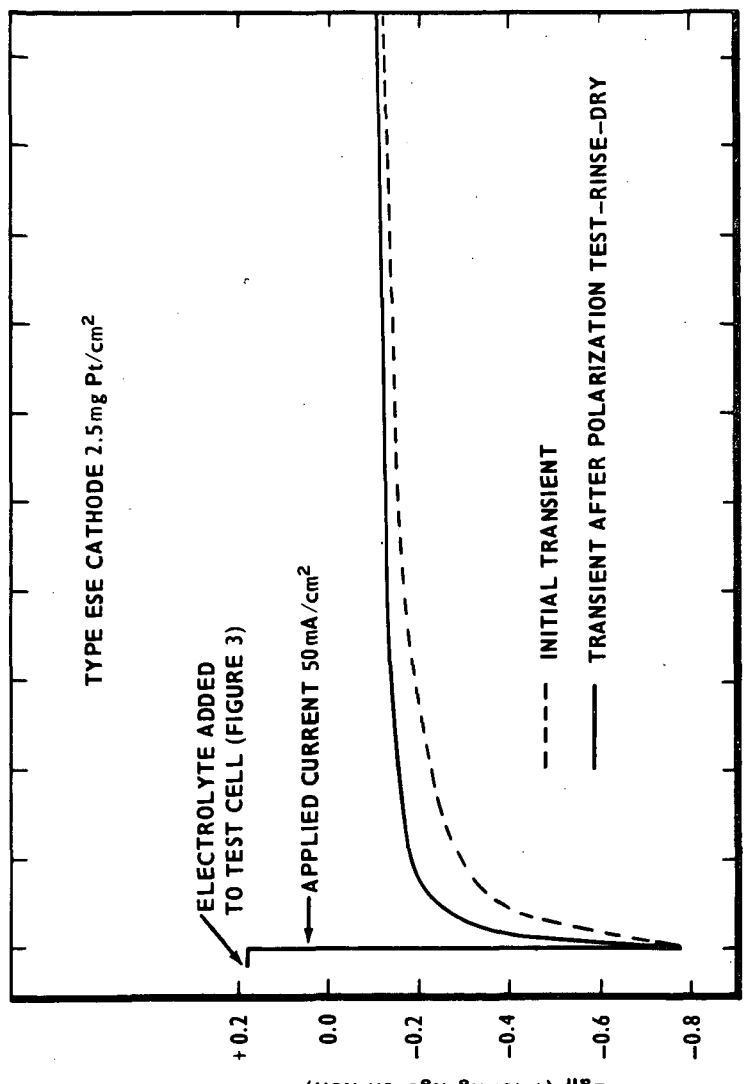

FIGURE 6: AIR CATHODE TRANSIENTS – 6N KOH, 25 °C

A NEW CONCEPT OF THE STRUCTURE OF THE POROUS GAS DIFFUSION ELECTRODE

Dr Olle Lindström

Central Laboratories, ASEA, Västerås, Sweden

1. Introduction

The author described the wetted porous fuel cell electrode in 1963 in the following way (1,2): "The reaction zone is assumed to lie in this extended meniscus. The walls in the gas-filled pores in the gas-diffusion electrode are thus covered by a thin film of electrolyte (cf. Fig. 1). The reaction gas is dissolved in the electrolyte film, diffuses to the electrode surface and reacts there so that electrons are taken from, or yielded to, the electrode. The reaction products diffuse away from the reaction site, which is released for a new reaction. The electrolyte film should obviously cover large surfaces in the interior of the porous electrode and stand in good communication with both the gas side and the electrolyte side." - This thin film hypothesis was presented independently by several fuel cell workers at that time. This was quite natural, since it is difficult to conceive that a sharp three-phase boundary could exist in a wetted porous electrode, where the contact angle is almost zero. Will was the first to present experimental evidence of the existence of an electrolyte film in the case of solid, partially immersed electrodes (3,4).

The studies of the gas-diffusion electrode have been dominated by the mathematical treatment of the system of basic equations governing the electrode processes. As a rule, the gas diffusion electrode is then considered to be a population of pores, irrespective of whether the theory utilises the thin-film hypothesis of the hypothesis of a linear three-phase boundary.

The question of structure, however, is the key problem in this connection. The creditable attempts made up to now to give an adequate and effective description of the structure of the porous gas-diffusion electrode on the basis of pore models have not been entirely successful. Ksenzhek admits that attempts to correlate the properties of porous electrodes with the simple pore models have only resulted in greater complexity (5). The porous electrode is therefore conceived by Ksenzhek to be a pseudohomogeneous medium, the properties of which are characterised by effective parameters defining the mass transfer and kinetic properties of the medium. Micka has coined the expression "fine-structure models" (6) for this type of continuous or semi-continuous electrode model, and this has also been utilised by Ksenzhek (5) and Micka in later works as well as by Newman and Tobias (7).

The electrode model presented below is an attempt in another direction. A geometrical model is developed, which corresponds as far as possible to reality. The electrode structure is characterised with the aid of structure parameters having a real physical import. The working electrode is conceived as a compressed powder with the powder grain surfaces covered by a film of electrolyte, cf. (4,5). This theory has previously been called the "powder film theory" (8,9) because of this conception of the electrode.

The cohesive gas phase between powder grains in the porous electrode structure is conceived as being a network of interstices. This initial concept is supplemented by a model of the cohesive film on the grain surfaces, the film network, which is utilised for describing the mass transfer conditions along the electrolyte film. The electrode structure can then be characterised on the basis of these models with the aid of structure parameters, mainly the film area, film perimeter, film thickness, interstice width, interstice tortuosity and film tortuosity. The structure parameters can be determined in a non-electrochemical way by means of dilatometer measurements, film resistance measurements, etc., under actual service conditions. The model therefore forms a good starting point for the formulation of an absolute electrode and fuel-cell theory.

2. Gas penetration into a porous gas-diffusion electrode

Gas-diffusion electrodes are often produced with the help of powder metallurgy by pressing (or rolling) of metallic powder, followed by a sintering process. Pressing gives the electrode plate a certain strength, which is considerably improved during sintering. During sintering, the grains in the contact surfaces become bonded under the influence of surface forces and plastic deformation. The structure developed during the pressing, however, remains largely speaking unaltered. This is especially true of active nickel electrodes, which are sintered at a low temperature, 500 to 600°C.

A section through the coarse layer of a working electrode is shown in Fig. 2. The powder grains are assumed to be covered by a cohesive electrolyte film. Cohesive electrolyte bridges are formed across narrow passages. The cross-sectional area is thus divided up into electrode material, film, electrolyte bridges and gas-filled spaces.

The electrode may be conceived as being a stack of sufficiently thin discs, electrode sections, which can be formed from a series of sections parallel to the electrode surface (in a homogeneous electrode material the structure of the sections is not affected by the orientation), cf. Fig. 3. The total electrode area in 1 cm^2 electrode sections available for electrochemical reaction consists of the electrode area covered by the electrolyte film, i.e., $dA = N \cdot dL \cdot s$, where N is the film length or film perimeter available, and s a tortuosity factor, the interstice tortuosity. (Electrocatalytically active material is assumed to be uniformly distributed over the electrode surface.) The area of the film covering the electrode, which can be called the film area dA, is sometimes considerably less than the actual area of the underlying electrode material.

With low differential pressures and an electrode body completely filled with electrolyte, the surface forces binding the electrolyte to the electrode material in the outer layer of the electrode exceed the gas pressure acting on the liquid body. When a certain critical pressure is reached, however, the first minute quantity of gas begins to penetrate into the electrode, see Fig. 4. The gas pressure, which acted on that part of the liquid body in the outer layer which had been forced back, then very slightly exceeds the capillary force which acted on this part of the liquid body at the instant when it was displaced. As the pressure increases, the electrolyte is displaced more and more for the same reason. The volume of the electrolyte displaced is equal to the cross-sectional area of the newly formed gas-filled spaces in a typical electrode section multiplied by the thickness, L, of the coarse layer.

An increase of dP for a differential pressure P, dyn/cm^2, results in a further gas penetration, dV, corresponding to a cross-section with an area equal to dV/L and the film perimeter dN. If the surface tension is denoted σ dyn/cm and the contact angle θ, the balance between the differential pressure and the capillary force for the elements in question gives

$$dN \cdot \sigma \cdot \cos \theta = P \cdot dV/L \qquad (1)$$

Dilatometer experiments, see below, give $V = f(P)$, from which

$$dV = f'(P) \cdot dP \qquad (2)$$

and

$$dN \cdot \sigma \cdot \cos \theta = P \cdot f'(P) \cdot dP/L \qquad (3)$$

are obtained.

Integration gives

$$N = \frac{1}{L \cdot \sigma \cdot \cos \theta} \int_0^P P \cdot f'(P) \cdot dP \qquad (4)$$

A number of significant conclusions can be drawn from Eq. (4). A high differential pressure P and a steep derivative f'(P) give a high value for N and thus a large film area for electrochemical reaction. A large film area clearly cannot be combined with a structure permitting low differential pressures, except when there is some means of altering the surface tension or contact angle.

Provided that V is an unequivocal function of P (no hysteresis), the integration, Eq. (4), can be accomplished and N is obtained as a function of P. The film area, A, is then determined with the aid of the interstice tortuosity s. Fig. 5 shows the film perimeter N as a function of the differential pressure. Since Eq. (4) has been derived on the assumption that there is no hysteresis, only the ascending curve branch in Fig. 4 has been utilised for the calculations.

The electrode activity for decreasing gas pressure often lies at a higher level than for increasing differential pressure, cf. Fig. 4. The size of the gas-filled volume per cm^2 electrode area, V, as a function of the differential pressure displays a similar hysteresis effect, which can also be seen from Fig. 4. A possible explanation of the hysteresis effect is that the electrode structure is not ideal with regard to internal communications. Certain spaces are blocked by small passages sealed with a liquid lock (the ink-stand effect). A higher gas pressure is required to open the passages and reach the blocked-off spaces.

The hysteresis effect depends partly, however, on the rate with which the process takes place. This suggests that electrolyte transport in the porous electrode is a slow process, which is not surprising in view of the large surfaces and the thin film layers.

Two different kinds of electrolyte transport can be conceived: plug flow and film flow. Plug flow would correspond to the normal flow in a pipe under the influence of a pressure gradient. This assumes that the entire cross-section in the pipe/pore is filled with liquid. The film flow would represent transport of liquid through the displacement of liquid from film regions having a higher thermodynamic potential to regions having a lower potential. Film flow compared with plug flow must be a less efficient process for material mass transfer, owing to greater frictional resistance and a low driving force. It should be possible, however, for mass transfer by means of film flow to take place independent of ink-stand structures, etc. This means that it should be possible for the hysteresis to be more or less eliminated, if the changes in pressure are made sufficiently slow to give time for the film flow. This is not contradicted by the experiments. Hysteresis is treated with the aid of an interstice model. The space between the grains in an electrode section, cf. Figs. 2 and 3, is assumed to be divided into interstices, cf. Fig. 6. These interstices are assumed to be gradually and successively filled with electrolyte as the differential pressure drops, or with gas as the differential pressure increases. This presentation is thus based on the geometrical relationships during the constriction process.

An interstice has the width D, height G and thickness equal to that, dL, of the electrode section. (D does not include the film.) The interstice thickness dL is constant and the height G is assumed to be constant so that the interstice cross-section will also be constant ($= dL \cdot G$). Under these conditions the interstice volume is consequently directly proportional to the interstice width D. Each interstice width, D, clearly corresponds to a certain differential pressure, P, which is just sufficient for gas penetration into the interstice, provided that the interstice in question can freely communicate with the gas and electrolyte side via a chain of other interstices of at least the same width.

The distribution of the interstices can be illustrated with the aid of frequency distribution curves. These can also be presented in histogram form. The associated differential pressure, P, can also be used instead of the interstice width, D, as an independent parameter in these histograms.

All interstices belonging to a given pressure class will not be filled with gas when the pressure is increased to the relevant pressure P_n under the conditions applicable to the rates of change of the pressure. To permit a simple numerical treatment of the hysteresis curve, it is assumed that a continued rise of the differential pressure to the next higher pressure class causes all interstices of the affected size not previously filled with gas now to be filled with gas. When the pressure returns to its original value, some of the interstices in question are filled with electrolyte. As a further simplification, it is assumed that all the interstices in question are filled with electrolyte again, when the pressure is reduced to the next lower pressure class.

With these assumptions it is possible to recalculate the experimentally determined hysteresis curve for the volume of the gas that has penetrated into the electrode as a function of the differential pressure to associated hysteresis curves for the film perimeter and film area. An Algol programme is utilised for the numerical treatment.

The gas penetration into the electrodes for varying differential pressure has been measured with the aid of a dilatometer, see Fig. 7. The interstice tortuosity,

s, can be determined in a conventional manner by means resistance measurements across an electrode completely filled with electrolyte in a measuring cell, see Fig. 8.

3. Structure of the electrolyte film

The area and thickness of the film are of importance to the transport of gas, e.g., hydrogen or oxygen, to the electrode surface from the gas phase right through the film to the electrode surface. Other reactants and reaction products are transported, however, in the liquid phase along the film to or from the reaction sites in the electrode surface. These transport paths run along the film covering the powder grains, and from grain to grain via electrolyte bridges and the sintered functions between the grains. This structure is called the film network, see Fig. 9. The ionic resistance of the film network and its resistance to diffusion of uncharged species depend in a similar manner on the structure. The resistance of the film network to material mass transfer can therefore be assessed through measurement of the ionic film resistance.

The available film area, A, in an electrode area of 1 cm^2 can be presented as an equivalent rectangular disc from the transport point of view with the electrode in question having a length f·L and thickness F. The transport is thus assumed to take place in the longitudinal direction.

The film tortuosity f has another significance than the interstice tortuosity, s, previously introduced. Film resistance measurements are carried out in a cell similar to that used for determining the interstice tortuosity, cf. Fig. 8. In this case, measurements are performed on electrodes provided with a fine layer on both sides of the coarse layer with the gas applied to a ring arranged around the periphery. Measurements can also be performed on normal electrodes provided with only one fine layer with the aid of a thin auxiliary fine-layer plate pressed direct on to the gas side of the test electrode.

4. Typical experimental results

Table 1 shows examples of the results obtained on different types of porous gas-diffusion electrode, but not ASEA's production electrodes.

The tortuosity factor s is utilised for determining the film area A from the film perimeter U. Values around $s = \sqrt{2}$ could be expected which corresponds to the mean value of the relationship between the surface of a plane surface element and its projection on a plane having an arbitrary slope relative to the surface element. This is in close agreement with the experimentally determined values of s according to Table 1.

The film areas for the oxygen electrodes at the maximum differential pressure in Table 1 agree fairly well with respect to order of magnitude with corresponding BET surfaces and with pore surfaces calculated from determinations on pore diameters with mercury porosimeter. As far as hydrogen electrodes are concerned, which contain nickel boride catalyst, the BET surface is considerably larger than the film area. These hydrogen electrodes clearly display a considerable atomic roughness compared with the oxygen electrode, which is also reflected in a higher value of the film thickness.

The mean value of the interstice width, $\bar{D}$, agrees rather well with the mean pore diameters determined with the mercury porosimeter, with the exception of the AMT electrode. The values of the film tortuosity, f, listed in Table 1, are very approximative owing to the inexactness of the film thicknesses determined here. When the transport properties of the film in the longitudinal direction are to be assessed, it is preferable to utilise the resistance z as a direct measure of this transport property of the film network.

Fig. 10 shows the film area as a function of the differential pressure for an oxygen electrode in 7-N KOH at 25°C. The current density at -100 mV versus Hg/HgO is plotted on the same diagram together with the film resistance. As the differential pressure increases, the current density rises in proportion to the film area, and then passes through a maximum for a further increase in the differential pressure, when the film resistance starts to become considerable. These conditions are suitable for a further simple analysis.

5. Division of electrode resistance into component terms

Limiting current density cannot be observed in technically interesting electrodes at the recommended service conditions. The current-voltage characteristic of a fuel cell during short-term runs is generally linear down to cell voltages close to zero. The apparent internal resistance in the fuel cell is thus practically speaking constant for a varying load, but with otherwise constant operating conditions, if low loads are neglected.

The internal resistance of the fuel cell can be divided up in the first place into three terms: one term associated with the ionic conductivity in the electrolyte space and the electronic conductivity in electrodes and current collectors, one term associated with the specific cathode functions and one term associated with the specific anode functions. These terms, which can each be experimentally determined are also largely speaking constant and independent of the current density, with the exception of oxygen electrodes under low load.

The apparent electrode resistance in its turn can be further divided into terms, partial resistances, having a physical significance. These partial resistances can be conceived as varying in such a way that their sum total will remain constant in agreement with experimental observations. As an alternative, the different component resistances are each constant, to the extent that they are not negligibly small compared with the total electrode resistance.

The reaction path from the gas space to the inside of the fine layer via the electrochemical reaction step in a section of an electrode is assumed to pass across three series-resistors. The first resistor can represent the resistance to gas diffusion across the film and is denoted R_g. The second resistor describes the slowness of the electrochemical reaction and is denoted R_r. The third resistor is associated with the slowness of the ion transport along the film and is denoted R_i. The reaction resistance R_r is assumed to be constant for the relevant low current densities, corresponding to a linear relationship between current density and activation polarisation. The gas-diffusion resistance, R_g, is inversely proportional, with the other conditions being constant, to the film area in the section dA and the absolute pressure p. (The film thickness F is assumed to be constant.) The ion migration resistance R_i is directly proportional to the film resistance z. The total resistance R_t can be written as

$$R_t = R_g + R_r + R_i = \frac{C_1}{dA \cdot p} + C_2 + C_3 \cdot z \qquad (5)$$

where C_1, C_2 and C_3 are assumed to be constant to the extent that the component resistances are small in relation to the total resistance. The quantities dA and z vary with the differential pressure, etc. If the electrode is assumed to be very thin, Eq. (5) may apply to the entire coarse layer, and therefore the film area A is introduced instead of dA in Eq. (5). The resistance terms R_t, R_g, R_r and R_i will then have the quantity ohm $\cdot$ cm^2 and represent weighted mean values.

Despite this considerable simplification of the actual conditions, Eq. (5) has been found to result in a qualitative agreement also with the relatively thick electrodes utilised for these measurements.

The film diffusion is the decisive factor for low film areas, and therefore the constant C_1 can be easily estimated from data for very low differential pressures. The constant C_1 is thus estimated from the plotting of the electrode resistance R_t as a function of the inverted product film area x absolute pressure, i.e., $1/(A \cdot p)$. (The electrode resistance for the hydrogen electrode has been determined through division of 0.10 V by the current density, in A/cm^2, at 0.1 V polarisation, and for the oxygen electrode by division of 0.17 V by the current density at -0.1 V versus Hg/HgO.) A straight line is drawn through the origin and points corresponding to small film areas, where the diffusion through the film is assumed to be rate-determining, Fig. 11. As a rule, the cluster of points is deflected near the Y-axis and intersects this at the ordinate, which does not lie at zero because other processes than diffusion bacome rate-determining for higher current densities. With the constant C_1 determined in this manner, $R_r + R_i = R_t - C_1/A \cdot p$ is plotted in a new diagram as a function of the film resistance z. A straight line is drawn through points associated with higher resistance values, cf. Fig. 12. This gives the constant term C_2, which is the ordinata in the origin, and the constant C_3, which is the slope coefficient for the line of regression. The constants are tested by means of calculation of current densities, which are compared with the measured values. As a rule, this gives a satisfactory relationship with a straight line across the entire range from very low current densities to high ones.

In this way it is clearly possible to divide up the apparent electrode resistance into a constant term, a term determined by the film area and a term determined by the film resistance, cf. Table 2. The constant term plays a relatively important role for the experimental electrodes and the comparatively low temperatures used during the measurements for Table 2, which implies that the electrocatalytic activity is the limiting factor in these cases. Table 2 also shows how the three component resistances vary with the differential pressure and thus how the rate-determining step depends on the differential pressure.

Table 3 lists calculated values of the electrode polarisation for the oxygen electrode type AHT at 50°C in Table 2. These calculated values agree with the measured value of 0.17 V across the entire hysteresis curve, which must be interpreted as indicating that Eq. (5), at least for this type of porous gas-diffusion electrode, effectively presents from the practical point of view the electrode resistance and its dependence on the structure parameters.

Table 1. Structure parameters for different types of fuel-cell electrodes

Type	Temp.	Differential pressure		Interstice tortuosity	Film area A	BET surface	Pore area	Mean interstice width	Mean pore diameter	Film thickness	Film resistance	Film tortuosity
	°C	Max.	Service	s	cm^2/cm^2	cm^2/cm^2	cm^2/cm^2	$\bar{D}\cdot10^{-5}$ cm	10^{-5} cm	$F\cdot10^{-5}$ cm	z ohm·cm	f
AHT (oxygen)	50	-	2.2	1.45	1000	3500	2980	8.0	7.6		29	~7
		3.4	-		2200		3900	6.3	7.1	<0.01	135	~1
-"-	25	-	2.2	1.49	860	3500	2930	8.6	7.6		23	~5
		3.4	-		2300		3900	5.9	7.1	<0.01	124	~1
ALT (oxygen)	25	-	1.2	1.69	130	2000	1150	42	15.0		52	~3
		2.6	-		1230		1740	8.1	12.5	0.02	> 358	~2
CHT (hydrogen)	25	-	3.0	1.31	1370	15000	2340	5.9	5.1		74	~8
		3.4	-		2430			5.9		0.5	~100	~5
CHT (hydrogen)	25	-	2.0	1.49	630	15300	1360	10	7.9		39	~8
		3.4	-		1250		1980	8.3	7.2	0.8	103	~6

Table 2. Calculated partial resistances for different types of fuel-cell electrodes as a function of the differential pressure (ascending branch of the hysteresis curve).

Type	Temp. °C	C_1 x 10^{-8} ohm·dyn	C_2 ohm·cm^2	C_3 cm	Differential pressure P · 10^{-6} dyn/cm^2	Film area A cm^2/cm^2	Film resistance z ohm · cm	Calculated resistance values R_g ohm·cm^2	R_r ohm·cm^2	R_i ohm·cm^2	R_t ohm·cm^2
AHT (oxygen)	50	2.4	0.85	0.0086	1.0	28	6.1	4.3	0.85	0.05	5.2
					1.8	450	9.2	0.18	0.85	0.08	1.1
					2.2	1000	29	0.07	0.85	0.25	1.2
-"-	25	7.4	1.7	0.023	1.0	13	8.3	29	1.7	0.19	31
					1.8	280	10.2	0.94	1.7	0.23	2.9
					2.2	860	23	0.27	1.7	0.53	3.5
AMT (oxygen)	25	2.8	4.3	0.0098	1.0	25	20	5.6	4.3	0.20	10
					1.2	130	52	0.98	4.3	0.51	5.8
					2.0	1000	360	0.09	4.3	3.5	7.9
CHT (hydrogen)	25	20	2.5	0.0038	1.0	10	8.5	100	2.5	0.03	103
					1.8	14	9.4	51	2.5	0.04	54
					3.0	1370	74	0.36	2.5	0.28	3.1
CMT (hydrogen)	25	1.2	2.0	0.023	1.0	40	8.2	1.5	2.0	0.19	3.7
					1.6	290	25	0.16	2.0	0.57	2.7
					2.0	630	39	0.06	2.0	0.90	3.0

Table 3. Calculated electrode polarisation for experimental electrode type AHT at 50°C (cf. Tables 1 and 2)

Differential pressure P · 10^{-6} dyn/cm^2	Direction of pressure change	Film area A cm^2/cm^2	Film resistance z ohm · cm^2	Calculated resistance R_t ohm · cm^2	Current density at 0.17 V polarisation I A/cm^2	Calculated polarisation V
1.0	up	28	6.1	5.2	0.039	0.20
1.8	"	450	9.2	1.1	0.123	0.14
2.6	"	1440	61	1.4	0.111	0.16
3.4	max.	2200	137	2.0	0.081	0.16
2.6	down	1970	95	1.7	0.108	0.18
1.8	"	1070	52	1.4	0.132	0.18
1.0	"	110	18	2.1	0.095	0.20

References

1. Lindström, O., Teknisk Tidskrift 93, 593 (1963).

2. Lindström, O., ASEA Journal 37, 3 (1964).

3. Will, F.G., J. Electrochemical Soc. 110, 145 (1963).

4. Will, F.G., J. Electrochemical Soc. 110, 152 (1963.

5. Ksenzhek, O.S., in Bagotskii, V.S. and Vasilév, Y.B., "Fuel Cells", Consultants Bureau, New York, 1966, p. 1.

6. Micka, K., Collection Czech. Chem. Commun. 29, 1998 (1964).

7. Newman, J.S. and Tobias, Ch.W., Electrochem. Soc. 109, 1183 (1962).

8. Lindström, O., ASEA Journal 40, 91 (1967).

9. Lindström, O., Entropie 14, 58 (1967).

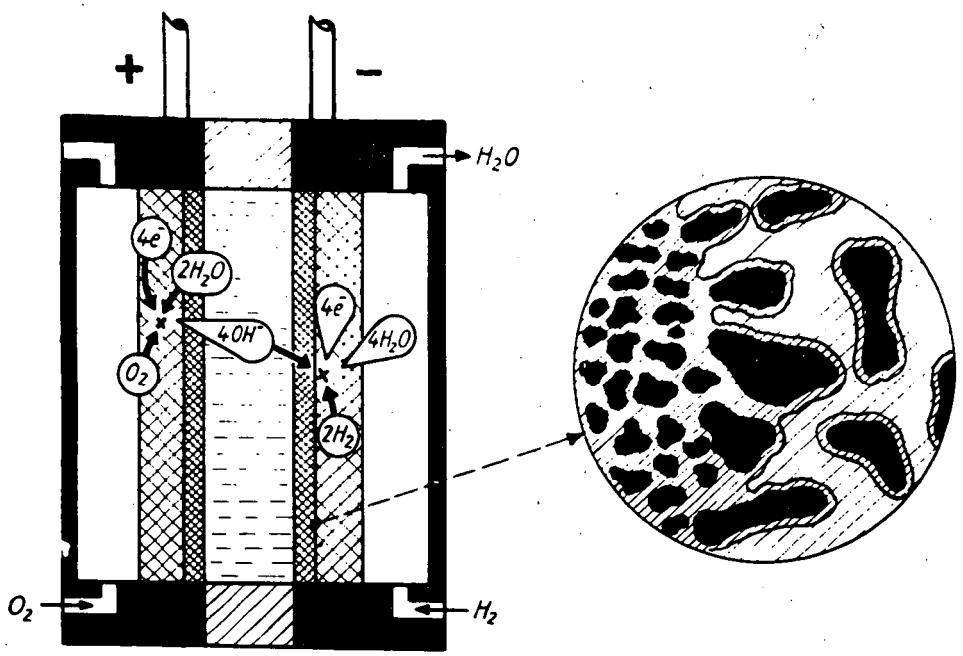

Fig.1. Electrolyte film in a porous gas-diffusion electrode (from references 1 and 2)

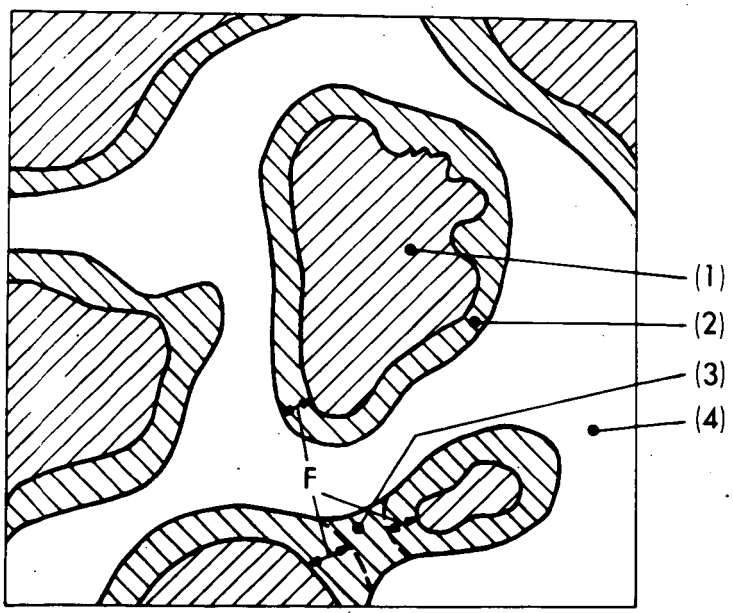

Fig.2. Section through the coarse layer of a working electrode

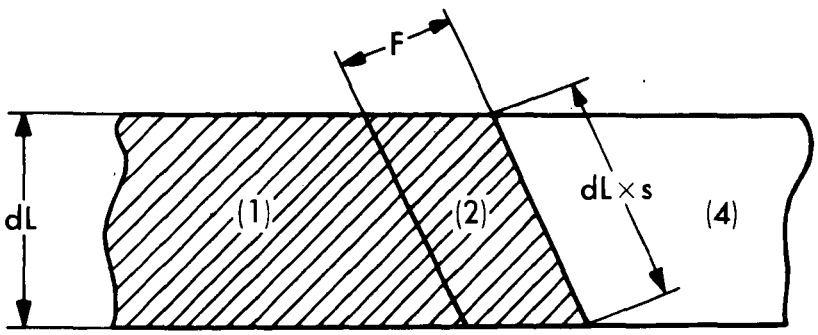

Fig. 3. The electrode section viewed from the side (for the notation see Fig. 2)

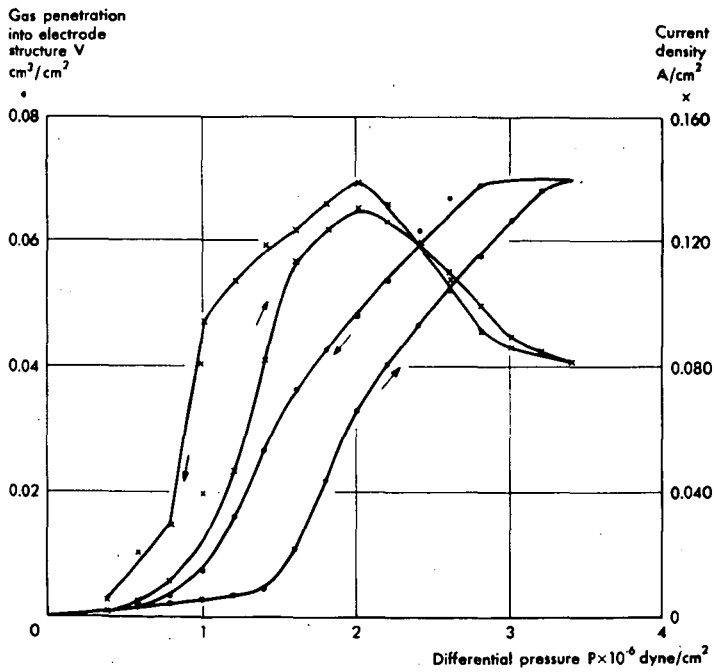

Fig. 4. Gas penetration into a hydrogen electrode, given as cm^3 gas/cm^2 electrode (V), and electrochemical activity, given as A/cm^2 at 800 mV versus Hg/HgO, as a function of the differential pressure P, dyn/cm^2

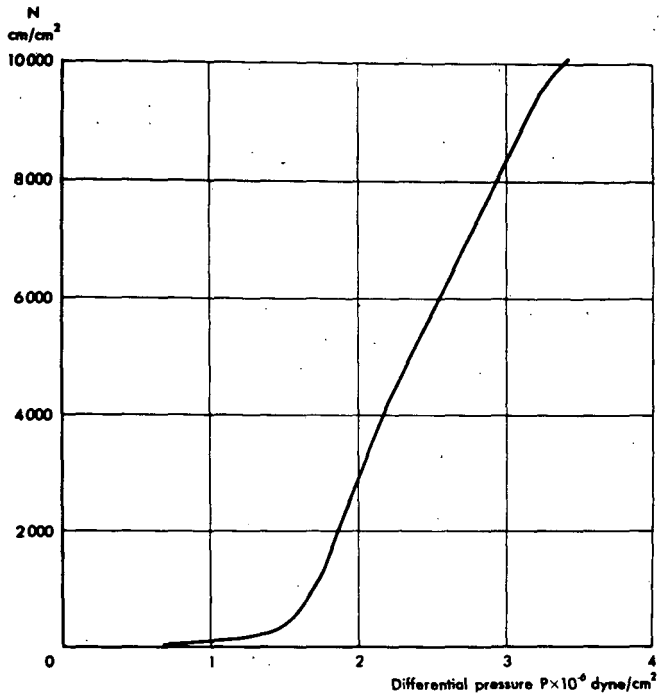

Fig. 5. The film perimeter N, cm/cm^2 electrode, as a function of the differential pressure P, dyn/cm^2

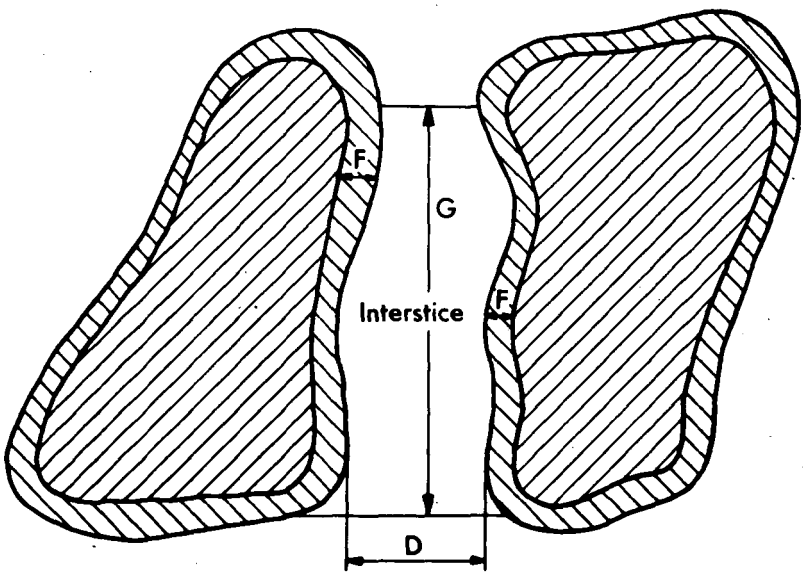

Fig. 6. Interstice model for the treatment of electrolyte penetration

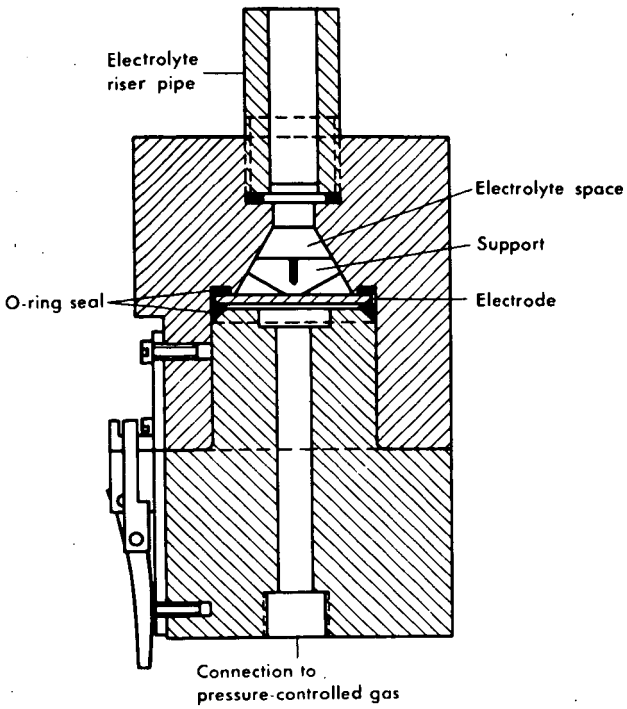

Fig. 7. Dilatometer for measuring the gas penetration into porous gas-diffusion electrode

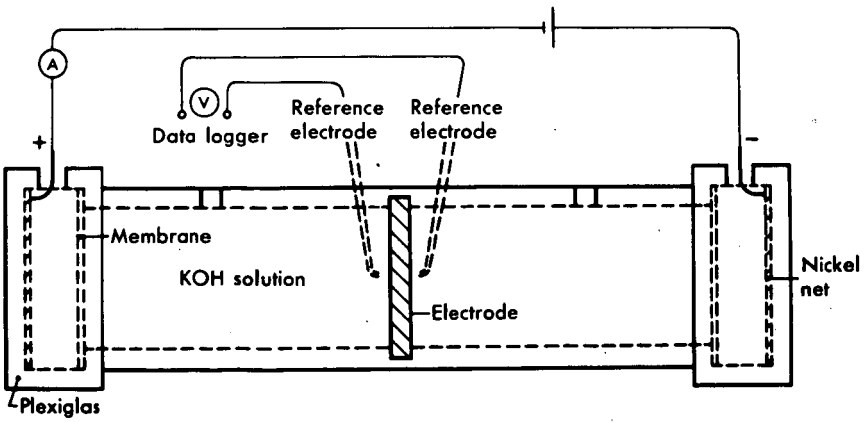

Fig. 8. Arrangement for determining the electrolyte resistance in fuel-cell electrodes

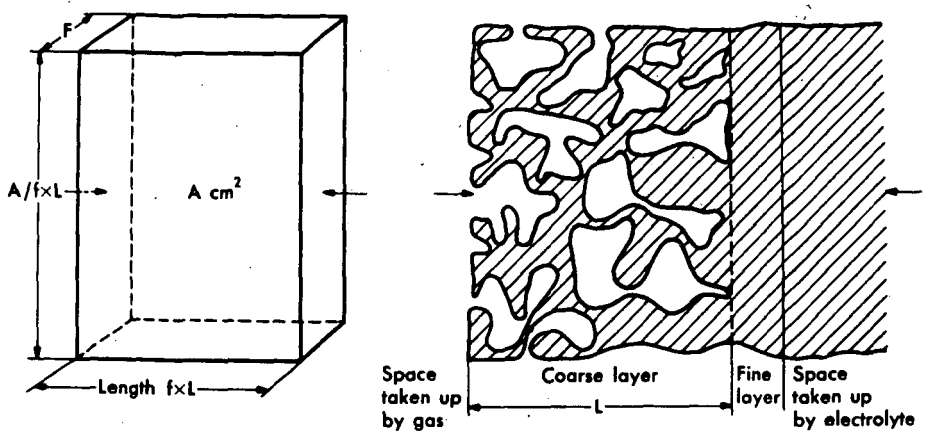

Fig. 9. Model of the film network and the equivalent disc

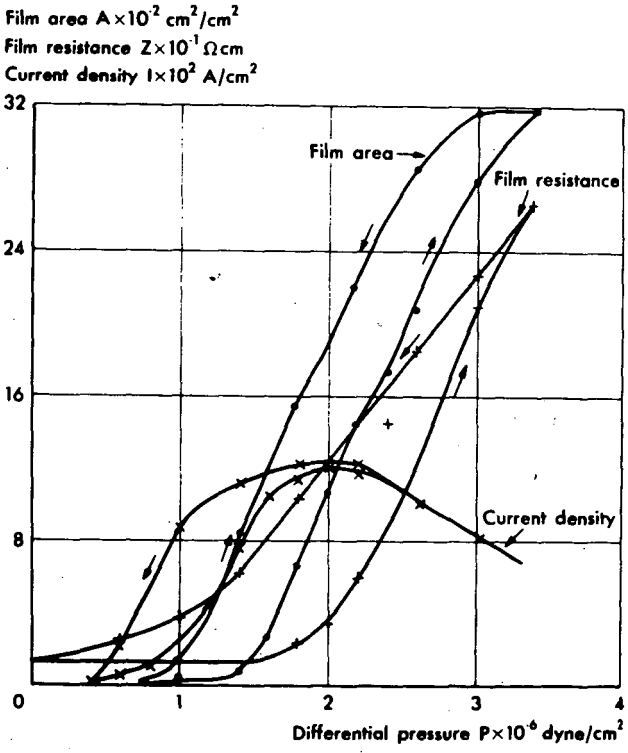

Fig. 10. Film area A, cm^2/cm^2 electrode, film registance z, ohm · cm, and electrode activity, mA/cm^2 at -100 mV versus Hg/HgO, as a function of the differential pressure P, dyn/cm^2, for an oxygen electrode in 7-N KOH at 25°C

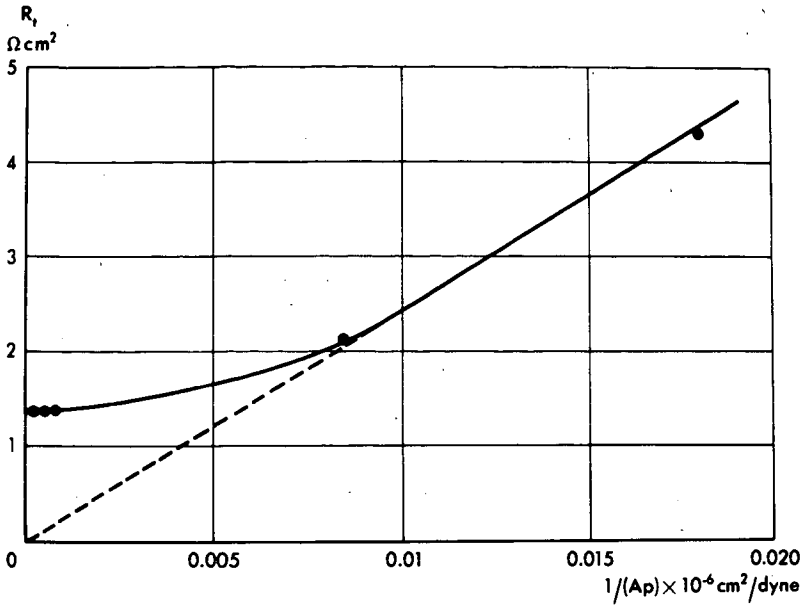

Fig. 11. Estimation of the constant C_1 in Eq. (5)

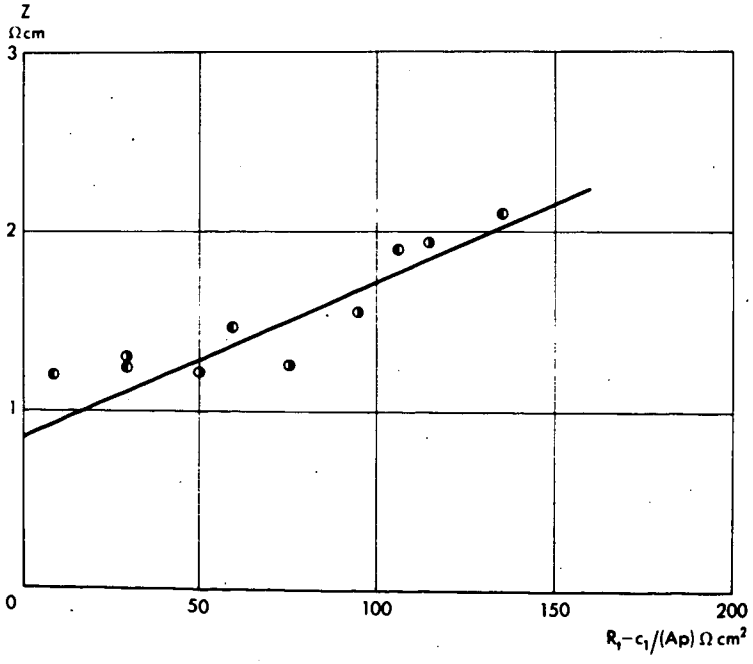

Fig. 12. Estimation of the constants C_2 and C_3 in Eq. (18)

MASS TRANSPORT IN THE INTERNAL REFORMING HYDROCARBON ANODE

William R. Alcorn

Leesona Moos Laboratories
Great Neck, New York

INTRODUCTION

An alkaline-electrolyte fuel cell based on an internal-reforming anode offers advantages of heat economy, compactness, and controllability over an external-reforming cell.[8, 11] The operating principle is illustrated in Figure 1. Experimental work has been reported for methanol[2] and hydrocarbons.[1, 3] In the preferred temperature range, 400 - 500° F, the thermodynamics of methanol reforming are favorable, permitting high current densities. The conversion of saturated hydrocarbons into hydrogen, however, is severely restricted by thermodynamics.

During the present investigation we have studied catalyst decay, anode preparation, thermodynamic limitations, and the performance of an experimental anode with methane. This paper is concerned with the last topic, and specifically with an examination of the limitations on performance and changes that might be made to maximize performance. The present performance goal for a liquid hydrocarbon fuel such as octane is approximately 100 amps/ft^2 at 500° F, 200 mV anode polarization (a full cell voltage of about .90 V), and 70% fuel utilization.

ANALYTICAL TREATMENT OF ANODE CELL PROCESSES

Figure 2 illustrates the cell dimensions used in the discussion. For fixed pressure, temperature, and fuel/water ratio, fuel flow rate may be taken as proportional to average velocity times cross-sectional area:

$$Q_F \propto uat \tag{1}$$

Current density is based on membrane area:

$$I/A = I/aL \tag{2}$$

Fuel utilization is proportional to total current divided by fuel flow rate:

$$\eta_u \propto \frac{I}{Q_F} = \frac{(I/A)\,aL}{uat} = \frac{(I/A)}{u}\,\frac{L}{t} \tag{3}$$

Data are reported in terms of the ideal hydrogen space velocity, which is volumetric flow of hydrogen (NTP) that would be produced by complete conversion of fuel, divided by cell volume. From equation (1) we note that:

$$S_v \propto \frac{uat}{aLt} = \frac{u}{L} \tag{4}$$

Utilization versus Current Density

As flow velocity is varied through an anode cell at fixed potential, the resulting current density will exhibit a maximum although it may occur at very low utilization. At very low flow rates, complete utilization is accomplished and current density is proportional to flow rate. At very high flow rates, the residence time is short and the average hydrogen concentration decreases towards zero, causing a decrease in I/A. These limits are shown in Figure 3 as a function of S_Y. Note that the proportional relation at low flow rate is an asymptote of slope + 1 on a log-log plot.

In determining the operating point to achieve a specified utilization and maximum I/A, two cases may be distinguished, depending on whether increasing flow rate has a beneficial effect on I/A through its effect on mass-transfer processes.

1. If there is no such effect, e.g., if transport is purely by molecular diffusion, then space velocity is set to give the desired utilization, and I/A is determined by reaction kinetics and utilization.

2. If I/A increases with flow rate over some range, e.g.,

$$I/A \propto u^n \tag{5}$$

where mass-transfer data suggest $0 < n < 0.5$ (see later), then from equation (3) at fixed bed thickness,

$$\eta_u \propto \frac{L}{u^{1-n}} \tag{6}$$

Thus, from equations (5) and (6) the design procedure would be to maximize I/A with respect to flow rate in a "short", one-pass cell and then increase the effective length of the anode to obtain the desired utilization. The average I/A will be lower than the maximum obtained in the short cell, but it should nevertheless be a maximum at the desired utilization.

There are various ways to increase effective flow length which are used in analogous situations: series gas flow through connected anode cells, partial recycle of gas, and internal baffling of the flow path. The three differ mainly in the way pumping power is introduced and dissipated, and in their effect on system control and reliability.

In any case, one expects that the optimization of an internal-reforming cell should involve a tradeoff between cost of pumping and the enhanced mass (and heat) transfer obtainable with high-velocity flow. In fact, a "perfect catalyst" might be defined as one so active that this optimization is required.

High-Velocity Range

As shown on Figure 3, I/A is depressed at low flow rates because of the extraction of hydrogen. In other words, the maximum available (equilibrium) hydrogen partial pressure decreases as utilization increases. For instance, for a 2.7 H_2O/CH_4 mixture at 500° F, the equilibrium p_H is 29 mm Hg with no extraction, and 9.1 mm Hg with 70% extraction of ideal hydrogen.

In the high-velocity range where utilization is low, I/A depends on both mass-transfer and reaction rates. As a first approximation, we assume that I/A, or H_2 flux toward the membrane, is proportional to a mass-transfer coefficient and a maximum available hydrogen partial pressure,

$$I/A \propto k_m p_H \tag{7}$$

As flow rate is increased, k_m will increase because of increasing convective diffusion and p_H will decrease because of kinetic rate limitations.

For this analysis it is assumed that k_m obeys the conventional correlation for mass transfer between particles and a flowing fluid:[4]

$$k_m \propto u^n \quad (0 < n < .5) \tag{8}$$

This is shown in Figure 4. The point of transition is designated S_x; it occurs near a particle Reynolds number of 1. The curve in Figure 4 may be satisfactorily represented by the following equation:

$$\frac{k_m}{k_o} = 1 + \left(\frac{S_v}{S_x}\right)^{.5} \tag{9}$$

Reaction Kinetics and Open-Circuit Behavior

Lacking knowledge of the true kinetic relations, the generation of H_2 is simply represented here as a first-order rate process which decreases as equilibrium is approached:

$$\frac{\text{rate}}{\text{unit volume bed}} = \frac{k_r}{RT}\left(p_{eq} - p_H\right) \quad (\text{mols/hr-cm}^3) \tag{10}$$

With the assumptions of no extraction (open circuit), plug flow, and zero H_2 concentration at the entrance, a differential mass balance on H_2 gives the following relation between local H_2 pressure and distance through the cell:

$$\frac{p_H}{p_{eq}} = 1 - \exp\left(-\frac{k_r}{S_v}\,\frac{x}{L}\right) \tag{11}$$

We wish to relate this H_2 gradient to the open-circuit voltage (OCV). Tests with known H_2/N_2 streams confirmed that the measured OCV corresponded closely to the theoretical value:

$$OCV = \frac{RT}{2F}\left(\ln \frac{760}{p_{eq}} - \ln \frac{p_H}{p_{eq}}\right) \tag{12}$$

In the presence of a pressure gradient, however, it is not physically obvious whether the observed OCV reflects an average partial pressure or an average potential with respect to anode length. In the first case the right-hand term becomes

$$\overline{\ln\left[p_H/p_{eq}\right]} = \ln \int_0^1 \left[p_H/p_{eq}\right] d\,(x/L) \tag{13}$$

and the integral is

$$\frac{\overline{p_H}}{p_{eq}} = 1 - \frac{\left[1-\exp\left[-k_r/S_v\right]\right]}{k_r/S_v} \tag{14}$$

In the second case

$$\overline{\ln\left[p_H/p_{eq}\right]} = \int_0^1 \ln\left[p_H/p_{eq}\right] d(x/L) = \frac{S_v}{k_r} \sum_{n=1}^{\infty} \frac{\left[1-\exp\left[-nk_r/S_v\right]\right]}{n^2} \tag{15}$$

Curves of OCV versus S_v for various k_r's are presented for the two calculation methods in Figures 5a and 5b respectively.

Flow-Rate Effect on Current Density

In a cell at fixed anode potential the current density depends on both mass-transfer and reaction rates, which in turn depend on flow (convection) rate. A nondimensional equation expressing these relations has been developed, based on equations (7), (9) and (10). The result is that the current ratio I_R is a function of three ratios of characteristic rates:

$$I_R = \frac{(I/A)}{\left(\frac{k_o p_{eq}}{RT}\right)} = f\left(\frac{S_v}{k_r}, \frac{S_x}{k_r}, \frac{k_o/t}{k_r}\right) \tag{16}$$

where,

S_v ≡ convection rate

k_r ≡ reaction rate

k_o/t ≡ mass-transfer rate

S_x ≡ transition space velocity for mass-transfer correlation, equation (9)

We have generated plots of I_R versus S_v/k_r for several values of the other two parameters. Representative curves are shown in Figure 6. Equation (16) applies directly to the high-flow region where p_{eq} is constant. It is also applicable to the low-flow region where extraction depresses the equilibrium H_2 concentration, if it is combined with an appropriate equation for p_{eq} as a function of flow rate. The following generalizations may be made from the results.

1. A significant maximum is obtained only when the transition in the mass-transfer relation occurs at a low velocity $(S_x/k_r << 1)$. Otherwise the current density decreases with flow velocity in approximately the same way as does $\overline{p_H}$ (equation 14).

2. Whether or not a significant maximum occurs, the current density always begins to decrease rapidly in the range $.2 < S_v/k_r < 2$.

3. The relative mass-transfer coefficient has a major effect on the absolute value of I/A but it has little effect on the relation between I/A and flow rate.

EXPERIMENTAL

Three types of data from the anode cell are presented: OCV versus S_v, I/A versus S_v, and OCV versus time when flow was stopped. Flow-visualization tests are also discussed.

Apparatus

The anode assembly consisted of a .001 inch 75 Pd/25 Ag activated membrane, 1.5 x 2.5 inches, backed up by a .187 or .125 inch thick bed of 20-mesh nickel catalyst (Girdler G60RS). Gas entered and left the cell through small ports along the 1.5 inch sides which in turn led to .25 inch tubes positioned at diagonally opposite corners of the holder. The feed was preheated H_2O/CH_4 in a mole ratio of 2.7/1. The anode was run as a half cell in 85% KOH at 500°F. The potential reference was 1 atm H_2 in a Pd-Ag tube in an etched Teflon Luggin capillary. Current density (no IR correction) was measured potentiostatically with an Anotrol controller, usually at an anode potential of 200 mV versus reference. Effluent was analyzed with a gas chromatograph. Performance was not significantly affected by 25% changes in the H_2O/CH_4 ratio, by pressurization of

the cell up to 20 inches H_2O, nor by vertical versus horizontal orientation of the anode in the electrolyte.

Open Circuit Voltage

Figures 5a and 5b show OCV data for three runs, including two bed thicknesses and both horizontal and vertical orientation of the anode. Fluctuations of OCV over several minutes are indicated by the height of the data points. According to the pressure-averaging method, k_r is about 3000 hours^{-1}; by the potential-averaging method it is about 15,000 hours^{-1}. The latter method fits the data better; it is mathematically correct if one accepts that the measured potential of a metallic electrode is the area average of point potentials and that a large potential gradient may be sustained in the plane of the electrode.

Current Density

Points from the same three runs along with data from previous work[3] are shown in Figure 7. These current densities are the steady values after several minutes; initial currents were generally 1.6 to 2.0 times the final values. Although experimental problems limited the flow range that could be tested, it may be seen that I/A decreases at both low and high flow rates, corresponding qualitatively with the analytical curves in Figure 6.

A rough estimate of k_r can be made from equation (10) and the total H_2 generation rate, which is the sum of current flux plus H_2 in cell effluent. For I/A = 80 amps/ft^2 at S_v = 3000 hours^{-1} in the .187 inch bed, we assume the average p_H in cell and effluent to be half of p_{eq} (29 mm Hg). Then H_2 rate as current is .039 mols/hr, and in the effluent .026 mols/hr, with the result that $k_r \cong$ 13,000 hours^{-1}.

Transient Behavior

An alternative way to measure the anode rate processes is to observe the change in OCV with time when flow is stopped. This was done during the same three runs. Figure 8 shows that OCV approaches the equilibrium value for CH_4 and H_2O (about 75 mV at 500° F), but requires several minutes to do so.

Flow Distribution

Some room temperature flow-visualization tests were made on the anode cell with a transparent window in place of the membrane. The cell was packed with indicating Drierite, and water-saturated N_2 was passed through at experimental flow rates. A peaked color profile was seen to move through the bed, the main flow taking a diagonal path between holder inlet and exit in spite of the small-diameter gas ports which had been intended to distribute the flow.

DISCUSSION

The open-circuit data (Figure 5) show that the simple model is adequate to describe the relationship between flow rate and kinetics, and k_r is about 3000 or 15,000 hours^{-1}, depending on how OCV is related to the gas-side gradient of p_H. The higher or potential-averaged value is supported by a better fit of data to theoretical curves and by a separate calculation of k_r from observed current density. Current densities (Figure 7) are unacceptably low, but in a qualitative sense are consistent with the model developed. On the basis of these two types of data one might conclude that catalyst activity is the major barrier to higher performance. However, arguments based on the transient behavior of OCV (Figure 8) and supporting calculations indicate a major role for mass transfer. These are discussed below.

Maximum Attainable Rate

It is important first to estimate the current density that could be achieved under various ideal conditions. The first case of interest concerns the current that could be supported by the activated .001 inch membrane if it were exposed to a gas mixture in equilibrium. A curve of I/A versus p_H for 500° F and 200 mV polarization has been estimated from previous unpublished data. Combining this curve with equilibrium calculations for $H_2O/C = 2.7$, Table 1 shows the estimated maximum performance for methane and octane at both zero and 70% utilization. Experimentally, the best current densities shown in this and previous work are about 35 - 45% of the tabulated values.

Table 1. Maximum Attainable Performance With .001 Inch Pd-Ag Anode, 500°F, 200 mV Polarization

Fuel	η_u (%)	Average p_H (mm Hg)	I/A (amps/ft^2)
C_1	0	29	330
C_1	70	14	210
C_8	0	17	240
C_8	70	12	190

Transient Behavior

Four processes may be postulated to account for the characteristic open-circuit equilibration time of several minutes (Figure 8).

1. reaction rate
2. orientation of the cell as it affects flow distribution

3. solution of H_2 in the Pd-Ag membrane

4. diffusion in the catalyst bed

The reaction kinetics may be checked by integrating equation (10). Then the time required for p_H to change from p_1 to p_2 is

$$\Delta t \text{ (min)} = \frac{60}{k_r} \ln \frac{p_{eq} - p_1}{p_{eq} - p_2} \tag{17}$$

Taking $k_r = 3000$ hours^{-1} from Figure 5a, $p_{eq} = 29$ mm Hg, $p_1 = 5$, and $p_2 = 28$, $\Delta t = .064$ min = 3.8 seconds. Larger values of k_r give even shorter times. Since there is so great a discrepancy between this and the observed equilibration time, some kind of diffusion process must be involved.

The anode orientation was changed from horizontal (membrane facing up) to vertical in order to ensure catalyst being in contact with the membrane and to decrease flow channeling that would probably occur if a gas gap existed. No significant change in performance or equilibration time resulted from this change, and we conclude that neither blockage of the membrane nor the existence of a gas space next to the membrane could account for the long equilibration times.

On the basis of unpublished data[7] and previous work,[6, 10] we estimate the solubility of H_2 in the membrane to be about 0.7 cc (NTP) at $p_H = 5$ mm Hg and 1.5 cc (NTP) at $p_H = 28$ mm Hg. In comparison, the gas space only contains about .16 cc of H_2 (NTP) at the higher pressure. Thus, during equilibration most of the H_2 produced is absorbed by the membrane. If the membrane is at all times in equilibrium with the gas, then by a calculation similar to equation (17) we estimate equilibration time (5 to 28 mm Hg) to be about 8 seconds. The current density supported by the membrane shows that the absorption rate is very rapid, so if the membrane solubility contributes to the long equilibration time it is because of slow diffusion of H_2 toward it.

Mass Transfer in Catalyst Bed

Three kinds of mass transfer may be important: pore diffusion in the catalyst particles, transport of reactants and products between bulk gas and catalyst, and transport of H_2 through the bed to the membrane. It may be shown that the first two processes are quite rapid relative to observed net reaction rates. For example, using standard correlations,[4] we estimate the bulk mass-transfer coefficient (the second process) to be on the order of 100 times the first-order reaction rate coefficient in the same units.

The third process, although related to the second, occurs on a larger scale, i.e., it involves a concentration gradient across the thickness of the catalyst chamber. To a first approximation, we may define the H_2 flux in the x-direction (as current density) in terms of an effective diffusivity D_e:

$$I/A \propto \frac{D_e}{RT} \frac{d\, p_H}{d\, x} \tag{18}$$

It should be noted that the coefficient k_m, as used in the mathematical analysis, and D_e describe the same process although defined in different dimensional terms. D_e is used for convenience in estimating.

D_e may be estimated by two methods. First, it may be calculated from molecular diffusivity and modified to account for the porous bed structure by an empirical equation:[9]

$$D_e = \frac{\epsilon}{\tau} D \tag{19}$$

For a characteristic multicomponent mixture of H_2O, CH_4, H_2, and CO_2 at 500° F, D_{H_2} is about 2.1 cm^2/sec and diffusivities of the other three gases range from .45 to .75 cm^2/sec. Measured bed porosity ϵ = .42 and tortuosity τ for an unconsolidated bed is generally 1.5 to 2.0.[9] Then D_e is about 0.5 cm^2/sec for H_2 and 0.1 to 0.2 for the other gases.

Secondly, if turbulent (convective) diffusion is the dominant transport process normal to the membrane, D_e may be estimated from the Peclet number:

$$P_e = \frac{d\, u}{D_e} \tag{20}$$

Taking d = .084 cm, the interstitial velocity u = 22 cm/sec (corresponding to S_v = 3000 $hours^{-1}$ in the .187 inch cell), and the Peclet number to be 13.6,[4] D_e is approximately 0.14 cm^2/sec. That it is about the same magnitude as the effective molecular diffusivity implies that both molecular and turbulent diffusion are important at this flow rate. Below a space velocity of about 1000 $hours^{-1}$ molecular diffusion dominates the lateral transport process.

The values of D_e may now be used in estimating the transient equilibration time due to diffusion. We start with the solution of the equation for one-dimensional diffusion from a surface source,[5] and focus on the relative partial pressures at the source and a fixed distance from it -- in this case half the cell width (1.9 cm). Letting f = the ratio of partial pressures at the fixed point to the source, the time elapsed between f_1 and f_2 is

$$\Delta t = \frac{(1.9)^2}{4\, D_e} \left[\frac{1}{\ell n\, f_1} - \frac{1}{\ell n\, f_2} \right] \tag{21}$$

Assuming that the initial p_H at the edge is 50% that at the center ($f_1 = .5$), equilibration times are shown in Table 2 for two final partial-pressure ratios, for H_2 $\left(D_e = .5\right)$ and for the average of the other gases $\left(D_e = .15\right)$.

Table 2. Transient Diffusion Times (Equation 21)

	Δt (min)	
D_e (cm^2/sec) =	.5	.15
$f_2 = .95$	0.5	1.6
$f_2 = .99$	2.8	9.3

The calculation probably underestimates diffusion time because no account is taken of the solubility of H_2 in the membrane (see earlier). We conclude that diffusion in the catalyst bed is a reasonable explanation for the observed equilibration times of several minutes. It is not possible to say whether the main diffusion process is parallel to the membrane (e.g., if there are "stagnant" corners which must come to equilibrium) or normal to the membrane in the process of absorption of H_2 into the Pd-Ag.

To estimate the current density with an "ideal" catalyst and real diffusion resistance, we assume the partial-pressure gradient is linear between equilibrium (average $p_{eq} \approx 14$ mm Hg for CH_4, 70% extraction) and the membrane over, say, one particle diameter or 0.1 cm. The relation between p_H and membrane flux (at 200 mV) reflected in Table 1 may be approximately written as

$$p_H \cong .07\ (I/A) \tag{22}$$

Then equation (18), with $D_e = 0.5\ cm^2/sec$ for H_2, becomes

$$I/A = 0.5 \left(\frac{cm^2}{sec}\right) x \frac{14 - .07\ (I/A)}{0.1} \left(\frac{mm\ Hg}{cm}\right) x\ 5.39 \left(\frac{amps/ft^2}{mm\ Hg\text{-}cm/sec}\right)$$

and $I/A = 130\ amps/ft^2$, compared with 210 in Table 1. This calculation may be made with different sets of assumptions, but the main point is that with a realistic value of D_e, a large partial pressure gradient must exist for high H_2 flux rates. We conclude that it is plausible that diffusion may account for a substantial portion of the difference between maximum I/A as given in Table 1 and the observed values.

Flow Distribution

Nonuniform flow along both width and thickness of the cell used in this study would be very difficult to avoid. The tendency of the thin membrane to expand

irregularly presents one design problem. Flow visualization tests have shown a tendency to nonuniformity in the horizontal plane.

We have not been able to make a meaningful estimate of the effects of nonuniform flow on performance, although the cases checked have all been detrimental. For example, stagnant gas pockets in the corners would tend to become depleted of H_2, probably inducing a potential gradient and electrolytic circuit in the plane of the membrane. This situation could occur at open circuit as well as on load, and would contribute to the observed increase of OCV with flow rate that we have previously ascribed to kinetic limitations. This problem is common to any flat rectangular gas electrode with a mixed feed; however it is accentuated with a packed gas chamber and a thin Pd-Ag anode.

Prereactor Concept

We have looked in principle at two design concepts in which the gas flows through a catalytic bed at cell temperature prior to entering the anode cell. In the case of a combination external-internal reformer, the cell is packed with catalyst. With a completely external reformer (at cell temperature), the anode chamber would not contain catalyst.

Current density would be somewhat higher in the combination reformer than in the strictly internal reformer because of better utilization of the membrane near the cell inlet. The penalty is the increased pressure drop and system volume. The best possible performance would be approximately the same as the case of the ideal catalyst and real diffusion resistance, calculated above. The second case would require very high flow rates with recycle, or series flow connection with alternating catalyst beds and anode cells. The only advantage -- flexibility in cell design -- is far outweighed by pressure drop, volume, and system complexity.

CONCLUSIONS

With a 500° F upper limit, the internal-reforming hydrocarbon anode is severely restricted by the thermodynamics of reforming. With a .001 inch activated Pd-Ag anode, 70% utilization of fuel at 1 atm total pressure, and 200 mV anode polarization, ideal performance is approximately 210 amps/ft^2 for methane and 190 amps/ft^2 for octane. Work to date has resulted in 35-45% attainment of these ideal values. Data and supporting calculations indicate that in the flow range tested, at least half of the deviation from ideal performance can be attributed to diffusion resistance between catalyst sites and membrane. Nonuniform flow distribution and kinetic limitations also contribute to the deviation although it is not possible to rank them in importance.

Higher flow velocity and a thinner bed would decrease the relative limitation due to diffusion and increase those due to catalyst and flow distribution. Changes in this direction would soon bring the cost of pumping power into significance.

Thinner and more active Pd-Ag membranes would improve performance by permitting a greater diffusion driving force between catalyst and membrane. A perfect membrane -- one with no transport resistance -- would possibly yield 20

to 30% greater current densities than obtained with the present .001 inch membranes.

If system considerations permit flow velocities high enough to have a beneficial effect on mass transport in the catalyst bed, then the design procedure should be to maximize I/A with velocity and adjust the effective length of the anode to achieve the desired utilization. This may be accomplished by using recycle, series flow connections, or baffling. A prereactor added to an internal-reforming cell would give some increase in current density at the expense of pressure drop and volume, and is best regarded as a secondary design option once the basic cell design is established.

The open-circuit voltage of a hydrogen electrode in the presence of an exponential pressure gradient is satisfactorily described by an equation that involves an average of point potentials over the anode surface. The equation gives better results than the simpler calculation where partial pressure is averaged and a single potential is determined from that average.

In summary, with a .001 inch Pd-Ag membrane at 500° F and at 1 atm total pressure, we estimate that the maximum feasible current density at 200 mV anode polarization for a liquid hydrocarbon feed with 70% utilization would be about 120 amps/ft^2 with a very good catalyst and careful design for gas flow.

ACKNOWLEDGMENTS

This work was part of a program sponsored by the U.S. Army Engineer Research and Development Laboratories under Contract DA-44-009-AMC-1501(T).

The author wishes to thank Messrs. J. Dafler, C. Bowman, and A. Schultz for their contributions to the work described in this paper.

NOMENCLATURE

a, L, t	cell dimensions (Figure 2) - cm
D	gas diffusivity - cm^2/sec
D_e	effective diffusivity - cm^2/sec
d	particle diameter - cm
I/A	current density - $amps/ft^2$
k_m	mass-transfer coefficient - cm/hr
k_o	limit of k_m at low flow rate (Figure 4)
k_r	reaction rate coefficient - hrs^{-1}
p_{eq}	equilibrium hydrogen partial pressure - mm Hg
p_H	hydrogen partial pressure - mm Hg
Q_F	fuel flow rate - cc/hr
R	gas constant
S_v	ideal hydrogen space velocity - hrs^{-1}
S_x	space velocity at mass-transfer transition (Figure 4)
T	temperature - ^oK
u	gas velocity - cm/sec
ϵ	porosity
η_u	fuel utilization
τ	tortuosity
F	Faraday constant

REFERENCES

1. Gregory, D.P. and Heilbronner, H. in "Hydrocarbon Fuel Cell Technology," (B.S. Baker, ed.), p 509, Acad. Press, N.Y., 1965.

2. Hartner, A.J. and Vertes, M.A., A.I.Ch.E. - I. Chem. E. Symposium Series No. 5, 12 (1965).

3. Heilbronner, H.H., Smarz, G.A., and Kramer, S., Phase II Tech. Rept., Liquid Hydrocarbon Fuel Cell Development, Contract DA-44-009-AMC-756(T), Aug. 1965.

4. Hougen, O.A., Ind. Eng. Chem., 53, 513-515 (1961).

5. Jost, W., "Diffusion in Solids, Liquids, and Gases," pp 16-17, Acad. Press, N.Y. 1960.

6. Jurisch, E., Metz, A., and Sieverts, A., Z. anorg. u. allg. Chem, 92, 329 (1915).

7. Lieberman, B., Leesona Moos Labs., private communication.

8. Palmer, N.I., Lieberman, B., and Vertes, M.A. in "Hydrocarbon Fuel Cell Technology," (B.S. Baker, ed.), p 151, Acad. Press, N.Y. 1965.

9. Satterfield, C.N. and Sherwood, T.K., "The Role of Diffusion in Catalysis," pp 14-15, Addison-Wesley, Reading, Mass. 1963.

10. Sieverts, A. and Hagen, H., Z. phys. Chem. A174, 247 (1935).

11. Vertes, M.A. and Hartner, A.J., Fuel Cell Symp., Brussels, June 1965.

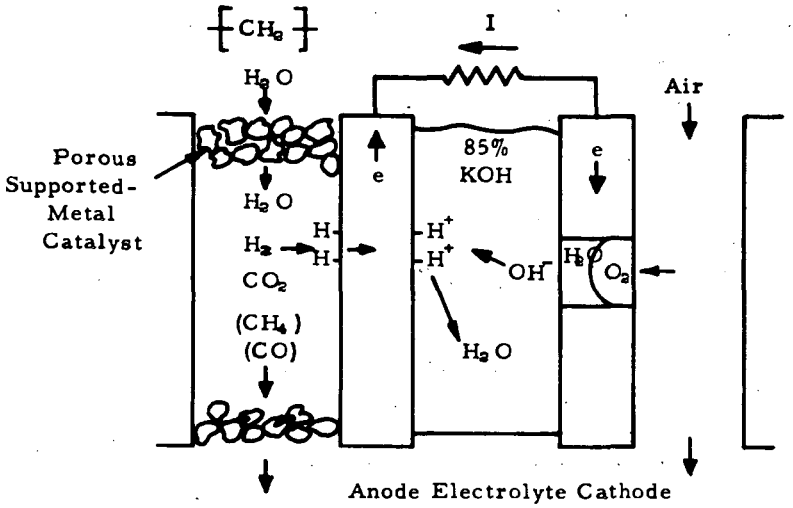

Figure 1. Operating Principle of Internal-Reforming Fuel Cell

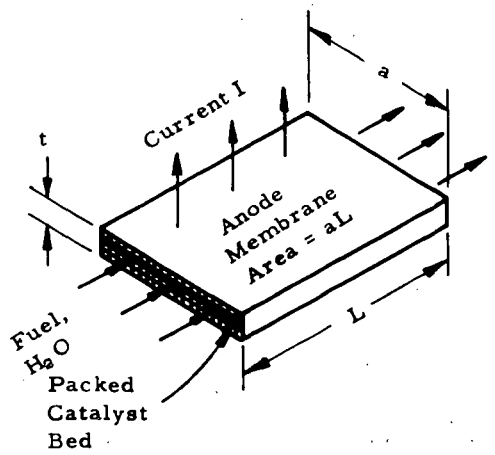

Figure 2. Anode Model Used in Analysis

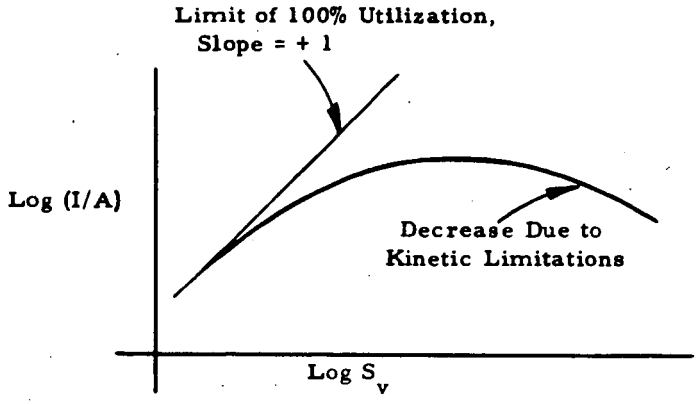

Figure 3. Dependence of Current Density on Space Velocity

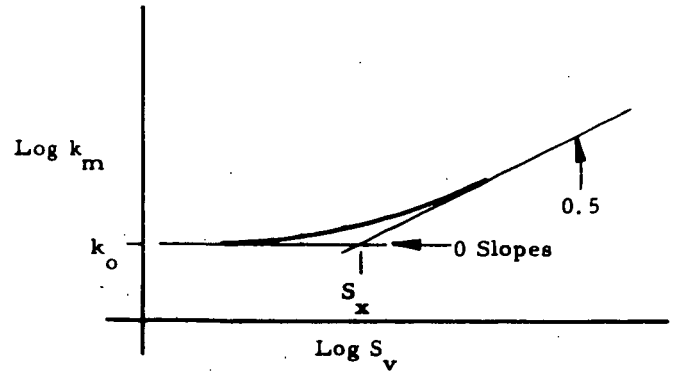

Figure 4. Dependence of Mass-Transfer Coefficient on Space Velocity in Packed Bed

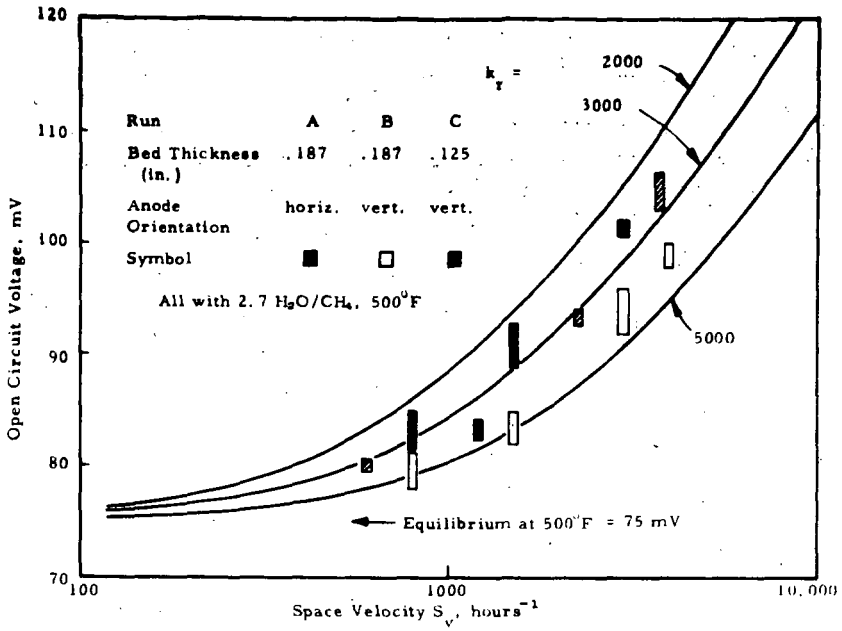

Figure 5a. OCV versus S_V - Calculated Curves by Averaging Partial Pressure (Equation 13)

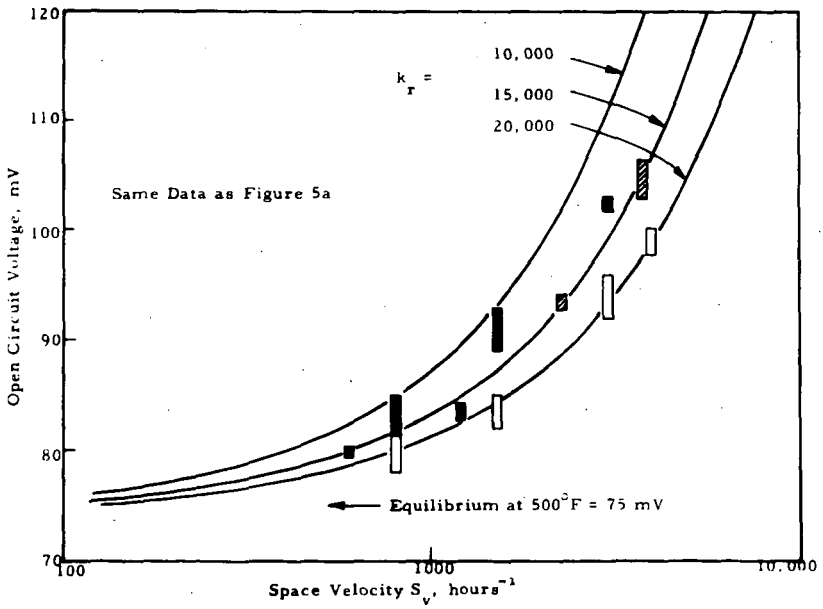

Figure 5b. OCV versus S_V - Calculated Curves by Averaging Potential (Equation 15)

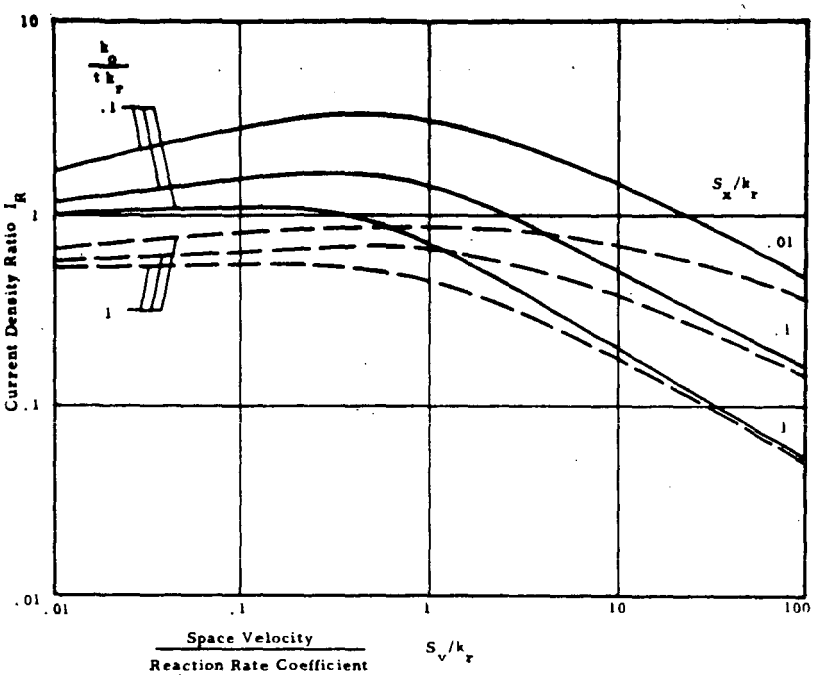

Figure 6. Dependence of Current Density on Mass Transfer and Reaction Rate Parameters (Equation 16)

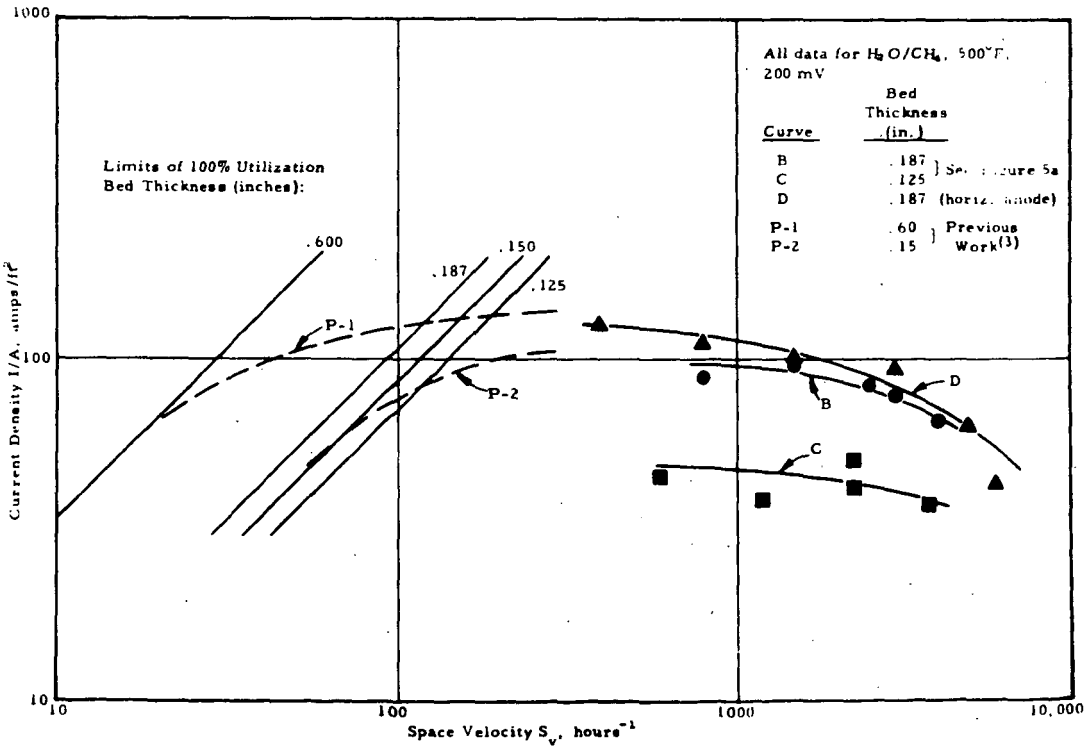

Figure 7. I/A versus S_v at 200 mV Polarization

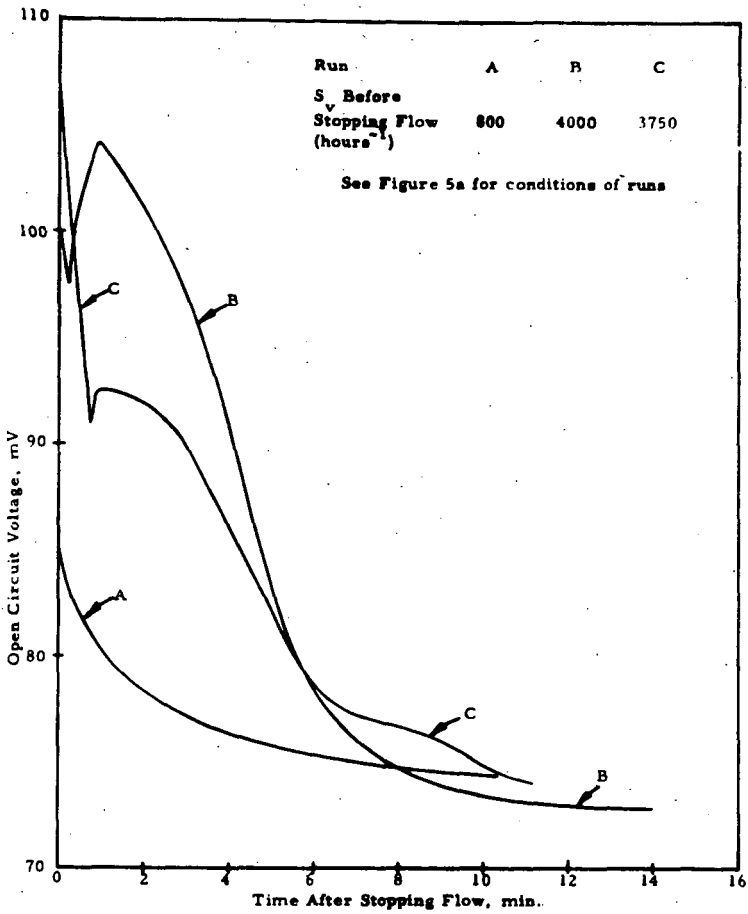

Figure 8. Transient Behavior of OCV When Flow of Fuel is Stopped

PULSED POWER FUEL CELLS

R. A. Sanderson, C. L. Bushnell, T. F. McKiernan

Pratt & Whitney Aircraft Division
United Aircraft Corporation
East Hartford, Connecticut

INTRODUCTION

Fuel cells are presently under development for a variety of applications. Hydrogen-Oxygen fuel cells were used in the Gemini Space Program and are now part of the Apollo Space Program. Fuel cells operating on preconditioned hydrocarbon fuels and air are also being developed in a variety of military and commercial programs as high efficiency electrical power supplies.

In these programs, the fuel cells are primarily subjected to steady direct current loading at relatively low power density, less than 300 watts per square foot of electrode area.

Fuel cell operation at high current density under pulsed loading was the subject of a recent program at Pratt & Whitney Aircraft. This work was sponsored by the Air Force Aero Propulsion Laboratory at Wright-Patterson Air Force Base. The object of the program was to investigate fuel cells as a source of short duration high intensity electrical discharge in the microsecond to 5 minute discharge time range.

This paper describes fuel cell performance characteristics noted during this investigation, including microsecond response following a single switch closure and the response to repeated square wave pulse loadings over a range of pulse frequency and pulse duration.

CELL PERFORMANCE CHARACTERISTICS

Figure 1 shows a typical fuel cell steady-state performance characteristic. If the cell is operating at a given point on the steady-state curve, then the voltage at the cell terminals is given by:

$$E_{oc} - E_p = IR$$

Where:

Ep	=	Ea + Ec + I (Rin)
Eoc	=	open circuit voltage
Ea	=	anode polarization
Ec	=	cathode polarization
I	=	cell current
Rin	=	internal cell resistance
Ep	=	total cell polarization
V	=	operating voltage
R	=	external circuit resistance

The left side of the above equation represents the difference between the cell open circuit voltage and the voltage at the operating point (V). This difference is the sum of the anode, cathode and internal polarizations of the cell. The external load line can be superimposed

upon the steady-state performance curve by connecting the origin and the operating point.

When the cell is initially at an open circuit condition and a load is applied, the load line changes from the initial value (slope = ∞) to the new value (slope = R). If the load is changed to this new value (slope = R) very slowly, the cell polarizations have sufficient time to develop, and the performance path follows along the steady-state characteristic A to C. If the load is changed rapidly, such as closing a switch, the performance path moves from A to B. Then, as the polarizations develop within the cell, the performance decays back to point C.

Tests were conducted at Pratt & Whitney Aircraft to investigate the performance path during switch closure.

TEST CIRCUIT

The circuit used to obtain fuel cell transient response is shown in Figure 2. Tests were generally conducted on cells with an active area of 0.5 in^2 to keep current in the electronic switch during repeated pulsing within the 50 amp rating of the transistors. In some of the single switch closure tests, a hand switch was substituted for the solid state electronic switch.

Connections between components in the circuit were made as short as possible to minimize inductance.

RESPONSE TO A SINGLE SWITCH CLOSURE

Initial tests were conducted on fuel cells using Pratt & Whitney Aircraft catalyzed screen type electrodes with the aqueous KOH electrolyte trapped in a 10 mil asbestos matrix. The tests were at 220°F with 15 psia H_2-O_2 reactants on 0.5 in^2 cells. Figure 3 shows voltage and current traces recorded from the oscilloscope following switch closure with minimum circuit resistance (later calculated at 0.0032 ohms).

The time scale is 50 microseconds per cm. The traces do not start at zero current and open circuit due to a delay in triggering the scope. Peak recorded current was approximately 55 amps (15,600 amps/ ft^2) at a cell voltage of 0.2 occurring about 100 microseconds after switch closure.

Figure 4 shows the same switch closure transient recorded at 10 milliseconds per cm. After 100 milliseconds the current is still above 8500 amps/ ft^2.

During this step transient roughly 100 joules/ft^2 of energy was released (in 100 milliseconds), and the calculated capacitance of the cell was 280 farads/ft^2. Maximum output power density during this transient was 5900 watts/ft^2.

Figure 5 shows the switch closure transient plotted as voltage versus current. The normal steady-state performance is shown for comparison.

The calculated electrolyte resistance is also plotted on the voltage-current curve. It can be noted that current from the cell exceeded the maximum expected, based on the electrolyte loss indicating the overall cell is behaving as a capacitor with higher discharge currents through the external circuit than through the cell itself.

Tests were also performed using a dual pore nickel electrode cell in free electrolyte. These tests were conducted at 400°F with 85 weight percent KOH. The electrolyte gap between the cells was 0.060 inch.

During the switch closure test, current densities up to 5750 amps/ft^2 were recorded, as shown in Figure 6 (Trace A). Peak power density was 6240 watts/ft^2.

A second test was then made with a Teflon barrier placed in the electrolyte between the electrodes, blocking the electrodes but allowing ion flow around the edges. The cell was once again pulsed from open circuit as shown in Figure 6 (Trace B). Peak current was 5370 amps/ft^2, nearly the same as when tested without the ion barrier between the cells. Voltage and current dropped off at a faster rate in this test.

A third test was then made. With the cell at open circuit, the cell was withdrawn from the electrolyte leaving an air gap between the cells. The switch was then closed. Current densities up to 3600 amps/ft^2 were recorded as a measure of the cell's pure capacitance, Figure 6 (Trace C). Voltage and current dropped off very rapidly as the cell discharged without the advantage of recharge current in the cell.

Calculated capacitance for the three tests was:

1. Normal configuration 0.060 inch free electrolyte — 550 farads/ft^2
2. With Teflon barrier between electrodes — 314 farads/ft^2
3. With air gap between electrodes — 19 farads/ft^2

Figure 7 shows voltage versus current curves for the three tests as well as the steady-state performance and the calculated maximum current based on electrolyte resistance.

Several trends were noted from these tests of cell response to a single switch closure:

1. Initial performance during step increases in load exceeds steady state due to cell capacitance. Peak current is limited by cell impedance during this initial period and the external circuit resistance.

2. Initial performance during step increases in load also exceeds the level predicted on the basis of pure resistance loss through the electrolyte. This can occur only if current through the external circuit exceeds ion current through the electrolyte.

3. Impedance during the initial time after switch closure is not limited by IR loss through the electrolyte but depends instead on the overall cell capacitance and resistive losses within the electrodes as well as current collection losses.

4. Capacitance of the cell increases with increasing electrode pore surface (electrode thickness, porosity). Cells with thin screen electrodes had a generally lower capacitance (200 farads/ft^2) than cells with thicker electrodes such as the dual porosity free electrolyte cell (500-700 farads/ft^2).

REPEATED PULSE TESTS

Cell performance was also investigated for a continuous pulse load in which a switch is opened and closed continuously at high frequency. Loading of this type could be imposed on the fuel cell by an input chopper stage on a voltage regulator or inverter, or by a pulse width modulation type motor speed control.

Repeated pulse loading tests were performed on a screen electrode low temperature trapped electrolyte cell using an electronic switch and square wave pulse generator. A range of pulse frequency (10 to 10,000 cps), pulse duration (20 to 95 percent), and pulse amplitude (1400 to 3600 amps/ft^2) was imposed on the cell. Voltage readings were taken from the oscilloscope during both the pulse on and off time.

Figure 8 shows an oscilloscope trace with typical response of the cell during repeated pulsing at one kilocycle and 90 percent pulse duration. During the switch off interval, the cell does not have time to recover, and the performance arrives at a quasi steady-state level.

Figure 9 shows performance during the pulse-ON portion of the cycle for a range of pulse durations. Data points are readings taken directly from the oscilloscope. Since the objective of the program was high power output, data was recorded primarily at higher currents.

The average power density was computed for square wave response by multiplying the power while the pulse is ON by the pulse duration. Figure 10 shows cell voltage while the pulse is ON, plotted against average power density. Steady-state power density is also shown. At a cell voltage of 0.75, the average power density in a pulsing mode at 90 percent pulse duration is twice the output with a continuous load (initial steady state).

The effect of pulse duration and frequency is shown in Figure 11. Average power density improves with decreasing frequency and peaks at 80-95 percent pulse duration.

The results of repeated pulse loading on a dual pore free electrolyte cell at 450°F are shown in Figure 12. Average performance while pulsing exceeded performance during continuous d.c. load for pulse durations above 50 percent.

Tests were also performed on an early experimental activated dual porosity nickel electrode cell with 1/4 inch free electrolyte at 160°F. Performance of the cell is shown in Figure 13. Although the general performance level was low, considerable improvement in performance was noted by operating the cell in a pulsing mode as shown.

Several trends were noted during these repeated pulse tests.

1. During repeated pulsing, the cell capacitance is charged during the open circuit periods and discharged during the closed circuit periods.

2. The voltage at which current is drawn from the cell during closed circuit conditions is considerably greater than if the cell were operated under a continuous d.c. load. As the pulse duration is increased, the performance falls off.

3. The integrated average performance in a pulsing mode can exceed steady state. The extent of performance improvement is affected by cell type, load level, pulse duration, and frequency.

4. In general, the integrated average performance improves with lower frequency (100-1000 cps) and higher pulse duration 80-95 percent. Improvement in cell performance by pulsing also appears to be greater at higher current density and in cells with a generally lower peformance. Further investigation is needed to evaluate the effect of pulse loading on cell endurance.

SUMMARY

The electrochemical capacitance of fuel cells has been evaluated in single switch closure tests and found to be in the order of 200-700 farads/ft^2 of cell area depending on cell type. This capacitance gives a fuel cell the ability to deliver high intensity microsecond-millisecond discharges up to 16,000 amps/ft^2 and 6000 watts/ft^2.

During continuous fuel cell operation, cell capacitance can be used by repeated pulsing at higher frequency. The results of repeated pulse testing indicates performance improvements up to 100 percent in current density at equal cell voltage.

References

1. AFAPL-TR-67-40 Pulse Power Fuel Cell, May 1967

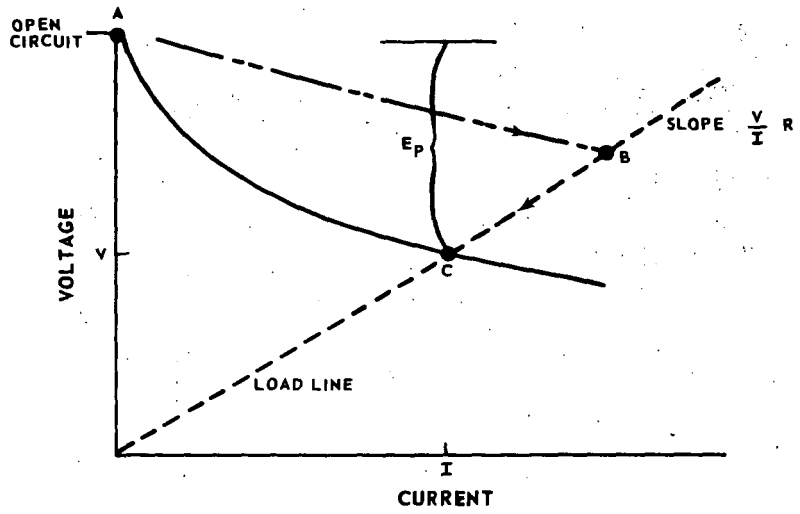

Figure 1 Fuel Cell and Load Characteristics

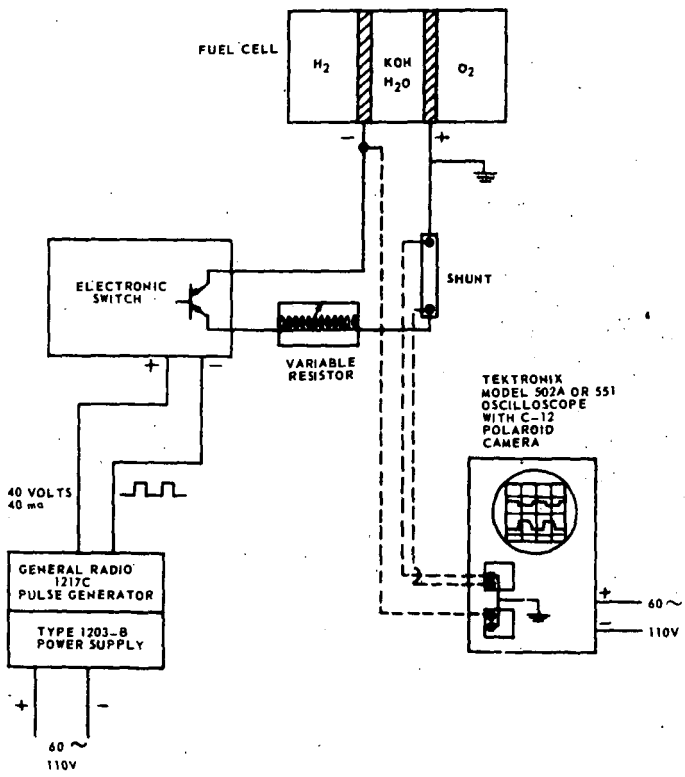

Figure 2 Circuit for Testing Fuel Cell Performance to Pulse Loads

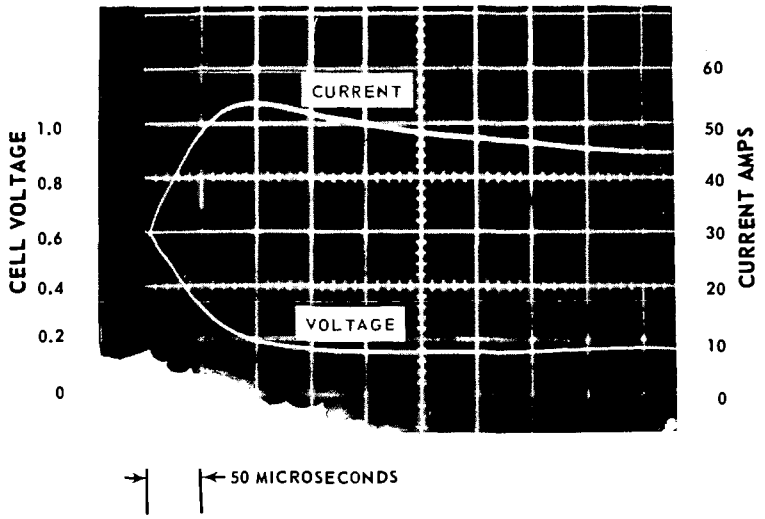

Figure 3 Trapped Electrolyte Cell Microsecond Response Following Switch Closure

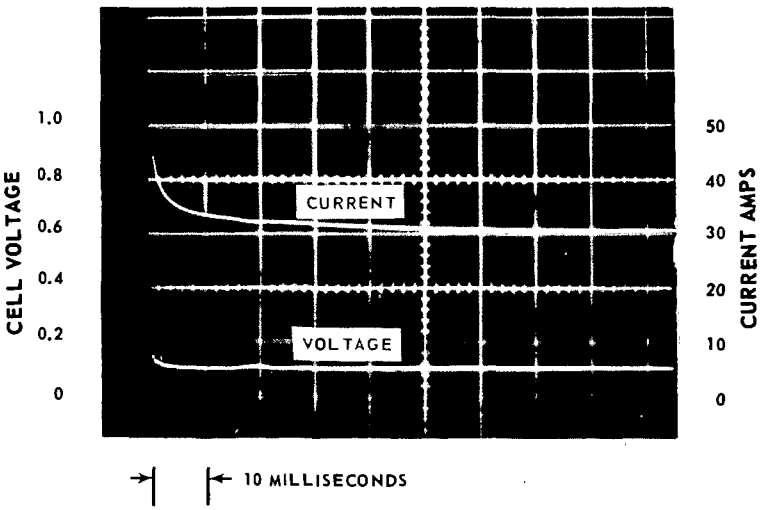

Figure 4 Trapped Electrolyte Cell Millisecond Response Following Switch Closure

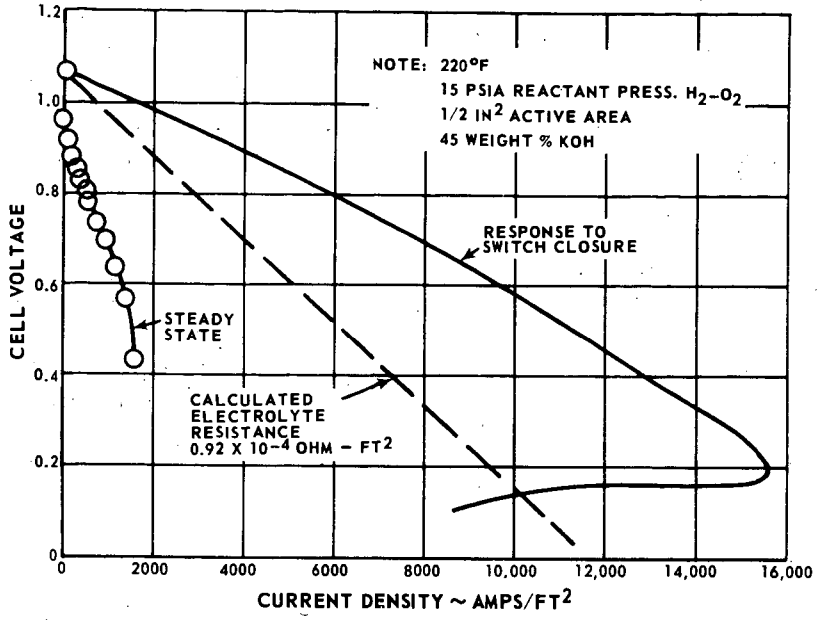

Figure 5 Trapped Electrolyte Cell Performance - Steady State and Transient

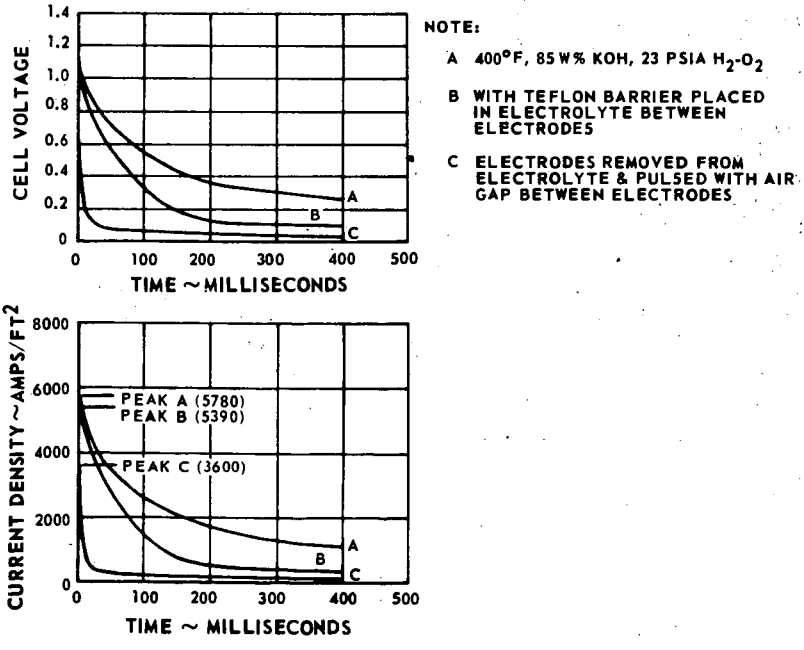

Figure 6 Free Electrolyte Cell - Millisecond Response

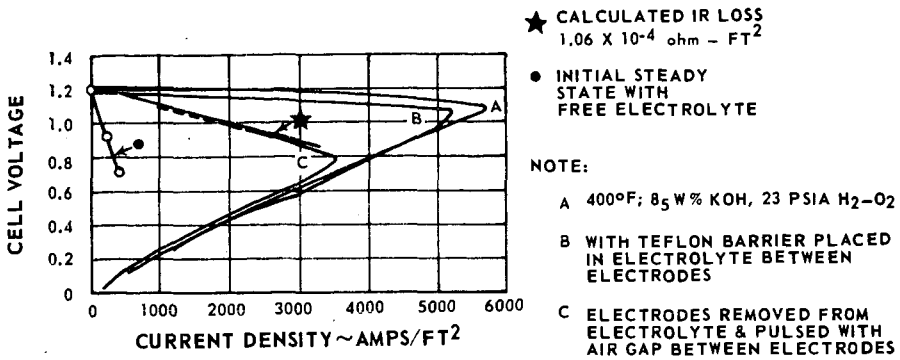

Figure 7 Free Electrolyte Cell - Performance Steady State and Transient

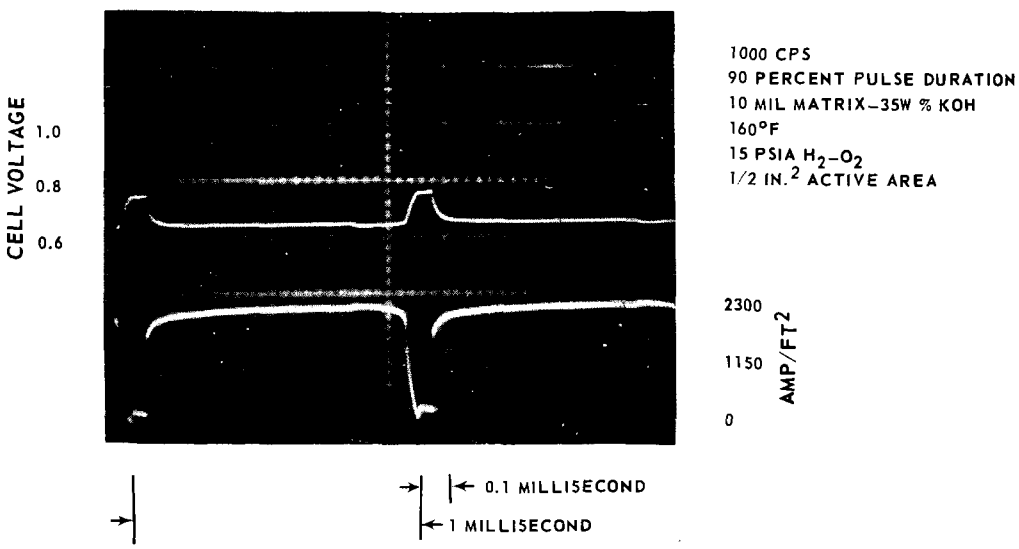

Figure 8 Trapped Electrolyte Cell Response to Repeated Pulse Loading

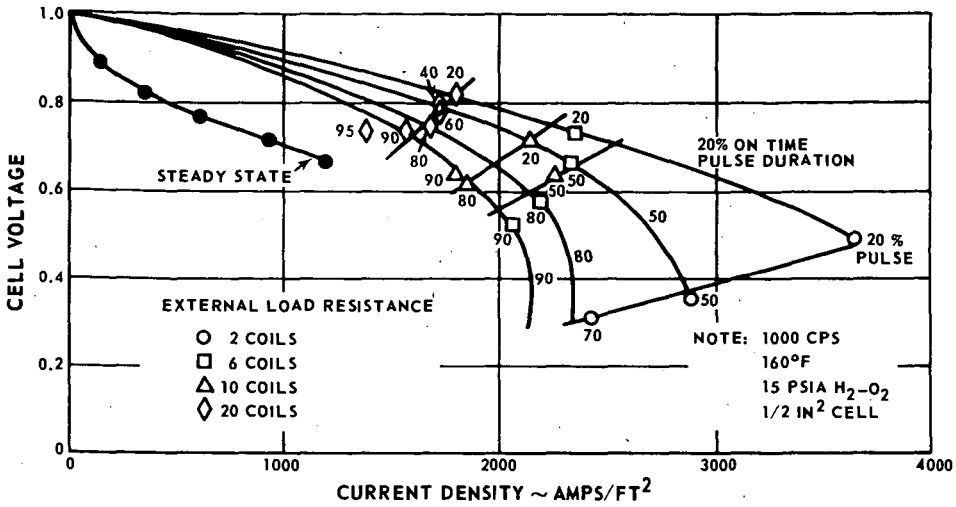

Figure 9 Trapped Electrolyte Cell Performance During Repeated Pulse Loading

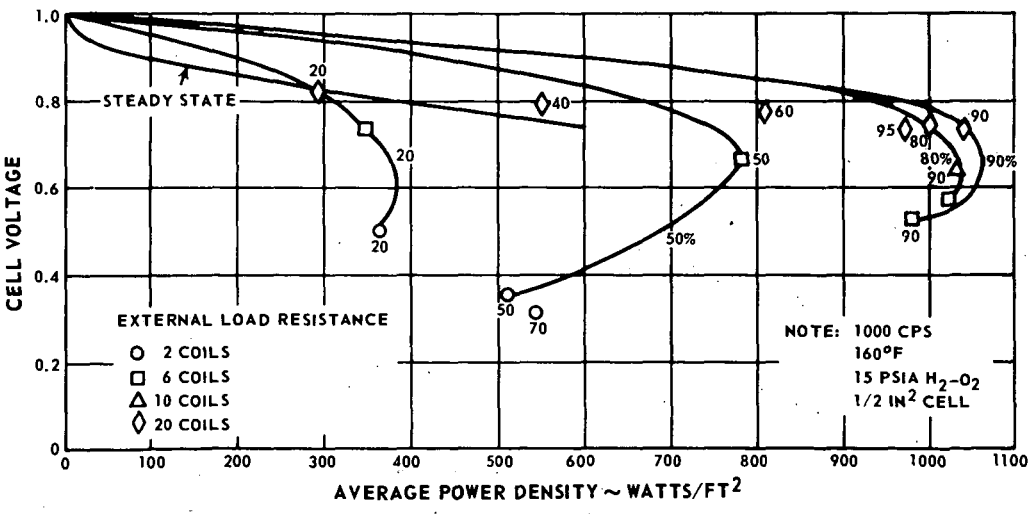

Figure 10 Trapped Electrolyte Cell - Average Power Density During Repeated Pulse Loading

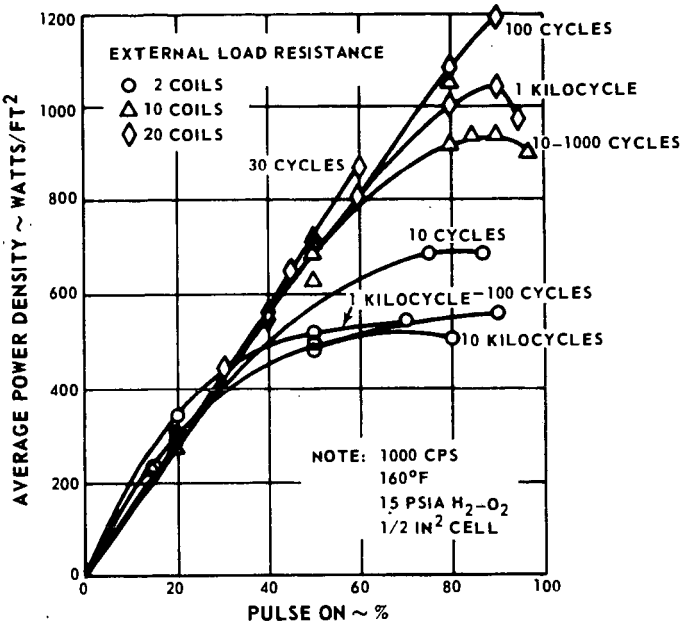

Figure 11 Trapped Electrolyte Cell - Effect of Pulse Duration and Frequency on Average Power Density

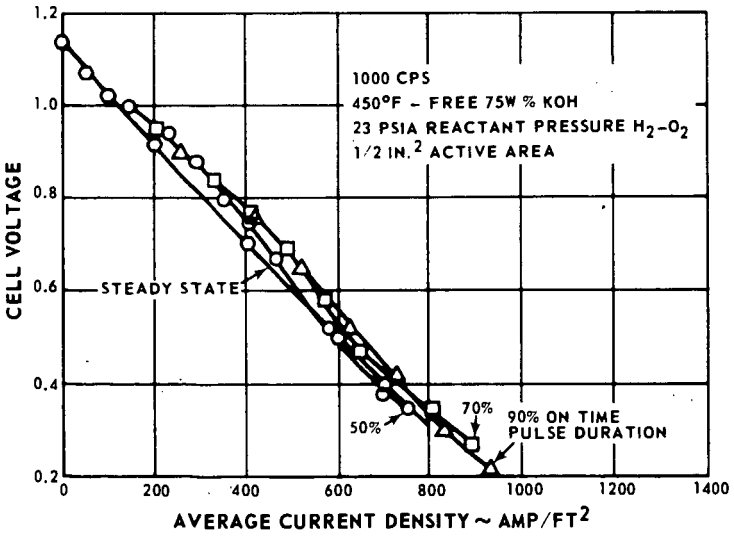

Figure 12 Free Electrolyte Cell - Average Performance During Repeated Pulse Loading

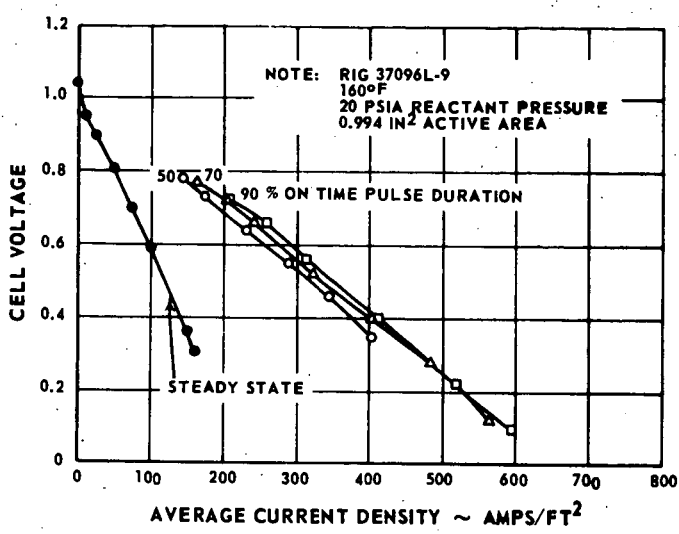

Figure 13 Low Temperature Free Electrolyte Effect of Repeated Pulsing on Performance

ON THE OPERATION MECHANISM OF A POROUS HYDROGEN ELECTRODE WITH A NICKEL CATALYST

R.Ch.Burshtein, A.G.Pshenichnikov, F.Z.Sabirov
Institute of Electrochemistry, Academy of Sciences of the USSR, Moscow.

It follows from our previous investigations of the operation mechanism of porous gas electrodes [1-3] that a porous electrode can be represented by a model shown in Fig.1. In Bacon's two-layer electrodes the fine pore layer practically does not participate in the electrochemical process. Electrochemical processes occur only in the layer of the electrode, which consists of two kinds of pores: macropores and micropores. Micropores are filled with electrolyte and macropores with gas. Electrochemical reaction occurs on the walls of macropores covered with a thin electrolyte film. The thickness of the electrolyte film determined from the data for a half-immersed nickel electrode is 0,5-1μ [4]. We used such a model of the porous electrode in the preparation of active electrodes for a hydrogen-oxygen cell.

According to Justi, active metalloceramic hydrogen electrodes can be prepared using nickel skeleton catalyst [5].

It should be noted that the preparation of electrodes by the Justi method requires a very long time because the aluminium elimination process occurs extremely slowly. These electrodes do not posess sufficient mechanical strength and operate steadily for a long period of time only at small current densities 30-50 ma/cm^2 [5].

We have developed a method of preparing hydrogen electrodes using a skeleton nickel catalyst, obtained from an alloy containing 50% Ni, 48% Al and 2% Ti [6].

It is known that such catalyst has larger catalytic activity and stability than the usual Raney catalyst. The influence of the heating temperature in hydrogen upon the specific surface of a catalyst containing a Ti addition was investigated. It was shown that the specific surface of a powder, measured by the BET method, remained practically unchanged upon heating in hydrogen up to 800°C and was equal to 80-90 m^2/g.

Electrodes were prepared as follows. The alloy previously ground in a vibrating mill and the powder obtained was freed of aluminium by treating with 5 N KOH. Such catalyst is highly pyrophoric, but when mixed in the wet state with carbonyl nickel, it loses this property and such a mixture can be stored dry a

long time. The loss of pyroforic properties by catalysts when they are mixed with carbonyl nickel is accounted for by the slow diffusion of oxygen through the water film and the formation of a thin oxide film on the catalyst surface. An investigation of the electrodes with varying structures activated by the skeleton catalyst carried out by the method similar to that used in [1].

In designing electrodes of large size of essential importance is the electrode strength. To ensure better strength a new design of electrodes with an internal gas feed was developed [7].

Such an electrode is shown schematically in Fig.2. The electrode consists of a shell made of readily sintering carbonyl nickel (edge - 1 and fine pore layer - 2) with the active layer - 3 inside (a mixture of skeleton catalyst and carbonyl nickel). Gas is supplied through side tubes-4. In the case of the electrodes having 120 mm in diameter strengthening and gas-feed paths - 5 are used. Strength is ensured by the electrode edge and gas-feed paths, which sinter well with the fine pore layers. Such electrodes were pressed in a special die in one operation. Gas feed paths can be of different forms. The electrodes operate both sides. Their operating surface is 165 cm^2 (both sides). When assembling the cell the electrodes are placed into a tank with electrolyte and connected in parallel with respect to gas and current.

The dependence of the current J_α upon the potential for a three-layer electrode with $\alpha = 0{,}25$ at different temperatures is given in Fig.3. Fig.4 shows the dependence of log J (at $\varphi = 80$ mv) upon the reciprocal temperature. The apparent activation energy of the process calculated from the slope of the straight line is 5 Cal/mol ^{o}C.

Tests on a large number of electrodes have shown good reproducibility of the results. The electrodes operated steadily in a hydrogen-oxygen cell for 12 months.

In the case of electrodes with high electrochemical activity the ohmic losses in the fine pore layer are large and therefore with a decrease in its thickness the current density increases. The experimental curve of the current density dependence upon the thickness of the fine pore layer is shown in Fig.5.

Of considerable interest is the dependence of the electrochemical activity of the electrode upon the skeleton catalyst content in the active mixture. As is evident from Table 1, with

an increasing ratio of the catalyst weight to that of the mixture (α) the current density rises up to $\alpha = 0,5$.

Table 1.

α	0	0,10	0,25	0,30	0,40	0,50	0,75	1,00
J ma/cm^2 (φ = 0,08 v)	50	108	140	151	168	185	136	108

With further increase in α (α= 0,75 and α= 1,00) the current density drops. As is shown by the structure measurements, it dependence on the change ratio of the macro- to micro pores. Of considerable interest in designing the three-layer electrodes is the dependence of the current density at a constant potential upon the active layer thickness. This dependence is shown in Fig.6. It is evident from the figure that at the thicknesses less than 1,5 mm the current density considerably decreases.

Now let us consider how the concepts of the porous electrode operation developed in [1-3] can be applied to the electrode activated with a skeleton catalyst.

The $J - \varphi$ dependences of the electrodes in question being linear at small polarization (see Fig.3), the electrode resistance R can be considered to be determined by the relation:

$$R = \varphi/J = z_a + z_f \qquad \ldots (1)$$

here z_a is the active layer resistance, z_f - the fine pore layer resistance. The fine pore layer resistance is expressed by the equation:

$$z_f = \rho \cdot \xi^2 \delta / v_f \qquad \ldots (2)$$

where ρ - is the electrolyte specific resistance, ξ - the sinuosity coefficient, v_f - total cross-section of the pores in the fine pore layer per unit of visible surface, equal to the fine pore layer porosity. In most cases $\xi = \sqrt{3}$ [8].

Now let us consider the dependence of the reaction resistance z_a upon the electrode activity.

According to (2), the dependence of the current density upon the gas electrode parameters is of the form:

$$J = (1/\xi)\sqrt{\lambda/\rho} \cdot \sqrt{P\Phi} \cdot \varphi \qquad \ldots (3)$$

where P is the total perimeter of the pores free of the electrolyte, Φ - the total cross-section of the pores filled with the electrolyte, $\lambda = \left(\frac{di}{d\varphi}\right)_{\varphi=0} \cdot \varkappa$, where i is the local

current density, χ - the ratio of the true to the visible surface. Let us assume that to the first approximation χ is proportional to the specific surface of the active mixture S_a. It is evident that in the mixture of the catalyst with carbonyl nickel.

$$S_a = \alpha \cdot S_{cat} + (1 - \alpha) \cdot S_{carb} \qquad \ldots (4)$$

The specific surface measurements using the BET method have shown the specific surface of the catalyst S_{cat}=80 m^2/gr, the specific surface of the carbonyl nickel powder S_{carb} = 0,55 m^2/gr.

According to the equations (3) and (4), for the electrodes with the same structure we obtain:

$$(\gamma_c/\gamma_a) = (S_a/S_{carb})^{1/2} = \left\{\alpha\left(S_{cat}/S_{carb} - 1\right)+1\right\} \qquad \ldots (5)$$

where γ_c and γ_a are the reaction resistances of the electrodes prepared from carbonyl nickel alone and from the active mixture, respectively.

Substituting the values of S_{cat} and S_{carb}, we obtain for the powdered catalyst used by us:

$$(\gamma_c/\gamma_a) = (144\alpha + 1)^{1/2} \qquad \ldots (6)$$

Substituting $\gamma_c = \varphi/\jmath$, obtained from equations (3) into (5) and using (2), we find for the total electrode resistance R the expression:

$$R = \frac{\left\{\alpha\left[\left(S_{cat}/S_{carb}\right) - 1\right] + 1\right\}^{1/2}}{(1/\zeta)\,(\lambda_c/\rho)^{1/2}\,(\rho\varphi)^{1/2}} + \frac{\rho\zeta^2}{v_f}\,\delta \qquad (7)$$

where $\lambda_c = \left(\partial i/\partial\varphi\right)_{\varphi\to\delta}$ for a non-active electrode.

Assuming for a 7 N KOH at 90°C ρ = 0,715 ohm.cm [5] and taking the value of λ_c from [2], we obtain: $(1/\zeta)\,(\lambda_c/\rho)^{1/2}$ = 0,024 $ohm^{-1}cm^{-3/2}$. It follows from the direct measurements of the fine pore layer porosity that v_f = 0,5. Substituting the values of ρ and ζ^2, we obtain for the coefficient before $\rho\zeta^2/v_f$ = 4,25 ohm.cm. Taking into consideration (6), we obtain from (7) for the active nickel hydrogen electrode:

$$R = \frac{41,5}{(\rho\varphi)^{1/2}\,(144\alpha + 1)^{1/2}} + 4,3\,\delta \qquad \ldots (8)$$

where

$$\gamma_a = \frac{41,5}{(\rho\varphi)^{1/2}\,(144\alpha + 1)^{1/2}} \qquad \ldots (8')$$

$$\gamma_f = 4,3\,\delta \qquad \ldots (8'')$$

The relation $(\rho\varphi)^{1/2} = f(\Delta P)$ obtained from the pores distribution curve of the electrode with the structure investi-

gated by us $\alpha = 0,25$ is shown in Fig.7b. The fine pore layer thickness $\delta = 0,071$ cm. In accordance with the determination of R (1) and eq (8), for an electrode with the operating surface $S_e = 165$ cm^2 at $= 0,08$ v, the current is equal to:

$$J = \frac{S_e}{R} \cdot \varphi = \frac{165 \cdot 0,08}{\frac{41,5}{0,1} + 4,45 \cdot 0,071}, a \quad \ldots (8''')$$

Fig.7 shows the experimental (Curve 1) and the calculated (Curve 2) dependences of the current strength upon the pressure difference between gas and electrolyte. At large values of ΔP the calculation and experimental results can be considered to agree fairly well. At small ΔP the discrepancy appears to be due to the small gas permeability of the worse owing to some of the gas supplying canals.

Using eq (8) and (1) it is possible to calculate the dependence of the current J on an electrode upon the fine pore layer thickness. The results of the calculation and the comparison with the experimental data of Fig.5 are presented in Table 2.

Table 2.

δ cm	γ_f ohm.cm^2	R ohm.cm^2	J, a $\Delta P = 600$ mm H $\varphi = 0,025$ v		$\varphi = 0,08$ v	
			calcul.	experim.	calcul.	experim.
0	0	0,32	12,9	-	41	-
0,01	0,042	0,36	11,2		37	
0,05	0,212	0,53	7,8	9,0	25	30
0,07	0,31	0,63	6,6	7,5	21	22
0,10	0,425	0,74	5,6	6,0	17	17

It is clear from the table that the agreement between the calculated and experimental values is quite satisfactory.

According to equation (8'), γ_a decreases and hence the current increases with increasing skeleton catalyst content (α) in the active mixture.

The experimental results for the electrodes with identical structure but varying catalyst content (α) are given in Table 1. The values of R and γ_a calculated from the data in Table 1 are listed in Table 3. Equation (6) relates the values obtained from the electrochemical and structure data for the electrodes with identical structures. The right hand and the left hand sides of equation (6) are given in Table 3 (columns 4 and 5). The comparison of the corresponding values shows that up to $\alpha = 0,5$ the experimental and calculated data agree with the accuracy up to

20%. The discrepancy between the data at $\alpha = 0,5$ is due, as stated above, to the change in the electrode structure.

Table 3.

α	R ohm.cm^2	r_a ohm.cm^2	S_a/S_{corr}	r_c/r_a	$\Delta p = 600$mm L	Δ_{cr} mm
0	1,6	1,29	1	1,0	1,3	4,0
0,10	0,74	0,43	3,92	3,0	0,4	1,3
0,25	0,57	0,26	6,10	5,0	0,25	0,8
0,30	0,53	0,22	6,65	6,9	0,2	0,65
0,40	0,476	0,166	7,65	7,8	0,15	0,5
0,50	0,433	0,123	8,55	10,5	0,1	0,30
0,75	0,588	0,278	10,4	4,65		
1,00	0,74	0,43	12,0	3,0		

As has been shown in [2-3], the characteristic thickness is determined by the equation(9)

$$L = (1/\xi)\ (\varphi/\rho \cdot \rho\lambda)^{1/2} \qquad \ldots (9)$$

Using the obvious relation $\lambda_a = \lambda_c \cdot S_a/S_{corr}$ and equation(5), we obtain for the electrodes with identical structure

$$L_c/L_a = (S_a/S_{corr})^{1/2} = r_c/r_a \qquad \ldots (10)$$

where L_c and L_a are characteristic lengths of the nonactive and active electrodes, respectively.

According to [2-3], at the thickness $l < 1,6L$ the electrode can be considered to be of infinite thickness. For such electrodes the current density is determined by eq (3). Using eq (3) and (9) and taking into consideration (1), we obtain:

$$L = r_a \cdot \varphi/(\xi^2 \rho) \qquad \ldots (11)$$

For the electrodes with the structure under consideration (NH_4HCO_3 240-340 mesh, 20%) at $\Delta p \sim 600$-900 mm Hg $\varphi \approx 0,2$ [2]. Then $L_a \approx 0,1 r_a$. The values of L_a thus calculated are given in column 6 of Table 3.

At $l \leq 1,6L$ [2-3] the current density is less than the maximum value determined from equation (3). The corresponding thickness Δ_{cr} of the three-layer electrode at which the current starts to decrease is $\Delta_{cr} = 2 \times 1,6L$. The values of Δ_{cr} are listed in column 7 of Table 3. For the electrodes with $\alpha = 0,25$ $\Delta_{cr} = 0,8$mm. According to Fig.6, the decrease in the activity on such an electrode occurs at $\Delta < 1,5$ mm, which appears to be due to a unsufficient gas distribution on the electrode.

Thus this concepts of the operation of the porous gas electrode can be used in the calculations and choice of the optimum conditions of operation of an active gas electrode. On the basis of the three-layer electrodes developed, it is possible to construct a cell of a simple design for a long time operation.

REFERENCES

1. R.Ch.Burshtein, A.G.Pshenichnikov, N.A.Shumilova, Dokl.Akad. Nauk SSSR, 143, 168 (1962).
2. A.G.Pshenichnikov, Dokl.Akad.Nauk SSSR, 148, 1121 (1963).
3. R.Ch.Burshtein, V.S.Markin, A.G.Pshenichnikov, Yu.A.Chizmadzhev, Yu.G.Chirkov, Electrochimica Acta, 9, 773 (1964).
4. A.G.Pshenichnikov, G.I.Shnaider, R.Ch.Burshtein, Elektrokhimiya, 1, 418 (1965).
5. E.Justi, A.Vinsel, Fuel Cells, Moscow, 1964.
6. A.G.Pshenichnikov, R.Ch.Burshtein, D.I.Lainer, Patent N147616, Sept.1961.
7. R.Ch.Burshtein, A.G.Pshenichnikov, N.A.Shumilova, Patent N 26596 of 10 Novemb.1961.
8. N.Bjerrum, E.Manegold, Koll.Z.,42, 97 (1927); 43, 5 (1927).

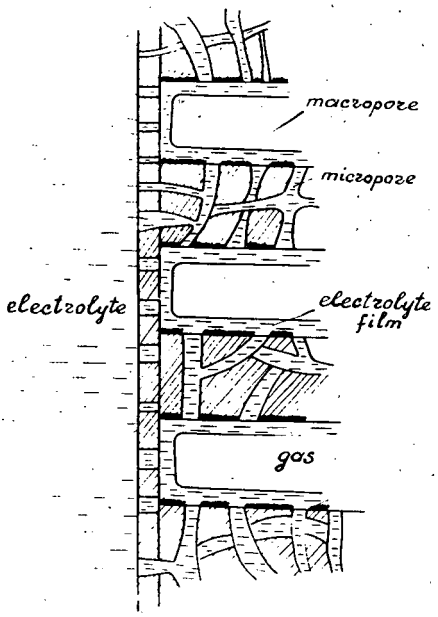

Fig.1. Porous gas electrode model.

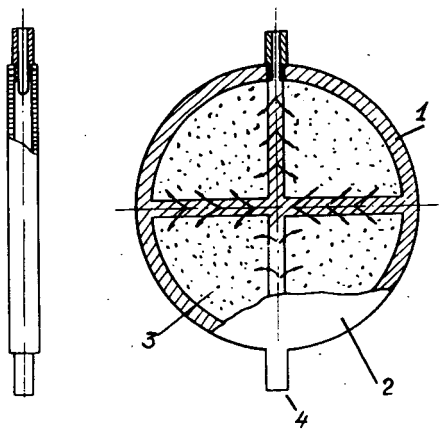

Fig.2. Scheme of an electrode with internal gas supply.

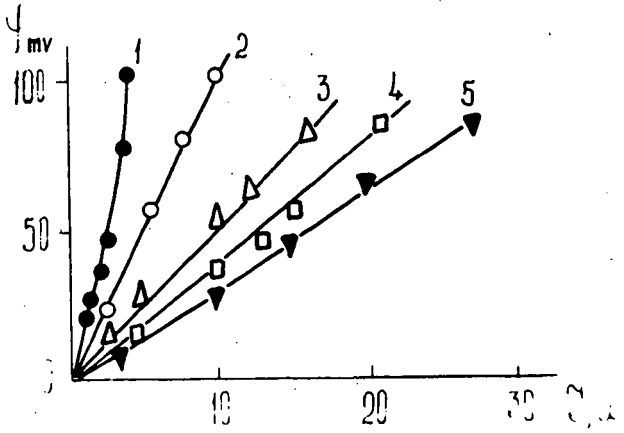

Fig.3. Polarization curves for different temperatures 1 - 20°, 2 - 40°, 3 - 60°, 4 - 77°, 5 - 92°.

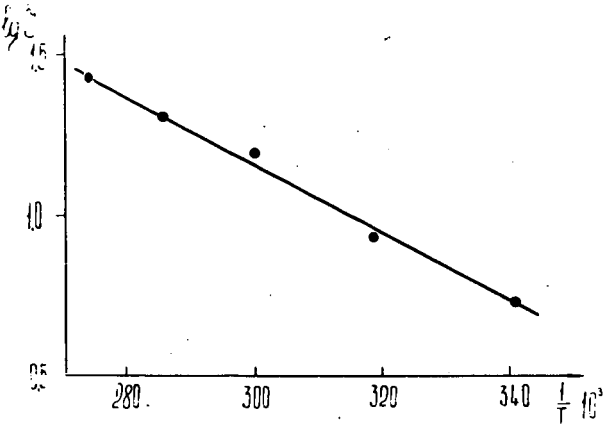

Fig.4. Dependence of $\lg J$ on $1/T$. φ = 0,08 v.

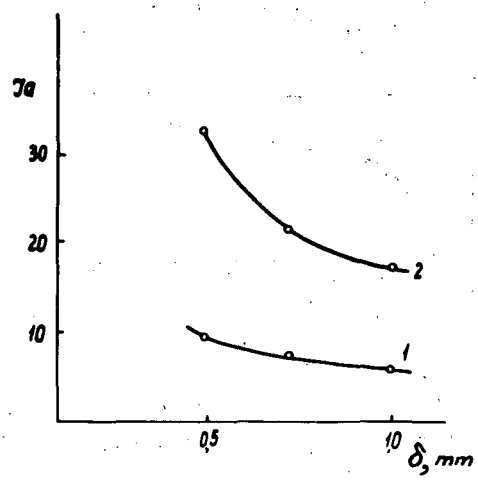

Fig.5. Dependence of J upon the fine pore layer thickness. 1 φ = 0,025 v. 2 - φ = 0,08 v.

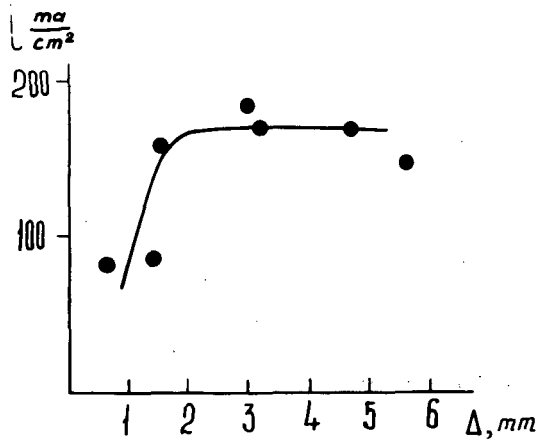

Fig.6. Dependence of current density upon the active layer thickness.

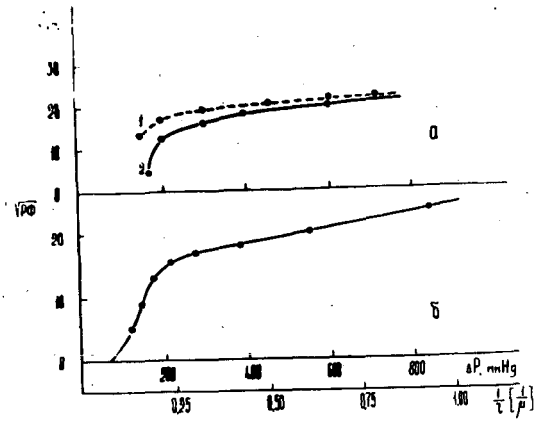

Fig.7. а - $J = f_1(\Delta P)$; $S_e = 165$ cm^2, $\varphi = 0{,}08$ v .
1 - calculation, 2 - experiment, b - $(\rho\varphi)^{1/2} = f_2(\Delta P)$.

HIGH SURFACE AREA SILVER POWDER AS AN OXYGEN CATALYST

James E. Schroeder, Dirk Pouli, H. J. Seim

Allis-Chalmers, Milwaukee, Wisconsin 53201

Introduction

The major voltage loss at current densities below 100 ma/cm^2 in modern hydrogen-oxygen fuel cells is due to the high overvoltage for the oxygen reduction reaction. Hence, much research has been expended in efforts to develop catalysts that are more active toward the reduction of oxygen. While the platinum group metals are well known oxygen catalysts, they have the disadvantage of being very expensive.

Boron carbide [1] and carbon black [2] have been suggested as less expensive oxygen reduction catalysts. Other catalysts of interest are certain organic materials such as cobalt phthalocyanine [3] and oxide materials such as the spinels. For the alkaline cell, however, the most promising catalyst to date appears to be silver [4,5,6].

Silver as an oxygen reduction catalyst may not possess a significant advantage over the platinum metals from technical considerations, but the difference in cost is significant. Silver will almost certainly replace the noble metals as the cathode in the alkaline hydrogen-oxygen fuel cell unless a less expensive and/or more active material is discovered.

The amount of the catalyst's surface area exposed to the fuel cell reactant in part limits the reaction rate. If the surface area is increased, some increase in reaction rate results. Therefore, we attempted to make a silver powder with a surface area 5-10 times higher than the surface area of commercially available silver powders. Further increases in surface area have diminishing returns and sometimes even adverse effects.

Silver powder with varying properties has been prepared in several ways. Some well known methods are chemical and electrolytic reduction of silver solutions and the decomposition of silver salts. Many investigators have studied the preparation and decomposition of silver oxalate [7,8,9,10,11]. It was shown by Erofeev et al [7] that the gradual acceleration of the decomposition of silver oxalate is due to the catalytic effect of the product, silver. They observed that for the first 20-30% of the decomposition the fraction decomposed, α, is given by the equation $\log (1-\alpha) = -kt^n$, where t represents time and k and n ($\approx$4) are constants. The decomposition reaction is essentially $Ag_2C_2O_4 \xrightarrow{\Delta} 2Ag+2CO_2$.

Macdonald [8] and Tompkins [9] found that partially decomposed silver oxalate crystals darkened uniformly and there was no preferential decomposition of the surface nor did the decomposition spread from a few isolated nuclei. These investigators were interested in the kinetics of the controlled decomposition and did not study the explosive decomposition reaction or the properties of the product of this reaction. Poltorak and Panasyuk [10] investigated the activity of sintered silver, produced by the decomposition of silver oxalate

in vacuo, for the decomposition of hydrogen peroxide. The catalytic activity reached a maximum for silver powder sintered at 600° C. Sviridov and Branitskii [11] investigated the catalytic activity of partially decomposed silver oxalate for the decomposition of hydrogen peroxide. The activity of this mixture of silver and silver oxalate was found to be a maximum after 35% of the initial silver oxalate was decomposed.

We investigated the rate of reduction of oxygen in alkaline media on silver powder made by the explosive decomposition of silver oxalate. It was found that silver powder with a surface area of 2-6 m^2/g could be made by the rapid explosive decomposition of silver oxalate [12].

Experimental Technique

Preparation and Decomposition of Silver Oxalate

Silver oxalate was made by adding crystalline silver nitrate to a saturated solution of oxalic acid at ambient temperature. The silver oxalate precipitate was filtered and the resultant slurry dried under a bank of heat lamps. It was crushed and sized and only particles between 0.5 and 2.0 mm were decomposed.

The silver oxalate was decomposed by dropping the particles onto a hot surface. The decomposition temperature of silver oxalate is 140° C but to increase the rate of decomposition the particles are dropped on a surface at 250-500° C. At higher temperatures the silver powder formed begins to sinter, thus lowering its surface area. The decomposition is accomplished in a container since otherwise the force of the explosion would scatter the silver. The container must be properly vented to exhaust the large volume of carbon dioxide released during the decomposition reaction. A schematic diagram of the decomposition apparatus is shown in figure 1. The silver decomposition product is screened to less than 0.15 mm in diameter to remove any oxalate particles or hard pieces of silver formed when the product is scraped from the decomposition chamber.

Electrode Preparation

Electrodes were prepared from the silver powder by incorporating poly-tetrafluoroethylene as a binder and pressing the mixture onto a metal screen in a method similar to that reported by Niedrach and Alford [13]. Electrodes 7.5 cm x 7.5 cm were used to determine the catalytic activity of the material in terms of fuel cell performance, while electrodes 10 cm x 23 cm were used in life tests. In life tests two cells in parallel were used to insure reliability and more significance in testing.

Determination of Catalytic Activity

The activity of electrodes for the reduction of oxygen was determined in a hydrogen-oxygen fuel cell using an asbestos matrix to contain the electrolyte. The test conditions are given in Table I. The same conditions were used for life tests.

TABLE I

Test Conditions

Thickness of Asbestos Matrix	- 0.75 mm
Electrolyte	- 30% KOH
Temperature	- 90° C
Gas Pressures	- 18 psig (26 psia)
Anode	- 3.0 mg Pt and 3.0 mg Pd per cm^2 plated on a porous sintered nickel plaque.

A transistorized 60 cps sine wave commutator [14] was used to drive the cell. For short term tests, such as those to determine the initial activity (electrical performance), no elaborate water removal system was required. Water may simply be removed by purging the gas cavities with the respective reactants. The asbestos is soaked with electrolyte until saturated. The gases are then applied to the cell and the cell is subjected to a load of 300 ma/cm^2. The gas cavities were purged until a maximum voltage was reached at the applied load of 300 ma/cm^2. A reverse current scan was adopted since it normally yielded better reproducibility than the forward scan. Total cell voltage, resistance-free voltage and the resistive voltage losses of the cell were then measured as a function of current density. The time required to determine the voltage-current curve is 2-5 minutes.

Voltammetric measurements were made using a potentiostat. It was developed in our laboratories and is capable of handling anodic and cathodic loads of up to 25 amperes. The test cell consisted of a working electrode held in place by an asbestos matrix with electrolyte flowing behind the asbestos. To keep oxygen from bubbling through the electrode a counter pressure was applied to the electrolyte. The oxygen pressure was approximately 3 psig higher than the electrolyte pressure. If a smaller differential pressure was used the working electrode flooded.

TABLE II

Conditions of Voltammetric Experiments

Temperature	- 90° C
Oxygen Pressure	- 18 psig (26 psia)
Electrolyte	- 30% KOH
Electrolyte Pressure	- 15 psig
Scan Rate	- 10 mv/sec
Reference Electrode	- Hg/HgO

Results and Discussion

Physical Properties of the Silver Powder

Particles of silver produced by the rapid thermal decomposition of silver oxalate are irregular in shape with many nodules. The nodules are approximately 0.1 μ in diameter. Analysis by X-ray indicates that the silver is crystalline.

The specific surface area of the silver powder, measured by the B.E.T. method, was in the range of 2-6 m^2/g. Decomposition of the hardest and driest silver oxalate particles yielded the highest surface area silver powder. Material decomposed rapidly also had higher surface areas than material heated slowly. Photo electronmicrographs of the rapidly decomposed material are shown in figure 2. Figure 2B shows in greater detail a portion of the particle shown in figure 2A. Figures 2B and C show different particles under the same magnification.

Catalytic Activity

The activity of the catalyst for the reduction of oxygen was determined in a hydrogen-oxygen fuel cell. Total cell voltage, resistance free voltage and resistive voltage losses of the cell were measured as a function of current density after optimizing the cell at 300 ma/cm^2. Representative total cell and resistance free voltages vs. current are shown in figure 3. All the voltage-current curves shown in figure 3 were obtained by reverse current scans. Half cell potentials are cited with respect to the potential of the standard hydrogen electrode unless stated otherwise.

The curve in figure 3 shows that appreciable reduction, say 10 ma/cm^2, commences at a potential of 1.05 volts with respect to the hydrogen electrode at 26 psia in the same solution. Voltage current curves for low loaded Pt-Pd electrodes (3.0 mg Pt and 3.0 mg Pd per cm^2 plated on a porous, sintered nickel plaque) and heavily loaded Pt-Pd electrodes (13.5 mg Pt powder and 27 mg Pd powder per cm^2, teflonated and pressed on a nickel screen) are shown for comparison (see figure 3). The Pt-Pd electrodes were tested in the same manner as the silver electrodes. On the basis of half cell measurements we believe that total reaction polarization of the cell (see figure 3), exclusive of resistive losses, occurs essentially at the oxygen electrode. The polarization losses indicated in figure 3 are therefore essentially those of the silver electrode.

Effect of Oxygen Pressure

The effect of oxygen pressure on cathode polarization was studied in a half cell. The resistance free curves are therefore a direct measure of the cathode polarization. The polarization increases nearly linearly with decreasing pressure for pressures exceeding one atmosphere of oxygen. The slope of the curve increases by a factor of five from 32 psia to 12 psia. This increase in slope is especially prominent at current densities above 200 ma/cm^2. Pressure vs. resistance free voltage of a typical high surface area silver electrode is plotted in figure 4.

Effect of Temperature

The effect of cell temperature on cathode polarization was also studied. A resistance free voltage vs. temperature curve for a typical electrode is plotted in figure 5. The slope is essentially independent of temperature between 50° and 90° C.

Performance at High Current Densities

Voltammetric measurements on these silver electrodes showed that the limiting current lies above 6000 ma/cm^2. A voltage vs. current

density curve is shown in figure 6. The measurement was carried out at such a sweep rate that build up of water during the voltage current measurement is so small that control problems do not arise. In manual testing the water build up is too rapid to study the limiting current density with any validity.

Corrosion of Silver

Voltammetric data indicate that silver tends to corrode at potentials exceeding 1.05 volts vs. the potential of the hydrogen electrode for the conditions specified in table I. Therefore, the silver electrode will tend to corrode at current densities less than 10 ma/cm^2. Since silver oxide is appreciably soluble in the fuel cell electrolyte at 90° C, the electrode will gradually dissolve. Furthermore, the silver oxide will be reduced on the anode after migration through the asbestos matrix. Both these effects, dissolution and redeposition of silver, are detrimental to fuel cell performance. In practice, the voltage of fuel cells operating at practical current densities is well below that required for the onset of corrosion. The problem of corrosion of the silver electrode is, therefore, eliminated by the relatively high overvoltage for the reduction of oxygen.

Life Tests

Life tests have shown that electrodes made from this high surface area silver are stable for more than 6000 hours. The increase in polarization for the total cell at a constant current density of 100 ma/cm^2 is about 10 μv per hour in a hydrogen-oxygen fuel cell at 90° C. We have no data available to indicate the rate of voltage degradation for the single electrodes. Since the total degradation for the cell is 10 μv/hour the cathode degradation is certainly less. Life test data is plotted in figure 7.

Conclusions

The rapid thermal decomposition of hard, dry particles of silver oxalate produces a silver powder with a surface area of 2-6 m^2/g. This powder is extremely active as an oxygen reduction catalyst in alkaline media. It exhibits lower polarization losses at all current densities than Pt-Pd electrodes when used in a hydrogen-oxygen fuel cell under the conditions cited in the text.

The dependence of the activity of this material on oxygen pressure is nearly linear for pressures above 18 psia. At pressures between 10 and 18 psia the polarization increases rapidly with decreasing oxygen pressure.

The dependence of activity on temperature is essentially linear from 50° C to 90° C in a hydrogen-oxygen fuel cell. At temperatures below 50° C the polarization increases at a much faster rate.

Life tests show that electrodes made from this material are stable for more than 6000 hours. The average voltage degradation was less than 10 μv/hour.

References

1) S. G. Meibuhr, Nature 210, 409 (1966).

2) K. S. Schwabe, Electrochem. Technol. 3, 189 (1965).

3) R. Jasinski, J. Electrochem. Soc. 112, 526 (1965).

4) S. Z. Beer and Y. L. Sandler, ibid. 112, 1133 (1965).

5) A. W. Czanderna, J. Phys. Chem. 68, 2765 (1964).

6) E. W. Justi and A. W. Winsel, J. Electrochem. Soc. 108, 1073 (1961).

7) B. V. Erofeev, P. I. Belkevich and A. A. Volkova, C.A. 49, 2970g.

8) J. Y. Macdonald, J. Chem. Soc. (1936), 832.

9) F. C. Tompkins, Trans. Faraday Soc. 44, 206 (1948).

10) O. M. Poltorak and G. P. Panasyuk, C.A. 52, 14029h.

11) V. V. Sviridov and G. A. Branitskii, C.A. 57, 4089f.

12) U.S. Patent Application #422,794.

13) L. W. Niedrach and H. R. Alford, J. Electrochem. Soc. 112, 117 (1965).

14) G. F. Pollnow and R. M. Kay, ibid. 109, 648 (1962).

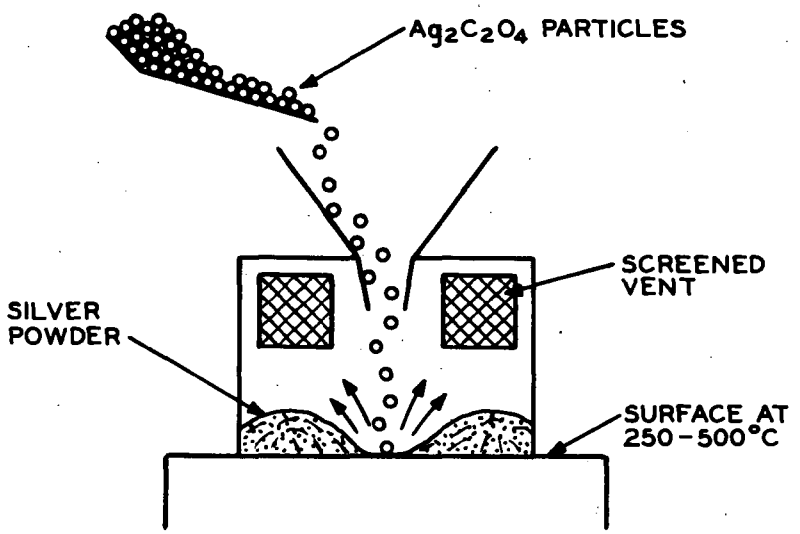

FIG. 1. APPARATUS FOR THERMALLY DECOMPOSING SILVER OXALATE PARTICLES.

FIG. 2. ELECTRONMICROGRAPHS OF HIGH SURFACE AREA SILVER POWDER

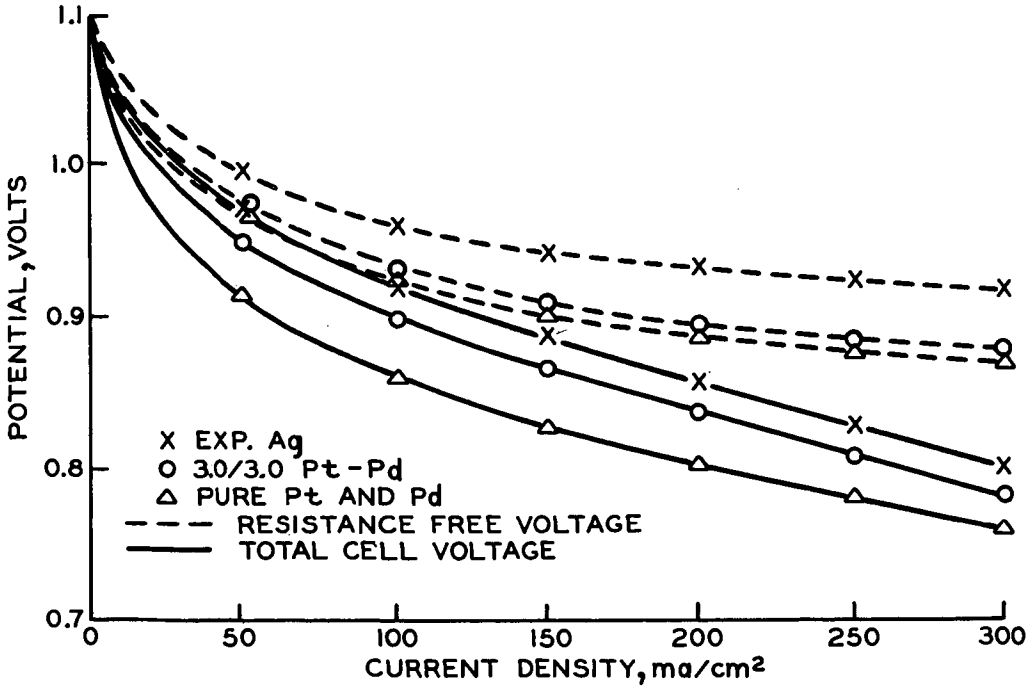

FIG. 3. PERFORMANCE CHARACTERISTICS FOR A FUEL CELL CONTAINING HIGH SURFACE AREA SILVER CATHODES.

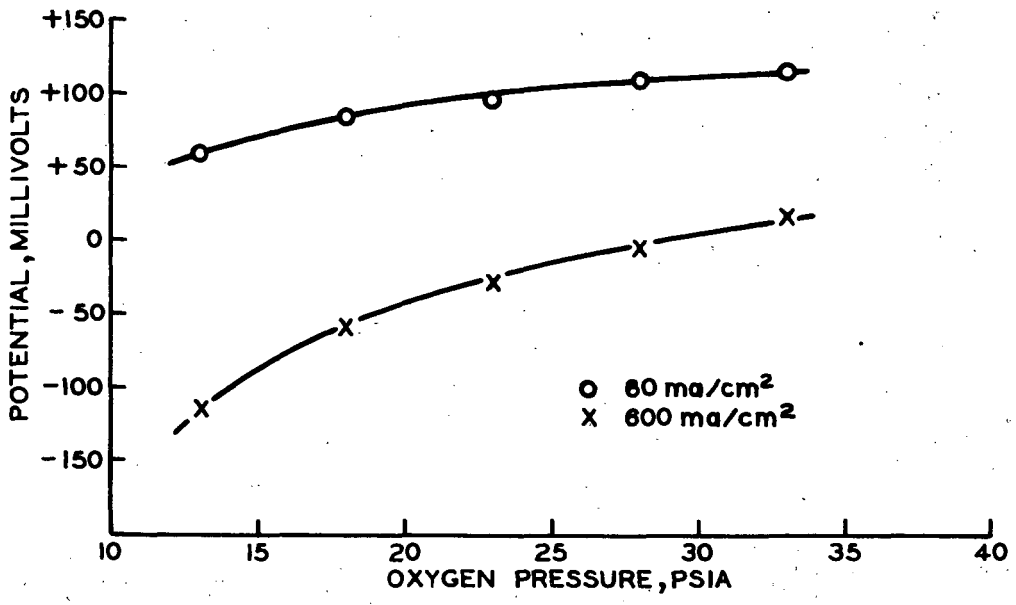

FIG. 4. EFFECT OF P_{O_2} ON THE POLARIZATION OF SILVER CATHODES.

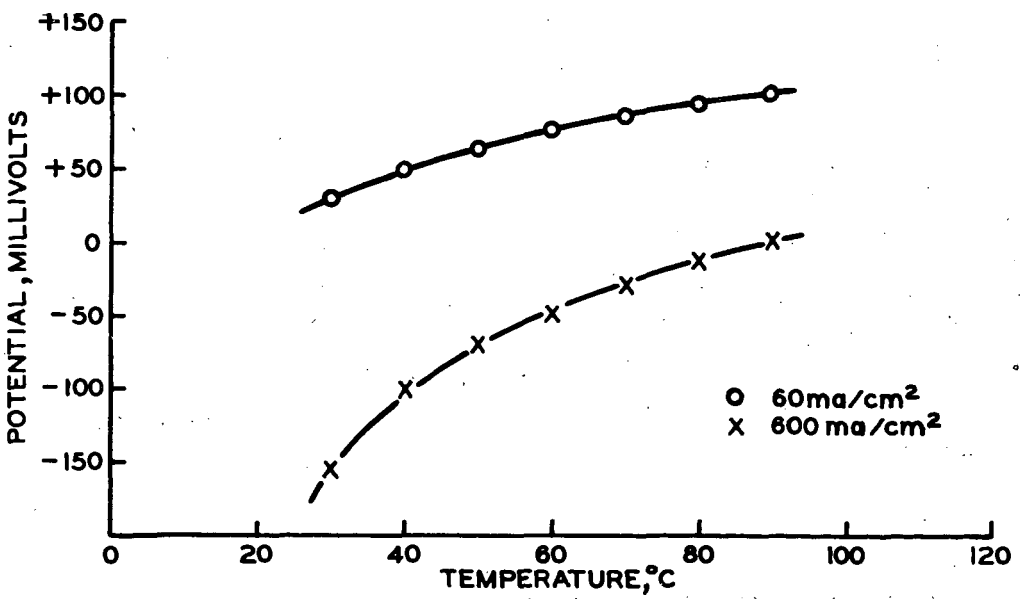

FIG. 5. EFFECT OF TEMPERATURE ON THE POLARIZATION OF SILVER ELECTRODES.

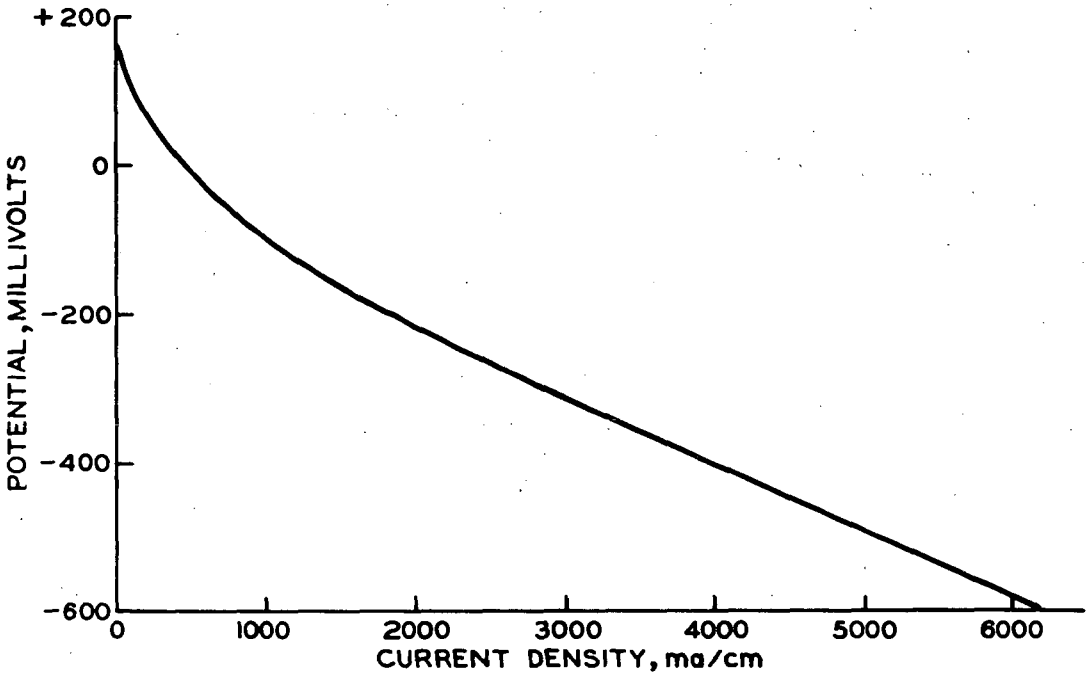

FIG. 6. PERFORMANCE OF HIGH SURFACE AREA SILVER CATHODES AT HIGH CURRENT DENSITY.

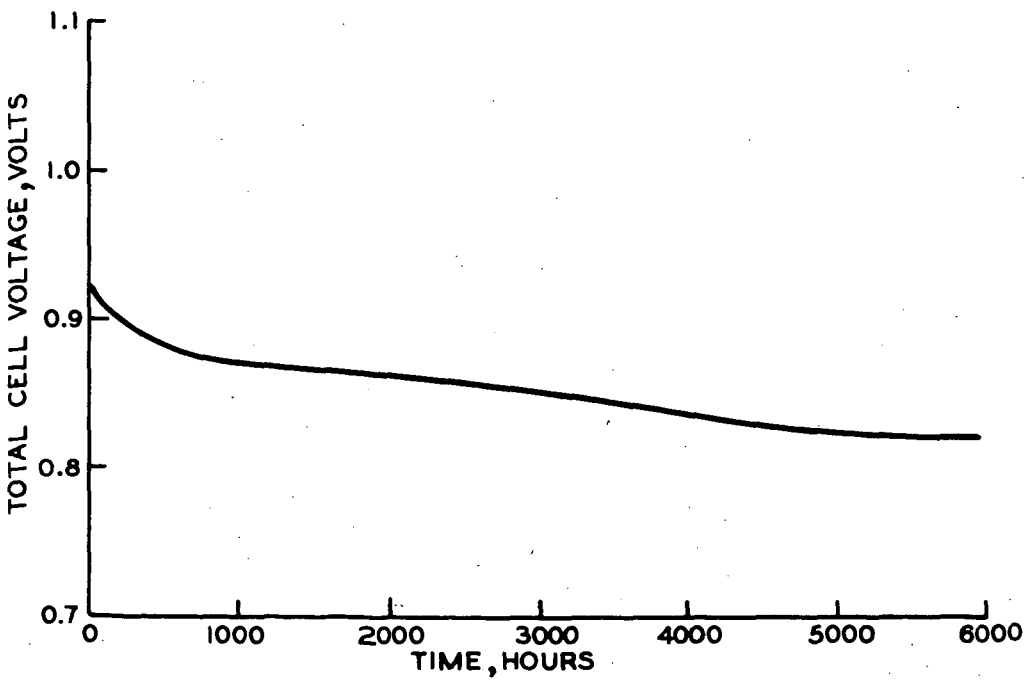

FIG. 7. LIFE TEST PERFORMANCE

INSTABILITY OF SUPPORTED-PLATINUM SURFACE AREA IN THE PRESENCE OF ELECTROLYTES

J. F. Connolly, R. J. Flannery, B. L. Meyers and R. F. Waters

Research and Development Department, American Oil Company, Whiting, Indiana

Supported platinum crystallites grow rapidly when in contact with electrolyte solutions at moderate temperatures (< 200°C). The absence of any growth in air at much higher temperatures indicates that the rate of area loss in solution is orders of magnitude greater than that of losses from dry sintering. This type of platinum-area loss is a serious handicap to the development of economic fuel-cell electrodes.

Measurements of platinum area, independent of the support area, were made by using a combination of integral capacitance measurements in the hydrogen-adsorption and double-layer regions. The possibility of poisoning was eliminated by checking the degree of crystallite growth with x-ray diffraction. Analyses showed that permanent dissolution of platinum was not a significant factor.

In addition to the effects of time and temperature, the rate of crystal growth was influenced by the support type, the solution, the platinum concentration, and the initial crystallite size. High support areas reduced crystal growth rates as did solutions with low conductivity. However, even water (10^{-4} mho/cm) showed some effect. The best dispersions are the most easily damaged because the very small initial crystallite size provides a large driving force for recrystallization. In such cases platinum-area losses up to 90% were observed.

Electrorecrystallization provides a possible mechanism for rationalizing these results; i.e., cells may be formed between large and small platinum crystallites, with the smaller crystallites acting as anodes because of their higher surface energies. Complex platinum ions would then be transported through the solution while electrons pass through platinum-platinum contacts, or through a conducting support, or through both. The transport of platinum complexes with no necessity for electron flow between crystallites would also be conceivable.

OXYGEN REDUCTION ON GOLD ALLOYS OF PLATINUM, PALLADIUM, AND SILVER

J. Giner, J. M. Parry, L. Swette

Tyco Laboratories, Inc.
Bear Hill
Waltham, Massachusetts 02154

ABSTRACT

Gold alloys of platinum, palladium and silver were prepared in which the composition varied by increments of 10% from 10 - 90% gold. They were examined as rotating electrodes for activity in the cathodic reduction of oxygen in 2 N potassium hydroxide at 25°C.

The activity of the Au/Ag alloys decreased progressively as the silver content was increased; the Au/Pt alloys showed an almost constant activity over the whole composition range; the Au/Pd alloys, however, showed a broad maximum of activity (greater than that of the Au/Pt alloys) over the composition range 70 - 20% Au. The order of activity of the pure metals at low polarization was Pd > Pt = Au > Ag.

The extent of oxygen film formation on each of the alloys was determined by fast potential sweep techniques, this information is used in the interpretation of the observed activities. Selected measurements were made at 75°C, the pattern of activity was substantially the same at 25°C. In the experimental work care was taken to ensure that the bulk alloy composition was preserved at the surface for all measurements. Variations in surface roughness were taken into account by measurement of double layer capacities using a triangular potential sweep.

THE ADSORPTION OF CARBON MONOXIDE ON PLATINUM AND RHODIUM ELECTRODES

S. Gilman

National Aeronautics and Space Administration, Electronics Research Center, Cambridge, Massachusetts

INTRODUCTION

The adsorption of carbon monoxide on noble metal electrodes is of current interest in connection with several areas in the field of fuel cell technology. These areas include anodic oxidation of CO (7), of impure hydrogen containing CO (8), and of organic substances where adsorbed CO is suspected of being an intermediate (9). In this paper, the author will compare the results of earlier (1-4) studies of CO adsorption on Pt with more recent observations (5) made on the adsorption of CO on Rh under roughly similar experimental conditions.

EXPERIMENTAL

The original papers (1-5) may be consulted for experimental details. The Pt and Rh electrodes were smooth polycrystalline wires. Pt wires were generally annealed in a hydrogen flame. Rh electrodes were annealed near the melting point in a high-vacuum bell jar. Both metals were sealed into soft glass supports at one end, using a cool hydrogen flame. The surfaces were given a light etch in aqua regia.

All potentials are referred to a reversible hydrogen electrode immersed in the same solution as the working electrode.

All values of charge and current density are reported on the basis of the geometric area, unless otherwise specified.

DISCUSSION

Hydrogen and Oxygen Adsorption on Clean Pt and Rh Electrodes-

Numerous voltametric studies have been made of the adsorption of hydrogen and "oxygen" (including possible formation of oxides or oxide precursers) on Pt and Rh electrodes, and the results have been reviewed by several authors (10-15). The following qualitative conclusions for sulfuric or perchloric acid electrolyte are useful in establishing proper conditions for the study of CO adsorption and in interpreting the results:

1) The coverage of both Pt and Rh electrodes with hydrogen atoms approaches a monolayer near 0 v.. The coverage gradually decreases to zero at 0.3 - 0.4 v. (depending on temperature) for Pt and at 0.1 - 0.2 v. for Rh. The adsorption and desorption of hydrogen atoms possesses a high degree of reversibility for both metals.

2) The adsorption of "oxygen" begins at potentials below ca. 0.8 v. for Pt and below ca. 0.6 v. for Rh. The "adsorption" is not reversible (except possibly at very low coverages) insofar as the dissolution of the "oxygen" film occurs at potentials several tenths of a volt less anodic than the formation.

Steady-State Oxidation of CO and H_2-

Information on the steady-state oxidation of CO and H_2 on Pt and Rh electrodes provides information useful in interpretation of results of adsorption studies. "Polarization curves" obtained in stirred sulfuric acid appear in Fig. 1. The curves were obtained under the conditions of a slow linear sweep but similar results may be obtained point-by-point at constant potential. For hydrogen on both Pt and Rh, (Fig. 1a and 1b), transport-controlled oxidation is observed slightly above the reversible potential. Onset of passivation of the oxidation is apparent at the potential of oxygen adsorption (above ca. 0.6 and 0.8 v. for Rh and Pt, respectively), and is almost complete within a few additional tenths of a volt. For CO, a flat limiting current is not observed, since initial CO oxidation and initial passivation almost coincide. The steep initial rise in CO oxidation current has previously been ascribed, for Pt (3), to a reversal of "self poisoning". A similar interpretation seems likely for Rh as well. Compared with hydrogen, the passivation of CO oxidation occurs over a wider range of potentials, particularly for the Pt electrode.

Electrode Pretreatment-

A convenient initial condition for the study of adsorption is that for which the surface coverage with the adsorbate (and with impurities) is initially zero and no reaction occurs between the surface and the adsorbate (hence the concentration of adsorbate near the electrode surface is the same as that in the bulk of the solution). For some adsorbates (e. g., some ions and hydrocarbons) this condition may be achieved at some potential with the Pt surface in the reduced state. For CO on Pt and Rh, this condition may only be achieved by passivating the surface with an "oxygen" film. For Pt (sequence of Fig. 2a) a potential as high as approximately 1.8v. (step A) is required, not only for sufficient passivation, but also to remove such refractory impurities as the hydrocarbons (16). Products of the anodization (CO_2, O_2) may be eliminated at some lower potential (e. g., step B) at which the "oxygen" film is still retained. Rapid reduction of the surface and subsequent adsorption occurs during step C. For Rh (sequence of Fig. 2b) the high-potential anodization of step B eliminates all refractory adsorbed substances, but the resulting "oxygen" film is reduced very slowly (as compared with Pt). After this more rigorous cleanup, the anodization of the surface at 1.2 v. (step D) is sufficient for Rh (unlike Pt) to strip off CO_2 and fully passivate the surface against CO re-adsorption or oxidation.

In Fig. 2a, trace A is believed to correspond to the clean Pt surface. Variations such as traces B and C are believed (2,6) to correspond to a surface contaminated by electrolyte impurities since such variations are accellerated by stirring and retarded by solution purification procedures. Similar observations have been made by Giner (17) and Brummer (18) for Pt in sulfuric and phosphoric acids, respectively. The situation for Rh (Fig. 2b) appears similar to that for Pt, with trace 1 corresponding to the clean surface and traces 2 and 3 corresponding to surface contamination.

Determination of CO Coverage by Anodic Stripping-

In the potential sequence of Fig. 3a, the Pt surface is pretreated as discussed above. The surface is them reduced during the first few milliseconds of step C, and CO adsorbs on the freshly reduced surface. Application of sweep D results in the current-time (potential) traces. Trace A of Fig. 3a corresponds to zero coverage with CO and the charge (area) obtained by integrating under the

curve starting at the potential of steeply-rising current corresponds to oxidation of the surface, charging of the ionic double layer and (at higher potentials) to evolution of molecular oxygen. Traces B-F correspond to increasing coverage of the surface with CO and compared with trace A, additional charge flows corresponding to oxidation of adsorbed CO to CO_2. Using trace F as example, we see that this trace merges with that for the clean surface at time t_1 (or potential E_1). This suggests that despite initial conditions, the two surfaces are in the same state by time t_1. This in turn, suggests (2) that, (in spite of the other coulombic processes occurring) ΔQ, the difference in charge under traces F and A may correspond almost exactly to Q_{CO}, the charge required to oxidize adsorbed CO to CO_2. This assumes that the sweep is sufficiently fast that diffusion and subsequent oxidation of CO during the sweep is negligible. In this case:

$$\Delta Q = Q_{CO} = 2F\Gamma_{CO} \qquad (1)$$

Where Γ_{CO} is the coverage of the surface with CO in moles per cm^2. The experimental observations (1,2) tend to support the validity of equation (1) for Pt. First, ΔQ is found to remain constant throughout a range of sweep speeds where errors due to diffusion of CO during the sweep are not anticipated. Second, the adsorption rate determined through anodic stripping obeys a calculated diffusion rate law to within 10% (2). Galvanostatic transients may also be used in determining the CO surface coverage (19-22) in a manner similar to the use of a linear sweep. Variations between investigators in reported maximum coverage are likely due in part to the details of correcting for oxidation of the surface (4).

Equation (1) seems to apply for Rh as well as for Pt (5). In the sequence of Fig. 3b, rapid reduction of the surface occurs during step F, but the major part of the adsorption may be allowed to occur at any other potential U (during step G). Step H is applied to eliminate "oxygen" adsorbed at larger values of U. Sweep I is applied to sample the extent of adsorption and the current-time (potential) traces obtained are similar to those obtained for Pt. As for Pt, ΔQ is relatively independent of sweep speed and the experimental adsorption rate follows a good linear diffusion law (5), until high coverages are achieved.

Kinetics of CO Adsorption-

Until the coverage exceeds at least 75% of the maximum, the kinetics of CO adsorption on both Pt and Rh is sufficiently rapid that transport control is observed in both quiescent and mechanically stirred solutions (2,4,5). This applies for potentials ranging from that of hydrogen gas evolution to that of anodic attack on CO.

Effect of Potential on the Structure of the Adsorbed Layer-

Carbon monoxide adsorbs on both Pt and Rh electrodes over a range of potentials extending from highly reducing to highly oxidizing conditions. It is reasonable to suspect therefore, that the adlayer may vary in composition or structure corresponding to partial oxidation or reduction of the original adsorbate. During a linear anodic sweep, there are coulombic processes in addition to the oxidation of CO and the situation is therefore kinetically complex. Nevertheless, the linear anodic sweep trace may be used to characterize the adlayer, if comparisons are made under carefully controlled conditions. In Fig. 4a and 4b, using the results for U=0.12 v. as the bases for comparison, traces for CO on Rh are compared from -0.2 v. to 0.5 v.. When the traces are compared at (approximately) equal values of Q_{CO}, the results are almost identical over this entire range of potentials. For Pt (Fig. 4c) at full

coverage the identical trace (trace 2) is obtained for potentials from -0.1 to 0.7 v.. Trace 3 is obtained at -0.2 v. and may correspond to partial reduction of the adlayer. Excluding potentials as low as -0.2 v. for Pt, it may therefore be concluded that there is no evidence for structural variations in the CO adlayer on either Pt or Rh over most of the range of potentials at which CO adsorbs.

Steady-State Coverage with CO-

Fig. 5 presents the fractional coverage of a Pt electrode surface with CO as determined under the conditions of a slow triangular sweep. Very similar results may be obtained on a point-by-point basis at constant potential. The decreased coverages observed during part of the descending sweep is due to the lag in reduction of the "oxygen" film formed at high potentials (1). For a hypothetical perfectly smooth electrode, the maximum value of Q_{CO}= 0.28 mcoul./cm^2 (4) (based on the hydrogen area) corresponds to Γ_{CO}=1.4x10^{-9} moles/cm^2 (based on the hydrogen area) with ca. 90% of the available (hydrogen) sites occupied by CO. This maxumum value remains constant for CO partial pressures over a range of at least 0.01 to 1 atmosphere (4).

The results for Rh (fig. 6) were obtained at constant potential. As for Pt, we see that a flat maxumum is obtained for a wide range of potentials and CO partial pressures. The maxumum value of Q_{CO} as calculated for a smooth surface is 0.44 mcoul./cm^2 (hydrogen area), equivalent to Γ_{CO}=2.2x10^{-9} moles/cm^2 (hydrogen area). This corresponds to almost complete coverage of available (hydrogen) sites with CO.

For both Pt and Rh the coverage with CO tends to fall off precipitously at the same potentials where CO is oxidized to CO_2, and where there is also the onset of "oxygen" adsorption for both Pt and Rh. For Rh as for Pt (15) it may be argued that the explanation most attractive at present, is that the adsorption of "oxygen" causes the rate of adsorption to become activation-controlled and sufficiently slow that it is overwhelmed by the rate of CO oxidation. This causes the surface coverage to drop down to a very small value (experimentally indistinguishable from zero). The decrease in surface coverage with CO is, in turn, largely responsible for the initial decrease in anodic corrent at high potentials (Fig. 1c and 1d).

Hydrogen Co-deposition Measurements and Structure of the Adlayer-

If a cathodic sweep is applied to a Pt or Rh electrode partially covered with CO (and in the absence of previously adsorbed hydrogen or "oxygen"), the major coulombic process will correspond to the deposition of hydrogen atoms on sites not previously blocked by CO (2,5). Fig. 7a and 7b are some typical traces obtained for Pt and Rh, and Fig. 7b demonstrates the construction lines that may be drawn to define a closedarea (charge), $_SQ_H$ corresponding to hydrogen codeposition. These construction lines serve mainly to differentiate between the end of the hydrogen adsorption and the onset of the molecular hydrogen evolution processes. It is to be noted that the implicit assumption involved is that appreciable molecular hydrogen evolution does not begin until the mixed monolayer is largely complete. The sweep is continued to any value of the potential required to force the hydrogen evolution process at the particular coverage with CO. The greater irreversibility of hydrogen adsorption on Rh is evidenced by the much higher overpotentials required at the particular sweep speed employed.

Subject to the limitations in evaluating $_SQ_H$, the following relationship may hold for either Pt or Rh:

$$ {}_{S}Q_{H} = F\,{}_{S}\Gamma_{H} = F[({}_{S}\Gamma_{H})_{o} - m\Gamma_{CO}] \qquad (2) $$

where ${}_{S}\Gamma_{H}$ saturation coverage of the surface with hydrogen atoms in the presence of adsorbed CO

$({}_{S}\Gamma_{H})$ =saturation coverage of the surface with hydrogen atoms in the absence of adsorbed CO

m=average number of hydrogen adsorption sites obscured per molecule of CO adsorbed.

For (2) to apply it is only necessary that no desorption of CO occur during the sweep, as may be verified experimentally. If we further assume that CO and hydrogen adsorption sites are similar and that hydrogen adsorption may only be blocked directly by formation of a CO - surface valence bond, then m may have the significance of representing the number of valences formed between a CO molecule and the surface. For CO on Pt at 30°C (2), m was found to have the value 2 for the first 30% of coverage, and 1 for the remainder [suggesting "bridged and "linear" structures (23) respectively]. The apparent bridging decreased at 60°C. For Rh at 80°C, only the one-site adsorption was suggested by the observed value of m=1, determined from the plot of Fig. 8(5). As for Pt, a two-site adsorption might be indicated at lower temperatures.

The Hydrogen-Adsorption Isotherm-

In somewhat different experiments to those discussed above, hydrogen atoms may be adsorbed at constant potential on a surface partially covered with a measured amount of CO. The coverage with hydrogen may then be determined by selective anodic stripping with a linear anodic sweep (5). The charge-potential plot of Fig. 9 is essentially an adsorption isotherm (since fractional coverage is proportional to the charge and the logarithm of hydrogen partial pressure is proportional to the potential) for the clean Rh surface, similar to those previously reported by Will and Knorr (24) and by Bold and Breiter (25). Fig. 10 reveals how the coverage with hydrogen at constant potential decreases linearly with increasing CO adsorption time. The CO surface coverage is increasing linearly under these conditions, and analysis of the plots reveal that the following empirical relationship exists at all potentials, between fractional hydrogen and CO surface coverages (below 80% of full coverage with CO):

$$ \theta_{H} = (\theta_{H})_{o}\left[1 - \frac{\theta_{CO}}{1.4}\right] \qquad (3) $$

where θ_{H}=fractional coverage with hydrogen atoms=$Q_{H}/{}_{S}Q_{H}$

$(\theta_{H})_{o}=\theta_{H}$ in absence of adsorbed CO

θ_{CO}=fractional coverage with CO=$Q_{CO}/(Q_{CO})_{maximum}$

Expression (3) implies that the shape of the adsorption isotherm for the clean surface is retained as CO adsorbs. The resulting implication is that there is a random distribution of CO molecules on hydrogen adsorption sites possessing different heats of adsorption. This contrasts with the conclusion of Breiter (22) for formic acid adsorption on Pt. According to Breiter, initial adsorption of formic acid on Pt occurs on those sites having the highest heats of adsorption for hydrogen atoms.

REFERENCES

1. S. Gilman, J. Phys. Chem. 66, 2657 (1962).

2. Ibid., 67, 78 (1963).

3. Ibid., 67, 1898 (1963); 68, 70 (1964).

4. Ibid., 70, 2880 (1966).

5. S. Gilman, Section 2.1.5 in General Electric Technical Summary Report No. 10, Hydrocarbon-Air Fuel Cells, 1 July-31 December, 1966, ARPA Order No. 247, Contract No. DA44-009-Amc-479(T) with U. S. Army Engineer Research and Development Laboratories, Ft. Belvoir, Va.

6. S. Gilman, Electrochem Acta 9, 1025 (1964).

7. H. Binder, A. Köhling and G. Sandstede, Adv. Energy Conv. 7, 77 (1967).

8. D. W. McKee, L. W. Niedrach, I. F. Danzig and H. I. Zeliger, General Electric Technical Summary Report No. 9, Hydrocarbon-Air Fuel Cells, 1 January-30 June, 1966, ARPA Order No. 247, Contracts Nos. DA-44-009-ENG-4909, DA-44-009-AMC-479(Y), DA-44-ENG-4853,pp.2-4.

9. D. R. Rhodes and E. F. Steigelmann, J. Electrochem. Soc. 112, 16 (1965).

10. A. N. Frumkin, Chapter 5 in "Advances in Electrochemistry and Electrochemical Engineering", Vol. 3, Ed. by P. Delahay, Wiley, New York, 1963.

11. J. A. V. Butler, Ed., Chapter IX in "Electrical Phenomena at Interfaces", Methuen, London, 1951.

12. L. Young, Chapter 22 in "Anodic Oxide Films", Academic Press, New York, 1961.

13. P. Delahay, "Double Layer and Electrode Kinetics", Wiley-Interscience, New York, 1965.

14. K. Vetter, Chapter 4 in "Elektrochemische Kinetic", Springer, Berlin, 1961.

15. S. Gilman, Chapter 3 in "Electroanalytical Chemistry", Vol. 3, Ed. by Allen J. Bard, Marcel Dekker, Inc, New York, 1967.

16. S. Gilman, J. Phys. Chem., In Press.

17. J. Giner, Private Communication.

18. S. B. Brummer, J. I. Ford, and M. J. Turner, J. Phys. Chem. 69, 3424 (1965).

19. R. A. Munson, J. Electroanal. Chem. 5, 292 (1963).

20. T. B. Warner and S. Schuldiner, J. Electrochem. Soc. 111, 992 (1964).

21. S. B. Brummer and J. I. Ford, J. Phys. Chem. 69, 1355 (1965)

22. M. Breiter, Electrochim. Acta 8, 447 (1963).

23. R. D. Eischens and W. Pliskin, "Advances in Catalyses", Vol. X, Academic Press, Inc., New York, 1958, p. 18.

24. F. Will and C. Knorr, Z. Elektrochem. 64, 258, 270 (1960).

25. W. Böld and M. Breiter, Z. Elektrochem. 64, 897 (1960).

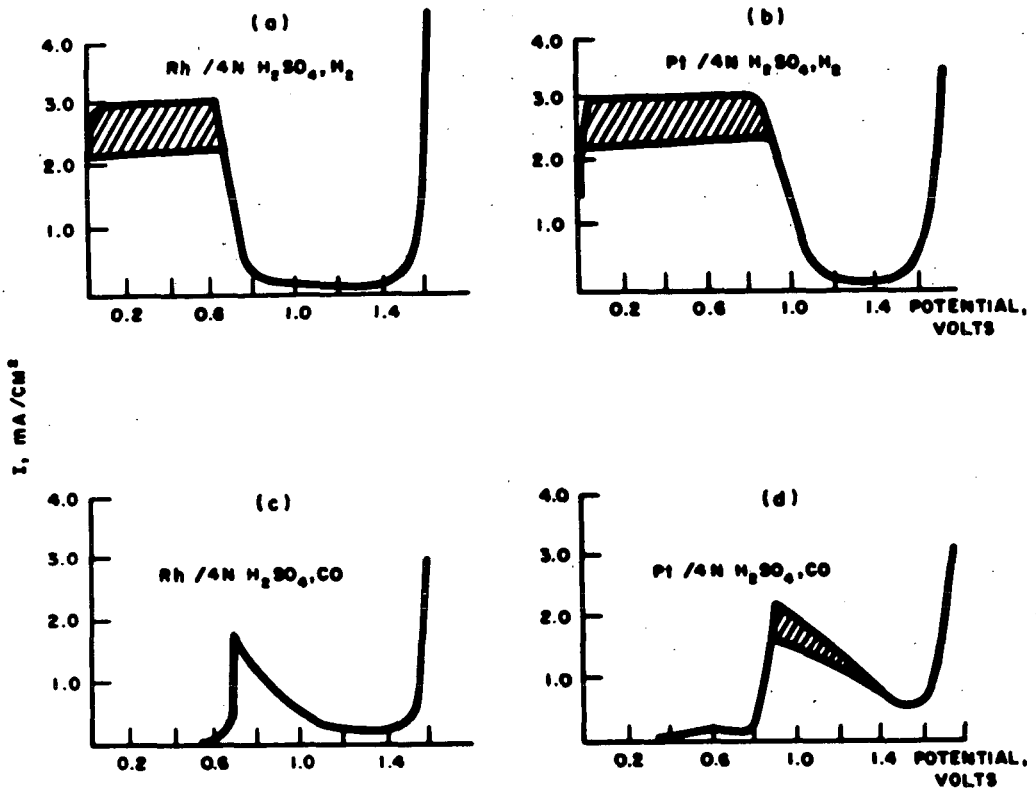

Figure 1. Polarization curves measured for smooth Pt and Rh electrodes during application of a linear anodic sweep of speed 0.04 v. sec. The electrolyte was saturated with the gas at either 30°C (Pt electrode) or 80°C (Rh electrode) and the solution was paddle-stirred (300 rpm) throughout the experiment. The hatched areas correspond to regions of oscillation of the current. (From Ref. 5)

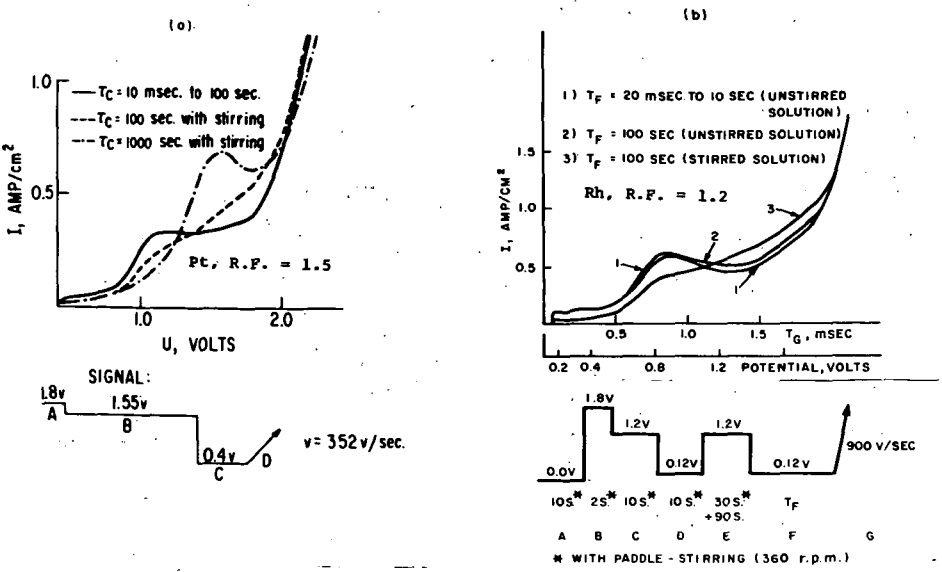

Figure 2. Adsorption of electrolyte impurities by smooth Pt and Rh electrodes. In Figure 2a, steps A and B are for pretreatment, adsorption occurs during step C (0.4 v., 1 N $HClO_4$ 30°C) and the traces are recorded during sweep D. In Figure 2b, steps A-E are for pretreatment, adsorption occurs during step F (0.12 v., 4 N H_2SO_4 80°C) and the traces are recorded during sweep G. (Figure 2a from Ref. 6; Figure 2b from Ref. 5).

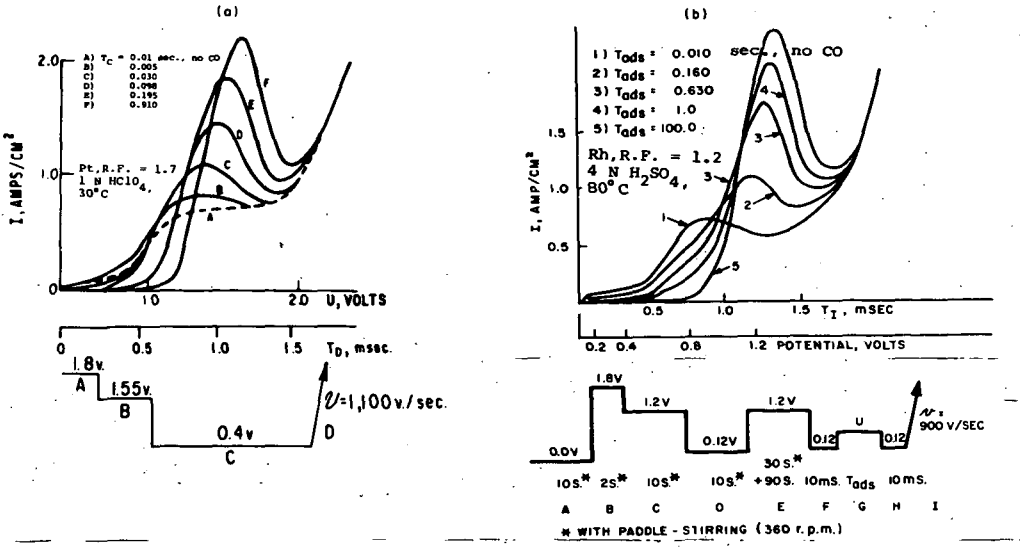

Figure 3. Determination of CO adsorption on Pt and Rh electrodes by anodic stripping. Steps C and G are adsorption steps in Figures 3a and 3b, respectively. The traces are measured during sweeps D and I in Figures 3a and 3b, respectively. All other steps are for pretreatment. (Figure 3a from Ref. 2; Figure 3b from Ref. 5).

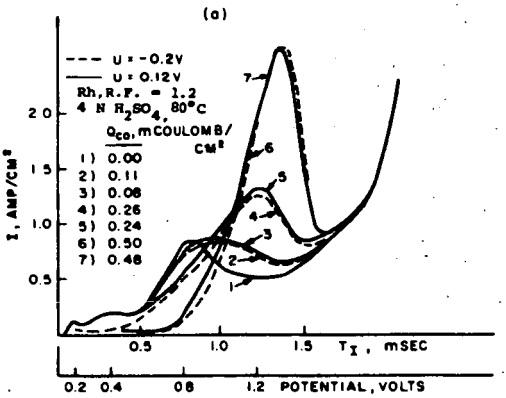

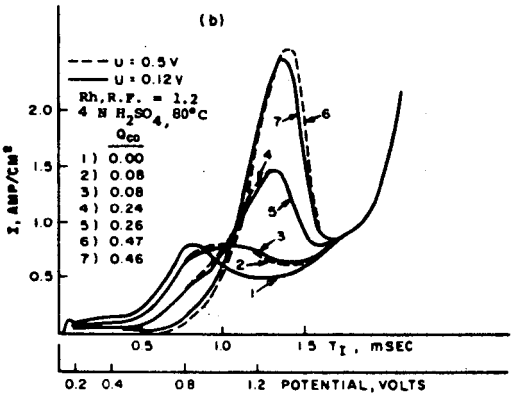

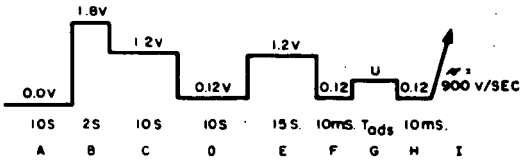

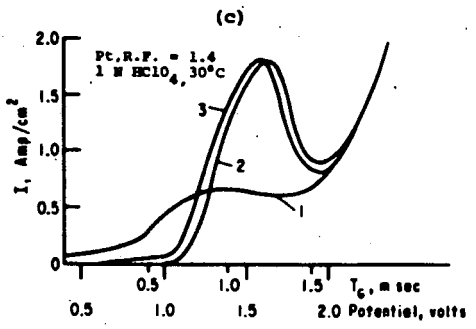

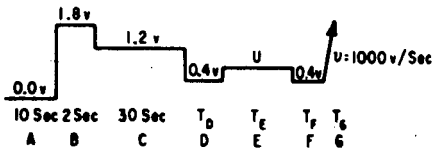

1) U = 0.4 v., T_E = 10 msec., absence of CO
2) U = -0.1 to 0.7 v., T_E = 10 sec.
3) U = -0.2 v., T_E = 10 sec.

Figure 4. Effect of electrode potential at which CO is absorbed upon the trace corresponding to anodic stripping of adsorbed CO. Adsorption on Rh and on Pt occurs during steps G and E of the respective sequences. Comparisons of the traces obtained at the different potentials is made at almost identical values of the surface coverage (as measured by Q_{CO}). (Figures 4a and 4b from Ref. 5; Figure 4c from Ref. 4).

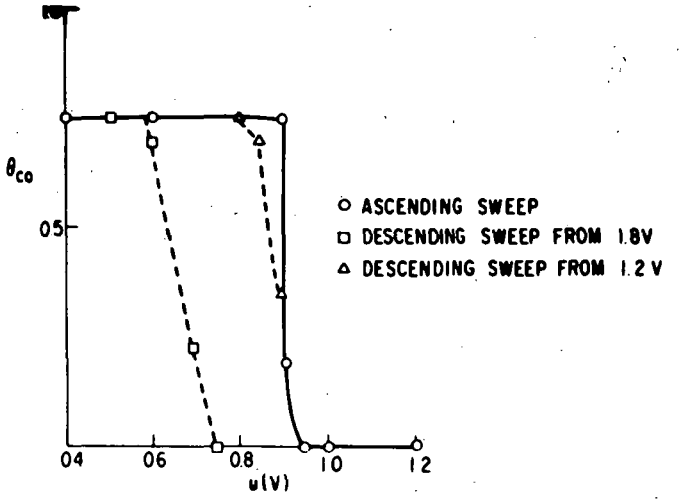

Figure 5. Coverage of a Pt electrode surface with CO. The 1 N $HClO_4$ was saturated with CO at 30°C and the solution was paddle-stirred throughout the experiment (360 rpm). The electrode potential was varied according to a triangular voltage-time sweep of speed 0.04 v./sec. θ_{CO} was defined relative to a hydrogen monolayer. The maximum value of θ_{CO} is equivalent to Q_{CO} (CO anodic stripping charge) of 0.28 mcoul. per cm of "true" (hydrogen) area. (After Ref. 1).

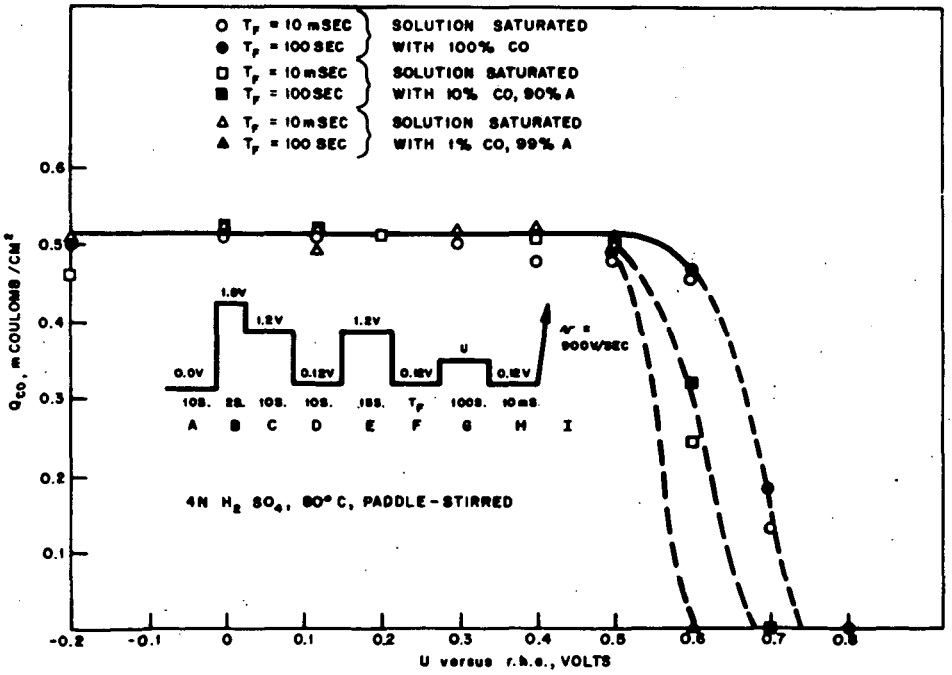

Figure 6. Coverage of a Rh electrode surface with CO. The 4 N H_2SO_4 was saturated with CO at 80°C, and Q_{CO} (charge required for anodic stripping of CO) was determined after adsorption at potential U of the indicated sequence. Q_{CO} is reported on the basis of geometric area and may be converted to "true" (hydrogen area) by dividing by the roughness factor of 1.16. (After Ref. 5)

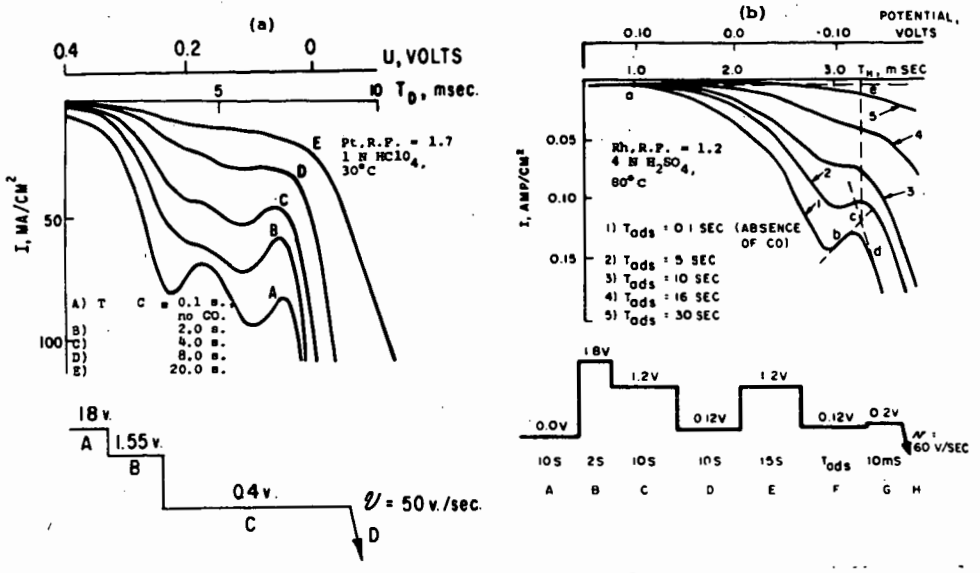

Figure 7. Determination of hydrogen co-deposition on electrodes partially covered with CO. The adsorption of CO occurs during steps C and F of Figures 7a and 7b, respectively. The traces correspond to hydrogen adsorption during sweeps D and H of Figure 7a and 7b, respectively. All other steps are for electrode pretreatment. (Figure 7a after Ref. 2; Figure 7b after Ref. 5).

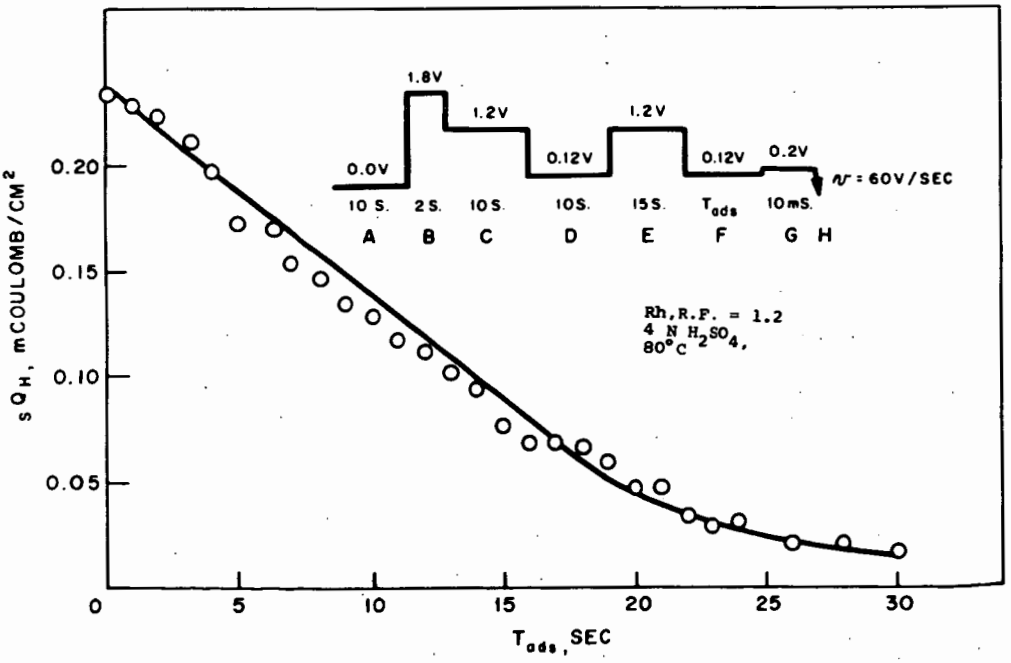

Figure 8. Variation of $_sQ_H$ (charge corresponding to saturation coverage with CO) with the time of adsorption of CO. The data was derived from traces such as those of Figure 7. (After Ref. 5)

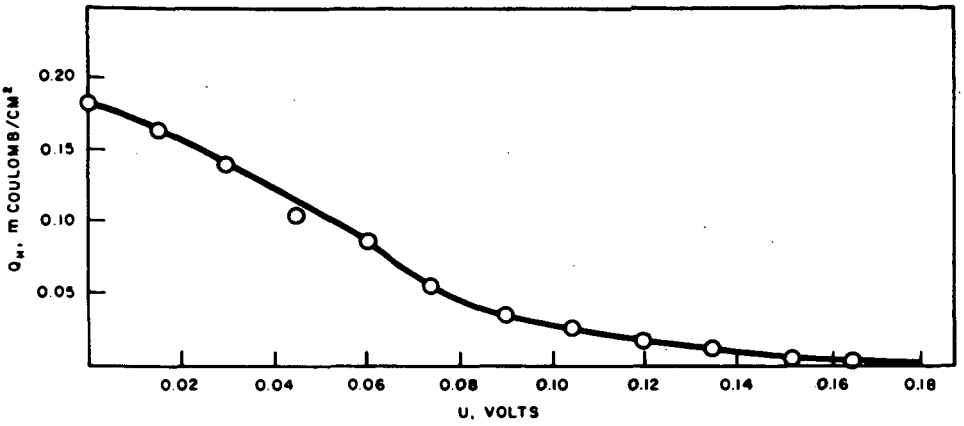

Figure 9. Equilibrium hydrogen coverage on a clean smooth Rh electrode (R.F. = 1.2, 4 N H_2SO_4 80°C). The coverage is expressed in terms of the equivalent charge, Q_H, for deposition or dissolution of the atomic hydrogen.

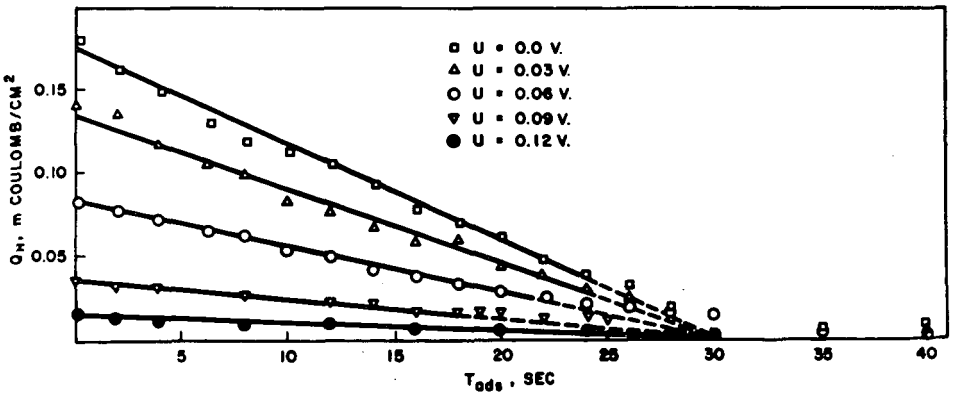

Figure 10. Decrease of equilibrium hydrogen coverage with time of adsorption of CO (4 N H_2SO_4 saturated with a gas mixture of 1% CO, 99% argon at 80°C; solution stirred). The coverage with hydrogen is expressed as the equivalent charge, Q_H, for deposition or dissolution of the atomic hydrogen.

ANODIC OXIDATION OF CARBON MONOXIDE AND FORMIC ACID ON PLATINUM COVERED WITH SULFUR

H. Binder, A. Köhling, G. Sandstede

Battelle-Institut e.V., Frankfurt am Main, Germany

1. Introduction

In recent years it was demonstrated by investigations of several authors (1)-(5) that CO is oxidized on platinum electrodes in an acid electrolyte at temperatures below 100°C. However, the current density achieved was only of the order of some ma/cm^2. In order to increase the current densities temperatures of up to 150°C were applied using phosphoric acid as electrolyte (6). In this way the current density was raised to about 50 ma/cm^2. We reported about the results obtained with our type of Raney-platinum electrodes (7) which allowed current densities of about 200 ma/cm^2 to be drawn using carbon monoxide as fuel in 3N H_2SO_4 at temperatures below 100°C (8,9).

However, polarization was large compared with that encountered in the oxidation of hydrogen; attempts at the simultaneous oxidation of hydrogen and carbon monoxide resulted in an enrichment of carbon monoxide in the effluent gas mixture.

The strong polarization encountered in the anodic oxidation of CO is due to an adsorption product which is slowly adsorbed on the electrode, thus blocking it. We found, however, that the blocking effect is not encountered on a platinum electrode onto which sulfur has been pre-adsorbed (10).

This paper describes the results of adsorption measurements and of the electrochemical oxidation of carbon monoxide and formic acid. The influence of sulfur on the adsorption is discussed and a modification of the oxidation mechanism is proposed*).

2. Experimental Conditions

The electrochemical measurements were performed by means of a half-cell arrangement. The reference voltages indicated in this paper relate to a hydrogen electrode in the same solution as the test electrode. The disk-shaped electrodes were prepared by compacting a mixture of 50 volume per cent gold powder or platinum powder as skeleton material and 50 volume per cent of a powdered platinum-aluminum alloy having a platinum content of 15 atomic per cent. The aluminum was leached out with potassium hydroxide solution. The skeleton material - platinum and gold - appeared to have no effect on the results of our measurements. The Raney platinum had a specific surface area of about 30 m^2/g. For measurements with formic acid, immersed electrodes were used, while bubbling electrodes were used in the case of carbon monoxide. The electrolyte was boiled thoroughly and protected from atmospheric oxygen by feeding nitrogen into the closed vessel above the electrolyte. The electrodes used for the determination of periodic current-voltage curves had a platinum content of about 50 mg/cm^2. Electrodes with

*) For papers concerning oxidation of formic acid and carbon monoxide cf. references (12) to (33)

a platinum content of 180 mg/cm^2 were used only in measurements of stationary current-voltage curves with carbon monoxide and for determining the quantity of the carbon monoxide chemisorbate. The potentiodynamic current-voltage curves were plotted by means of a mechanically operated xy-recorder.

3. The Sulfur Chemisorbate

If a platinum electrode is exposed to an atmosphere of hydrogen sulfide, it is covered with a sulfur chemisorbate. A characteristic feature pointing to the presence of this adsorbate is the observation made in measurements of periodic potentiodynamic current-voltage curves that the peaks corresponding to the oxidation of H_{ad} atoms (34) become smaller or vanish completely (Fig. 1). Complete disappearence of the maxima is consistent with complete sulfur coverage of the electrochemically active platinum surface. The degree of coverage can thus be derived from the periodic current-voltage curve by determining the ratio between the atoms of the platinum surface available for hydrogen adsorption before and after coverage of the platinum with sulfur*).

Above a specific reference voltage, which ranges between 600 and 800 mv depending on the degree of coverage, the sulfur chemisorbate is oxidized anodically. Complete oxidation occurs at 1450 mv, so that the normal current-voltage curve of platinum is obtained after reversal of the voltage. The charge required for the oxidation of sulfur can be determined from the difference of those areas in the voltage range between 600 and 1450 mv which are enclosed by the curves (Fig. 1, area hatched horizontally). It was found that the required charge is about four times as large as the charge necessary for oxidation of the corresponding number of H_{ad} atoms. From this finding and from the observation that gas is evolved at the electrode during oxidation, we infer that for each platinum atom one sulfur atom is adsorbed which is oxidized to give sulfur dioxide.

In contrast to the oxygen adsorbate, the sulfur adsorbate is stable even at a voltage of -100 mv, although the thermodynamic limits for the stability of elemental sulfur are 150 and 450 mv. Methods for covering the platinum with sulfur, other than the exposure of the electrode to an atmosphere of hydrogen sulfide, include its exposure to sulfur vapor or sulfur solution (in CS_2) and the cathodic reduction of sulfuric acid or sulfurous acid at high current densities.

4. Influence of the Sulfur Chemisorbate on the Anodic Performance

4.1 Carbon Monoxide

On a platinum surface covered with a sulfur chemisorbate, the rate of the anodic oxidation of carbon monoxide is much higher than on an uncovered surface. At a temperature of 90°C even small quantities of sulfur increase the current density considerably (Fig. 2), but as in the case of 30°C the maximum current density is achieved only at nearly complete monatomic coverage of the catalyst.

This increase in current density with increasing sulfur coverage of the platinum is observed between 30 and 90°C in the whole voltage range up to at least 500 mv (Fig. 3). As soon as monatomic

*) This is based on the assumption that one hydrogen atom is chemisorbed per platinum atom.

coverage is exceeded, the current density again decreases.

At an uncovered electrode the current density is much more dependent on the temperature than at an electrode covered with sulfur. From the different slopes of the straight lines in an Arrhenius diagram a decrease in the activation energy of about 7 kcal/mole is calculated. By calculating just the difference of the activation energy, the contribution of the overvoltage to the activation energy is approximately eliminated.

4.2 Formic Acid

In the anodic oxidation of formic acid, the influence of the sulfur adsorbate on the reaction rate is even more pronounced than in the oxidation of carbon monoxide (Fig. 4). If the electrode is covered with sulfur, the current density depends more strongly on the concentration of formic acid than in the absence of sulfur (Fig. 5), i.e. the rate constant of the oxidation reaction is raised. From the ratio of the rate constants the decrease in the activation energy can be estimated to be 8.4 kcal/mole. In contrast to CO oxidation, the maximum influence is reached throughout the temperature range investigated at a coverage of only 40 per cent and not at nearly complete coverage (Fig. 6).

From the varying dependence of the current density on the temperature the decrease in activation energy for the oxidation of formic acid on a platinum electrode with a 45 per cent sulfur coverage is calculated to be about 8 kcal/mole. This value is in fair agreement with that calculated for the oxidation of carbon monoxide.

5. Reaction under Open Circuit Conditions

Under open circuit conditions the following shift reaction takes place at a Raney platinum electrode:

$$CO + H_2O \longrightarrow CO_2 + H_2. \qquad (1)$$

On pure platinum this reaction is very slow. In the presence of a sulfur adsorbate, however, its rate is substantially increased. This reaction takes place even if the carbon monoxide is mixed with hydrogen or carbon dioxide. The reaction rate can be measured at temperatures as low as 30°C.

Formic acid decomposes on a platinum electrode under open circuit conditions according to the following reaction:

$$HCOOH \longrightarrow CO_2 + H_2. \qquad (2)$$

The rate of this reaction again is increased by the sulfur chemisorbate. In 3N H_2SO_4 + 2M HCOOH at 90°C the reaction rates differ by a factor of about 25. The composition of the effluent gases at a temperature of 70°C was determined to be 40.4 volume per cent H_2, 41.6 volume per cent CO_2, and 18 volume per cent O_2/N_2. No CO (< 0.2 per cent) was formed during the decomposition of formic acid, because the shift reaction takes place at a platinum electrode partly covered with sulfur.

6. Adsorption Measurements

The potentiostatic current density-time curves (Fig. 7a) reveal that the inhibition of the anodic oxidation of formic acid at a platinum electrode is due to a comparatively slow blocking of the electrode [see e.g. (13)] . For plotting these curves, the electrode was held at one of the voltages indicated in Fig. 7 by means

of a potentiostat. Oxidizable contaminations had been previously removed by anodic stripping (up to 1,600 mv). Inhibition occurs also under open circuit conditions: if the circuit is closed one hour after addition of formic acid, the small stationary current density is observed immediately, e.g. at a voltage of 300 mv. Our porous electrodes required about two hours to be completely covered with the formic acid chemisorbate. Thereafter, H_{ad} atoms are no longer detectable at the platinum surface.

This inhibition effect is not observed at potentials above, say, 600 mv.

No inhibition is observed either if the electrode is partly covered with pre-adsorbed sulfur (Fig. 7b): the comparatively high current densities are reached immediately and decrease only insignificantly.

Similar inhibition effects which can be avoided by pre-adsorption of sulfur, are observed during the anodic oxidation of carbon monoxide.

For measuring the quantity of adsorbate, potentiodynamic curves have been plotted at low voltage speed after thorough rinsing of the electrode with pure sulfuric acid. These curves clearly show the influence of the hydrogen and oxygen adsorbate on the oxidation and permit the double layer capacity to be readily determined. Furthermore, these curves provide information about the position of the oxidation maximum and the electrochemical stability of the organic adsorbate.

The charge necessary for the oxidation of adsorbed hydrogen is derived from the potentiodynamic curve obtained for the clean platinum electrode by substraction of the charge of the double layer from the total charge. The double layer capacity results from the current flowing between 400 and 700 mv. Prior to adsorption measurement the electrode is placed in dilute sulfuric acid. In order to remove all adsorption layers, it is exposed first to a voltage of 1,400 mv, then to 200 mv, and finally to 500 mv. Then, formic acid is added under open circuit.

Between 0.1 and 2M, the quantity of chemisorbed formic acid is independent of the concentration of formic acid in the electrolyte. However, it is necessary for this result that the adsorption equilibrium has been reached. At 30°C the oxidation of the adsorption product (Fig. 8) starts at about 400 mv, and at 70°C it starts at about 300 mv. Thus, the chemisorbate is stable up to this potential. The maximum oxidation currents are observed at 660 mv and 530 mv for 30 and 70°C, respectively.

The quantity of adsorbate was derived from the measured charge, taking into account the integral capacity of the double layer of the uncovered platinum surface. The potential of zero charge for platinum has been assumed to be 400 mv [see also (31)]. In accordance with Brummer (15), the specific charge required for oxidation of the adsorbate totals 1.5 e/Pt atom. The amount of HCOOH chemisorbed on a platinum electrode partly covered with sulfur is smaller than that on the uncovered electrode (Fig. 9a) and decreases with increasing degree of coverage. For a coverage of 70 per cent, this effect is easily recognized by the smaller oxidation peak. If the quantity of chemisorbed HCOOH is related to the platinum surface

not covered with sulfur, the charge required for oxidation corresponds to a transfer of 2.1 e/Pt atom. At a sulfur coverage of only 40 per cent, 1.7 e/Pt atom are required for the oxidation of the HCOOH chemisorbate.

H_{ad} atoms are never detectable on the platinum surface once the equilibrium of formic acid adsorption has been reached. Thus, the surface is always covered with a chemisorbate (in the voltage range between 0 and about 400 mv), either with a pure HCOOH adsorbate or with a mixed HCOOH and S adsorbate. In steady state, oxidation of formic acid occurs on the platinum surface covered with a mixed chemisorbate at a higher rate than on platinum covered with the pure HCOOH chemisorbate. In the case of the periodic curve (Fig. 9b) the current necessary for the oxidation of the chemisorbate is superposed on the steady state current-voltage curve.

For the adsorption of carbon monoxide on the electrode, the gas was pressed through the porous electrode at a very low flow rate under open circuit conditions. The amount of adsorbate was determined at the completely immersed electrode which had been rinsed thoroughly with boiled sulfuric acid prior to the measurement.

At 70°C the oxidation maximum is observed at a voltage of 530 mv. At 30°C the peak is shifted to 650 mv (Fig. 10). Thus, the maxima are reached almost exactly at the same voltage as in the case of oxidation of the HCOOH chemisorbate.

The quantity of CO chemisorbate again decreases with increasing coverage of the platinum with sulfur (Fig. 11). At a coverage of about 100 per cent the adsorbed amount is insignificant.

In the case of uncovered platinum, 1.5 e/Pt atom are required for the oxidation of the CO chemisorbate. At a sulfur coverage of 60 per cent the charge corresponds to a transfer of 1.9 e/Pt atom.

7. Oxidation Mechanism and Influence of the Sulfur Adsorbate

The most important question in the discussion of the mechanism underlying the anodic oxidation of formic acid and carbon monoxide on platinum is the influence of the adsorbate or intermediate blocking the electrode.

It is important to note that the chemisorbate is oxidized in both cases only at a voltage above 300 mv, being stable at lower voltages, and that in both cases only one oxidation peak occurs at the same potential. Another significant finding is that no H_{ad} atoms are found on the surface of the electrode after the adsorption equilibrium has been reached.

As an explanation of the fact that for each platinum site less than 2 e are required for the oxidation of the inhibitory chemisorbate, several authors - e.g. (15) - state that the platinum surface is covered only partially with chemisorbate. This is contradictory to our finding that no H_{ad} atoms can be detected after the equilibrium has been reached, not even at a voltage as small as 100 mv. The reactions assumed by many authors for the adsorption of formic acid

$$HCOOH \longrightarrow COOH_{ad} + H_{ad} \qquad (3)$$

and

$$2\ H_{ad} \longrightarrow H_2 \qquad (4)$$

are certainly initiated on a completely free platinum surface.

The hydrogen thus formed is physically dissolved in the electrolyte or escapes as a gas: this is the process of dedydration. In the hydrogen-covered regions of the electrode, however, the following reaction will take place:

$$HCOOH + H_{ad} \longrightarrow COOH_{ad} + H_2 \qquad (5)$$

On the free platinum surface the decomposition of the carboxyl radical proceeds in accordance with the reaction

$$COOH_{ad} \longrightarrow CO_2 + H_{ad} \qquad (6)$$

With increasing inhibition of the electrode by the chemisorbate, the formic acid will be dehydrated according to the electrochemical mechanism postulated by Gottlieb (23) and finally, though at a very low rate, it will be dehydrated even on the platinum surface covered with chemisorbate.

However, the poisoning of the platinum by reaction (3) does not provide an explanation for all the findings. Since the average charge of the adsorbate per platinum site is larger than 1 but smaller than 2, it has to be assumed that a further reaction takes place; the most plausible appears to be dismutative adsorption:

$$2\ HCOOH \longrightarrow COOH_{ad} + CHO_{ad} + H_2O \qquad (7)$$

Each species has one platinum bond; $COOH_{ad}$ has one oxidation equivalent per C atom, CHO_{ad} has three. This means that, on the average, two equivalents are available for each C atom, which would also be the case in the adsorption of $HCOOH_{ad}$. It is unlikely that even glyoxylic acid (15) with a C-C bond is formed, because it has no free electron for the bond with platinum [see also (17)]. If H_{ad} atoms are to be found on the surface, the formic acid may also be hydrated to give the radical of formaldehyde in the reaction assumed by Podlovchenka et al. (17):

$$HCOOH + H_{ad} \longrightarrow CHO_{ad} + H_2O \qquad (8)$$

The combination of reactions (3) and (8) would result in (7):

$$HCOOH \longrightarrow COOH_{ad} + H_{ad} \qquad (3)$$

$$H_{ad} + HCOOH \longrightarrow CHO_{ad} + H_2O \qquad (8)$$

$$2\ HCOOH \longrightarrow COOH_{ad} + CHO_{ad} + H_2O \qquad (7)$$

This would, however, involve an additional platinum site for H_{ad} in contrast to the direct process of (7). Besides, the following reaction may occur:

$$COOH_{ad} + 2\ H_{ad} \longrightarrow CHO_{ad} + H_2O \qquad (9)$$

The platinum atoms set free during this reaction would then be again available for reaction (3).

The chemisorbate obtained after the adsorption of CO is identical with the HCOOH adsorbate. This is due to the fact that the oxidation peak is reached in both cases at 530 mv and that the same charge is required for the oxidation. Besides, the required charge depends to the same extent on the sulfur coverage.

Dismutative adsorption also appears most plausible for the adsorption of CO:

$$2\ CO + H_2O \longrightarrow COOH_{ad} + CHO_{ad} \qquad (10)$$

because it furnishes the same mixture of species as the adsorption of formic acid. In addition, there is always a sufficient amount of adsorbed water on the electrode immersed in the electrolyte.

Reaction (10) may be followed by the shift reaction observed on platinum, for example, in accordance with the following equation:

$$CHO_{ad} + H_2O \longrightarrow COOH_{ad} + 2\ H_{ad} \qquad (11)$$

followed by

$$2\ H_{ad} \longrightarrow H_2 \qquad (4)$$

and

$$COOH_{ad} \longrightarrow CO_2 + H_{ad} \qquad (6)$$

These reactions should occur as long as there are free platinum sites to take up the H_{ad} atoms. When all the platinum atoms are covered with the mixture of CHO_{ad} and $COOH_{ad}$, the rate of the shift reaction becomes insignificant.

However, this hypothesis postulating a chemical mechanism for the shift reaction and formic acid decomposition is rather improbable if we consider our finding that a sulfur adsorbate strongly increases the rate of these reactions. This is true despite the fact that - as in the case of carbon monoxide - the sulfur adsorbate occupies practically all the platinum sites when maximum rates are reached.

Our experiments rather suggest that the electrochemical oxidation of formic acid and carbon monoxide at potentials below 300 mv and the decomposition of formic acid or the shift reaction observed in steady state do not take place on the free platinum surface, but on a chemisorbate covering the platinum surface. We postulate that

a) reactions on sulfur-free platinum always take place on the complete "monomolecular" chemisorbate of formic acid or carbon monoxide (at an extremely low reaction rate);

b) reactions on platinum covered with sulfur take place on the mixed chemisorbate of sulfur and formic acid, or of sulfur and carbon monoxide;

c) reactions involving oxidation of carbon monoxide take place even on a surface completely covered with sulfur chemisorbate.

This concept contradicts the dehydrogenation mechanism of the oxidation, which would have to involve the following reactions

$$HCOOH \longrightarrow COOH_{ad} + H_{ad} \qquad (3)$$

and

$$COOH_{ad} \longrightarrow CO_2 + H_{ad} \qquad (6)$$

with

$$H_{ad} \longrightarrow H^+ + e^- \qquad (12)$$

as the potential-determining step. A prerequisite for this mechanism would be dissociative adsorption, which is assumed to be possible only on the free platinum surface.

Anodic oxidation of formic acid may rather be expected to take place on the chemisorbate or chemisorbate mixture in accordance with a modified electron-radical mechanism (20,26,27):

$$HCOOH \longrightarrow (HCOOH)^{+}_{ad} + e^{-} \quad (13)$$

$$(HCOOH)^{+}_{ad} \longrightarrow (COOH)_{ad} + H^{+} \quad (14)$$

$$(COOH)_{ad} \longrightarrow (COOH)^{+}_{ad} + e^{-} \quad (15)$$

$$(COOH)^{+}_{ad} \longrightarrow CO_2 + H^{+} \quad (16)$$

where either equation (13) or equation (15) determines the potential. In no instance will $(COOH)_{ad}$ be identical with $COOH_{ad}$, since the chemisorbate covering the electrode permits physisorption rather than chemisorption.

Dehydrogenation of formic acid in the steady state of the electrode involves reactions (13) to (16) as the anodic step of the total electrochemical reaction, with

$$H^{+} + e \longrightarrow 1/2\ H_2$$

as the cathodic partial step [see (23)]. The charge transfer reaction occurs more readily at the sulfur sites than at the formic acid chemisorbate, so that dehydrogenation is measurable even at room temperature.

The electron-radical mechanism for the anodic oxidation of carbon monoxide may be described as follows:

$$CO + H_2O \longrightarrow (CO \times H_2O)^{+}_{ad} + e^{-} \quad (17)$$

$$(CO \times H_2O)^{+}_{ad} \longrightarrow (CO \times OH)_{ad} + H^{+} \quad (18)$$

$$(CO \times OH)_{ad} \longrightarrow (CO \times OH)^{+}_{ad} + e^{-} \quad (19)$$

$$(CO \times OH)^{+}_{ad} \longrightarrow CO_2 + H^{+} \quad (20)$$

The intermediates are reaction complexes which are probably not identical with the corresponding complexes involved in the oxidation of formic acid, since the relationship between the course of the reaction and the sulfur coverage of the electrode is different in each individual case.

Carbon monoxide appears to be physisorbed on the sulfur sorbate, so that the charge transfer reaction can take place. The sulfur adsorbate appears to be unsuitable for the physisorption of formic acid; it is rather to be assumed that a carbonyl group is necessary to which the formic acid molecule is attached by hydrogen bonding, thus coming into the neighborhood of the chemisorbed sulfur by which the electron transfer is effected.

This model requires further substantiation by experiment. For a closer characterization of the chemisorbate it is in particular necessary to know the number of charges required for the formation of one molecule of carbon dioxide.

Literature

(1) L.W.Niedrach, J.electrochem.Soc.109, 1092(1962)

(2) S.Gilman, J.phys.Chem.67, 78(1963)

(3) S.Gilman, J.phys.Chem.67, 1898(1963)

(4) T.B.Warner and S.Schuldiner, J.electrochem.Soc.111, 992(1964)

(5) S.B.Brummer and J.I.Ford, J.phys.Chem.69, 1355(1965)

(6) R.Jasinski, Ber.Bunsenges.Phys.Chem.68, 400(1964)

(7) H.Krupp, H. Rabenhorst, G.Sandstede, G.Walter and R.McJones, J.electrochem.Soc.109, 553(1962)

(8) H.Binder, A.Köhling, H.Krupp, K.Richter and G.Sandstede, J.electrochem.Soc.112, 355(1965); Abstract: Chem.Engng.News, May18, p.42(1964); Chem.Ingr.Tech.36, A1695(1964)

(9) H.Binder, A.Köhling and G.Sandstede, paper presented at C.I.T.C.E.Meeting, London, Sept.1964 (Summary: Electrochim. Acta9, XXX(1964)

(10) H.Binder, A.Köhling and G.Sandstede, Advd.EnergyConversion7, 77(1967)

(11) H.Binder, A.Köhling and G.Sandstede, Advd.EnergyConversion, inpress; Nature214, 268(1967)

(12) M.W.Breiter, Electrochim.Acta8, 457(1963)

(13) M.W.Breiter, Electrochim.Acta10, 503(1965)

(14) J.Giner, Electrochim.Acta9, 63(1964)

(15) S.B.Brummer, J.phys.Chem.69, 1363(1965)

(16) P.Stonehart, FifthInt.PowerSourceSymposium, Brighton, Sussex, Sept.1966

(17) B.J.Podlovchenco, O.A.Petry, A.N.Frumkin and HiraLal, J.electroanal.Chem.11, 12(1966)

(18) A.Kutschker and W.Vielstich, Electrochim.Acta8, 985(1963)

(19) W.Vielstich and U.Vogel, Ber.Bunsenges.68, 688(1964)

(20) J.Eckert, Electrochim.Acta12, 307(1967)

(21) V.S.Bagotzky and Yu.B.Vassiliev, ElectrochimActa11, 1439(1966)

(22) L.W.Niedrach and M.Tochner, J.Electrochem.Soc.114, 17(1967)

(23) M.H.Gottlieb, J.Electrochem.Soc.111, 465(1964)

(24) D.R.Rhodes and E.F.Steigelmann, J.Electrochem.Soc.112, 16(1965)

(25) E.Müller and K.Schwabe, Z.Elektrochemie34, 170(1928)

(26) K.Schwabe, Z.Elektrochemie61, 744(1957)

(27) G.A.Bogdanowsky and A.J.Schlygin, Zh.fiz.Khim.33, 1769(1959)

(28) T.B.Warner and S.Schuldiner, J.Electrochem.Soc.111, 992(1964)

(29) P.R.Johnson and A.T.Kuhn, J.Electrochem.Soc.112, 599(1965)

(30) J.O'M.Bockris, and S.Srinivasan, J.Electroanalytical Chem.11, 350(1966)

(31) E.Gileadi and B.Piersma in "Modern Aspects of Electrochemistry", no.4, p.47 (J.O'M.Bockris,ed.), Butterworths, London, 1966

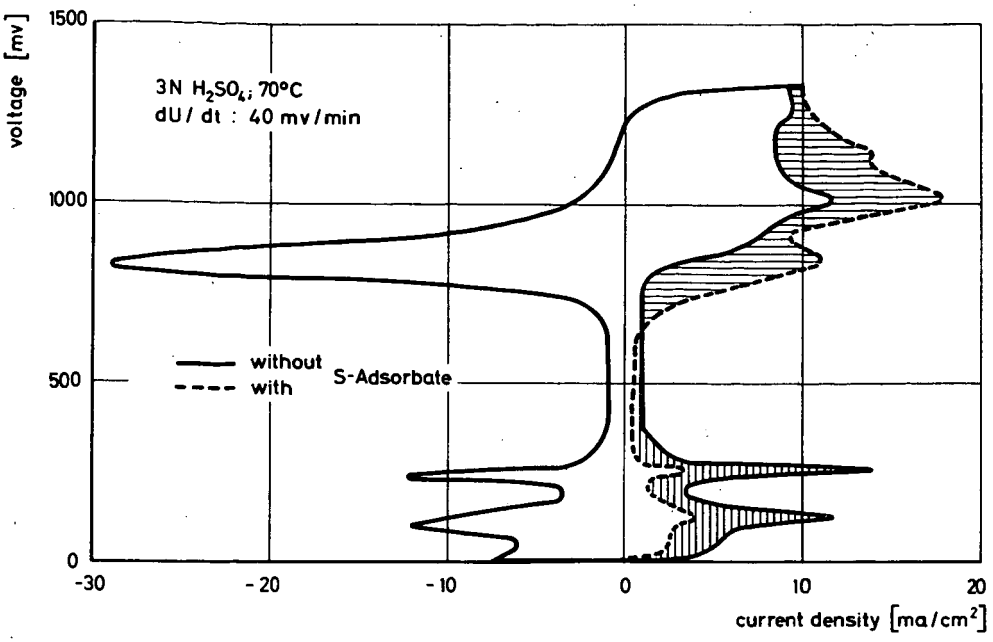

Fig. 1 Oxidation of a sulfur chemisorbate on Raney-Pt in 3N H_2SO_4 at 70°C; voltage speed: dU/dt = 40 mV/min

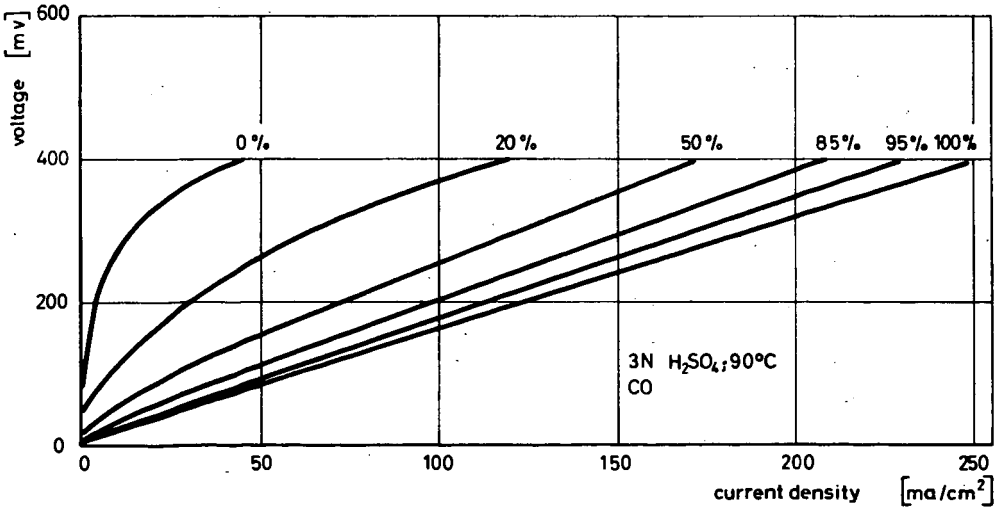

Fig. 2 Shift of current density-voltage plots of a Raney-Pt electrode in the case of CO-Oxidation caused by chemisorbed sulfur

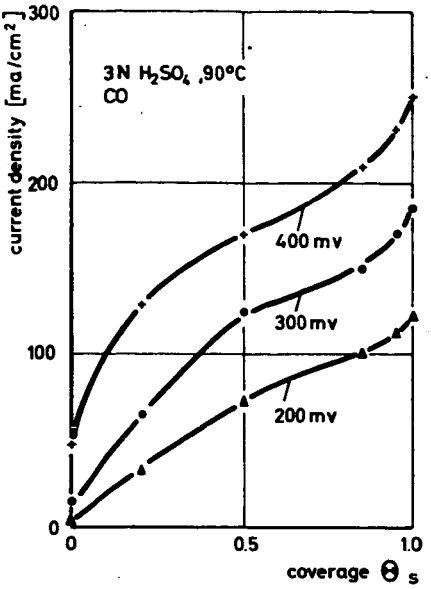

Fig. 3 Effect of chemisorbed sulfur on the performance of CO at a Raney-Pt electrode

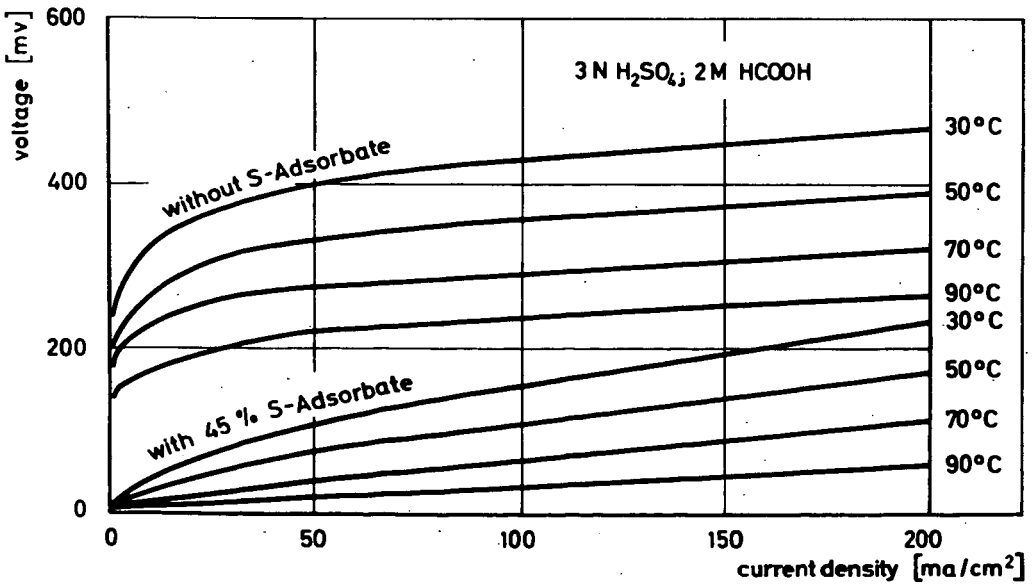

Fig. 4 Shift of current density-voltage plots at a Raney-Pt electrode in the case of HCOOH-Oxidation caused by chemisorbed sulfur

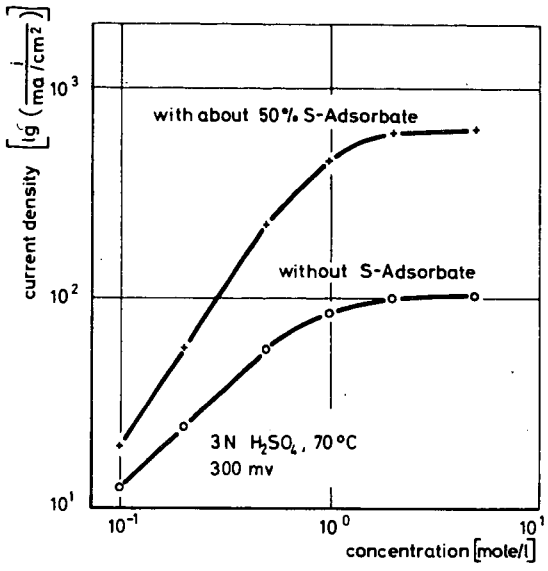

Fig. 5 Current density at a Raney-Pt electrode as a function of HCOOH concentration

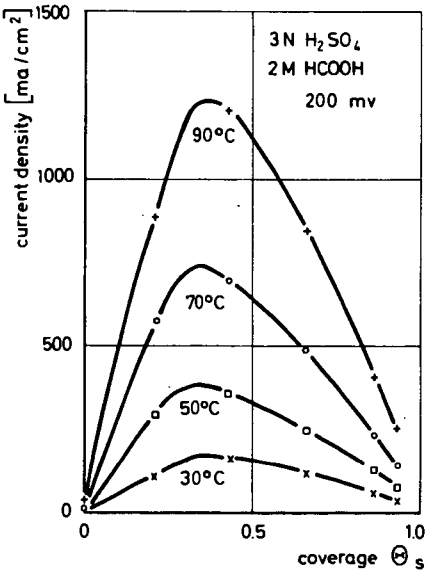

Fig. 6 Effect of chemisorbed sulfur on the performance of HCOOH at a Raney-Pt electrode

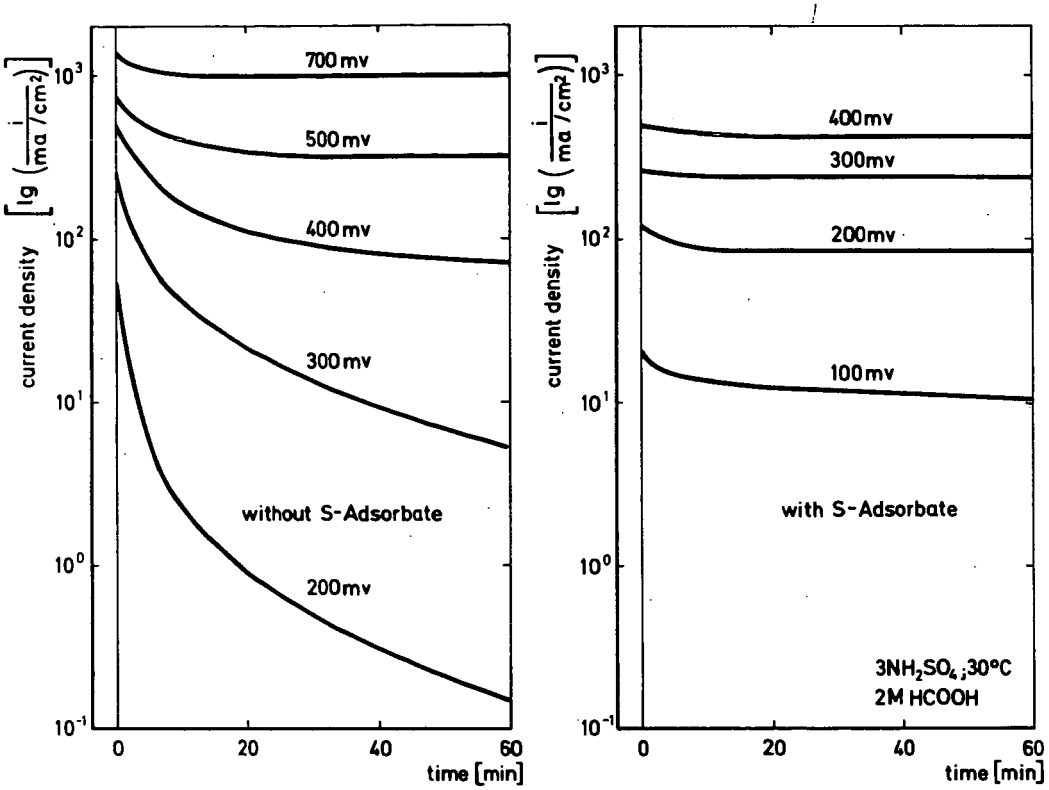

Fig. 7 Decay of current density at a Raney-Pt electrode during oxidation of HCOOH

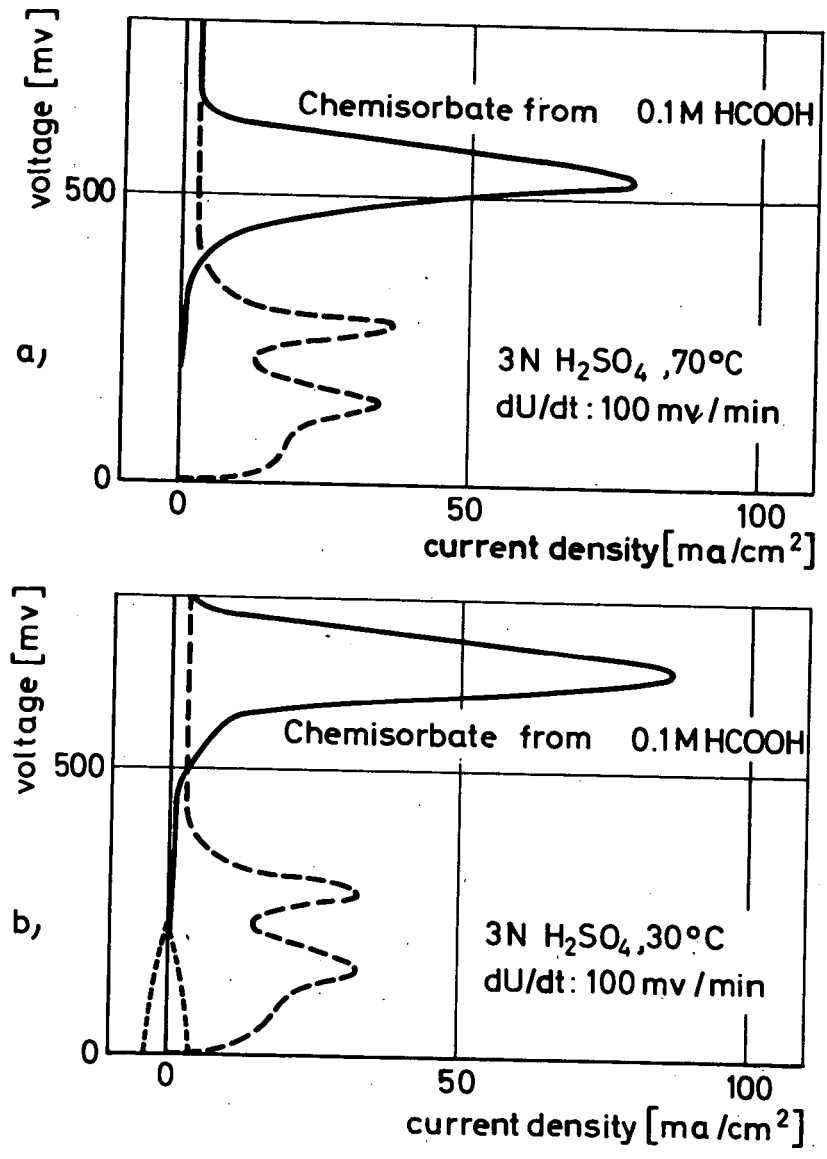

Fig. 8 Oxidation of the HCOOH chemisorbate on Raney-Pt a) at 70°C (single sweep); b) at 30°C (single sweep)

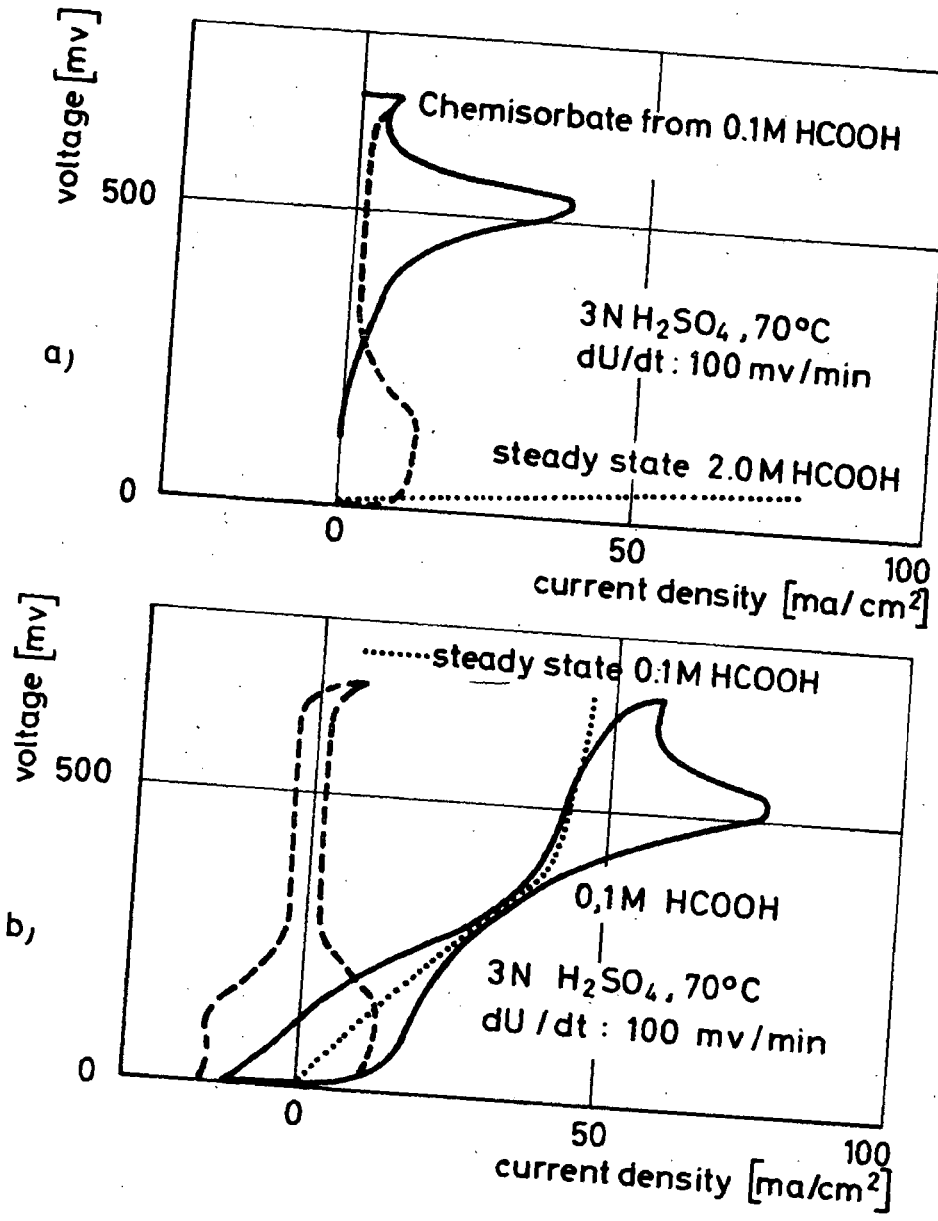

Fig. 9 Oxidation of HCOOH at a Raney-Pt electrode covered with a sulfur chemisorbate (θ_S = 70 per cent)
a) oxidation of the HCOOH chemisorbate (single sweep);
b) oxidation in the presence of 0,1 M HCOOH (periodic curve)

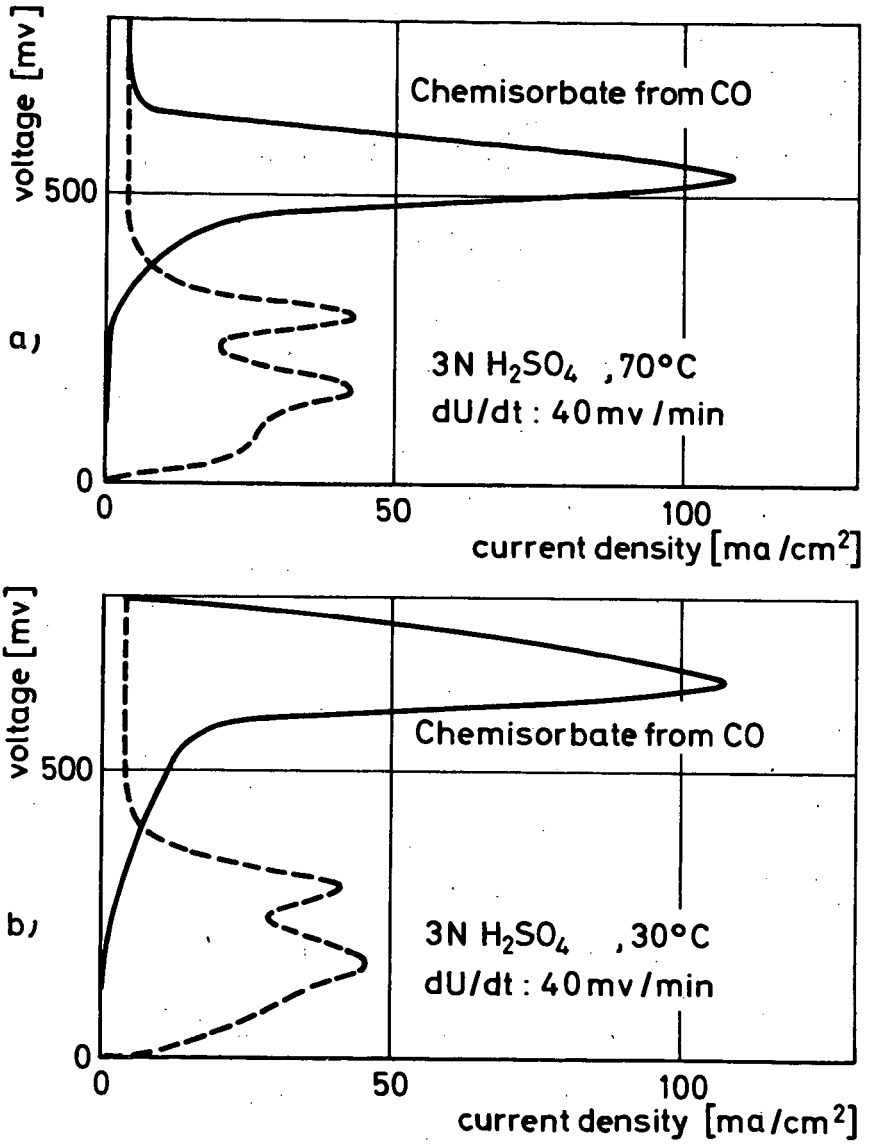

Fig. 10 Oxidation of CO chemisorbate on a Raney-Pt electrode a) at 70°C (single sweep); b) at 30°C (single sweep)

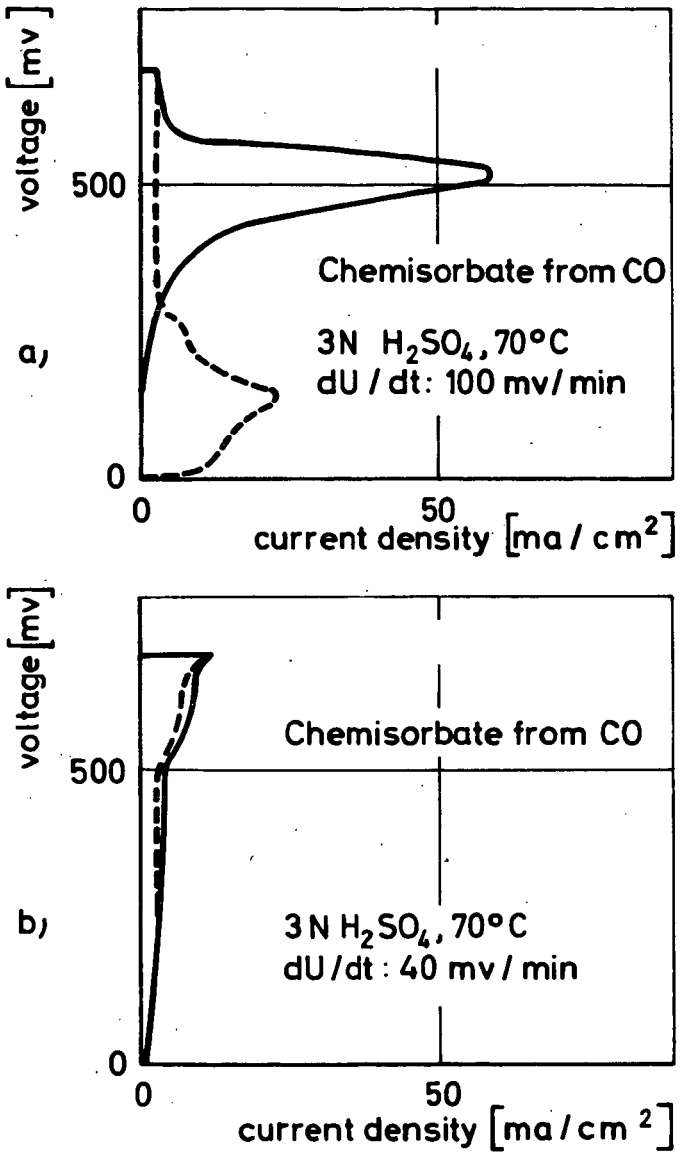

Fig. 11 Oxidation of the CO chemisorbate on a Raney-Pt electrode covered with an additional sulfur chemisorbate a) θ_S = 60 per cent (single sweep); b) $\theta_S \approx 100$ per cent (single sweep)

PREPARATION AND CHARACTERIZATION OF Pt-BLACK FOR ANODIC HYDROCARBON OXIDATION

J. Giner, J. M. Parry, and S. M. Smith

Tyco Laboratories, Inc., Waltham, Massachusetts

A. Introduction

The work presented here is part of a wider study to develop a correlation between the physical characteristics of Pt-black and its activity for the anodic oxidation of saturated hydrocarbons. Since the physical characteristics of a black should be a function of its preparation, some emphasis has been placed on studying a preparative method in order to obtain Pt-black of varying characteristics. Because of the technical importance of Pt-black and the scarcity of information on its preparation available in the recent literature, this phase of the study is of interest on its own.

B. The Formaldehyde Reduction of Pt-black

Of the many reductions proposed and used to prepare Pt-black, one of the most widely studied reactions concerns the reduction of a chloroplatinic salt with formaldehyde in a basic medium.

The over-all reaction is mainly a combination of the following reactions:

$$PtCl_6^{2-} + 2\,HCHO + 6\,OH^- \rightarrow Pt + 2\,HCOO^- + 4\,H_2O + 6\,Cl^-$$

and

$$PtCl_6^{2-} + HCHO + 6\,OH^- \rightarrow Pt + CO_3^{2-} + 4\,H_2O + 6\,Cl^-$$

with one or the other being more dominant according to the preparation conditions[1].

This system was selected for our study because it is the best known process and because it offers the possibility of separating the initial nucleation and the subsequent growth of the nuclei to a well defined precipitate of Pt-black. Furthermore, the growth stage can be considered to occur as a mixed electrode process. According to this latter mechanism, the initial nucleation is followed by an electrochemical deposition of Pt coupled with an anodic oxidation of formaldehyde. Although both electrode processes occur on the same particle simultaneously and at the same rate, they are essentially independent of each other. The principle is illustrated in Fig. 1 which shows the individual i(E)-curves obtained for the anodic

oxidation of formaldehyde and the cathodic electrodeposition of Pt from a chloroplatinic salt, both in acid and in basic electrolyte on a Pt-microelectrode. From these curves it can be concluded that a mixed electrode reaction is only possible in basic solution since the anodic reaction occurs at lower potential than the cathodic reaction. This is not the case in acid medium, agreeing with the observation that, although thermodynamically possible, a chloroplatinic salt is not reduced by formaldehyde in acid medium even over extended periods of time.

Figure 2 shows the change in potential of a Pt-microelectrode vs. RHE immersed in a solution of chloroplatinic acid and formaldehyde after the addition of NaOH. The absolute value of potential should indicate the potential of the particles formed during reaction. An interesting observation from this experiment is that the potential of the microelectrode changes slowly during a period of time which coincides with the induction time of the reaction, i. e. time between mixing of the reactants and visual observation of precipitation. Simultaneously with the observed blackening of the solution, the potential drops steeply to remain at about +100 mv (vs. rev. H_2-electrode in same solution) during the reaction. The fact that the potential always remains positive with respect to the hydrogen electrode indicates that hydrogen evolution, which is thermodynamically possible. does not occur under these conditions.

In considering the precipitation of Pt-black as a mixed electrode process, it is tempting to use criteria similar to those used in electrodeposition of powders[2] for predicting the effect of reaction parameters. The major difference is that the current would be supplied by the formaldehyde oxidation, and would vary according to the reversibility of the reaction and the concentration of formaldehyde. Thus, by extension of the experience on electrodeposition of powders, factors favoring deposition of Pt at conditions closer to the diffusion limiting transport should tend to give finer particles.

On the other hand, the nucleation process (i. e. the formation of a cluster of a few atoms without metallic properties) has to occur by a mechanism different from the electrochemical mechanism. In addition, heterogeneous nucleation in the walls of the vessels and on impurity particles is also possible.

A phenomenon related to the nucleation process is the formation of a bright mirror on the solution surface and walls of the container. Under some conditions, in absence of stirring the formation of the mirror on the surface can be observed before any reaction appears in the bulk solution. The reaction (characterized by blackening of the solution) progresses slowly down from this surface mirror into the solution as a very well defined layer, which can reach a thickness of up to several centimeters before complete mixing occurs. This observation indicates a dendritic growth on the mirror with possible detachment of crystals that serve as secondary nuclei.

In order to obtain active materials, the formation of this mirror is to be avoided since after drying, platelets of very low BET surface area are formed. In general, the longer the induction time, the larger the amount of mirror material will be formed.

Another difficulty when studying the effect of preparation parameters involves transformations occurring after preparation, such as agglomeration and recrystallization. These factors are affected by the gas bubbled during preparation, by the presence of protective colloids and ions, and by the adsorption of intermediates of HCHO oxidation and/or of its polymerization products, etc.

Finally, in an actual preparation drastic changes of parameters occur (especially, for example, the concentration of $PtCl_6^{2-}$) as the reaction progresses which results in the formation of black under varying conditions.

C. Physical Characterization and Determination of Electrochemical Activity

In order to study the effect of the parameters on the precipitation process, many preparations with different reaction conditions were made, and the resulting materials were characterized using the BET surface area, pore size distribution, bulk density, electron microscope shadowgraphy, selected area electron diffraction and X-ray diffraction. The last method was an extension of the method of Warren and Averbach (3); the technique utilized a Fourier analysis of the diffraction intensity data to provide information on the average crystallite size. In addition, strain and resulting stored energy, stacking and twinning fault probability are separated. The combined use of these methods allows characterization of the crystallites, the elementary particles, and the agglomerates which form a black (4).

The activity of the prepared blacks for the anodic oxidation of propane at 150°C in 85% H_3PO_4 was measured, using a Pt-Teflon structure (5, 6) and the floating electrode technique (7). In addition to the conventional over-all activity determination, a nonsteady-state method has been developed to determine the intrinsic activity of the black in the Pt-Teflon structure (8).

From these measurements the current at a potential of 400 mv vs. rev. H_2 (i_{400}) and the value of the current peak (Ep) were used as parameters characterizing the activity.

D. Results on Pt Preparation

Separation of nucleation and growth phases. After preliminary experiments which showed poor reproducibility, attention was directed to the separation of the nucleation and growth stages of the process. This was accomplished (1) by adding Na_2CO_3 to a solution of $PtCl_6^{2-}$ and HCHO to raise the pH to ~ 9 where the mixed electro-growth process is insignificant, (2) by allowing the resulting solution to nucleate for a predetermined time, and (3) by adding this mixture to the NaOH solution. The number of nuclei per unit volume of solution was varied by changing the nucleation time and the portion of $PtCl_6^{2-}$-HCHO solution submitted to this process. This procedure was derived from that of Turkevich, Hillier, and Stevenson (9) for the precipitation of gold. Two fast-addition funnels were used to insure quick mixing of reactants in order to achieve the desired initial concentrations. The apparatus is shown in Fig. 3.

The effect of nuclei concentration on crystallite size for experiments performed with the same reactant concentrations, the same sequences of addition, the same temperatures, etc., but with varying nucleation times, is indicated in Table I.

TABLE I

Black #	Time (min)	Average Crystallite Size (Å) 111	200	220	311
73-44	1	87	75	82	77
73-45	3	70	62	75	70
73-46	10	72	60	67	63

The black produced from the 1 minute nucleation time had the largest crystallite size, while the materials produced from the 3 and 10 minute nucleation have approximately the same size. Since crystallite size is inversely related to the number of nuclei present at the beginning of the growth stage of the preparation, these results indicate that after 1 minute nuclei are still forming and by 3 minutes the formation of nuclei has reached a steady state condition.

In additional preparations the relative number of nuclei/unit volume was changed by reducing the volume of the nucleating solution without changing the concentrations, as mentioned above, at a constant time of 10 minutes and at constant concentration of the final reacting solution. Comparing solutions with the number of nuclei in the ratio 1; 1/2; 1/4; 1/8, the most active material was that corresponding to 1/4 ratio.

Effect of order of addition. Adding HCHO to a premixed solution of $PtCl_6^{2-}$ and NaOH resulted in inactive catalysts with surface areas varying between 2.6 and 7 m^2/g when using high NaOH conc = 5 M (Table II). An example of the electron microscope pattern of these preparations is given in Fig. 4 which shows very large spherical particles. Selected area electron diffraction of individual particles shows that they are polycrystalline. In contrast, a material obtained by adding the mixture of $PtCl_6^{2-}$ and HCHO to 5 M NaOH at the same temperature, concentration, etc., shows a lace-like structure (Fig. 5) made of single crystals and high over-all activity. In experiment #73-25, nucleation time was not controlled.

TABLE II

High NaOH Concentration (NaOH-5.0M)
(All Concentration Refer to Electrogrowth Phase)

a) HCHO added to $PtCl_6^{2-}$/NaOH mixture

Black #	$PtCl_6^{2-}$ Conc. (M)	HCHO Conc. (M)	BET (m^2/g)	Electrochemical Activity i_{400} ma/cm^2	i_p ma/cm^2
73-26	0.25	1.50	3.0	Inactive	------
73-30	0.25	1.50	5.0	Inactive	------
73-31	0.25	1.50	6.9	Inactive	------
73-32	0.25	1.50	4.1	Inactive	------
73-35	0.05	1.50	2.5	Inactive	------
b) $PtCl_6^{2-}$/HCHO mixture added to NaOH					
73-25	0.25	1.50	31.7	58	235
73-58	0.13	0.39	25.2	72	107
73-56	0.06	0.19	22.2	28	52

Effect of reactant concentrations. The higher concentration of HCHO during the growth produced a faster reaction rate and consequently a smaller particle size. When the molar ratio of HCHO to $PtCl_6^{2-}$ was equal to or lower than unity, long induction times were found which resulted in extensive mirror formation during preparations at or below room temperature. It was apparent from the stoichiometry of the reaction that the reduction requires at least a 2 to 1 molar ratio of HCHO to $PtCl_6^{2-}$; however, preparations were made a ratio of unity or lower in order to study the relation between low HCHO concentration and mirror formation. At high temperatures, the induction time was considerably shorter, but the same mirror product was obtained. However, at molar ratios of HCHO to $PtCl_6^{2-} \geq 3$, there was no appreciable effect contributable to the HCHO concentration.

Therefore, working at molar ratios of HCHO to $PtCl_6^{2-} \sim 3$, blacks were prepared either at different $PtCl_6^{2-}$ concentrations or at various NaOH concentrations in the growth stage while keeping constant the temperature, nucleation time, and the concentration of $PtCl_6^{2-}$ and HCHO in the nucleation stage. Rather than attempt to determine the effect of varying the concentration of the $PtCl_6^{2-}$ or NaOH separately, the results are better presented in the form of the molar ratios. Plotting the current/geometric cm^2 at 400 mv of the various blacks as determined in the over-all activity against the molar ratio of $[NaOH]/[PtCl_6^{2-}]$, there is an apparent optimum ratio of ~ 25:1 (Fig. 6). Above and below this value, activity falls off.

In particular, the active materials formed at molar ratios of HCHO to $PtCl_6^{2-}$ of 11 and 25 were obtained from reasonably reproducible preparations from an electrochemical activity standpoint. X-ray diffraction data on identical preparations 73-60, 61, and 62 (molar ratio of 11) gives very good agreement on crystallite size (Table III)

TABLE III

Black	Average Crystallite Size (Å)				Electrochemical Activity	
	111	200	220	311	i_{400} ma/cm^2	i_p ma/cm^2
73-60	51	53	52	49	102	147
73-61	51	50	50	48	70	143
73-62	55	50	52	51	67	105

Effect of temperature. The only apparent effect of temperature was to increase the rate of reaction. Many early investigators[10] emphasize the need to prepare the blacks at low temperatures to avoid formation of resinous material (probably polymers of HCHO) and formation of mirror. Attempts to reproduce Willstatter preparation at 5°C, with special precautions to avoid local heating, failed to produce a black of higher activity than those prepared at high temperatures. Since the more active blacks obtained in the present work were prepared at 80-90 C, it is tempting to conclude that higher temperature is beneficial insofar as it accelerates the reaction, decreasing the induction time, and possible mirror formation.

Effect of oxygen. It has been claimed that adsorbed oxygen plays an important role in the catalytic activity of platinum black in the sense that materials freed of oxygen were generally inactive[11]. To test this, a series of identical preparations were made under O_2 and N_2. The bubbling of oxygen through the reaction solution was useful in coagulating the resulting colloid solutions of platinum. As to their effect on BET area or electrochemical activity, no clear difference could be detected between black produced under O_2 or under N_2.

The beneficial effect mentioned in the literature may be related to the slower sintering rate of platinum when covered with oxygen, reported by McKee[12], or to a cleaning by oxidation of chemisorbed intermediates of the HCHO oxidation.

E. Relation Between Structure and Activity

In general, the over-all activity per unit weight is high in blacks having agglomerates of high internal porosity and relatively large particle size. This may be a pure structural effect confirming those electrode models in which electrolytic transport to the reaction site through the flooded agglomerates is postulated[13, 14]. Surface areas larger than $\sim 15\ m^2/g$ are necessary to obtain high activity; above this value no correlation between activity and surface area was found.

A somewhat surprising result is that a black with low stored energy produced higher over-all activity than the blacks with considerably more stored energy. Preliminary measurements show a similar effect on intrinsic activity. Work is continuing to define better the properties of the black and to relate these properties to the structure after electrode manufacture.

REFERENCES

1. A. Sieverts and H. Brüning, Z. Anorg. Ch. 201, 113 (1931).

2. N. Ibl, "Advances in Electrochemistry and Electrochemical Engineering," Vol. 2. edited by C. W. Tobias, John Wiley and Sons, New York, 1962.

3. B. E. Warren and B. L. Averbach, J. Appl. Phys. 23, 1059 (1952).

4. B. N. Das, A. D. Sarney-Loomis, F. Wald, and G. A. Wolff, to be published.

5. L. W. Niedrach and H. R. Alford, J. Electrochem. Soc. 112, 117 (1965).

6. R. G. Haldeman, W. P. Colman, S. H. Langer and W. A. Barber, Fuel Cell Systems, Advances in Chemistry Series, No. 47, Amer. Chem. Soc. 47, 106 (1965).

7. J. Giner and S. Smith, J. Electrochem. Technology, 5, 59 (1967)

8. J. Giner, J. M. Parry and S. M. Smith, to be presented at the Spring Meeting of the Electrochem. Society in Dallas.

9. J. Turkevich, P. G. Stevenson and J. Hillier, Disc. Faraday Soc. 11, 55 (1951).

10. R. Wilstätter and E. Waldschmidt-Leitz, Ber. 54, 115 (1921); O. Loew, Ber. 23, 289 (1890).

11. J. W. Döbereiner, J. pr. Ch. [2] 32, 398 (1885) and Schw. J. 66, 299 (1832); H. Euler, Ofvers, Akad, Stockholm 1900, 271, A. Gutbier, and O. Maisch, Ber. 52, 1370 (1919); N. I. Kobosew and W. L. Anochim. Z. phys. Ch. B13, 68 (1931); L. Mond, W. Ramsay, and J. Shields, Phil. Trans. A186, 661 (1895), Z. phys. Ch. 19, 29 (1896), Phil. Trans. A190, 138, 141 (1897), and Z. phys. Ch. 25, 667, 671 (1898). R. Willstätter and J. Jaquet, Ber. 51, 770 (1918). R. Willstätter and E. Waldschmidt-Leitz, Ber. 54, 115 (1921). L. Wöhler, Ber. 36, 3481 (1903). L. Wöhler and C. Engler, Z. Anorg. Ch. 29, 5 (1902).

12. D. W. McKee, J. Phys. Chem. 67, 841 (1963).

13. E. A. Greens, II, I & E Fundamentals 5, 542 (1966).

14. Yu. A. Chizmadzhev, Soviet Electrochemistry 2, 1 (1966).

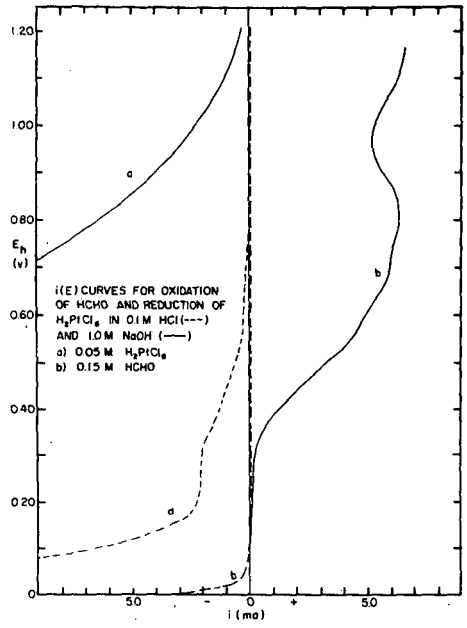

Fig. 1 i(E) curves

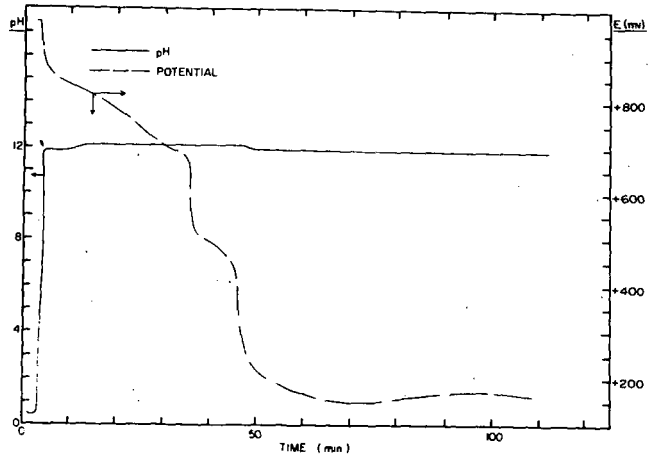

Fig. 2 Variation of potential with time

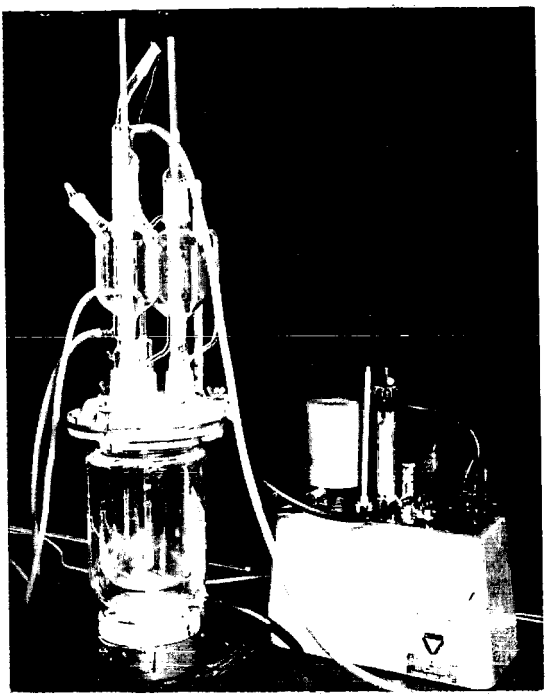

Fig. 3 Apparatus for preparation of Pt blacks

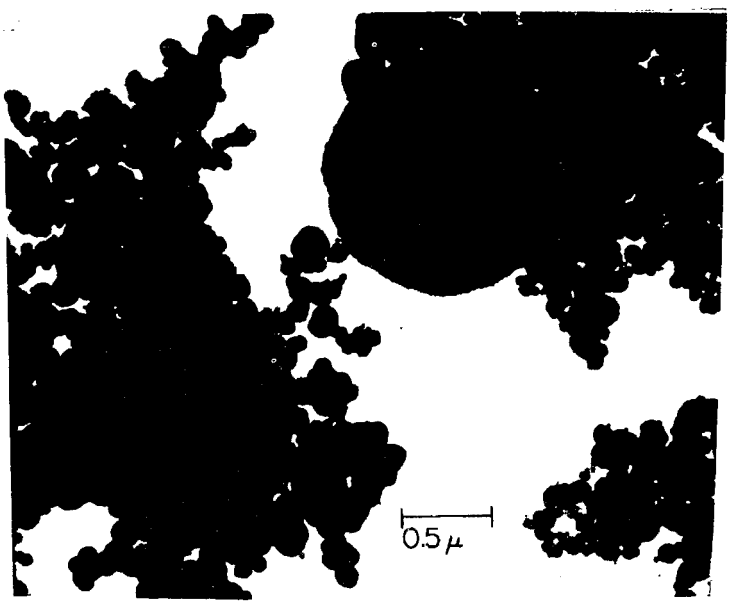

Fig. 4 Pt black, 73-26

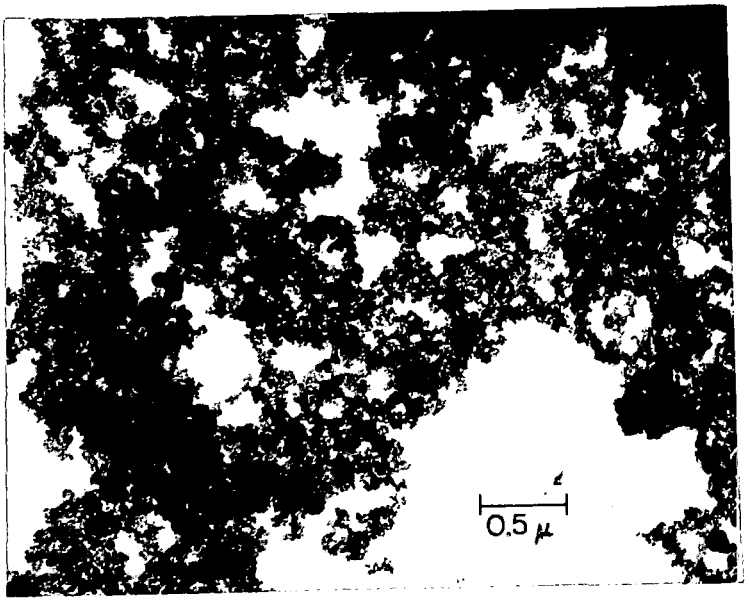

Fig. 5 Pt black, 73-58

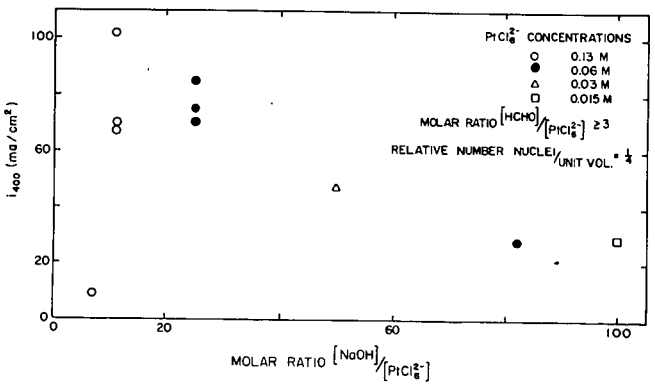

Fig. 6 Activity as a function of molar ratio

NORMAL ALKANES AT PLATINUM ANODES

H.A. Liebhafsky and W.T. Grubb

General Electric Research & Development Center, Schenectady, N.Y.

Extensive work on direct hydrocarbon cells has shown the normal alkanes to be the most suitable family of fuels (1). How their performance changes with molecular weight has consequently become important. The most straightforward way of establishing this relationship is by measuring for an anode (or similar anodes) under conditions intended to be identical the steady-state current densities supported by the several homologues at fixed anodic overvoltage. The anodic overvoltage η_a is usually measured as the potential difference E_{A-R} between the working anode and a reversible hydrogen reference electrode in the same cell. Figure 1 shows the results of an early comprehensive study of this kind.(1a,b)

A plot like Figure 1 is adequate as a record of experimental results or as a basis for comparing results for a single fuel. But when comparisons that involve more than one fuel are to be made, one must remember that each alkane (or other fuel) can surrender a different number, n_e, of electrons per molecule upon anodic oxidation. Experiment has shown that the normal alkanes are often completely oxidized, yielding H^+ and CO_2 at fuel-cell anodes(2,a,b,c). When this is true, $n_e = 6n + 2$ for the n'th member of the homologues series of normal alkanes.

Current densities like those in Figure 1 will be expressed in molecular units (further specification unnecessary)* if each of them is divided by the value of n_e for the corresponding normal alkane. When this is done (Figure 2), the maxima in Figure 1 disappear, and methane takes its place as the fuel of highest molecular performance. We have similarly transformed data by Binder and co-workers(2b), and by Cairns(2c) with the results in Figures 3, 4, and 5. Figure 3 is in accord with Figure 2; in the other figures, methane fails to achieve top performance to a degree that increases with E_{A-R} and with current density. (E_{A-R} and i increase together in this range.)

The experimental conditions under which the presumed steady-state current densities were measured varied so widely that they will not be discussed. The experimental conditions most nearly certain to have given true steady-state current densities are those of Binder and co-workers. Only here were all fuels at a known identical pressure, 1.5 atm. The gases at this pressure flowed through an anode heavily loaded (180 mg/cm^2) with Raney platinum; unreacted fuel and carbon dioxide(2b) bubbled through the electrolyte, 3N H_2SO_4 at 100°C. The first reading was taken after 24 hours, and subsequent readings at 2-hour intervals. These data consequently provide the best test of whether the maxima in performance curves disappear when they are placed on a molecular basis. Comparison of Figure 3 with Figure 5

---

*With 10^5 coulombs as the Faraday, and with current density in ma/cm^2, the current density in molecular units (i/n_e) is 10^8 times the moles fuel/sec oxidized on 1 cm^2 of electrode surface. The number of electrons per molecule, n_e, yielded up by the fuel during oxidation is of course equal to the experimental number of Faradays for a mole of fuel. When the anodic reactions are complex, n_e may be only an average value.

of Reference 2b shows that the test was successfully passed.

A hydrocarbon anode at a steady state is a complex system in which various consecutive processes (physical, chemical, electrochemical) proceed at the same absolute rate. No one process is therefore rate-determining, although the rate constants associated with each process help establish the absolute steady-state rate of all. Reliable data for the detailed analysis of such steady states do not exist.

Attempts to interpret current densities as rates in terms of overvoltages usually founder because one cannot establish the contributions that the individual processes make to the measured overvoltage. "Tafel plots" for the data of Figures 1 and 2 appear in Figures 6 and 7. Clearly, these plots are not straight lines, and this testifies to the complex and composite character of the measured overvoltage. Figure 7 is tidier than Figure 6, which supports the "molecular units" as more rational that ma/cm^2. Note, especially in Figure 7, that increasing anodic overvoltage increases current density more markedly at intermediate values of n: the plots for CH_4 and for $C_{16}H_{34}$ resemble each other. Evidence too extensive for discussion here (3,4) has shown that methane is adsorbed more slowly on platinum than are its homologues, and that the oxygenation process on the anode (which leads ultimately to CO_2) is simplest for methane. For the first fact, the symmetry of methane may be responsible; and the absence of C-C bonds is responsible for the second. The gain in performance occruing to methane from the second fact appears to override any loss from the first. The greater effect of increasing overvoltage on current density for the higher homologues can be explained as resulting from accelerations in the rates of breaking carbon-carbon bonds, and in the rates of other reactions that rid the anode of dehydrogenated alkane residues.

Though Tafel slopes cannot of themselves establish mechanism, we must admit the possibility that similarities in Tafel plots, such as that between the plots for CH_4 and $C_{16}H_{34}$, point to similarities in the mechanism for anodic oxidation. For example, such a possibility is that cetane, being a large molecule, is held by the surface only at isolated points where anodic oxidation occurs (as for methane) without the breaking of carbon-carbon bonds and perhaps with desorption of incompletely oxidized molecules. Note, however, that complete oxidation to CO_2 has been shown by Grubb and Michalske (unpublished) to occur within experimental error for the normal alkanes up to and including octane. The suggestion just made for higher alkanes needs to be tested experimentally, and it serves as a reminder that $n_e = 6n + 2$ cannot always be taken for granted.

We shall use current densities in molecular units in comparing the reforming of methane before it reaches the anode with its direct oxidation at the anode. We make this comparison on the basis of the endothermic reaction

$$CH_4 + H_2O = CO + 3H_2 \qquad (1)$$

At an overvoltage of 0.3 volt, observed current densities under the conditions of Figure 1 are: CH_4, 13.2 ma/cm^2; CO, 58 ma/cm^2; H_2, >500 ma/cm^2. Expressed in molecular units, these current densities become CH_4, 1.65; CO, 29; H_2, >250. The attractiveness of reforming, from a kinetic point of view, is enhanced when current densities are expressed in molecular units.

We wish to thank Dr. L.W. Niedrach for providing us with the CO datum used above.

We shall not claim that the current density in molecular units is always to be preferred in comparing performances of different fuels or in judging the effectiveness of electrocatalysts. But we do wish to point out the advantages of basing current densities upon the molecule - especially when the anode process is as complex as the steady state at the hydrocarbon anode, which was alluded to above. In the series of consecutive processes that proceed at the steady-state rate on this anode, the first are probably transport processes, and they are known to involve the molecule. After these come the processes (e.g., dissociative adsorption, electron transfer, breaking of bonds, oxygenation) that take place on the anode surfaces. These processes are unknown in number and involve unknown intermediate species. Because one (or at most two) electrons are transferred in a single process, the number of processes in which electron transfer occurs will vary from one alkane to another as n_e varies. By basing comparisons on the current density in ma/cm^2 (or similar units), we base the comparison on the integrated contribution of all electron-transfer processes, the nature and number of which vary from one alkane to another. We hope that current densities in molecular units will be used by others as a basis for comparing the anodic performances of different fuels so that the usefulness of these units can soon be decided.

SUMMARY

1. Current densities in molecular units as opposed to, say, ma/cm^2, are logical for comparing the performance of the various normal alkanes at hydrocarbon anodes. The statement holds also for other cases.

2. Current densities being expressed in molecular units, methane outperforms other normal alkanes at fuel-cell anodes under certain steady-state conditions with sulfuric and phosphoric acid as electrolytes. With electrolytes containing hydrofluoric acid, the statement does not hold. Further work is needed, but the absence of carbon-carbon bonds in methane strongly supports the idea that it ranks first in anodic reactivity among normal alkanes.

3. It is possible that heavy alkanes, such as cetane, are oxidized incompletely at anodes and without the rupture of carbon-carbon bonds, which would cause their (partial) anodic oxidation to resemble somewhat the anodic oxidation of methane. Further work is needed.

4. Current densities in molecular units need and deserve further testing as a basis for comparing the performance of different fuels at fuel-cell anodes.

REFERENCES

1. (a) Grubb, W.T. and Michalske, C.J., Proc. 18th Annual Power Sources Conference, PSC Publications Committee, Red Bank, N.J. (1964), p.17.
(b) Fig. 1, which completes the publication of performance results by Grubb and Michalske.

2. (a) Grubb, W.T. and Michalske, C.J., J. Electrochem. Soc., 111, 1015 (1964).

(b) Binder, H., Kohling, A., Krupp, H., Richter, K., and Sandstede, G., ibid., 112, 355 (1965).
(c) Cairns, E.J., ibid., 113, 1203 (1966).

3. Niedrach, L.W., ibid., 113, 645 (1966).

4. Gilman, S. in Hydrocarbon Fuel Cell Technology, B.S. Baker, Ed., Academic Press, New York, N.Y. (1965), p.349.

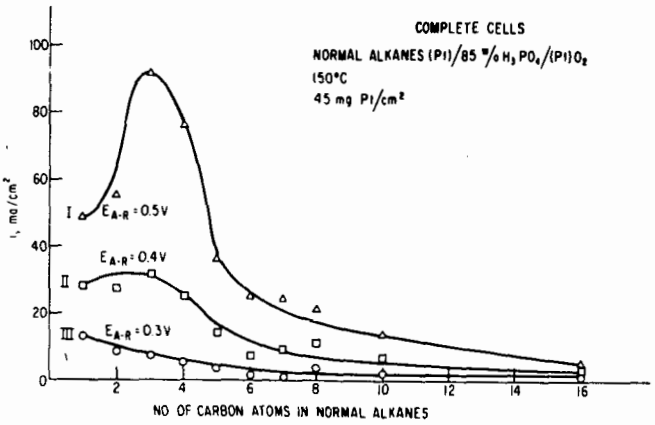

Figure 1. Performance of normal alkanes as fuels.[1]

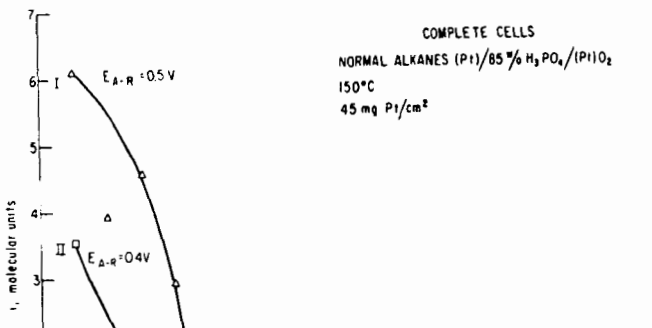

Figure 2. Performance data of Figure 1 in molecular units.

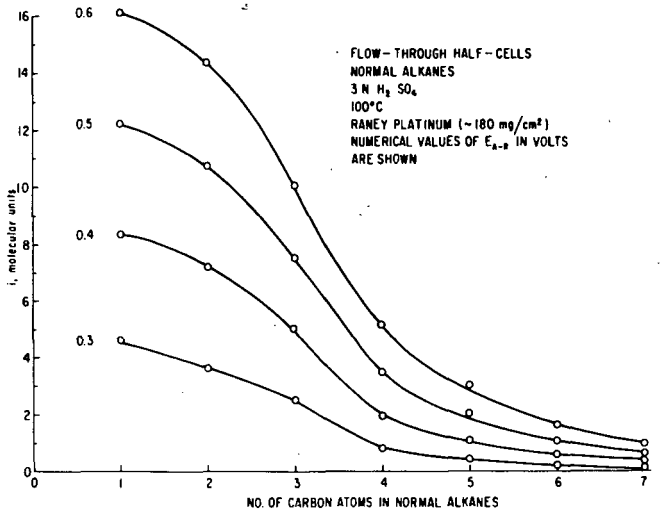

Figure 3. Performance data of Reference 2b in molecular units.

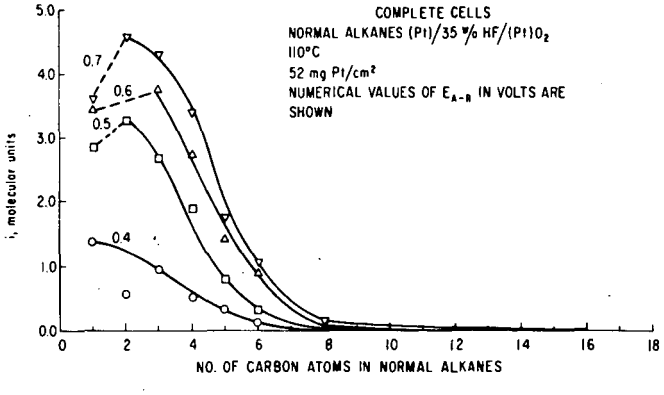

Figure 4. Performance data from Reference 2c in molecular units.

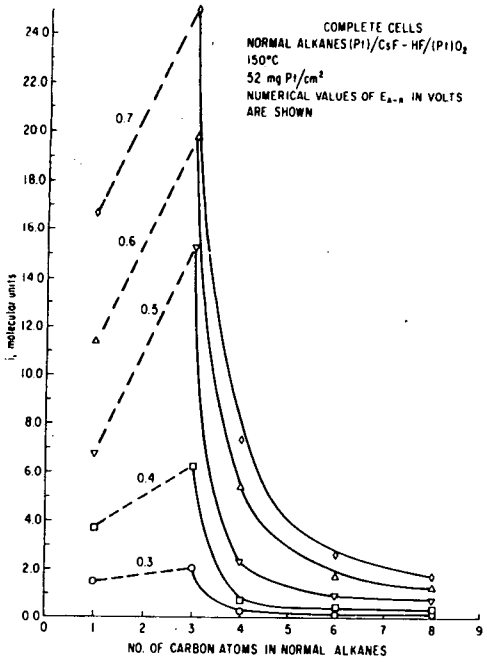

Figure 5. Performance data from Reference 2c in molecular units.

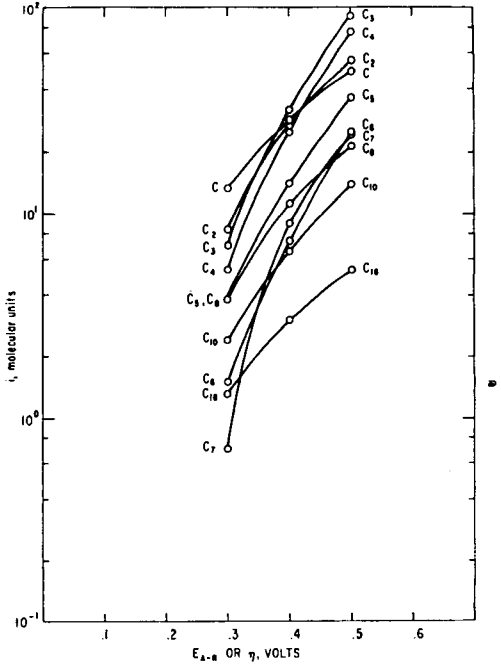

Figure 6. Tafel plots for Figure 1.

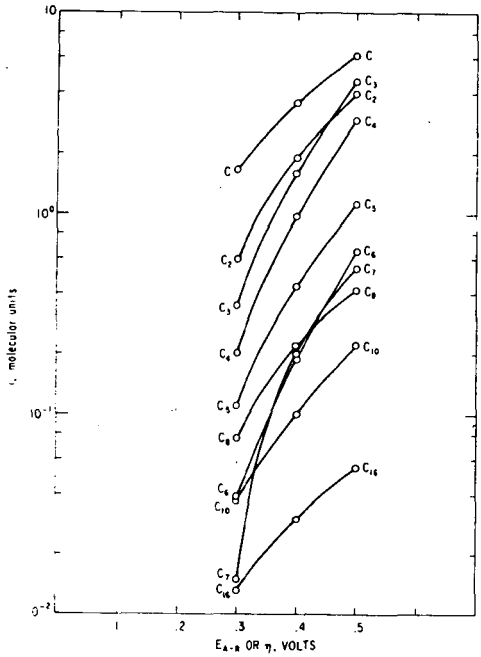

Figure 7. Tafel plots for Figure 2.

AN EQUIVALENT ELECTRIC CIRCUIT APPROACH TO THE STUDY OF HYDROCARBON OXIDATION KINETICS

Arthur A. Pilla and Gabriel J. DiMasi
Power Sources Division, Electronic Components Laboratory
USAECOM, Fort Monmouth, New Jersey

ABSTRACT

A technique for the determination of the frequency response of an electrochemical system between 1 Hz and 10 Hz is described and applied to the study of the anodic oxidation of hydrocarbons. Special emphasis is placed upon the treatment of data in the frequency domain. Thus, it is shown that the combined use of specific frequency functions of the real and imaginary parts of the measured impedance as well as the phase angle, magnitude and Argand functions constitute a powerful method to establish an equivalent electric circuit for hydrocarbon oxidation, In addition, the concept of total electrode impedance is used to permit the evaluation of the double layer capacity in the presence of the electrode reaction. It is shown that appropriate treatment of frequency response data obtained over a wide enough frequency range allows a unique circuit to be obtained under the particular conditions of the experiment. The equivalent electric circuit thus established is compared with those obtained from an analysis of the reaction schemes which have been proposed by other workers. In this respect, the method of establishing equivalent circuits representative of a given reaction scheme is discussed in detail and it is shown that each mechanism has a unique circuit. The variation of impedance as a function of potential and of reactant gas is studied allowing the possibility of detecting changes in reaction mechanism at different steady-state potentials.

ANODIC OXIDATION OF CYCLIC HYDROCARBONS

M.L. Savitz and R.L. Carreras

U.S. Army Engineer Research and Development Laboratories
Fort Belvoir, Virginia

In order to obtain efficient practical direct hydrocarbon fuel cells for military use, it is necessary to oxidize the components of logistically available fuels. Military specifications[1] allow these fuels to contain as high as 25% aromatics and 5% olefins. Recently Luksha[2] found that a Niedrach-Alford Teflon bonded platinum electrode with phosphoric acid electrolyte at 150°C could tolerate a fuel containing up to 5% olefins, 1% aromatics, 5% six ringed napthenes, 15% five ringed napthenes and the remainder saturated normal or isooctane with an increase loss of only 50 mv in polarization from that of pure octane. Previously we had reported[3] the adsorption characteristics of some of these representative compounds on bright platinum wire in 85% H_3PO_4 at 130°C. For all of the compounds studied, the rate of adsorption appeared to be diffusion controlled. Benzene adsorbed the most rapidly; cyclohexene and cyclopentene adsorbed the next fastest and both at the same rate; hexene-1 and hexene-2 also adsorbed at the same rate, but less rapidly than the unsaturated cyclic compounds; and cyclohexane and cyclopentane had the lowest rate of diffusion. For all compounds, maximum adsorption was between 0.2 and 0.4V. The highest steady state coverage for a specific concentration was obtained for the most rapidly adsorbing species. The maximum amount of adsorption at each potential follows the same order as did the rate of adsorption (i.e. benzene adsorbed the most).

In fuel cell tests,[2] it has been found that cyclohexyl compounds affect octane performance more adversely than five c-ringed napthenes and they do not behave like normal saturated hydrocarbons. Open circuit values indicated dehydrogenation to benzene was occurring for the six member ringed compounds; however, in the initial adsorption studies on a wire electrode, cyclohexane appeared to behave as a normal saturated hydrocarbon. To obtain more evidence as to whether there was dehydrogenation under our conditions, the composition of electrochemically adsorbed species formed from benzene and cyclohexane was investigated using cathodic and anodic desorption techniques developed by Brummer.[4]

Experimental

The experimental set up was similar to that which we have described previously.[5] In brief, the electrochemical studies were performed on a flamed bright platinum wire of thermocouple grade platinum of geometric area 0.5 cm^2 maintained at 130°C in 85% H_3PO_4. The acid had been pretreated with hydrogen peroxide and was contained in a standard three compartment electrochemical cell made of quartz. The reference electrode was the dynamic hydrogen reference electrode described by Giner.[6] The hydrocarbon was introduced into the working compartment by using an argon carrier gas through a glass tube containing organic compound maintained at a controlled temperature to give the desired partial pressure. For low partial pressures, the organic was contained in a tube cooled in an ice-methanol bath. For higher partial pressures, the tube containing the hydrocarbon was heated in an oil bath to the desired temperature. Phillips research grade hydrocarbons of 99.6 mole % purity were used in all cases.

In order to obtain a reproducible platinum surface for the electrochemical measurements, potentiostatic procedures similar to those of Brummer[7] and Gilman[8] were employed. Essentially, the electrode was held at 1.35 V for 1 min., the last 30 sec without stirring, at 0.05V for 10 msec, and then maintained at a potential of interest for varying times before examining the surface state of the electrode with an anodic or cathodic galvanostatic pulse.[7] Potential sequences were obtained by switching of a series sequence of potentiometers with H_g-wetted relays. Time intervals at the potentials were controlled by Tektronix Type 162 waveform generators.[9] The potentials were applied to the cell through the input of a Wenking potentiostat.

All areas are based on real electrochemical areas with 210 μcoul equal to 1 cm^2 of real area as obtained from deposition of a monolayer of hydrogen with a cathodic galvanostatic charging curve.[10]

Results and Discussion

Anodic galvanostatic charging (Q) using current densities from 500 μamp to 150 ma/cm^2 gives a reliable estimate of oxidizable material on an electrode.[7] The charge occurring from the oxidation of the electrode and adsorption of H_3PO_4 under argon is subtracted from the charge obtained with organic reactant. To obtain the amount of irreversibly adsorbed material on the electrode, cathodic galvanostatic pulses are used. The ratio of hydrogen deposition obtained in the presence of organic with that obtained in an argon atmosphere gives θ_H. The fraction of the surface covered by organic material is $1-\theta_H$. The initial adsorption studies with benzene[3] indicated that at higher concentrations (200 mm partial pressure) of benzene, 15% of the electrode was covered with material after adsorption at potential for 1 msec, the least amount of time of adsorption that could be reproducibly measured. In order to have a clean surface at initial adsorption, benzene at a partial pressure of 5 mm was used in these studies. Since cyclohexane[3] adsorbed very slowly at the lower concentrations and at higher partial pressures behaved like normal saturated hydrocarbons,[5,7,11] a higher concentration was used. This would also enable dehydrogenation to benzene to be detected more easily.

Maximum Amount of Adsorption

The adsorption of benzene and cyclohexane appears to be initially diffusion controlled, the rate of adsorption then decreases and the surface concentration of adsorbed species reaches a constant maximum value.[3] This value is reached within 30-60 seconds at all potentials except with the low concentration of cyclohexane where steady state coverage is not obtained until 300 seconds. Figure 1 shows the maximum amount of adsorption obtained from anodic galvanostatic pulses as a function of potential for benzene at 5 mm pressure and cyclohexane at 200 mm pressure. The electrode is pretreated as mentioned, held at the potential of interest for 2 minutes and then treated with an anodic galvanostatic pulse of 50 ma/cm^2. Both compounds have appreciable adsorption from 0.05 to 0.80 V, and benzene even has adsorption at 0.9 V. Between 0.2 and 0.4, maximum adsorption is observed. There is not, however, a sharp maximum at 0.2 V as has been observed with n-paraffins,[7,11] but more of a bell shaped appearance for both of the compounds. Figure 2 is a plot of the maximum fraction of the surface covered vs potential as obtained after 2 minute adsorption with a cathodic galvanostatic pulse of 50 ma/cm^2. These measurements indicate maximum coverage for both compounds at 0.2 and 0.3 V. Both figures (1) and (2) indicate that the maximum amount of surface coverage does not differ too much for both compounds though it must be kept in mind that there is a much lower concentration

of benzene. Figure 2 also shows maximum amount of coverage for 200 mm pressure of benzene. Maximum amount of adsorbed species for a specific compound might be expected to be independent of concentration if long enough times of adsorption at potential are maintained, and little or no oxidation is taking place. Figure 2 indicates about 68% maximum coverage with benzene and 65% coverage with cyclohexane - numbers within experimental error of each other. Compounds of similar size and reactivity would be expected to occupy same space of the electrode. The maximum charge to oxidize the adsorbate is slightly higher for the cyclic hydrocarbons than the n-paraffins.[4,7,11,12]

These results compare with 50% electrode coverage in the region 0.3-0.5V vs normal hydrogen electrode obtained by Bockris et al[13] using radiotracer techniques for benzene adsorption in H_3PO_4 at 50°C.

Type of Adsorbed Species

Gilman,[14] Niedrach[15] and Brummer[4,11,12] have obtained evidence for several types of intermediates adsorbed on the electrode surface with normal saturated hydrocarbons or ethylene as reactant. Part of the adsorbate designated CH-γ can be cathodically desorbed and is thought to contain only C and H. Another CH material not removed by cathodic treatment and seems to be a combination of a CH polymer (CH-β) and a more highly oxidized material thought to contain at least one C-O bond (O-type). To determine whether benzene and cyclohexane give the same type of adsorbed intermediates - specifically whether cyclohexane dehydrogenates to benzene - the composition of the steady state adsorbed residues was investigated. Cathodic and anodic desorption techniques similar to those used by Brummer[4] have been employed. After the usual pretreatment, the electrode was held at a potential for 60 sec at which point steady state coverage was obtained. Then the potential was lowered to 0.01 V where little or no adsorption occurred (benzene had appreciable adsorption at potentials higher than 0.01 V, but not at 0.01 V). At 0.01 V part of the adsorbate, CH-γ, desorbs. The potential was held at 0.01 V for various periods of time after which the surface was examined with a galvanostatic pulse. $Q_{res}^{CH-\beta \& C-O}$, the charge required to oxidize the remaining adsorbed species to CO_2, and θ_{org}, the fraction of the surface occupied by the remaining organic species C-O and CH-β obtained from the cathodic stripping curve were followed as a function of time. Before applying the galvanostatic pulse, the potential was raised to oxidize any H_2 adsorbed at 0.01 V. In the time necessary to oxidize H_2 off, there is no readsorption of organic material. The slope of Q vs θ plot gives [e] the number of electrons released per covered site during oxidation of adsorbate. Changes in [e] during the desorption of a given adsorbed species are taken as evidence for the presence of different adsorbed species.[4] Figure 3 is an example of Q vs θ plot for benzene and cyclohexane for which steady-state was obtained after adsorption for 60 sec. at 0.4 V. Desorption proceeds from the right to the left of the figure. The easiest material to be desorbed occurs at the right. For both compounds, a constant value of Q and θ are obtained after desorbing at 0.01 V for 5 seconds which indicates all of the CH-γ is desorbed. Both compounds give a slope corresponding to 5.5 electrons per covered site on the path to oxidation. A methylene group (CH_2) in cyclohexane would require 6 electrons to oxidize completely to CO_2, a methine group (CH) of benzene requires 5 electrons to oxidize completely to CO_2. This result indicates that the cathodically desorbable material might be an equilibrium mixture of benzene and cyclohexane. There is a certain amount of scatter in the plotted points; therefore, it is difficult to distinguish whether there are two separate slopes: one equal to 5 electrons and another equal to 6. Thermodynamic equilibrium data for the gas phase dehydrogenation reaction:

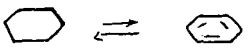

indicates that there would be an equimolar amount of the two compounds.[16] There is substantial evidence that the CH-ψ material is a composite of several species. Using a fuel cell electrode and propane as the reactant, Grubb[17] and Barger and Savitz[18] found that upon cathodic desorption, methane and ethane were observed with the gas chromatograph. Brummer has not examined the fine structure of CH-ψ for propane or hexane adsorption on a wire electrode. Using our experimental set-up, inconclusive results were obtained for the CH-ψ from propane adsorption, as the species occupied only 6% of the covered surface and CH-ψ had desorbed completely at 0.01 V in 100 msec. Figure 3 also indicates a small part of the surface covered with a highly reduced species for the benzene adsorbed species. This could be a polymeric material although in desorption experiments with propane at a fuel cell electrode, no species higher than propane was observed in the gas chromatograph.[18] Figure 4 indicates that the 5.5 electron species appears to be relatively potential independent from 0.1 to 0.7 V. At 0.05 where there is most likely to be hydrogen along around with hydrocarbon, a lower number of electrons is obtained. The oxidation of hydrogen would account for 1 [e] and the average of the mixture would be lower. These results do not tell us whether the relative amount of the species which comprise CH-ψ is potential independent. Barger found the ratio of methane to ethane formed on cathodic desorption was very potential dependent.[18] Definite proof of whether there is an equilibrium of cyclohexane and benzene and the relative amounts is currently being obtained with gas chromatographic procedures.[18] The value of 5.5 electrons is obtained for species which have been adsorbed at the potential of interest for 120 sec to indicate steady state of adsorption had been obtained at 60 sec.

The total amount of Q CH-ψ is defined as $Q_{ads}^{org} - Q_{res}$ after desorption for 5 sec at 0.01 V. The charge of CH-ψ for benzene and cyclohexane with potential varies similarly to that of the total charge for each compound with a maximum amount between 0.2 and 0.4 V (figure 5). This is similar to the results for propane[4] and n-hexane[11] except there is more CH-ψ for benzene and cyclohexane. At 0.2 V, 650 μcoul/rcm^2 charge to oxidize CH-ψ is observed for benzene, 600 μcoul/rcm^2 for cyclohexane, 400 μcoul/rcm^2 for n-hexane,[11] and 175 μcoul/rcm^2 for propane.[4] In both cyclohexane and benzene from 0.1 V to 0.4 V, 70% ($\pm$5%) of the covered surface is with CH-ψ. At 0.5 to 0.7 V, about 60% of the covered surface is with CH-ψ. As oxidation increases, less of the surface should be covered by the more reduced species.

In order to determine the composition of the remaining adsorbed species, desorption at more anodic potentials was pursued. The electrode is pretreated, held at a given potential for 60 sec at which point steady state coverage has been obtained, and maintained at 0.01 V for 10 seconds to desorb all of the CH-ψ material, returned to 0.4 V to oxidize H_2 formed at 0.01 V, and then raised to a potential of 1.0 V where it is held for varying amounts of time before examining the surface with galvanostatic charging curves. The potential is lowered to 0.40 V before making the measurement to reduce any oxide formed. No readsorption of organic material occurs during the time at 0.4 V. The slope of a θ vs Q plot gives a value of 1.95 electrons per site when it is oxidized to CO_2 (figure 6). This species is potential independent from 0.1 to 0.8 V as shown in figure 4. There is a certain scatter at 0.3 where a value of 1.4 electrons is obtained. It is unexpected that both cyclohexane and benzene should give the same deviation. Since we are dealing with a relatively small charge oc-

cupying only 15% of the total electrode coverage (up to 30% of the adsorbed species), there is more likely to be some uncertainty than where there is more of the O-type and one must be cautious in comparing with other O-type species. Brummer has found O-type species for propane for which [e] is 1.3[4] and covers about 80% of the electrode at 0.4 V and for n-hexane for which [e] is 1.4[11] and covers 40% of the electrode. Our value for the cyclic compounds is higher, but repeating Brummer's experiments with propane we obtain [e] of 1.1 and covers 70% of the electrode. With benzene and cyclohexane, we have been unable to desorb all of the material on the electrode at 1.0 V, even after setting for 120 sec. About 5% of the surface remains covered with a species requiring a charge of 50μcoul/rcm^2 to oxidize it.

These results do not give the answer as to what the sequence of steps from benzene or cyclohexane to CO_2 are. On a fuel cell electrode, both cyclohexane and benzene were found to be 1/4 as reactive as hexane and 1/8 as reactive as propane.[19] Benzene is slightly less reactive than cyclohexane. The decrease in reactivity might be explained by the fact there is much more CH-$\equiv$ for cyclohexane and benzene than propane and its oxidation is the slow step for the overall oxidation. Whether this CH-$\equiv$ is unreacted benzene or cyclohexane, a mixture of it and some of the possible cracking products (C_1, C_2, C_3 etc)is being determined by adsorbing on a fuel cell electrode, desorbing cathodically, and analyzing the desorption products with a gas chromatograph.

ACKNOWLEDGEMENT

The interest and helpful suggestions of Dr. H.J. Barger, Jr. is gratefully acknowledged.

References

1. Military Specification, MIL-T-5624G, Nov. 5, 1965

2. E. Luksha and E.Y. Weissman, Preprint of papers presented, A.C.S., Miami, Fla., April 1967, Vol 11, No. 1, p.247.

3. M.L. Savitz, R.L. Carreras, and G.R. Frysinger, presented at Electrochem. Soc., Phila., Pa., Oct. 1966, Extended Abstracts of Battery Division No. 7.

4. S.B. Brummer and M.J. Turner, Oxidation and Adsorption of Hydrocarbons on Noble Metal Electrodes, Part 3, J. Phys. Chem., in press.

5. M.L. Savitz, R.L. Januszeski, and G.R. Frysinger, "Hydrocarbon Fuel Cell Technology" (Ed. by B.S. Baker, Academic Press, New York, N.Y. 1965) p.443.

6. J. Giner, J. Electrochem. Soc. 111, 376 (1964).

7. S.B. Brummer, J.I. Ford, and M.J. Turner, J. Phys. Chem. 69, 3424 (1965).

8. S. Gilman, J. Phys. Chem. 67, 78 (1963).

9. S.B. Brummer in Tyco Laboratory Report, April, 1965 on Contract DA-44-009-AMC-410(T).

10. M.W. Breiter, H. Kammermaier, and C.A. Knorr, Z. Electrochem 60, 37, 119 (1956).

References Cond:

11. S.B. Brummer and M.J. Turner, Oxidation and Adsorption of Hydrocarbons on Noble Metal Electrodes Part 4, J. Phys. Chem., in press.

12. S.B. Brummer and M.J. Turner, "Hydrocarbon Fuel Cell Technology" (Ed. by B.S. Baker, Academic Press, New York, N.Y., 1965) p.409.

13. W. Heiland, E. Gileadi, and J. O'M. Bockris, J. Phys. Chem., 70, 1207 (1966).

14. S. Gilman, Trans. Faraday Soc. 61, 2561 (1966).

15. L.W. Niedrach and M. Tochner, J. Electrochem. Soc. 114, 17 (1967).

16. F.D. Rossini et al. "Selected Values of Properties of Hydrocarbons," Circular C 461, N.B.S. 1947.

17. W.T. Grubb in General Electric Report No. 6 on Contracts DA-44-009-AMC-479(T) and DA-44-009-ENG4909.

18. H.J. Barger, Jr. and M.L. Savitz, Chemical Identification of Adsorbed Species in Fuel Cell Reactions, J. Electrochem. Soc., submitted.

19. W.T. Grubb and C.J. Michalski, Proceeding from the 18th Annual Power Sources (May 1964) p.17.

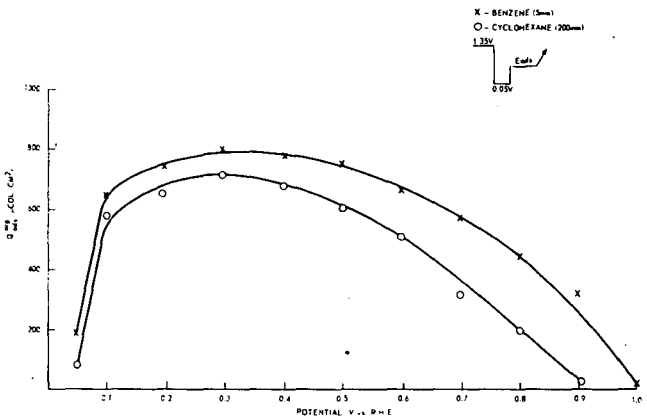

Figure 1. Steady-state adsorption of benzene and cyclohexane as a function of potential

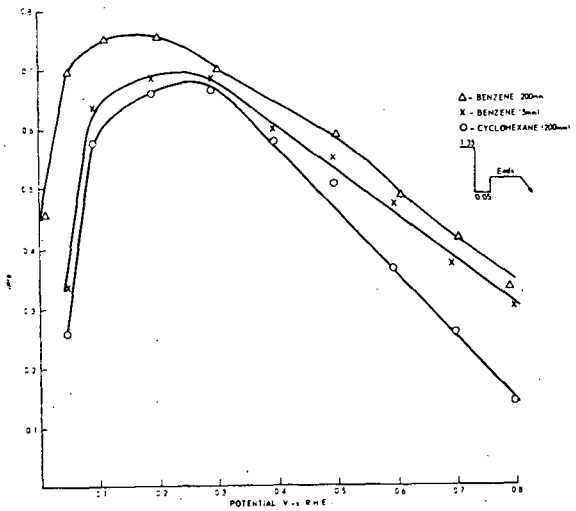

Figure 2. Maximum fraction of surface of electrode covered for steady-state adsorption of benzene and cyclohexane as a function of potential.

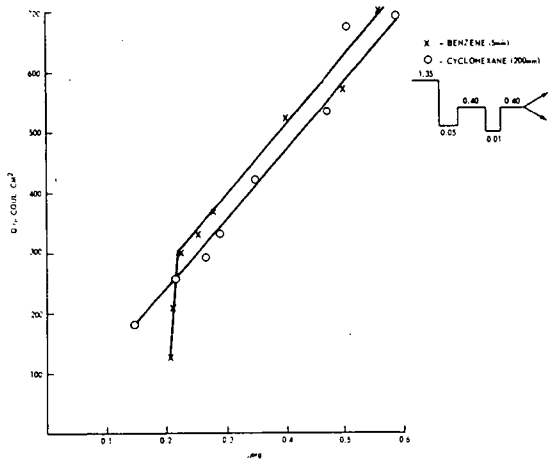

Figure 3. Desorption at 0.01 V of cathodically desorbable material adsorbed at 0.40 V.

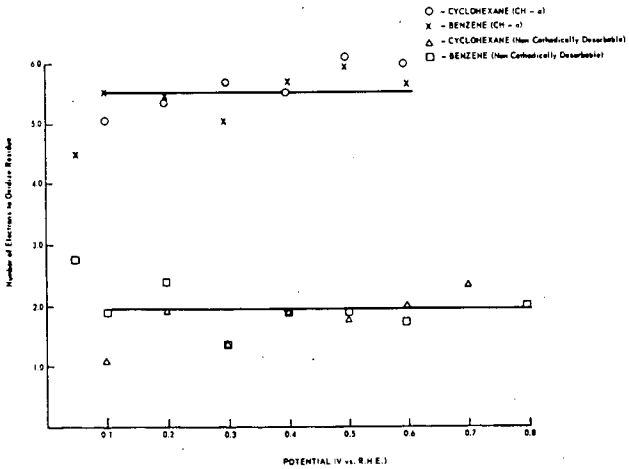

Figure 4. Electrons per covered site to oxidize residue to CO_2 as a function of potential.

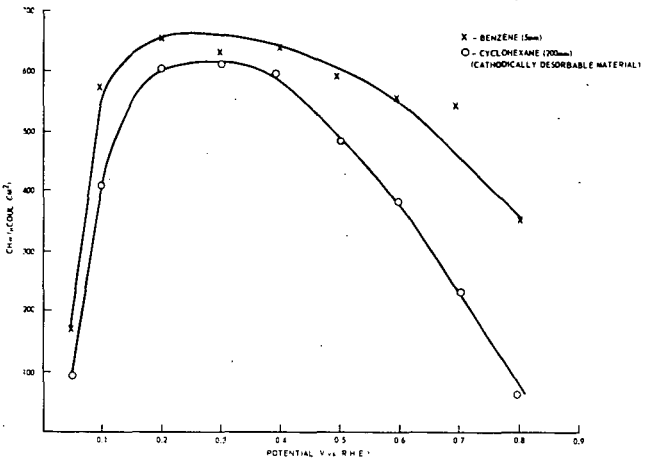

Figure 5. Charge lost on cathodic desorption (CH-$\frac{1}{4}$) for benzene and cyclohexane as a function of potential.

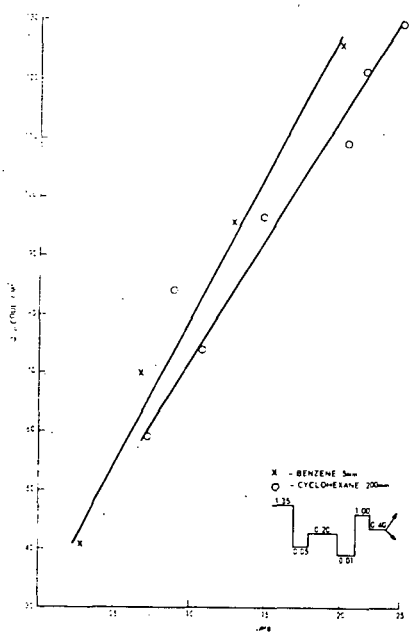

Figure 6. Desorption at 1.0 V after prior cathodic desorption.

RELATIVE REACTIVITIES IN THE ELECTROCHEMICAL OXIDATION OF HYDROCARBON FUEL COMPONENTS

Eugene Luksha and Eugene Y. Weissman

General Electric Co.
Direct Energy Conversion Operation
West Lynn, Massachusetts 01905

Introduction

The tolerance of a fuel cell anode to n-octane containing various types of hydrocarbon additives, aromatic, olefinic, and naphthenic was determined (1). It was found that the octane-based fuel of the composition shown in Table 1 behaved very similarly (50 mv or less difference), at least on a short term basis, to n-octane alone.

Table 1

Model Hydrocarbon Fuel Cell Fuel

Compound Type	Concentration Mole %
Olefins	0-5
Aromatics	1
Naphthenes (cyclohexane type)	5
(cyclopentane type)	15
n + i octane	balance

If the reactivities of each one of the fuel components in Table 1 are different it can be inferred that anodic oxidation will proceed, at steady-state, according to the extent of electrode coverage by the most reactive species. This implies, of course, that probably a major portion of the anode will be covered by more refractory species; these may be present in the original fuel and may also consist of reaction intermediates.

Experimental

The details of the experimental features were outlined earlier (1). The following additional procedures apply specifically to this case:

A fuel, after making a single pass through the fuel cell (anode compartment value 7.5 cm^3), was passed, with its oxidation products, into a Perkin-Elmer 801 gas chromatograph, equipped with a heated gas sampling valve and a differential flame ionization detector. The chromatographic measurements of the exhaust composition were made after the cell was operated for long enough to eliminate biases introduced by concentration gradients in the exhaust system and/or adsorption effects. The gas chromatograph was calibrated before each measurement by injecting several fuels in the concentration range of interest to determine retention times, peak heights, and areas. The gas chromatograph was operated isothermally at 100°C and the calibrations were made in terms of peak areas determined with a disc integrator fitted on a Leeds and Northrup 5 mv recorder. The column, prepared by Perkin-Elmer was a 12 foot, 1/8 inch o. d. Stainless steel tube packed with 10 wt. % Apiezon-L supported on 80-100 mesh chromosorb W. Helium gas was used as a carrier, air and hydrogen gases were used for the fiame detector. All were zero grade (hydrocarbon free) supplied by Matheson.

Since all the fuels used in this study are liquids at room temperature, the sample valve, sampling tube, and the fuel exhaust lines were heated to prevent condensation. The temperatures of the lines were maintained at about 130°C and monitored frequently with the aid of appropriately positioned thermocouples.

Prior to entering the hot lines, the anode exhaust passed through a heated electrolyte trap made of Teflon. Fuel flows in the microliter range were measured with a capillary tube flowmeter. A schematic diagram of this system is shown in Figure 1.

Measurements of the inlet fuel flow, the cell current, and the exhaust composition supplied all the data that were necessary to calculate the current contributions of each component in the binary fuel. However, since a flame ionization detector was employed, it was not possible to measure the CO_2 or H_2O in the exhaust stream. Therefore, the concentrations measured only refer to mixtures of hydrocarbon components. The calculations were performed on a General Electric 625 computer using programs written in Fortran IV. The complete programs are given elsewhere (2).

The anodes were platinum-Teflon-screen composites of a type described in the literature (3). They were of 3 x 3 inch (0.05 ft^2) active geometric area. The electrolyte was phosphoric acid, maintained at 95 wt. % by controlled addition of water. All measurements were made at 350°F.

The anodes were operated, for the most part, at potentials in the range of 0.5 volt vs. H_2/H^+; this is a practical potential at which hydrocarbon anodes can be operated for extended periods with reasonable power outputs (1).

Results

A. Binary Fuels

1. Aromatic Additive (benzene/n-octane)

To study the relative reactivity of aromatics and n-paraffins, a binary fuel consisting of benzene + n-octane was examined.

For this particular fuel the benzene concentration was varied from 1 to 5 mole %, and the liquid fuel flow rate was varied from 5 to 40 μ l/min. For n-octane, this corresponds to at least two times the stoichiometric amount for all cases. The experimental results for all the benzene/n-octane mixtures studied are summarized in Table 2. Columns 4 and 7, respectively, give the exhaust composition of the cell and the current contribution from benzene. A comparison of columns 1 and 4 indicates that benzene is preferentially oxidized. In Figure 2 the quantity I_A/I_T the current fraction from benzene, is plotted against the fuel flow rate for a fuel consisting of 99 mole % n-octane + 1 mole % benzene. These data points were obtained at an essentially constant current (~1.5 amps) and anode potential (~0.5 volt vs. N.H.E.). The current fraction from benzene is directly proportional to the fuel flow rate. This indicates that the aromatic is consumed as rapidly as it is supplied, at least for the range of flow rates studied, and provided that $I_T > I_A$.

Further generalization is provided by Figure 3 which is a plot of I_A, the current from benzene, vs. the benzene flow rate, for fuels consisting of n-octane + 1, 3, and 5 mole % benzene. The current from benzene is proportional to the benzene flow rates, again indicating that the aromatic is consumed as rapidly as it is supplied, independent of whether it is supplied at high concentrations and low total fuel flow rates or low concentrations and high total fuel flow rates.

Table 2

Current Contribution and Exhaust Composition for Benzene

Inlet Fuel Composition, mole %	Liquid Fuel Flow Rate, μl/min.	Benzene Flow Rate, mole/min. x 10^6	Benzene Concentration in Exhaust, mole % x 10^2	Total Current, I_T - amp	Anode Potential vs. H_2/H^+, volt	Current from Benzene, I_A - amp
99% n-octane + 1% benzene	5	0.313	13.0	1.46	0.510	0.014
	11	0.688	5.0	1.55	0.447	0.032
	20	1.25	5.3	1.53	0.525	0.047
	30	1.88	4.6	1.52	0.456	0.087
	38	2.38	4.39	1.52	0.550	0.110
	40	2.48	26.8	0.49	0.505	0.089
	40	2.48	29.2	0.49	-----	0.086
	40	2.48	16.5	1.01	0.530	0.101
	40	2.48	15.6	1.01	0.525	0.102
	40	2.48	10.9	1.46	0.514	0.108
	40	2.48	11.7	1.44	0.540	0.107
	40	2.48	16.9	1.50	0.525	0.101
	40	2.48	14.7	1.51	0.500	0.104
	40	2.48	7.95	2.03	0.490	0.111
	40	2.48	6.55	2.00	0.510	0.113
	40	2.48	5.35	2.00	0.480	0.114
	40	2.48	7.62	2.52	0.520	0.112
	40	2.48	6.35	2.49	0.497	0.113
	40	2.48	5.55	2.97	0.500	0.114
	40	2.48	4.97	3.01	0.500	0.114
97% n-octane + 3% benzene	10	1.87	17.8	0.78	0.485	0.085
	20	3.73	9.72	2.54	0.535	0.176
	30	5.62	26.8	1.26	0.540	0.25
	38	7.03	23.5	1.39	0.535	0.315
95% n-octane + 5% benzene	10	3.15	24.5	0.75	0.502	0.146

The current contribution from benzene, I_A, under these conditions can be represented by the relation:

$$I_A = 4.51 \times 10^4 V_A \quad (1)$$

where V_A is the benzene flow rate in units of gm. mole/min.

If this result can be generalized to all aromatics, at these conditions of operation, the following relationship can be obtained:

$$I_A = 0.934\, nF\, u N_A \quad (2)$$

where:

u = mole feed rate, moles per minute
N_A = mole fraction of aromatic in feed stream

and the other terms have their usual significance.

2. Olefin Additive (pentene-1/n-octane)

The reactivity of olefins in a fuel was determined by studying a binary fuel consisting of 95 mole % n-octane + 5 mole % pentene-1. The experimental data is summarized in Table 3. Colums 4 and 7 give the exhaust composition of the cell and the current contribution for pentene-1, respectively. A comparison of columns 1 and 4, the pentene-1 inlet and exhaust concentrations, respectively, shows that the olefin is preferentially oxidized irrespective of the fuel flow rate. As for the case with benzene, this indicates that the olefin is consumed as rapidly as it is supplied for the range of flow rates studied, and provided that $I_T > I_{ol}$.

The average values of the current contribution from penten-1, are plotted against the pentene-1 flow rate in Figure 4. It can be seen that there is a linear relationship between the current, I_{ol}, and flow rate, and since there is virtually no pentene-1 in the exhaust, the current produced is the stoichiometric amount calculcated from its flow rate. It is noted that at the higher flow rates there is a curvature towards the abscissa. This suggests that at high flow rates or high concentrations of the olefin the current from this compound will probably reach a limiting value.

The current contribution from pentene-1 for these reaction conditions and at low flows, as determined from Figure 4, can be expressed as:

$$I_{ol} = 4.83 \times 10^4 V_{ol} \quad (3)$$

Table 3

Current Contribution and Exhaust Composition for Pentene-1

Inlet Fuel Composition, mole %	Liquid Fuel Flow Rate, μl/min.	Pentene-1 Flow Rate, moles/min. x 10^6	Pentene-1 Concentration in Exhaust, mole % x 10^1	Total Current, I_T, amp	Anode Potential vs. H_2/H^+, volt	Current from Pentene-1 I_{o1}, amp	
95% n-octane + 5% Pentene-1	5	1.58	2.82	1.00	0.445	0.074	
	10	3.16	0.054	1.00	0.483	0.152	
	10	3.16	0.067	1.00	0.485	0.152	
	10	3.16	0.058	1.00	0.520	0.152	
	10	3.16	0.060	1.00	0.496	0.152	Ave.
	20	6.31	0.043	2.00	0.535	0.304	
	20	6.31	0.037	2.00	0.510	0.304	
	20	6.31	0.033	1.50	0.505	0.304	
	20	6.31	0.030	1.50	0.525	0.304	
	20	6.31	0.075	1.50	0.475	0.304	
	20	6.31	0.077	1.50	0.475	0.304	
	20	6.31	0.109	1.00	0.480	0.304	
	20	6.31	0.114	1.00	0.475	0.304	
	20	6.31	0.174	0.50	0.475	0.304	
	20	6.31	0.153	0.50	0.515	0.304	
	20	6.31	0.105	0.50	0.510	0.304	
	20	6.31	0.124	0.50	0.525	0.304	
	20	6.31	0.090	----	0.500	0.304	Ave.
	30	9.47	0.100	0.99	0.525	0.456	
	30	9.47	0.112	0.99	0.525	0.456	
	30	9.47	0.106	0.99	0.525	0.456	Ave.
	40	12.6	3.06	1.00	0.550	0.575	

where V_{ol} is the pentene-1 flow rate in gm mole/min. If the results are generalized to apply to all olefins the following result is obtained:

$$I_{ol} = nF u N_{ol} \quad (4)$$

where the symbols have the same meaning as described above for benzene.

3. Naphthene Additive (cyclohexane/n-octane)

Experiments to determine the relative reactivity of cyclohexane-type naphthenes and n-octane were conducted on a binary fuel consisting of 95 mole % n-octane and 5 mole % cyclohexane. The experimental results are summarized in Table 4.

The cyclohexane-type naphthenes are considerably different from the aromatic and the olefin compounds previously discussed. By comparing columns 1 and 4 which show the cyclohexane concentration in the inlet and exhaust streams, respectively, it is seen that only 27 to 44% of the naphthene is removed. This is in marked contrast to the aromatics and olefins which were virtually entirely removed (93 to 100%). However, it is of importance to note that the cyclohexane concentration in the exhaust is always substantially lower than the inlet concentration. This is shown in Figure 5 in which the cyclohexane concentration in the exhaust is plotted against the liquid fuel flow rate. It is seen that the cyclohexane concentration levels out at about 44% of the inlet concentration.

From a consideration of thermodynamic equilibrium data (4) for the gas phase dehydrogenation reaction:

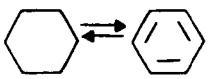

(5)

it shows that, for the conditions prevailing at the anode, the product of Reaction (5) will contain 2.3 mole % benzene and 2.7 mole % cyclohexane. The benzene (and hydrogen) will be rapidly and almost completely consumed.

From these equilibrium considerations, 46% of the naphthene would be consumed with some consumption of the accompanying cyclohexane. This compares favorably with the experimental values ranging from 56 to 72% (Table 4). The agreement with the low value (56%) obtained at the higher flow rates is in better agreement since under high flow conditions the electrochemical utilization of cyclohexane is lower than under low flow conditions.

Table 4

Current Contribution and Exhaust Composition for Cyclohexane

Inlet Fuel Composition Mole %	Liquid Fuel Flow Rate, μ l/min.	Cyclohexane Flow Rate, mole/min. x 10^6	Cyclohexane Concentration in Exhaust, mole %	Total Current, I_T, amp	Anode Potential vs. H_2/H^+, volt	Current from Cyclohexane, I_N, amp	
95% n-octane + 5% cyclohexane	10.7	3.34	1.39	0.800	0.475	0.148	
	10.7	3.34	1.37	0.800	0.485	0.149	
	10.7	3.34	1.35	0.800	0.485	0.149	
	10.7	3.34	1.37	0.800	----	0.149	Ave.
	20	6.25	1.94	0.990	0.525	0.236	
	20	6.25	1.98	0.990	0.525	0.233	
	20	6.25	1.99	0.980	0.525	0.233	
	20	6.25	1.97	0.987	----	0.234	Ave.
	30	9.37	1.89	0.980	0.510	0.352	
	30	9.37	2.01	0.960	0.540	0.339	
	30	9.37	1.93	0.960	0.510	0.347	
	30	9.37	1.94	0.967	-----	0.346	Ave.
	40	12.5	2.23	0.980	0.540	0.419	
	40	12.5	2.19	0.970	0.500	0.426	
	40	12.5	2.20	0.960	0.510	0.423	
	40	12.5	2.21	0.970	-----	0.423	Ave.

The average values of the current contribution from the naphthene I_N, is plotted vs. the naphthene flow rate in Figure 6. A linear relationship is again obtained as with benzene and pentene-1, but here it is noted that the line does not pass through the origin.

The experimental results in Figure 6 can be fitted to the following empirical equation:

$$I_N = 0.05 + 3.55 \times 10^4 V_N \quad (6)$$

where V_N is the flow rate of cyclohexane in mole/min.

Once again, if the results are generalized to all cyclohexane-type naphthenes the following relationship is obtained:

$$I_N = nF (8.65 \times 10^{-7} + 0.613 \mu N_N) \quad (7)$$

when N_N is the mole fraction of the naphthene at the inlet and the other terms have the significance described above.

B. Five Component Fuel

A fuel consisting of 74 mole % n-octane + 15 mole % methylcyclopentane + 5 mole % methylcyclohexane + 5 mole % pentene-1 + 1 mole % m-xylene was studied to determine whether the results reported above using binary fuels are applicable to more complex fuels. It is possible that one or more of the components are selectively oxidized at the expense of the others. A fuel of this particular composition was chosen since it was previously shown (1) to behave very similarly to pure n-octane. Furthermore, this study comes closer to simulating operations with a real commercial fuel. The experimental results are given in Table 5.

For the sake of better resolution in the chromatographic analysis, benzene and cyclohexane, which had been used as model additives in studies with binary fuels, were replaced by m-xylene and methylcyclohexane, respectively. The results should not be greatly affected. The exhaust compositions of the five fuel components are shown as a function of liquid fuel flow rate in Figures 7 thru 11. It is important to note that the n-octane concentration in the fuel actually increases from 74 to 96 mole % after a single pass through the cell as is shown in Figure 7. The naphthene concentrations for both the five and six-membered ring types are substantially reduced in the exhaust stream, especially at low fuel flow rates; this is shown in Figures 8 and 9.

Figures 10 and 11 show the pentene-1 and m-xylene concentrations in the exhaust, respectively, plotted as a function of liquid fuel flow rate.

Table 5

Current Contributions and Exhaust Composition of Components of a Synthetic Fuel

Inlet Fuel Composition, mole %: 74% n-octane + 15% methylcyclopentane + 5% methylcyclohexane + 5% pentene-1 + 1% m-xylene

Liquid Fuel Flow Rate, μl/min.	10	20	30	40
Octane Flow Rate, moles/min. x 10^6	49.16	98.32	147.5	196.6
MCP Flow Rate, moles/min. x 10^6	9.92	19.8	29.8	39.7
MCH Flow Rate, moles/min. x 10^6	3.32	6.64	9.96	13.28
Pentene-1 Flow Rate, mole/min. x 10^6	3.32	6.64	9.96	13.28
Xylene Flow Rate, mole/min. x 10^6	0.664	1.33	1.99	2.66
n-Octane Concentration, mole %	95.6	85.0	83.0	80.7
MCP Concentration, mole %	3.49	11.7	13.1	14.1
MCH Concentration, mole %	0.822	2.84	3.19	4.17
Pentene-1 Concentration, mole %	0.0581	0.267	0.534	0.774
M-Xylene Concentration, mole %	0.000	0.177	0.226	0.273
Total Current, amp	1.20	1.45	1.50	1.50
Anode Potential, volt	0.550	0.550	0.590	0.580
I_p, Octane-amp	0.320	0.422	0.268	0.267
I_N, MCP-amp	0.479	0.405	0.396	0.326
I_{N2}, MCH-amp	0.198	0.239	0.292	0.217
I_{ol} Pentene-1, amp	0.159	0.306	0.436	0.551
I_A, M-Xylene, amp	0.0449	0.0768	0.108	0.135

As for the case of binary fuels, the unsaturated compounds are virtually entirely depleted from the fuel stream at low fuel flow rates (approximately 10 µl/min.). The breakthrough of these compounds above these flow rates must be a result of competition for surface sites between the various fuel component molecules. However, the concentrations of these compounds are greatly reduced; thus, better than 70% removal of the aromatic compound and better than 80% of the olefin is observed. This fact is extremely significant, since it indicates that the more harmful components are preferentially oxidized resulting in an "exhaust fuel" that is richer in the more desirable components.

The current contributions of the five components under consideration are shown in Figures 12 thru 16. They were obtained by means of the simultaneous solution of five linear equations (2). Unfortunately, the solutions are quite sensitive to relatively small variations in each of the variables. Thus, an experimental error of about 1 to 3% in the chromatographic analysis can cause rather severe distortions in the calculated current contributions of the components for which the errors were made. Furthermore, the assumptions made for the parameter n (number of gm-equivalents/gm-mole) of each species and for the Faradiac efficiency, which was assumed to be 100%, will also influence the results.

These comments are pertinent, in view of the curve discontinuities observed in Figures 12 thru 14. These discontinuities were unexpected, considering the smooth variation of the exhaust composition data with flow rate (Figures 7 thru 9).

On the other hand, the relative reactivity of olefins and aromatics yield results as exhibited in Figures 15 and 16. These results are reminiscent of the binary fuel results and reflect the situation where it was shown that there is not necessarily an additive effect on performance when two or more "refractory" additives are present in a given fuel (1).

It is clear from the above discussion that the current contributions from n-octane, methylcyclopentane, and methylcyclohexane are difficult to calculate. This is not the case, however, for m-xylene and pentene-1. The current contributions for each of these components, at low flow rates, are given by the equations:

$$I_{ol} = 0.963\ nF\ \mu N_{ol} \qquad (8)$$

$$I_{A} = 0.93\ nF\ \mu N_{A} \qquad (9)$$

Equations (8) and (9) are in very good agreement with Equations (2) and (4) which apply to binary fuels. It should be noted that a different aromatic

additive was used in the binary mixture. This is an alternate way of expressing the fact that the electrochemical oxidation of olefins and aromatics at low fuel flow rates appears to proceed independent of the other species present in the fuel.

C. General Considerations

Figure 17 shows that aromatics, olefins, and naphthenes in pure form exhibit considerably poorer polarization characteristics than n-octane when oxidized electrochemically.

The rather unexpected relative reactivities observed in the present work for fuel mixtures is, therefore, probably due to competitive adsorption effects, with the more refractory species achieving high coverages of the active sites and being selectively oxidized. Unfortunately, no electrosorption data are available for the classes of compounds studied to put this discussion on a more quantitative basis.

Discussion

A clearer understanding of the preceding results can be obtained from some fundamental relationships. Consider an anode compartment of thickness t, containing an electrode of area A, as is shown in Figure 18. There is a steady flow, μ, of reactant mixture expressed as moles per unit time. A volume element, dA, is selected so that the concentration of component i is N_i expressed as mole fraction and the concentration leaving is $N_i - dN_i$. The rate of change in the number of moles of component i at a given point in the anode compartment, m_i, can be expressed by the equation:

$$\frac{dm_i}{dt} = \mu dN_i + r_i \, dA \qquad (10)$$

where r_i is the rate of oxidation of component i in the anode compartment expressed as moles of reactant converted per unit area of electrode per unit time, and the remaining symbols have their usual significance.

Considering the anode compartment as a flow reactor at steady-state, Equation (10) simplifies to:

$$r_i \, dA = -\mu dN_i \qquad (11)$$

Considering mainly activation effects and expressing the current density of a component i in terms of the reaction rate, we obtain:

$$i_i = n_i F r_i \qquad (12)$$

Combining Equations (11) and (12) and integrating yields:

$$\int_{o}^{A} dA = -nF\mu \int_{N_o}^{N} \frac{dN}{i} \tag{13}$$

here the subscript i has been eliminated for sake of simplicity and N_o is the mole fraction of the component under consideration at the inlet.

Expressing the current density in terms of the electrochemical kinetics of an activation-limited, anodic, forward reaction

$$\left| \eta_a \right| >> \frac{RT}{nF} ,$$

where η_a is the anodic activation polarization, we can write

$$i = nFN^{\gamma}k \exp\left(\frac{-\Delta G^*}{RT}\right) \exp\left(\frac{-\alpha nFE^o}{RT}\right) \exp\left(\frac{(1-\alpha)nF\eta_a}{RT}\right) \tag{14}$$

where γ is the reaction order, k is a rate constant, ΔG^* is the standard free energy of activation, E^o is the reversible potential, and α is the transfer coefficient. It is recognized that Equation (14) is the correct kinetic expression for the hydrocarbons studies, but for our purposes the following simplified equation can be

$$i = k' N^{\gamma} e^{\beta E} \tag{15}$$

more easily fitted to the experimental data, where k' and β are now constants to be fit to the experimental data. Substituting Equation (15) into Equation (13) yields:

$$\int_{o}^{A} dA = \frac{-nF\mu e^{-\beta E}}{k'} \int_{N_o}^{N} \frac{dN}{N^{\gamma}} \tag{16}$$

where upon integration and rearrangement gives:

$$\frac{k'A(1-\gamma)}{nF\mu} e^{\beta E} = N_o^{(1-\gamma)} - N^{(1-\gamma)} \tag{17}$$

for the case where $\gamma \neq 1$. Since none of the additives studied have a reaction order of unity this case was not considered. The constants in Equation (17) are listed in Table 6 for the additives studied.

Table 6

Constants for Equation (17)

Compound	k', ASF	β	γ
Benzene	0.039	9.3	-0.11
m-xylene	0.17	6.7	-0.11*
Methylcyclohexane	0.029	11.4	
Pentene-1	0.26	9.3	-0.16*
n-octane	0.12	13.1	~0.5

The empirical constants k' and β were determined from the linear portion of curves in Figure 19. The reaction order for benzene was given in a recent study by Bockris et. al. (5) and the values of the orders for m-xylene and pentene-1 were estimated from Bockris's data. The other values for γ were obtained by fitting the binary fuel data to Equation (17). Equation (17) permits the calculation of the exhaust composition of any compound for which the constants are known. It is hoped that the constants for various compounds in a particular class will be sufficiently similar to make Equation (17) general enough to calculate the exhaust composition (and therefore current contribution) of a fuel cell anode at any given set of anode operating conditions.

The fit of the experimental data for the five component fuel to Equation (17) is only fair if the condition:

$$e^{\beta E} \leq \frac{nF\mu N^{(1-\gamma)}}{k' A (1-\gamma)} \qquad (19)$$

is obeyed. The utilization of the components that were believed to be unreactive prior to this investigation can be explained by Equation (18), indicating that the results obtained can be explained from simple fundamental considerations.

Conclusions

1. Under anode operating conditions that present-day direct hydrocarbon fuel cell technology permits, the components of a practical fuel (aromatics, olefins, and to a certain extent naphthenes) can be preferentially oxidized. This is apparently a result of the magnitude of the relative coverage of the active sites with the components in question. The anode effluent becomes enriched in the more desirable paraffin component.

2. The preferential oxidation of the "unreactive" components can be explained by simple kinetic considerations.

The engineering significance of these findings is extremely important since it is now evident that no fuel pretreatment beyond established limits is necessary and that the fuel can be recycled without any harmful side effects.

Acknowledgements

This work is a part of the program under contract DA44-009-AMC-479(T) with the U.S. Army Engineer and Development Laboratories, Ft. Belvoir, Virginia, to develop a technology which facilitates the design and fabrication of practical military fuel cell power plants for operation on ambient air and hydrocarbon fuels.

The authors are grateful for the able assistance of Mr. Lucien Brassard who performed much of the experimental work.

References

1. Technical Summary Report No. 9, Hydrocarbon-Air Fuel Cells, January 1965-June 1966, ARPA Order No. 247, Contract Nos. DA44-009-ENG-4909, DA44-009-AMC-479(T), and DA44-009-ENG-4853, p. 2-107 et. seq.

2. Technical Summary Report No. 10, Hydrocarbon-Air Fuel Cells, July 1966-December 1966, ARPA Order No. 247, Contract Nos. DA44-009-ENG-4909, DA44-009-AMC-479(T), and DA44-009-ENG-4853, p. 4-27 ff.

3. L. W. Niedrach and H.R. Alford, J. Electrochem. Soc., 112, 117 (1965).

4. F.D. Rossini et. al., "Selected Values of Properties of Hydrocarbon", Circular C461 N.B.S. 1947.

5. J.O.M. Bockris, et. al., Trans. Faraday Soc., 61, 515, 1965.

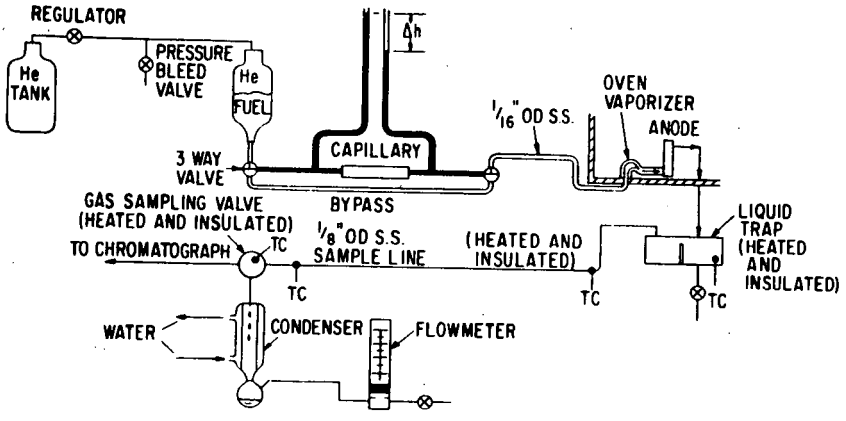

Figure I Fuel Feed and Exhaust for Chromatographic Study of Binary Fuels.

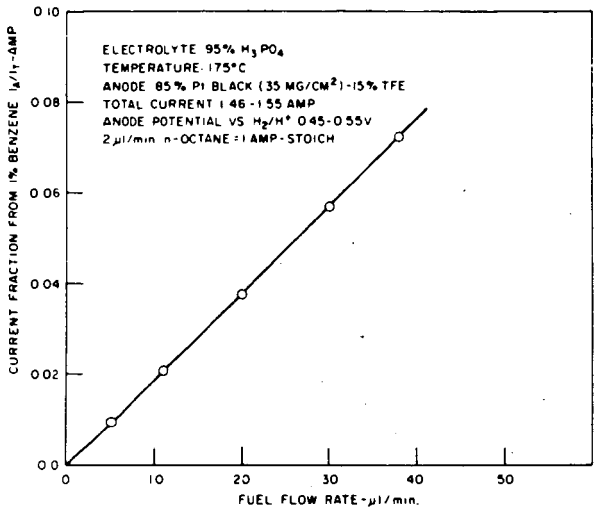

Figure 2. Current Fraction from Benzene vs. Fuel Flow Rate

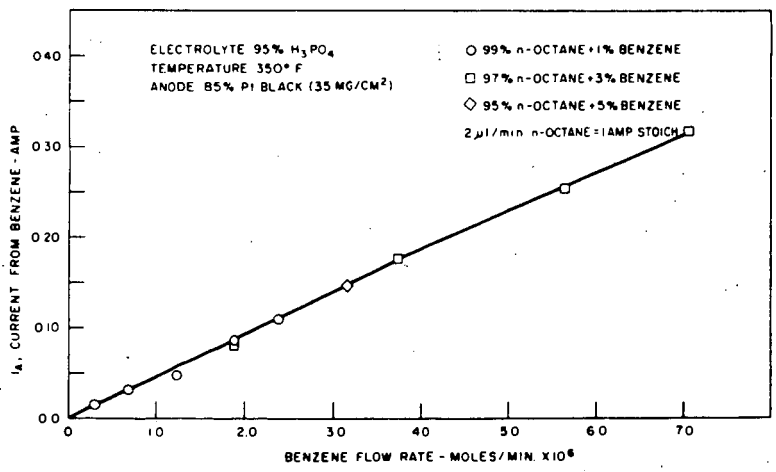

Figure 3 Current from Benzene vs. Benzene Flow Rate for Fuels Containing 1-5 mole % Benzene

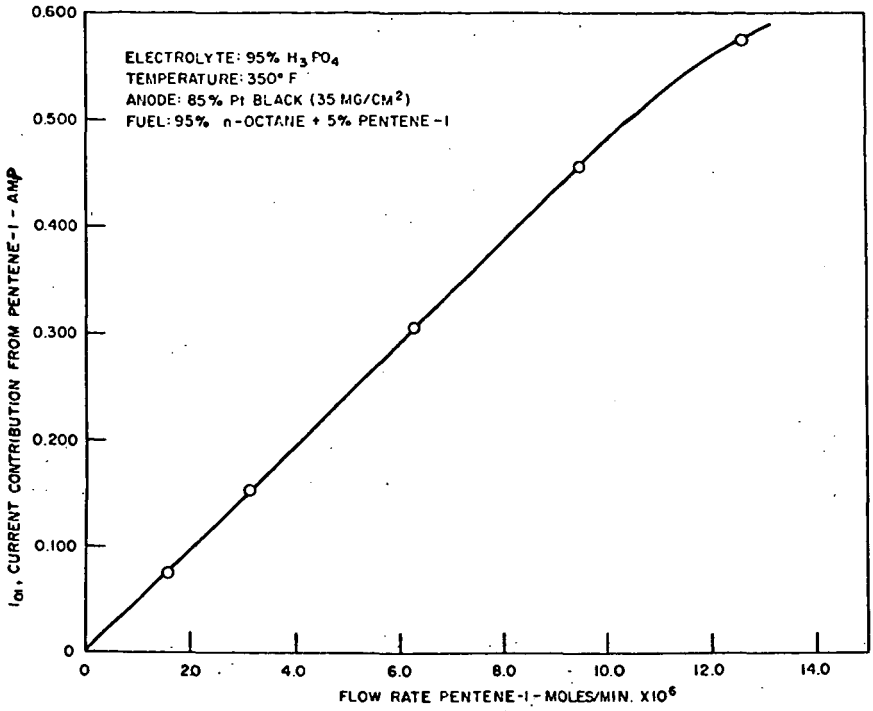

Figure 4 Current Contribution from Pentene-1 vs. Pentene-1 Flow Rate from a Fuel Containing 5 mole % Pentene-1

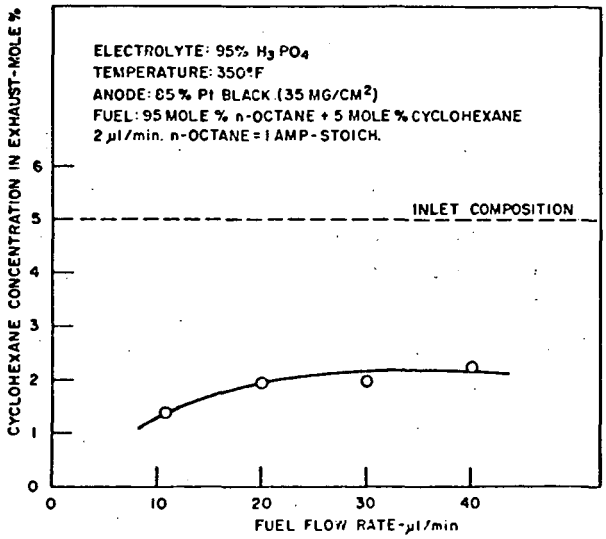

Figure 5 Effect of Liquid Fuel Flow Rate on Cyclohexane Concentration in Exhaust for a Fuel Containing 5 mole % Cyclohexane at Inlet

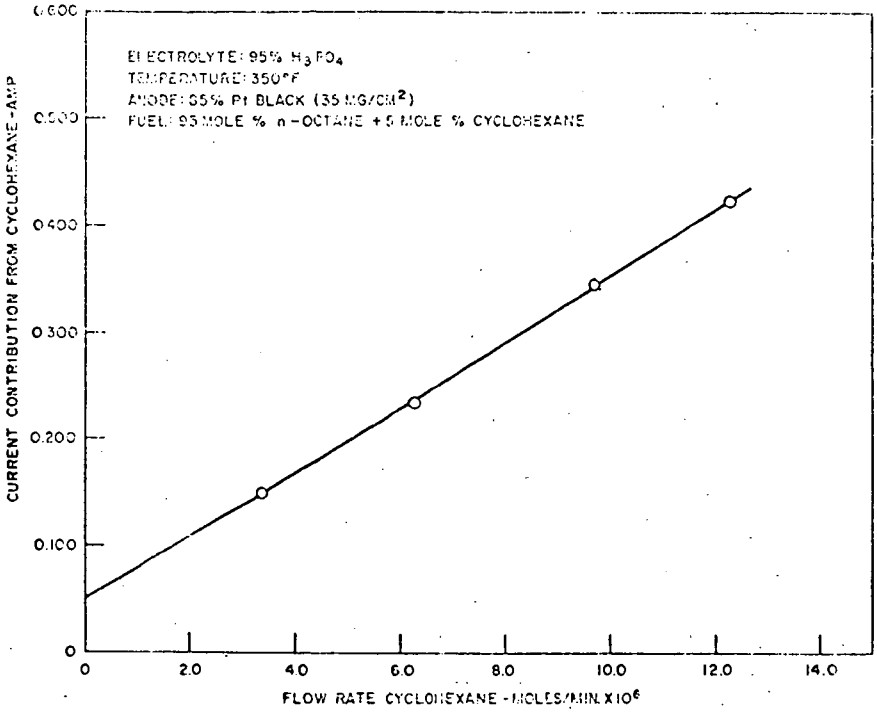

Figure 6 Current Contribution from Cyclohexane vs. Cyclohexane Flow Rate for a Fuel Containing 5 mole % Cyclohexane

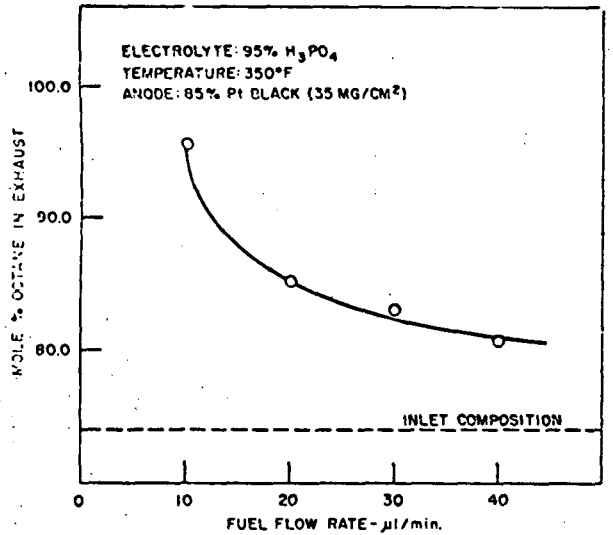

Figure 7 Effect of Liquid Fuel Flow Rate on Octane Concentration in Exhaust for a Fuel Containing 74% n-Octane + 15% Methylcyclopentane + 5% Methylcyclohexane + 5% Pentene-1 + 1% M-Xylene

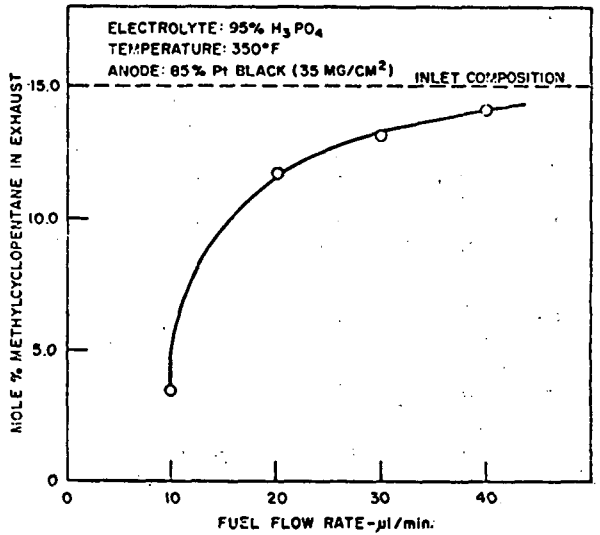

Figure 8 Effect of Liquid Fuel Flow Rate on Methylcyclopentane Concentration in Exhaust for a Fuel Containing 74% n-Octane + 15% Methylcyclopentane + 5% Methylcyclohexane + 5% Pentene-1 + 1% M-Xylene

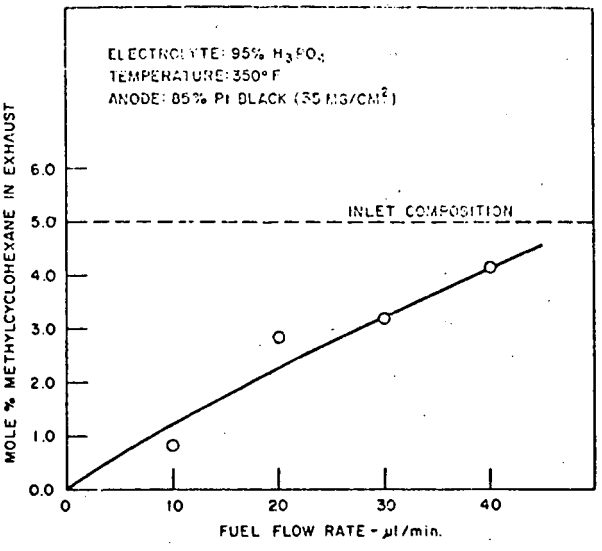

Figure 9 Effect of Liquid Fuel Flow Rate on Methylcyclohexane Concentration in Exhaust for a Fuel Containing 74% n-Octane + 15% Methylcyclopentane + 5% Methylcyclohexane + 5% Pentene-1 + 1% M-Xylene

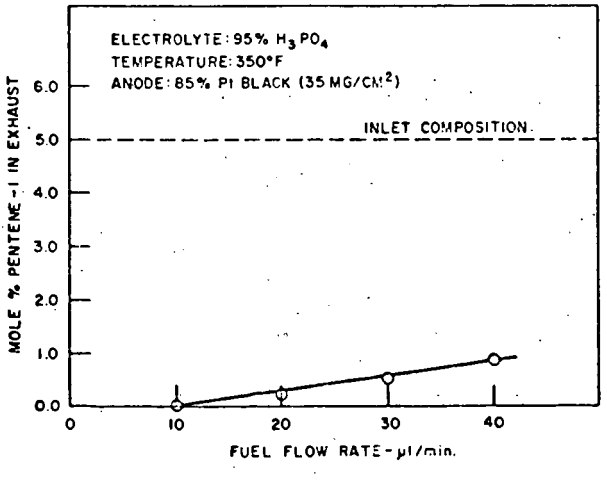

Figure 10 Effect of Liquid Fuel Flow Rate on Pentene-1 Concentration in Exhaust for a Fuel Containing 74% n-Octane + 15% Methylcyclopentane + 5% Methylcyclohexane + 5% Pentene-1 + 1% M-Xylene

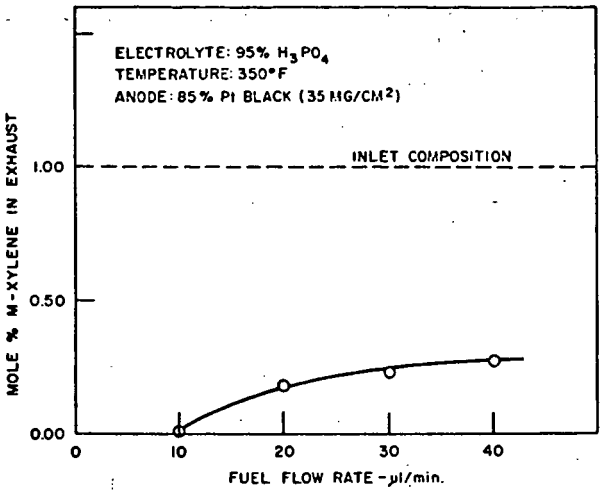

Figure 11 Effect of Liquid Fuel Flow Rate on M-Xylene Concentration in Exhaust for a Fuel Containing 74% n-Octane + 15% Methylcyclopentane + 5% Methylcyclohexane + 5% Pentene-1 + 1% M-Xylene

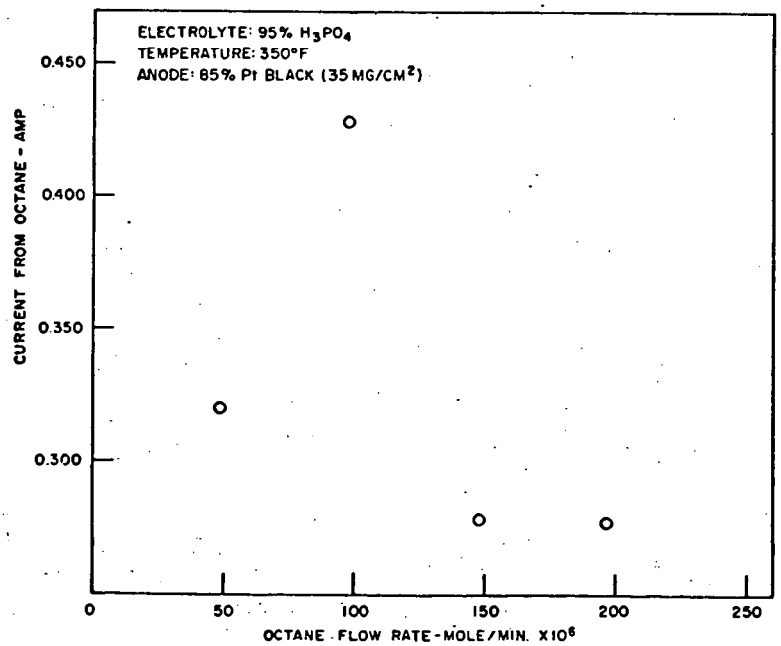

Figure 12 Effect of Octane Flow Rate on Current Contribution from Octane for Fuel Containing 74% n-Octane + 15% Methylcyclopentane + 5% Methylcyclohexane + 5% Pentene-1 + 1% M-Xylene

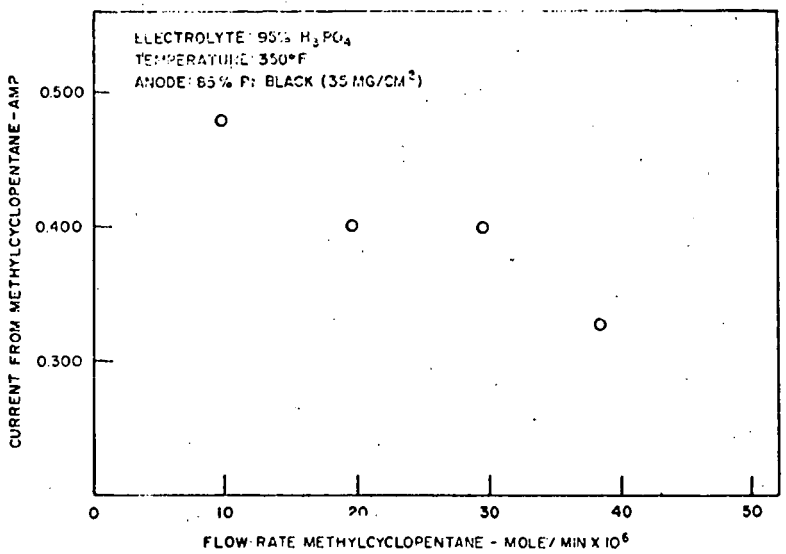

Figure 13 Effect of Methylcyclopentane Flow Rate on Current Contribution from Methylcyclopentane for Fuel Containing 74% n-Octane + 15% Methylcyclopentane + 5% Methylcyclohexane + 5% Pentene-1 + 1% N-Xylene

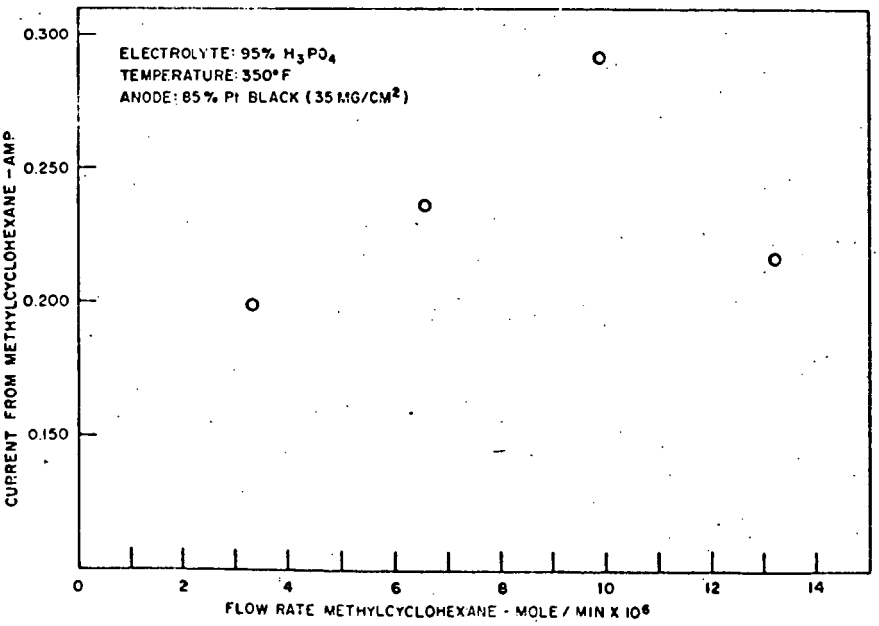

Figure 14 Effect of Methylcyclohexane Flow Rate on Current Contribution from Methylcyclohexane for Fuel Containing 74% n-Octane + 15% Methylcyclopentane + 5% Methylcyclohexane + 5% Pentene-1 + 1% M-Xylene

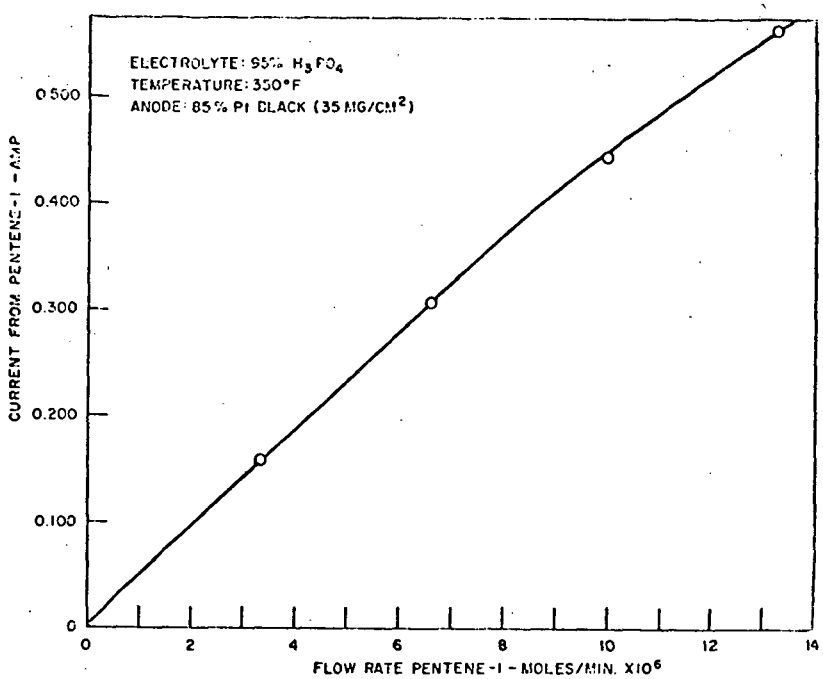

Figure 15 Effect of Pentene-1 Flow Rate on Current Contribution from Pentene-1 for Fuel Containing 74% n-Octane + 15% Methylcyclopentane + 5% Methylcyclohexane + 5% Pentene-1 + 1% M-Xylene

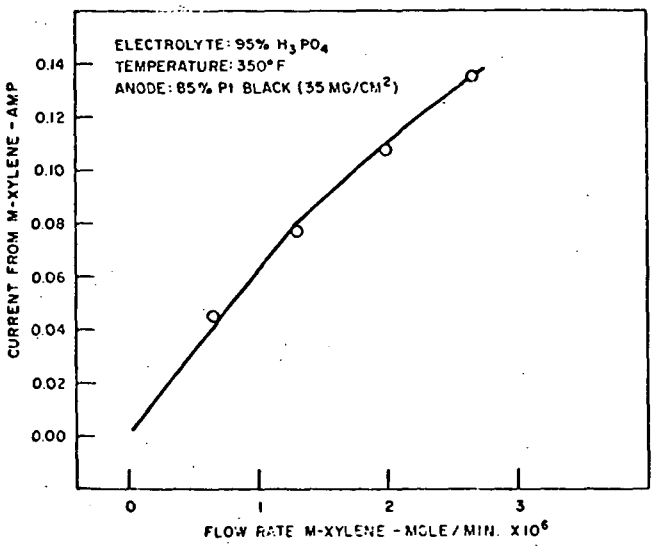

Figure 16 Effect of M-Xylene Flow Rate on Current Contribution from M-Xylene for Fuel Containing 74% n-Octane + 15% Methylcyclopentane + 5% Methylcyclohexane + 5% Pentene-1 + 1% M-Xylene

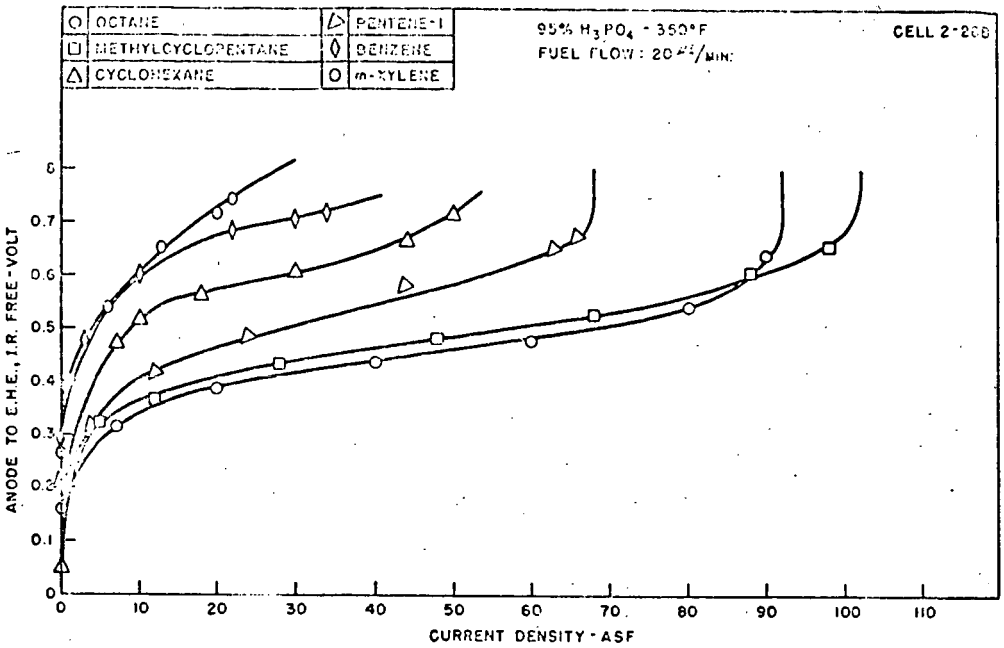

Figure 17 Polarization Curves for n-Octane, Methylcyclopentane, Cyclohexane, Pentene-1, Benzene, and M-Xylene

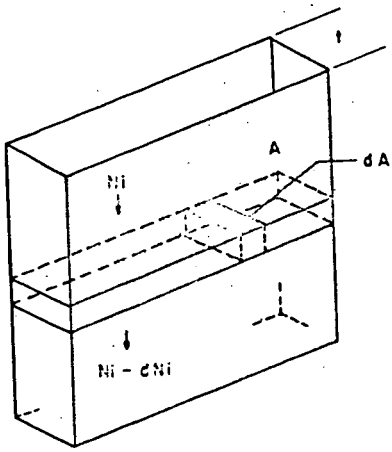

Figure 18 Fuel Cell Anode Compartment

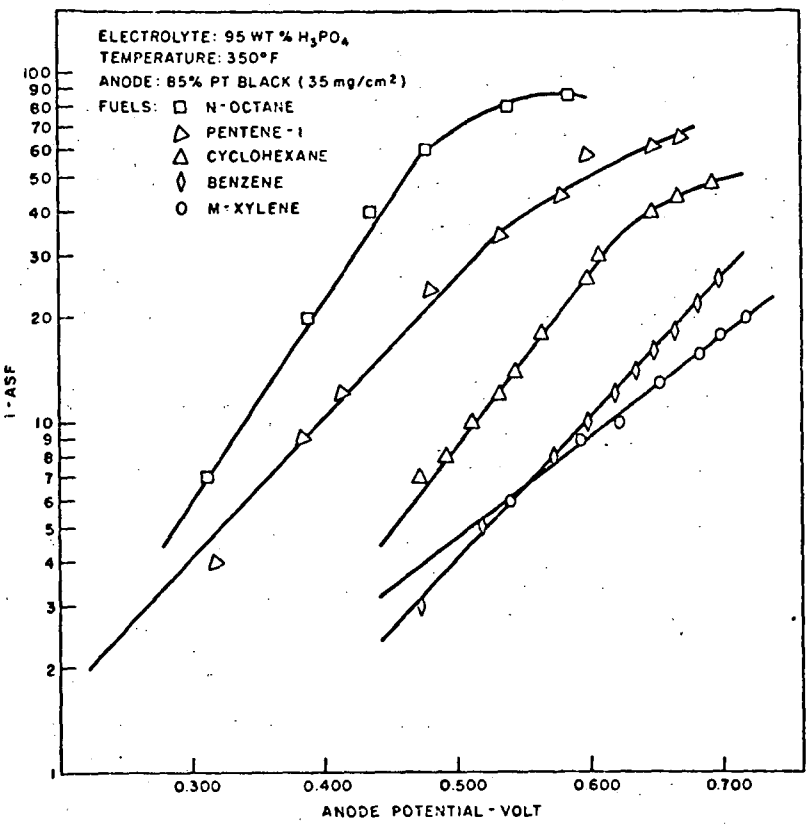

Figure 19 Current Density vs. Anode Potential for n-Octane, Pentene-1, Cyclohexane, Benzene, and M-Xylene

OXIDATION AND ADSORPTION OF HYDROCARBON ON NOBLE METAL ELECTRODES. 6. A discussion of the Mechanism of Saturated Hydrocarbon Oxidation on Pt.

S. B. Brummer

Tyco Laboratories, Inc., Waltham, Massachusetts 02154

ABSTRACT

The mechanism of the anodic oxidation of saturated hydrocarbons on Pt electrodes in strongly acid solutions at elevated temperatures is discussed. Since the coulombic efficiency for CO_2 production is 100% even for complex fuel molecules, the need to examine the adsorption processes in order to obtain mechanistic information is emphasized. From adsorption studies it has been found that three principal types of material accumulate in the steady state adsorbate: these are CH-β (polymeric), CH-α (mixture of alkyl radicals), and O-type (oxygenated C_1 species). The O-type is the predominant species and oxidizes the most readily at high potentials. Its coverage is high below about 0.4 v. This coverage is insensitive to hydrocarbon pressure. This observation, coupled with previous reports that the overall reaction order is unity, prompt the suggestion that O-type is a poison for the overall hydrocarbon-to-CO_2 reaction. However, recent results indicate that in the region of high coverage the overall reaction order is considerably less than unity and even negative at low potentials. This suggests that the slow step of the overall reaction involves a reaction of an adsorbed species (e.g. O-type) at high or limiting coverage. A tentative overall mechanism for the oxidation of hydrocarbons is suggested.

INTRODUCTION

The anodic oxidation of saturated hydrocarbons is required for the economic utilization of the fuel cell principle. Consequently, there has been much interest in this area in the past five years. The earliest reports of saturated hydrocarbon oxidation at low temperatures and interesting rates were by Grubb and Niedrach (1) in 1963. They used extensive amounts of Pt as the anode catalyst and concentrated H_3PO_4 at 150°C as the electrolyte and achieved moderate current densities at reasonable potentials. Since then there has been a large number of studies and it is clear that while many saturated hydrocarbons can be oxidized the kinetics are rather unfavorable. The ultimate utilization of the hydrocarbon anode requires an enhancement of these kinetics, or requires the development of a sufficiently cheap, i.e. non-noble metal, catalyst that the electrode area can be appropriately expanded.

It appears that maximum activity is found for the C_2 - C_4 (2,3) range that straight chain hydrocarbons are better than bridged chains (4) and that Pt is one of the better catalysts that we have (5). In the present work, we have undertaken to investigate the mechanism of anodic hydrocarbon oxidation with a view to elucidating those features, structural, electronic and ionic, which determine the path and the rate of the overall reaction. In the first instance we have studied the adsorption and oxidation of C_3H_8 (6, 7, 8) and n-C_6H_{14} (9) at elevated temperatures using hot concentrated H_3PO_4 and smooth Pt electrodes. While the chemical mechanism has not been fully unravelled at this point, a number of significant features of the reaction path have been revealed and the present paper summarizes the result of our own work and discusses mechanistic conclusions which can be drawn, both from our own work and from that of others.

OVERALL COURSE OF REACTION

It is well known that saturated hydrocarbons are very stable materials and it would be expected that their oxidation would be very difficult, and indeed as mentioned, stringent conditions are required for the reaction to occur at any reasonable rate. By analogy with gas phase reactions and in particular, the heterogeneous catalysis reactions of these compounds, one might expect that the reaction path would be very complicated and as a consequence that there would be a number of products. However, it has been shown that the general reaction

$$C_nH_{(2n+2)} + 2n\,H_2O \rightarrow n\,CO_2 + (6n+2)\,H^+ + (6n+2)\,e^- \qquad (1)$$

occurs to completion with no side products accumulating in the solution or in the gas phase (10, 3, 11).

This 100% faradaic efficiency for the product of CO_2 is remarkable and unexpected and has important mechanistic implications. Thus following the initial adsorption all the intermediate products between the reactant and the final product, CO_2, are adsorbed on the electrode. There is no other way to account for the observations. This suggests that the fruitful way to investigate the reaction mechanism is to study the adsorption processes. This has been the prime approach of our experiments and in conjunction with the work of others, notably Gilman (12) and Niedrach (13-17), it has led to a considerable understanding of the nature of the products formed on the electrode.

NATURE OF ADSORBED PRODUCTS

The methods we have used to examine the adsorbed products involve their determination with anodic stripping and with H-atom deposition. Using these techniques in conjunction with controlled potential adsorption regimes onto a clean electrode, we can define the charge to oxidize the adsorbed species, Q_{ads} and their coverage θ_{org}. From the relationship between Q and θ_{org} we can determine [e] which is the number of electrons released when the adsorbed product is oxidized to CO_2. This is quantitatively of prime importance in discussing the nature of the adsorbed products and their likely relationship to the overall reaction.

We have shown that when C_3H_8 (8) or n-C_6H_{14} (9) are adsorbed, three partially oxidized residues accumulate on the electrode. These residues are of three generic types: the CH-α, the CH-β and the O-type. The CH-α is cathodically desorbable, relatively unreactive towards oxidation and probably comprises a mixture of (partly dehydrogenated) alkyl radicals. Its composition changes with potential. The composition of the CH-β species is also a function of potential. It is unreactive towards both reduction and oxidation and is probably a carbonaceous polymer. The O-type, the major species in terms of coverage, has the same composition at all potentials. It releases $\sim$ 1.3 electrons per covered site on oxidation to CO_2 and this indicates that it is oxygenated. We have found (18) that O-type is electrochemically identical to the reduced CO_2 species of Giner (19), confirming his results (20).

Other workers have also reported evidence for these types of adsorbed product. Niedrach et al (14) following Gilman's (12) suggestion have suggested two distinct paths which the initially adsorbed hydrocarbon can adopt. The first path, the preferred path, involves the production of what we would call O-type. The second path involves the production of what we would call CH-α. The distinction between the types was based on the current waves which appeared during the

linear anodic sweep stripping of the adsorbed layer. The fact that O-type was oxidized more readily under these conditions than CH-α was taken to mean that those reactions leading to O-type were preferable to those leading to CH-α. In support of this view we may note that CH-α plays a greater role with higher hydrocarbons which are less reactive. The implication of this view of course is that the production of O-type and CH-α are parallel reactions.

We found that (8, 9) oxidation kinetics of O-type are faster than those of CH-α and that its coverage is high compared with CH-α. These observations support the view of Niedrach. However, there is a large difficulty. The corrolary of this view would be that at low potentials the oxidation of O-type is the rate limiting step in the overall reaction with a very slow side reaction involving CH-α oxidation in parallel with it. If this were so, we would expect that variations in the rate of O-type oxidation with potential and with hydrocarbon concentration would closely parallel the variation of the rate of the overall reaction. Since it has been reported that the overall reaction for both C_3H_8 (11) and n-C_6H_{14} (21) is first order with respect to fuel pressure, we would expect $\theta_{O\text{-type}}$ to be strongly pressure dependent. However, we found O-type coverage for both C_3H_8 and n-C_6H_{14} to be almost independent of fuel pressure (8, 9). This led us to the view that the reaction occurs via a general mechanism which was recently proposed (22), i.e.

$$\text{Hydrocarbon} \longrightarrow \text{reduced } CO_2 \ (\theta_{\text{poisoning}}) \quad (2)$$

$$\text{Hydrocarbon} \xrightarrow{(1-\theta_p)} CO_2 \ . \quad (3)$$

In this mechanism the overall reaction occurs on that part of the electrode which is not occupied by adsorbed species, or at least is not occupied by the poisoning adsorbed species. It was suggested that reduced CO_2, i.e. O-type, was the worst kind of poisoning species since being a C_1 species it very likely consumed just those C_1 reactive radicals which maintain the rate of the overall reaction. This view is in sharp contrast to that of Niedrach et al and suggests that those reactions which lead to the production of O-type are undesirable.

Since some adsorbed species must be controlling the rate of the overall reaction, we suggested the possibility that the CH-α species comprises several parts (8, 9). Some of these parts, following Niedrach et al (14) are undesirable but some of them, the CH-α_{active}, were desired to promote the overall reaction.

REACTION ORDER

As indicated, a central point in the divergence of our view from that proposed by Niedrach et al is the reaction order. In an early study we reported that the reaction order on smooth Pt is positive (23). Recently it has been reported (11, 21) that on platinized Pt the reaction order for C_3H_8 and n-C_6H_{14} is accurately unity. These experiments, on platinized Pt, were the reasons for our adopting the views expressed above.

We have, however, reexamined the reaction using platinized Pt and two important points have emerged.

Firstly, we have found that coverage with O-type, is much more dependent on fuel concentration than it is on smooth Pt. For example, at 0.35 v on smooth Pt at 130°C the O-type concentration does not change when the C_3H_8 pressure in-

creases from 2.2 mm to 223 mm (8). Similar insensitivity is found with $n\text{-}C_6H_{14}$ (9). On platinized Pt, however, the concentration of O-type increases by from 0 to ~ 250 μcoul/r.cm^2 for C_3H_8 under the same conditions (24). These observations prompted us to examine the order of the reaction.

This second and crucial finding was that at low potentials, e.g. below 0.35 v, the reaction order is not unity. In fact, we find a small negative order for the overall reaction rate (24) and this is precisely the kind of complication which would be expected if the reaction were coming under extensive adsorption control at relative high coverage. There is little experimental conflict between our results and those reported by Gileadi et al (11) since most of their studies refer to the potential region above 0.35 v where the coverage with adsorbed materials becomes very low.

RELATION OF ADSORBED PRODUCTS TO OVERALL REACTION

These observations show that there is still a sharp disagreement between the orders of the overall reaction and of O-type coverage. However the results are more ambiguous than was previously thought (8). The unity order for the overall reaction reported by Gileadi, Stoner and Bockris for C_3H_8 oxidation (11) implies a relatively simple mechanism. Specifically, the reaction could not proceed via O-type since the coverage with O-type was thought to be high and virtually independent of C_3H_8-pressure (8). For this reason, we postulated that the reaction proceeded on the part of the surface not occupied by O-type, a similar poisoning mechanism to HCOOH oxidation (22, 25). The negative reaction order we have observed in conjunction with the increase in O-type coverage with pressure on platinized Pt (24), could certainly be interpreted in terms of such a poisoning mechanism (reactions (2) and (3)). However, these results on the overall order show that at low potentials the reaction could proceed via an adsorbed species present at high coverage, e.g. O-type.

Consideration of such a mechanism allows an alternative interpretation of the data. Thus we note that coverage with CH-α has an even stronger dependence on C_3H_8 pressure than has O-type for smooth (8) and for platinized Pt (24). If the oxidation of O-type involved a "reactant pair" mechanism, involving the adsorbate itself and free sites, as postulated by Gilman for CO_{ads} (26), CH-α could act as a poison for the reaction due to its occupation of surface. Since CH-α is so pressure dependent, we can entertain this mechanism as an explanation of the above conflict in reaction order whilst still asserting that the main reaction proceeds via O-type. We have found an increase in the rate of O-type oxidation in circumstances where we deliberately desorb CH-α (24) and this supports such a mechanism.

These observations allow possibly the maintainance of the views expressed by Niedrach et al concerning the role of O-type. A third observation with platinized Pt electrodes leads to further elaboration of the mechanism. We have investigated the oxidation kinetics of the adsorbed species on platinized Pt in presence of C_3H_8 with anodic chronopotentiograms. These were taken at sufficiently low current densities that the adsorbate oxidation occurs well before the electrode's oxidation but at sufficiently high current densities that insignificant solution C_3H_8 is oxidized. Two predominant features are observed, a prewave and a more extensive potential plateau (24). The behavior of the plateau leaves no doubt that it corresponds to the oxidation of O-type material, i.e. reduced CO_2. The oxidation rate corresponding to the plateau is about 40-50% of the overall reaction rate of the hydrocarbon. This is a reasonable value if O-type lies between C_3H_8 and CO_2 and indeed strongly suggests this conclusion.

The prewave is associated with adsorbed material on the electrode other than O-type, presumably CH-α. At low currents, the prewave is found at lower potentials than O-type but at high oxidation rates it merges into the O-type wave. Eventually, both processes are displaced to the region of electrode oxidation. The crucial point is that whereas at high potentials (e.g. in our "anodic desorption" experiments (8, 9) or in fast linear sweeps (12, 14)) CH-α will oxidize less easily than O-type, it oxidizes more readily at low potentials. The relative oxidation rates at low potentials are what are significant for the operation of the hydrocarbon anode. Hence we can no longer assert that formation of CH-α is necessarily undesirable. Similarly, our previous conclusion (8, 9) that CH-α production is parallel to O-type production can no longer be maintained.

There is no reason to suppose that the reaction sequence

$$C_3H_8 \rightarrow \text{CH-}\alpha \ , \tag{4}$$

$$\text{CH-}\alpha \rightarrow \text{O-type} \ , \tag{5}$$

$$\text{O-type} \rightarrow CO_2 \ , \tag{6}$$

does not occur.

If this is so, the oxidation of O-type must be rate-limiting at least as far up the homologous series as n-C_6H_{14}. This is because O-type's coverage is so high. An additional complication may also arise from the above-mentioned poisoning of O-type oxidation by CH-α occupying the surface. As the homologous series is ascended, CH-α coverage increases and at some stage it is clear that its reaction, reaction (5), becomes rate limiting.

From the coulometry of the adsorbed species, we have suggested the following numbers of electrons in these various reactions (24):

$$C_3H_8 \xrightarrow{6-7} \text{CH-}\alpha \xrightarrow{3-6} \text{O-type} \xrightarrow{8-10} 3\,CO_2 \ . \tag{7}$$

Confirmation of this reaction mechanism is required and, in particular, the chemical structures of the intermediates are the aim of our further work.

ACKNOWLEDGEMENTS

It is a pleasure to thank Mrs. M. J. Turner who carried out the experiments whose results are described above. This work is supported by the U. S. Army Engineer Research and Development Laboratories, Fort Belvoir, Virginia, on Contract DA 44-009-AMC-1408(T).

REFERENCES

(1) W. T. Grubb and L. W. Niedrach, J. Electrochem. Soc., 110, 1086 (1963).
(2) Report by General Electric Co. to U. S. A. E. R. D. L. on Contract DA 44-009-ENG-4909 dated Dec. 31, 1963.
(3) H. Binder, A. Köhling, H. Krupp, K. Richter and G. Sandstede, J. Electrochem. Soc., 111, 1015 (1964).
(4) W. T. Grubb and C. J. Michalske, "Proceedings 18th Power Sources Conference" (1964) p. 7.
(5) W. T. Grubb, J. Electrochem. Soc., 113, 191 (1966).
(6) S. B. Brummer, J. I. Ford and M. J. Turner, J. Phys. Chem., 69, 3434 (1965).
(7) S. B. Brummer and M. J. Turner, "Hydrocarbon Fuel Cell Technology" (Ed. by B. S. Baker, Academic Press, New York, N. Y., 1965), p. 409.
(8) S. B. Brummer and M. J. Turner, "CH-type and O-type Intermediates During the Oxidative Adsorption of C_3H_8 on Pt", J. Phys. Chem., 71, 0000 (1967).
(9) S. B. Brummer and M. J. Turner, "n-Hexane Adsorption on Smooth Pt at 130°C", J. Phys. Chem., 71, 0000 (1967).
(10) W. T. Grubb and C. J. Michalske, J. Electrochem. Soc., 111, 1015 (1964).
(11) Report by E. Gileadi, G. Stoner and J. O'M. Bockris (Univ. of Pennsylvania) to U. S. A. E. R. D. L. on Contract DA 44-009-AMC-469(T), April 1966, AD 632 319.
(12) S. Gilman, Trans. Faraday Soc., 61, 2546, 2561 (1965).
(13) L. W. Niedrach, J. Electrochem. Soc., 111, 1309 (1964).
(14) L. W. Niedrach, S. Gilman and I. Weinstock, J. Electrochem. Soc., 112, 1161 (1965).
(15) L. W. Niedrach, "Hydrocarbon Fuel Cell Technology" (Ed. by B. S. Baker, Academic Press, New York, N. Y., 1965), p. 377.
(16) L. W. Niedrach, J. Electrochem. Soc., 113, 645 (1966).
(17) L. W. Niedrach and M. Tochner, J. Electrochem. Soc., 114, 17 (1967).
(18) S. B. Brummer and M. J. Turner, "Relation of Reduced CO_2 to Adsorbed Hydrocarbons", J. Phys. Chem., 71, 0000 (1967).
(19) J. Giner, Electrochimica Acta, 8, 857 (1963).
(20) J. Giner, Paper presented at 15th C. I. T. C. E. Meeting, London (1964).
(21) Report by G. Stoner and J. O'M. Bockris (Univ. of Pennsylvania) to U. S. A. E. R. D. L. on Contract DA 44-009-AMC-469(T), Oct. 1966.
(22) S. B. Brummer, J. Electrochem. Soc., 113, 1041 (1966).
(23) Report by Tyco Laboratories to U. S. A. E. R. D. L. on Contract DA 44-009-AMC-410(T), Nov. 1964.
(24) Report by Tyco Laboratories to U. S. A. E. R. D. L. on Contract DA 44-009-AMC-1408(T), June 1967.
(25) S. B. Brummer and A. C. Makrides, J. Phys. Chem., 68, 1448 (1964).
(26) S. Gilman, J. Phys. Chem., 67, 1878 (1963); 68, 70 (1964).

STUDY OF THE EFFECT OF ELECTROLYTE ON ELECTROCHEMICAL HYDROCARBON OXIDATION

Arthur A. Pilla, John A. Christopulos, and Gabriel J. DiMasi

Power Sources Division, Electronic Components Laboratory
USAECOM, Fort Monmouth, New Jersey

ABSTRACT

The influence of the electrolyte upon the kinetics of the electrochemical oxidation of hydrocarbons is discussed in terms of reactant gas solubility and the general interaction of the electrolyte with the electrode. It is shown, through the use of the voltage sweep technique, that electrolytes normally employed in these studies are relatively active. Thus the current response to a voltage sweep, both in the presence and absence of active species, evolves in such a way as to indicate that adsorption competition occurs between the reactant gas and the electrolyte. This renders the adsorption process involved in hydrocarbon oxidation more complex than previously considered. A preliminary indication of this is the decrease of peak hydrogen currents with a respective increase in the oxidation current of the competing species. This phenomenon is discussed in terms of the proposed mechanisms involving dehydrogenation of the hydrocarbon with subsequent H adsorption. A comparison of the behaviors of H_2SO_4, H_3PO_4 and CF_3COOH in the presence and absence of gaseous hydrocarbons is given. The different rates of hydrocarbon adsorption indicate the degree of influence which the electrolyte has upon hydrocarbon oxidation.

SOLUBILITY OF GASES IN MOLTEN CARBONATE BEHAVIOR OF SILVER-AIR CATHODES IN CORRESPONDING FUEL CELLS

G.H.J. Broers and M. Schenke

Central Technical Institute T.N.O., The Hague, Netherlands *

ABSTRACT

The solubility of oxygen in three different carbonate melts was determined by means of an amperometric titration method. At 700°C, the order of magnitude is $4 \cdot 10^{-7}$ moles/atm.ml melt. The dissolution is endothermic and dependent on cation environment. On basis of the oxygen data the solubilities of both H_2 and CO at 700°C could be estimated from limiting diffusion currents at a rotating Pt electrode: $9 \cdot 10^{-7}$ and $8 \cdot 10^{-7}$ moles/atm.ml melt respectively. A strightforward analytical method to check the above results is in progress.

Silver metal and copper (II) oxide, being suitable cathode materials in fused carbonate fuel cells, tend to dissolve in the melt. The solubility of Ag^+ ions was determined in various eutectic alkali carbonate mixtures. There is a marked influence of the cation environment. In absence of K^+ ions (Li-Na melts) the temperature coefficients of the solubilities have "anomalous" (positive) values; in K^+ -rich melts a more normal behavior is found (greater solubility and negative temperature coefficients).

The solubility of copper (II) ions in $LiNaCO_3$ has been determined also. Here the results are completely anomalous and, in contrast to Ag ions, strongly point to complex formation; possibly CuO_2^{2-} ions. The effect upon cathodic operation of fuel cells (corrosion phenomena) is pointed out briefly.

---

* Correspondence on this subject to the laboratory address: 198, Hoogte Kadijk, Amsterdam-C, Netherlands.

SINGLE GAS ELECTRODES IN MOLTEN CARBONATES

Alina Borucka

Institute of Gas Technology
3424 South State Street
Chicago, Illinois 60616

ABSTRACT

The principles and the experimental requirements underlying accurate use of single gas electrodes as the reference electrodes in fuel cell studies are discussed in relation to typical geometric difficulties. In the case of the molten carbonate fuel cells, the most compatible gas electrodes for this purpose are the O_2/CO_2 and the CO/CO_2 electrodes supported by noble metals. The experimental study of these electrodes over the whole range of gas compositions and temperatures up to 800°C shows that their equilibrium potentials are determined respectively by the following overall reactions: $\frac{1}{2} O_2 + CO_2 + 2\bar{e} \rightleftharpoons CO_3^{=}$ and $CO + CO_3^{=} \rightleftharpoons 2CO_2 + 2\bar{e}$. Both these electrodes obey their respective Nernst equations accurately, but only the CO/CO_2 electrode provides a convenient standard potential scale based in $E_{CO/CO_2} = 0$ when $P_{CO} = P^2_{CO_2}$. The individual characteristics of these electrodes are presented graphically and discussed in relation to their practical limitations as well as their use as the reference electrodes in molten carbonate fuel cells. The results of an experimental correlation study between the O_2/CO_2 and the CO/CO_2 electrodes are compared with the thermodynamic predictions, and the potential of the O_2/CO_2 electrode is located on the standard CO/CO_2 potential scale for molten carbonate electrolytes.

ELECTROLYTE INTERACTIONS IN MOLTEN CARBONATE FUEL CELLS

Isaac Trachtenberg and David F. Cole

Texas Instruments Incorporated, Dallas, Texas

Performance data have been presented for a variety of fuel cells employing mixtures of molten alkali carbonates as electrolyte (1-6). Depending on the particular cell design chosen, the operating conditions, age of cell and a number of other parameters, almost any kind of operating characteristics (current-voltage relationships) desired can be obtained. Various investigators have emphasized certain operating characteristics; in fact, the entire experiment, cell design and operating conditions are optimized to maximize one of several parameters. Emphasis has been, for the most part, on power output per unit area of electrode and operating life. Efficiency, power output per unit weight and volume, and other fuel cell and system characteristics have received only moderate attention. However, at the present state of development it is obvious that the particular set of fuel cell system characteristics chosen will be very greatly influenced by the application. Rather than adding more fuel to the fire, this communication will emphasize certain interactions of the electrolyte which to some extent will be applicable to all molten carbonate fuel cell systems, regardless of their design and application.

There are many electrolyte interactions in a fuel cell containing molten alkali carbonates. The following text will discuss some aspects of three of these interactions: electrolyte stability in some of the gas atmospheres encountered in operating fuel cells, corrosion of silver electrodes as a function of atmosphere and electrolyte composition, and the effect of atmospheres and electrolyte composition on cathode polarization.

Electrolyte Stability

A material suitable for use as an electrolyte in a fuel cell should be chemically stable to the electrodes and atmospheric environments it will encounter during the operating life of the cell. In fuel cells employing molten alkali carbonate electrolytes CO_2 is added to the various gas streams to insure this stability. However, if insufficient CO_2 (7) is added, it is possible under certain operating conditions to obtain a condition at the cathode-electrolyte interface in which no CO_2 is present. The effects of various gas atmospheres on the stability of molten $LiNaCO_3$ were investigated.

Samples of 50-50 mole % Li_2CO_3-Na_2CO_3 were exposed to various gas atmospheres at 650°C for extended time intervals, and the composition was determined by standard analytical techniques. In an atmosphere of 20% CO_2 - 80% air, tests ranging from 246 hours to 1615 hours duration indicated no decomposition of $LiNaCO_3$ or change in Li/Na ratio. Similar tests in 50% H_2 - 50% CO_2 for 408 hours and in 8% H_2O - 12% CO_2 - 10% O_2 - 70% N_2 for 384 hours produced no change in electrolyte composition. However, when CO_2 was not added to the air, some decomposition in the electrolyte could be detected. Data in Table I illustrate the effect of no CO_2 added to the air. The decomposition is indicated by the rise in OH^- content. Because of the analytical techniques employed both $O^=$ and OH^- present in the melt will be reported only as OH^-. There is no significant change in the Li/Na ratio. The OH^- concentration appears to remain constant after 48 hours, which indicates an equilibrium hydroxide (oxide) concentration has been established. The 0.03% CO_2 present in air may have been sufficient to prevent further decomposition.

Date for a second gas composition are also presented in Table I. The gas composition of 10% H_2O, 10% O_2 and 80% N_2 was obtained by burning a mixture of 9.5% H_2 in 76% air and 14.5% N_2. Although there is no significant change in Li/Na ratio, there is significant decomposition of the electrolyte, as illustrated by both the decrease in % $CO_3^=$ and the increase in % OH^-. The CO_2 content is slightly more than 3/4 of what it was in the previous experiment and can account for only a small part of the difference observed for the two gas compositions. Water removes $O^=$ in the form of OH^- and promotes further decomposition of the carbonates. Here again, the equilibrium condition appears to be established after 21 hours, and further exposure to this gas composition produces no additional decomposition.

As pointed out by Stepanov and Trunov (7), a low ratio of CO_2/O_2 (<2.35), particularly in a cathode gas mixture containing a large amount of inert gas, results in depletion of CO_2 at the electrode-electrolyte interface and a change in electrode mechanism. This effect is further complicated by decomposition of the electrolyte, particularly if appreciable amounts of H_2O are present.

Evaporation of $LiNaCO_3$ was investigated using a radiochemical technique with C^{14} labeled $LiNaCO_3$. A sample containing C^{14} labeled $LiNaCO_3$ was placed in an Al_2O_3 boat in a tube furnace and heated to 700°C with a mixture of 23% CO_2 - 77% O_2 flowing over the free electrolyte. The experiment was started at the time the CO_2 - O_2 mixture was replaced by pure N_2. The effluent gas from the furnace was passed through a bubbler containing $Ba(OH)_2$. The $BaCO_3$ precipitate was then beta-counted at infinite thickness. The results of this experiment are shown in Figure 1. Apparently, two processes result in $C^{14}O_2$ in gas phase. The first process appears to fall off rapidly (an order of magnitude change in one hour) and is essentially complete in about six hours. The second process, which is much slower, shows only a slight decrease with time up to 250 hours. The first process (fast) is believed to be the decomposition of $LiNaCO_3$ into LiNaO and CO_2. The second process (slow) is believed to be the evaporation of $LiNaCO_3$. This slow process has an approximate rate of 10^{-5} mole of CO_2 per mole of N_2 passed. Broers (1) reported that in an operating fuel cell containing Li, Na and K carbonates evaporation losses were about 10^{-5} mole of $CO_3^=$ per mole of fuel, air and CO_2 passed over the electrolyte.

Evaporation losses were also determined by very careful weight loss measurement. A sample of 30% $LiNaCO_3$ - 70% fused MgO was mixed in an Al_2O_3 boat and placed in a tube furnace at 700°C. A gas mixture of 5% O_2, 12% CO_2, 83% N_2 was passed over the electrolyte mixture. Three separate runs of 123, 113 and 117 hours were made. The total gas flow was 3.2 moles/hr for the first two runs and 3.5 moles/hr for the third run. The average weight loss for the three runs was 6×10^{-5} gram/mole of effluent $\pm$ 3×10^{-5} gram/mole of effluent. Two runs of 117 and 161 hours were made using pure N_2 at 2.0 and 2.1 moles/hr. The average weight loss was 4.9×10^{-4} gram/mole of effluent $\pm$ 0.9×10^{-4} gram/mole of effluent. The sample was then re-exposed to the first gas mixture containing CO_2 for 17 hours. The weight of the sample increased by an amount that was 68% of the weight lost during the N_2 runs. This is equivalent to 7.5×10^{-6} mole of CO_2/mole of gas effluent, assuming that this portion of the weight loss can be attributed to electrolyte decomposition. The net evaporation loss during the N_2 runs is 1.6×10^{-4} gram/mole of gas effluent. If the latter weight loss is assumed to be $LiNaCO_3$, this represents an additional CO_2 loss of 2×10^{-6} mole/mole of effluent gas. The total loss of CO_2 during the N_2 runs thus became 0.95×10^{-5} mole/mole of N_2, which agrees very well with the 1×10^{-5} mole/mole of N_2 found by the radiochemical technique.

The rate of evaporation loss appears to be higher in the absence of CO_2 in the gas phase (1.6×10^{-4} vs 0.6×10^{-4} gram/mole of N_2). However, both values have considerable uncertainty, and the difference may not be significant.

These studies indicate that electrolyte stability (decomposition and/or evaporation) may well become a problem in long-lived molten carbonate fuel cells. Further, they point up the requirement for sufficient CO_2 in contact with the electrolyte, particularly in the cathode gas where relatively large amounts of inerts will be present if air is used as the O_2 source. The suggestion of Stepanov and Trunov (7) that the CO_2/O_2 ratio be about 2.35 should be seriously considered by molten carbonate fuel cell system designers.

Silver Corrosion

The corrosion of silver in molten carbonates has been studied by several groups (10, 11, 12) and observed qualitatively by many others, but the conditions employed in the experiments have not been representative of the operation of a molten carbonate fuel cell except for those reported by Broers (8).

The results presented here were obtained by weight loss measurements. The samples used were 20 gauge silver wire, 5.1 sq cm in geometric surface area. The samples were immersed completely and to a uniform depth in either 50% Li_2CO_3 - 50% Na_2CO_3 or 37% Li_2CO_3 - 39% Na_2CO_3 - 24% K_2CO_3 contained in an 80% Au - 20% Pd crucible of 250 cc capacity. Atmospheric composition was maintained at 90% N_2 - 10% CO_2 until the desired operating temperature was reached and thereafter was maintained at the desired composition as determined by Orsat analyses. The most extensive experiments have been performed in an atmosphere (5% O_2 - 10% CO_2 - 85% N_2) believed likely to be typical of operating conditions in molten carbonate fuel cell systems using air and spent fuel in the cathode gas supply. (In operating fuel cell systems about 10% of N_2 will be replaced by H_2O.)

Visual examination of the weight loss samples after completion of the experiments indicated apparently uniform attack with no dendritic growths from reprecipitation of dissolved silver.

Table II lists the results of experiments under a variety of atmospheric conditions in binary melts. Weight loss was negligible in the pure CO_2 atmosphere at 600°C. Where oxygen was present, the rate of weight loss increased with increasing partial pressure of oxygen.

Table III shows the constancy with time of the weight loss of the silver samples in both ternary and binary carbonate melts under the conditions shown.

There is no significant difference in rates in the binary and ternary mixtures. Accordingly, the rate-limiting process is apparently not the diffusion of dissolved oxygen to the metal surface but rather a process such as diffusion of silver ions away from the dissolution sites.

Diagrams analagous to those of Pourbaix have been constructed by Ingram and Janz (13) to show the thermodynamic positions of metals in ternary molten carbonate eutectic with respect to corrosion as a function of O_2 and CO_2 partial pressures. These gases determine the $O_2/O^=$ redox potential in the melt.

There are important factors which would tend to make the corrosion of silver in operating molten carbonate fuel cells less severe than in these experiments. These factors include cathodic polarization of the silver electrode when the cell is subjected to current loading, immobilization of the electrolyte by the matrix and the limited amount of electrolyte available in the cell.

Cathode Polarization and Melt Composition

The solubility of oxygen in molten alkali carbonate mixtures has recently been shown by Broers to be dependent on the melt composition (8).

Oxygen was found to be more soluble in ternary (Li, Na, K) than in binary (Li, Na) mixtures. This seems ample reason to suspect that polarization of the molten carbonate fuel cell cathode (an oxygen - carbon dioxide electrode) is also dependent on melt composition. This has been observed experimentally.

Presented here are the results of a series of experiments in which the IR-free polarization of silver cathodes has been determined in melts of two compositions, 50%* Li_2CO_3 - 50% Na_2CO_3 and 37% Li_2CO_3 - 39% Na_2CO_3 - 24% K_2CO_3. Temperature was varied from 600 to 780°C. Partial pressures of CO_2 and O_2 were fixed so that CO_2/O_2 was about 2-2.5 and were determined by Orsat analysis. These experiments were performed in operating fuel cells of a design which has been previously described (2). The silver cathodes were 1 in. x 4 in. and were constructed of 120 mesh twill weave screen with 3.7 mil wire diameter. The resistance measurements for the IR corrections to the polarization were made by a current interruption technique which has also been described previously (8). Voltages were measured with respect to either a Danner-Rey Ag/Ag^+ reference electrode or a Ag-wire idling oxygen electrode. Reproducibility of voltages was quite satisfactory in both cases.

Figures 2 and 3 show the effects of temperature on the cathode polarization in binary and ternary electrolyte, respectively, at a fixed gas composition of 15% O_2 and 30% CO_2 (55% N_2). Figure 4 combines some of the data of Figures 2 and 3 for easier comparison. Figure 5 presents data exhibiting the effect of gas composition on cathode polarization in the two carbonate mixtures at a fixed temperature (700°C). It should be noted that the data at higher oxygen concentration (in the gas phase) were more reproducible, partly because of the greater ease of measuring and maintaining constant the gas composition.

What is the cause of this electrolyte composition effect? The structure and properties of molten alkali carbonates and other ionic liquids are known to depend on the particular alkali metal ions present (14). As the size of the alkali metal ion increases, the volume expansion of the carbonate on melting increases. Most of this volume expansion is accounted for by introduction of "holes" into the melt structure. The smaller cations have a greater tendence to become involved in formation of ion-pairs, but the larger ions are more effective in stabilizing other complex ions which may be formed.

Janz (15) reported that experimentally determined conductances, surface tensions and densities are much nearer the values computed by simple additivity relationships in the case of a Li_2CO_3 - Na_2CO_3 mixture than in that of a Li_2CO_3 - Na_2CO_3 - K_2CO_3 or a Li_2CO_3 - K_2CO_3 mixture.

The heat of solution of oxygen, like the activation energies for viscosity and conductance (16), is higher for the ternary than for the binary (Li-Na) mixture. All these properties seem related to the degree of dissimilarity of the cations. Most attempts (17) at explanation of this behavior have been in terms of competition of the cations for certain orientations with respect to the carbonate ion, the larger cations orienting so as to allow more freedom of rotation for the anion.

---

* mole %

Improvements in cathode polarization in molten carbonate fuel cells utilizing ternary electrolyte are not, unfortunately, directly reflected in greater power densities than those of cells using binary electrolyte. Anode polarization in the ternary electrolyte cells is poorer than that in the binary electrolyte cells, so power densities do not differ significantly. However, the electrolytic composition might be chosen so as to improve power output if there is a considerably more severe polarization of one electrode in a cell than of its counterpart.

Anode polarization behavior may be clarified by determinations of hydrogen solubility in the melts.

SUMMARY

Studies of three areas of influence of molten carbonate fuel cell system operating conditions on interactions with the electrolyte have helped to define certain problems which may arise. Electrolyte loss (decomposition and evaporation) may be minimized by optimizing CO_2 distribution to the electrolyte-gas interface. Corrosion of silver is increased by raising O_2 partial pressure in the cathode gas supply but there is little latitude for change in this composition in a system utilizing air and spent-fuel CO_2. Cathode polarization characteristics are better in Li-Na-K ternary melt than in Li-Na binary melt but power densities are not significantly different because of anode polarization behavior.

ACKNOWLEDGEMENTS

The authors wish to acknowledge the work of Graydon Larrabee and Gail Heinen for the radiochemical measurements, Antoinette Queen and Regitze Hansen for carbonate analyses and Roy Deviney and Charles R. Clark for assistance in performing the experiments and collecting the data.

REFERENCES

1. Broers, G.H.J. and Schenke, M. in "Hydrocarbon Fuel Cell Technology" (B.S. Baker,ed.)p. 225, Academic Press, New York,1965.
2. Trachtenberg, I.,ibid,p. 251.
3. Baker, B. S., Marinowski, L. G., Zimmer, J. and Price, G., ibid, p. 283.
4. Baker, B. S., Marinowski, L. G., Meek, J. and Linden, H. R., ADVAN. CHEM. SER. 47, 247 (1965).
5. Broers, G.H.J. and Schenke, M. in "Fuel Cells" (G. J. Young, ed.), Vol. II, p. 6, Reinhold, New York, 1963.
6. Broers, G.H.J. and Ketelaar, J.A.A. in "Fuel Cells" (G. J. Young, ed.), Vol. I, p. 78, Reinhold, New York, 1960.
7. Stepanov, G. K. and Trunov, A. M., in "Electrochemistry of Molten and Solid Electrolytes", Vol. III (A. N. Baraboshkin, ed.) p. 73. Consultants Bureau, New York, 1966.
8. Schenke, M. and Broers, G.H.J., Fifth International Power Source Symposium, Brighton, Sussex, 20-22 September, 1966 (uncorrected preprint).
9. Reid, L., Cole, D. and Trachtenberg, I., J. Electrochem. Soc., 113, 954 (1966).
10. Degobert, P. and Bloch, O., Bull. Soc. Chim. Fr. 13, 1887 (1962).
11. Janz, G. J. and Conte, A., Corrosion 19, 292 t (1963).
12. Dubois, J., Thése Universite de Paris, 1964 (Masson et Cie, Paris 1965).
13. Ingram, M. D. and Janz, G. J., Electrochimica Acta 10, 783 (1965).
14. Bloom, H., Disc. Faraday Soc. 32, 7 (1962).
15. Ward, A. T. and Janz, G. J., Electrochimica Acta 10, 849 (1965).
16. Janz, G. J., Symposium on Fused Salt Reactions, Toronto, February, 1967.
17. Zarzycki, J., Disc. Faraday Soc., 32, 38 (1962).

Table I
$LiNaCO_3$ Electrolyte Composition as a Function of Time at 650°C

Gas Composition 100% Air

Hours	$\%CO_3^=$	$\%OH^-$	$\%Na^+$	$\%Li^+$	Li/Na
0	66.6	0.0	25.7	7.5	.29
3	66.7	0.2	25.6	7.5	.29
48	66.9	0.5	26.4	7.6	.29
98	66.8	0.5	26.4	7.9	.30
144	67.2	0.4	26.4	8.1	.31
216	66.6	0.5	26.2	7.8	.30
336	67.1	0.6	26.0	7.9	.30

Gas Composition 10% H_2O - 10% O_2 - 80% N_2
(9.5% H_2 - 76% Air - 14.5% N_2)

Hours	$\%CO_3^=$	$\%OH^-$	$\%Na^+$	$\%Li^+$	Li/Na
0	66.5	0.0	25.7	8.0	.31
3	65.1	1.2	25.5	8.0	.31
21	63.5	3.1	25.6	8.3	.32
71	64.1	3.2	25.6	8.0	.31
165	64.0	2.1	25.7	8.1	.32
333	62.4	3.0	25.9	8.1	.31
477	63.3	2.3	25.9	8.2	.32

Table II
Silver Corrosion in Molten Alkali Carbonates

Electrolyte: 50 Mole % Li_2CO_3 - 50 Mole % Na_2CO_3

Area of Sample: 5.09 Sq. Cm.

Time (Hrs)	Temperature °C	Gas Composition %			Wt. Loss (Mg/Cm^2)	Rate of Wt Loss (Mg/Cm^2Hr)
		O_2	CO_2	N_2		
100	600	--	100	--	<.06	<.0006
48	600	5	12	83	5.1 ± 1.1	0.11 ± 0.02
168	600	5	10	85	17.9 ± 0.2	0.11
100	600	10.5	89.5	--	20.6 ± 2.8	0.20 ± 0.03
111	600	27.5	72.5	--	40.8 ± 2.2	0.36 ± 0.02

Table III

Silver Corrosion in Molten Alkali Carbonates

Electrolyte: 37 Mole % Li_2CO_3 - 39 Mole % Na_2CO_3 - 24 Mole % K_2CO_3

Area of Sample: 5.09 Sq. Cm.

Time (Hrs.)	Temperature (°C)	Gas Composition (%) O_2	CO_2	N_2	Wt. Loss (Mg/Cm^2)	Rate of Wt. Loss ($Mg/Cm^2/Hr$)
26	700	5	10	85	6.2 ± 0.8	0.24 ± 0.03
48	700	5	10	85	10	0.21
95	700	5	10	85	21.8 ± 1.2	0.23 ± 0.01

Electrolyte: 50 Mole % Li_2CO_3 - 50 Mole % Na_2CO_3

Area of Sample: 5.09 Sq. Cm.

Time (Hrs.)	Temperature (°C)	Gas Composition (%) O_2	CO_2	N_2	Wt. Loss (Mg/Cm^2)	Rate of Wt. Loss ($Mg/Cm^2/Hr$)
24	700	5	10	85	5.8 ± 0.7	0.24 ± 0.03
48	700	5	10	85	8.0 ± 1.3	0.17 ± 0.03
72	700	5	10	85	18.5 ± 1.5	0.26 ± 0.02
96	700	5	10	85	21.5	0.22

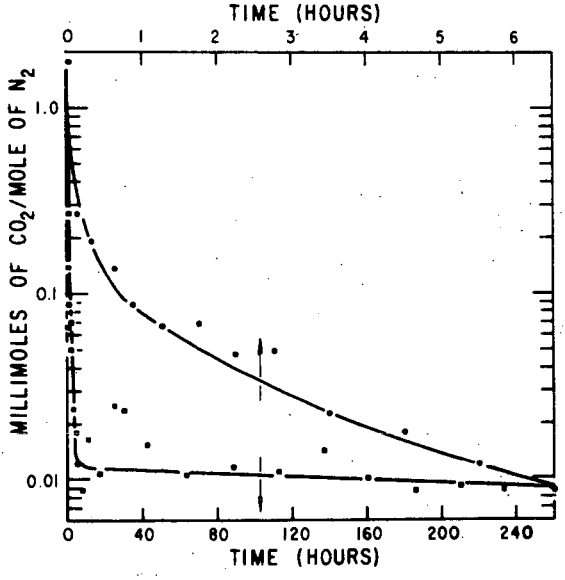

Fig. 1. Rate of CO_2 evolution from $LiNaCO_3$ at 650° C

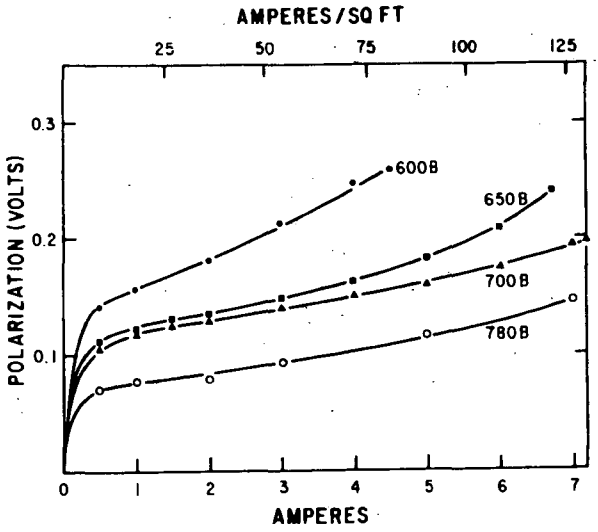

Fig. 2. Cathode polarization in binary (Li-Na) electrolyte vs temperature (°C). Gas composition: 15% O_2, 30% CO_2, 55% N_2

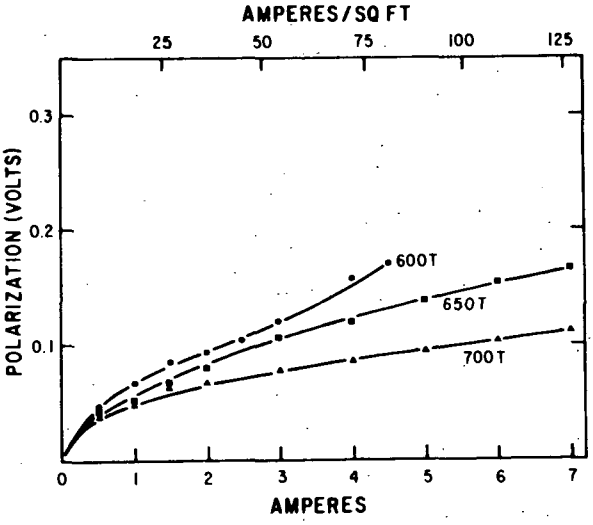

Fig. 3. Cathode polarization in ternary (Li-Na-K) electrolyte vs temperature (°C). Gas composition: 15% O_2, 30% CO_2, 55% N_2

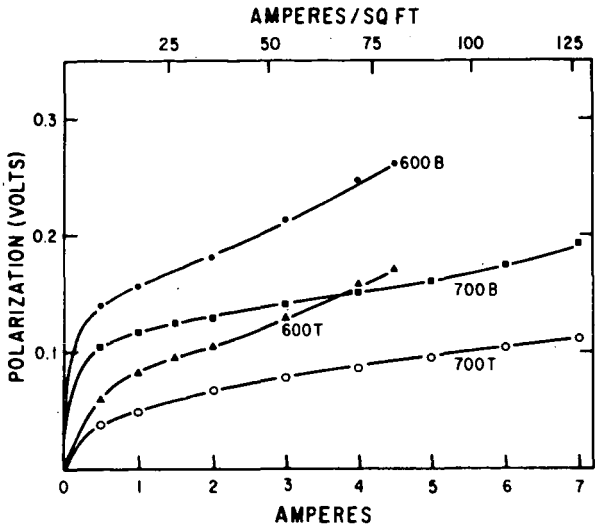

Fig. 4. Cathode polarization in binary (B) and ternary (T) electrolyte vs temperature (°C). Gas composition: 15% O_2, 30% CO_2, 55% N_2

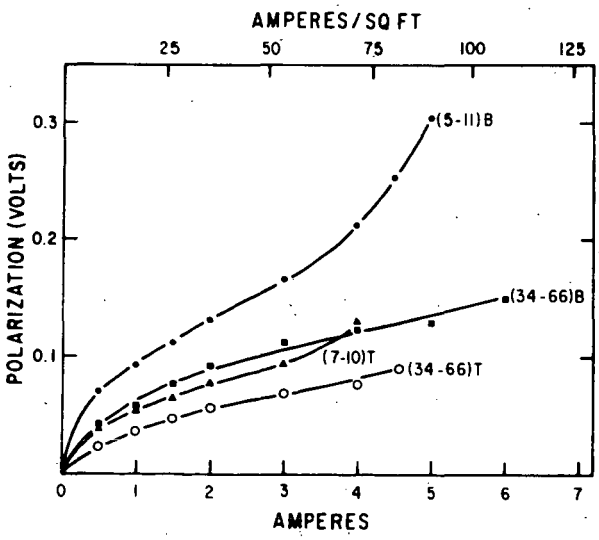

Fig. 5. Cathode polarization at 700°C in binary (B) and ternary (T) electrolyte vs gas composition (% O_2 - % CO_2).

THE BEHAVIOUR OF SILVER CATHODES IN SOLID ELECTROLYTE FUEL CELLS

H. Tannenberger and H. Siegert

Institut Battelle, 7, route de Drize
1227 Carouge-Genève, Switzerland

INTRODUCTION

Fuel cells with solid zirconia electrolytes which work at 750°C to 1000°C are promising systems to convert the chemical energy of cheap fossil fuels into electrical energy. Expensive platinium catalyst can be avoided because of the high working temperatures. Silver as the cathode material and nickel as the anode material have proved to be successful up to 900°C (1) (Fig. 1). In these fuel cells, the resistance of the electrolyte predominates in the total internal resistance of the cell, if the electrolyte has a thickness of more than 1 mm. To increase the power output per unit area of surface of the cell, the thickness of the electrolyte should be reduced. In so doing, polarisation phenomena become important.

This paper deals with the polarisation of silver electrodes. A tentative explanation for the observed phenomena will be given.

Polarisation phenomena in high temperature solid electrolyte fuel cells

A fuel cell with an oxygen-ion conductor as the solid electrolyte creates a voltage between its electrodes due to the difference of the oxygen partial pressure on both electrodes. This voltage is expressed by the Nernst equation :

$$E = \frac{RT}{4F} \ln \frac{p_{O_2}^{K}}{p_{O_2}^{A}}$$

If a current flows through a solid electrolyte fuel cell, the potential between the terminals will drop due to the internal resistance of the cell.

The internal resistance which limits the power output of the fuel cell can be devided into the following parts :

- polarisation of the cathode
- ohmic resistance of the electrolyte
- polarisation of the anode

The electrode polarisation thus defined contains all sorts of losses in the electrodes, such as the electronic resistance, diffusion resistance of the gases, activation polarisation and so on.

The voltage at the terminals of the fuel cell under load can then be expressed by :

$$V = E_o - V_C - V_{El} - V_A$$

V = Terminal voltage

E_o = Open circuit voltage

V_C = Polarisation of the cathode

V_{El} = Ohmic voltage drop in the solid electrolyte

V_A = Polarisation of the anode

The mechanism of the electrode polarisations is far from being understood. It is not yet even possible to determine unequivocably the voltage losses due to polarisation from the total internal resistance.

Current interrupting techniques are frequently used to separate electrode polarisation from the ohmic resistance of the electrolyte (2) (3).

We tried to obtain further information about polarisation phenomena by investigating cells of the type

$$Ag\ (O_2)\ /\ (ZrO_2)_{0.9}\ (Yb_2O_3)_{0.1}\ /\ Ag\ (O_2)$$

with varying electrolyte thickness, which permits the determination of the influence of the electrolyte resistance on the total internal resistance more readily.

EXPERIMENTAL

Fig. 2 shows schematically the experimental set-up. The cell to be studied was made of a wafer of the electrolyte of ~ 30 mm diameter and about 3 mm thickness, held between two tubes made of steel.

In the centre of the electrolyte wafer there was a hole, at the bottom of it was placed the one electrode, the other electrode being on the opposite side of the wafer. The surface of the electrodes was about 1 cm^2. By varying the depth of the hole, the thickness of the electrolyte between the two electrodes could be adjusted to the desired value.

Current collectors made of silver, were pressed against the electrodes by springs. Thermocouples were placed on both sides of the electrolyte wafer.

An oxygen stream of 100 cc/min was directed against both electrodes.

The electrical circuit, shown in Fig. 3, allowed measurement of the current-voltage characteristics of the cell. A current interruptor technique was used to measure the ohmic and the non-ohmic part of the total cell resistance. To do this a short time interruption relay (type Struthers-Dunn M1CC-C5-6.3 AC) was placed in the current circuit, which could break the current periodically for 0.4 milliseconds at a frequency of 100 cycles per second. The voltage-time curve was observed on an oscilloscope Tektronix type 503, and could be easily photographed.

As electrolyte, cubic zirconium dioxyde of the composition of

10 mol % Yb_2O_3

and 90 mol % ZrO_2

was employed. The resistivity as a function of temperature of this composition is shown in Fig. 4. The electrolyte wafer was prepared by sintering a compact of the mixed oxide powders at 1900°C for 3 hours. The apparent density was about 92 % of the theoretical density and the wafers were gas tight.

The surface was prepared by rubbing with SiC paper, then rinced with distilled water and heated at 1000°C for a short time.

Silver electrodes were prepared by painting 2 layers of a silver paste, Degussa Leitsilber 200, followed by a heat treatment up to 850°C.

RESULTS

Fig. 5 and Fig. 6 show typical characteristics of the cells. They are straight lines passing through the origin of the coordinates as they should, because the partial pressure on the two electrodes is the same :

$$p^C_{O_2} = p^A_{O_2} = 1 \text{ atm.}$$

At current densities higher than about 200 mA/cm^2 the characteristics begin to flatten out. This phenomenon, also observed by other workers (3), may be explained by the heating of the electrolyte due to the current flow. This hypothesis is supported by the fact, that the current density, above which the internal resistance of the cell decreases, depends on the thickness of the electrolyte and the nominal operating temperature.

We restrict further discussions to the linear part of the characteristics.

Fig. 7 shows the total resistance per cm^2 of cells having different electrolyte thicknesses, as a function of temperature. It is remarkable, that the temperature dependence of the total resistance of the cell is sensibly the same as that of the resistivity of the electrolyte, independently of the thickness of the electrolyte which varies by a factor of ten.

Fig. 8 shows a cross-plot of Fig. 7, that is the total resistance of the cell as a function of the thickness of the electrolyte at three temperatures. As can be seen, a residual resistance R_0 remains, if the thickness of the electrolyte is extrapolated to zero. The temperature dependence of R_0 is nearly the same as that of the resistivity of the electrolyte.

The separation of the total potential drop into the rapid ("ohmic") and slow ("non-ohmic") part by the current interrupting technique did not show a coherent result. It was not possible to relate the "non-ohmic" potential drop with the residual resistance R_0.

DISCUSSION

The essential result of our measurement is, that we were able to determine the influence of the electrolyte resistance on the total resistance of the cell and so to define a total polarisation of the electrodes. This total polarisation, expressed by the residual resistance R_0, depends on the temperature in approximately the same way as the resistivity of the electrolyte.

In the tentative explanation of the observed phenomena we shall assume, that the cathodic and anodic polarisation will be about the same, that is half of the observed total polarisation, and that the temperature is the same throughout the sample. Where these assumptions may alter significantly the interpretation, we shall discuss the possible consequences of a deviation from our assumptions.

At first, we may attempt to ascribe the residual resistance R_0 to a concentration polarisation at the cathode due to the diffusion of oxygen through a compact silver layer.

The potential drop due to concentration polarisation is

$$\eta = - \frac{RT}{2F} \ln (1-j_1)$$

where

R = gas constant

T = absolute temperature

F = faraday constant

j_1 = limiting current density

The limiting current density can be expressed by

$$j_1 = \frac{4F\,C_o D}{d}$$

where

C_o = solubility of oxygen in silver

D = diffusion coefficient of oxygen in silver

d = thickness of the silver layer

Fig. 9 shows the potential drop η as a function of current density with the limiting current density as unity.

The characteristics of our cells are practically linear and never showed a tendency to limiting currents in the measured current range. If, nevertheless, we assume that the polarisation is due to the diffusion of oxygen in silver, and the limiting current density is much higher than the measured current density range and therefore the logarithmic behaviour of the concentration polarisation may approximate to the observed linear behaviour, theory predicts much smaller values for the polarisation e.g.

$$\eta = 13 \text{ mV}$$
$$\text{for } j = 0.25\, j_1 \text{ at } 800°C$$

than the observed polarisation, which is about

$$\Delta\varphi = 80 \text{ mV} \quad \text{for} \quad 200 \text{ mA/cm}^2$$

We may therefore exclude that concentration polarisation occurs in our cells.

Activation polarisation, involving losses associated with adsorption, or surface reactions, seems to us improbable at these high temperatures. In addition it would seem quite surprising that the temperature dependence of these losses should be the same as that of the resistivity of the electrolyte.

We propose therefore to explain the residual resistance by the fact that the electrodes are active only on discrete spots of small size, distant one from each other. In the case of molten salt fuel cells such a model has already been put forward (4).

The residual resistance, found by extrapolating the total internal cell resistance to zero electrolyte thickness, is then due to the loss of effective cross-section for the current flow through the electrolyte and the dependence of R_o on the temperature should be the same as that of the electrolyte resistivity. Fig. 10 shows schematically the dependence of the total internal cell resistance on the electrolyte thickness expected.

In the following a quantitative estimation of the dimensions of and the distance between the active spots will be given with the aid of simulating the element in an electrolytic tank.

To simplify the situation for the simulation we assume that the active spots have the form of parallel strips with constant width (Fig. 11).

The resistance of one "element", dependent on its thickness, was measured in the electrolytic tank. By putting in parallel n of these elements, the resistance of the unit area of the cell can be calculated.

Fig. 12 shows the simulated element in this electrolytic tank.

Fig. 13 shows the resistance $\mathcal{R}$ of this element as a function of its thickness expressed by the parameter

$$\vartheta = \frac{d}{\frac{p}{2}}$$

for a conductivity :

$$\varrho = 1\ \Omega\ \text{cm}$$

and for a bath depth B :

$$B = 1\ \text{cm}$$

It is important to note, that the resistance $\mathcal{R}$ can be expressed in the form of

$$\mathcal{R} = \mathcal{R}_o + \vartheta$$

for values of ϑ

$$\vartheta \geqslant 1$$

independently of $\frac{b}{p}$. This means, that the current flow is homogenous above a distance d, where :

$$d \geqslant \frac{p}{2}$$

Fig. 14 gives the residual resistance $\mathcal{R}_o$ as a function of $\frac{b}{p}$.

The resistance R of an element with

resistivity ϱ
and width B

is then given by

$$R' = \frac{\varrho}{B} \cdot \mathcal{R} = \frac{\varrho}{B} \mathcal{R}_o + \frac{\varrho}{B} \cdot \frac{d}{\frac{p}{2}}$$

By putting 2 n elements in parallel we get the resistance of a whole cell of length L and width B.

$$R = \frac{1}{2n} R'$$

Referring to Fig. 11 we have

$$n \cdot p = L \quad \text{or} \quad n = \frac{L}{p}$$

and obtain finally

$$\boxed{R = \frac{\rho}{LB} \cdot \frac{p}{2} \cdot \mathcal{R}_o + \rho \cdot \frac{d}{BL}}$$

In this formula the term

$$\frac{\rho}{LB} \cdot \frac{p}{2} \cdot \mathcal{R}_o = R_o$$

can be identified with the measured residual resistance R_o we obtained by extrapolating the electrolyte thickness to zero (Fig. 8).

It should be noted, that from the knowledge of R_o by experiment, it is not possible to determine p and b (from $\mathcal{R}_o$) separately but only pairs of values p and b.

To interpret the results obtained at 800°C (Fig. 8), suppose that

$$L = B = 1 \text{ cm}$$

We can first calculate ρ of the electrolyte from the slope of the straight line in the diagram of total resistance versus electrolyte thickness. This yields

$$\rho = 28 \Omega \text{ cm}$$

in good agreement with the value of resistivity measured independently.

The residual resistance R_o was

$$R_o = 0.8 \Omega \text{ cm}^2$$

If we assume that the element behaves symmetrically with respect to its electrodes, we have, for instance, for the cathode

$$R_o^C = 0.4 \Omega \text{ cm}^2$$

and therefore

$$R_o = 0.4 = \frac{\rho}{LB} \cdot \frac{p}{2} \cdot \mathcal{R}_o$$

From this and Fig. 14 we can calculate the following table :

p (μ)	400	100	40	20
b (μ)	88	1.7	$180 \cdot 10^{-4}$	$6 \cdot 10^{-4}$

CONCLUSIONS

The hypothesis that the silver electrodes are active only on discrete spots, the one distant from the other, is able to explain the observed dependence of the total resistance of the cell

$$Ag\ (O_2)\ /\ (ZrO_2)_{0.9}\ (Yb_2O_3)_{0.1}\ /\ Ag\ (O_2)$$

on the thickness of the electrolyte. As the residual resistance R_o in this model is directly linked to the electrolyte, its temperature dependence should be the same as that of the resistivity of the electrolyte.

The quantitative evaluation of the data shows that the dimensions of the active spots become very small if the distance between them decreases.

Local overheating of the active spots, lowering the resistivity of the electrolyte in their vicinity, would yield still smaller dimensions for the spots having the same distance.

Conforming to Figs 8 and 13 we must admit, that the maximum distance between the spots should be less than about 500 μ .

It is evident, that the model of the strips employed for the simulation does not correspond to reality. Certainly, the active spots are of irregular shape and are distributed irregularly over the electrode surface. However, the order of magnitude of b and p, calculated on the basis of our experimental value of R_o, would not be altered by orders of magnitude.

There remains the question of how to interpret the "non-ohmic" part of the total potential drop. We would suggest, that the phenomenon, yielding the "slow" potential drop, also lies in the electrolyte.

At least for the cathodic polarisation, it may be suggested that the electrolyte region below the active spot is slightly reduced by the cathodic current. If the current is interrupted, the open circuit potential corresponds in the first instant to the chemical potential of oxygen in the slightly reduced electrolyte. After having interrupted the current the reduced region of the electrolyte below the active spots is reoxidized by the oxidizing atmosphere in the cathode compartment and the initial open circuit potential will slowly re-establish itself.

REFERENCES

1) "Comportement d'anodes en nickel dans les piles à combustible à électrolyte solide"
H. Schachner, H. Tannenberger
Revue "EPE", Vol. II, N° 1, 1966

2) "Investigation of the polarisation of electrodes in solid electrolyte cells"
A.T. Filjaev, C.F. Palguev, C.V. Karpatchev
Akademia Nauk SSSR. Uralskii Filial, Trudi instituta electrochimii 1961, 2, (p. 199-209)

3) "Testing of electrodes for high temperature solid electrolyte fuel cells"
E.F. Sverdrup, D.H. Archer, J.J. Alles, A.D. Glaser
Proc. of the Symposium on Hydrocarbon Air Fuel Cells 9, N° 3, part 2 (1965)

4) "High temperature fuel cells"
E. Gorin, H.L. Recht
Fuel Cells (W. Mitchell ed.) Academic Press, p. 193, (1963)

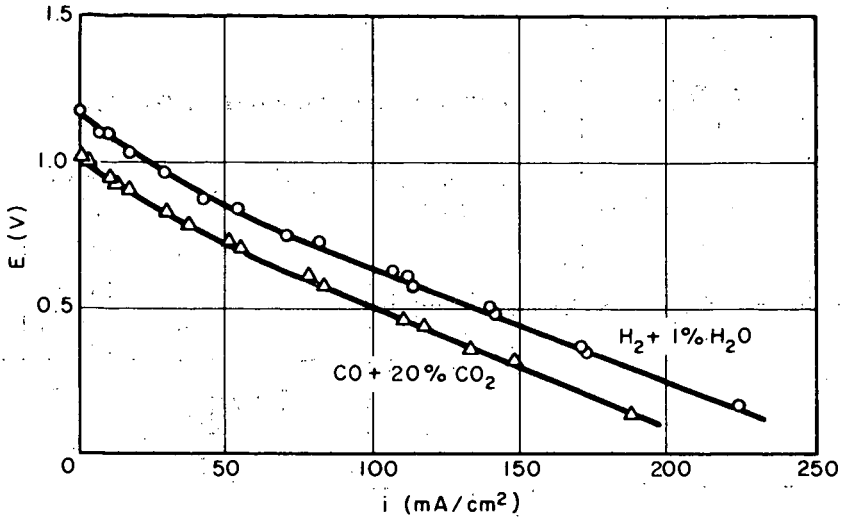

Fig. 1 Performance of solid electrolyte cell
$Ag / (ZrO_2)_{0.9} (Yb_2O_3)_{0.1} / Ni$
T = 800°C , electrolyte thickness : 1.5 mm

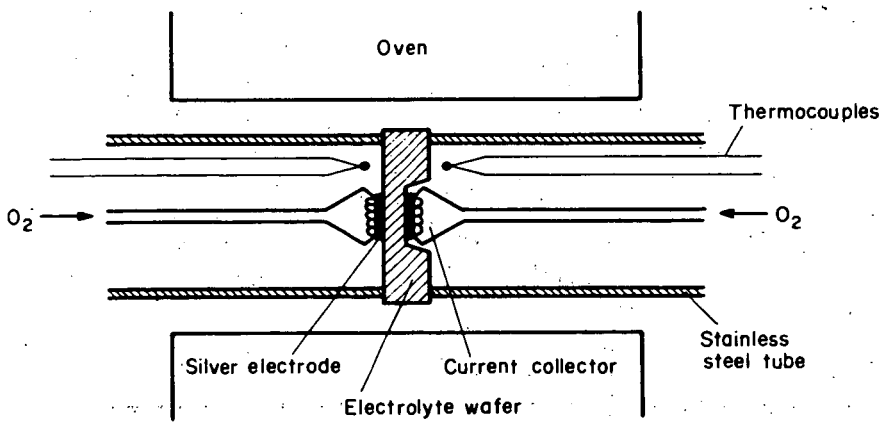

Fig. 2 Experimental set-up of the solid electrolyte cell
$Ag(O_2) / (ZrO_2)_{0.9} (Yb_2O_3)_{0.1} / Ag(O_2)$

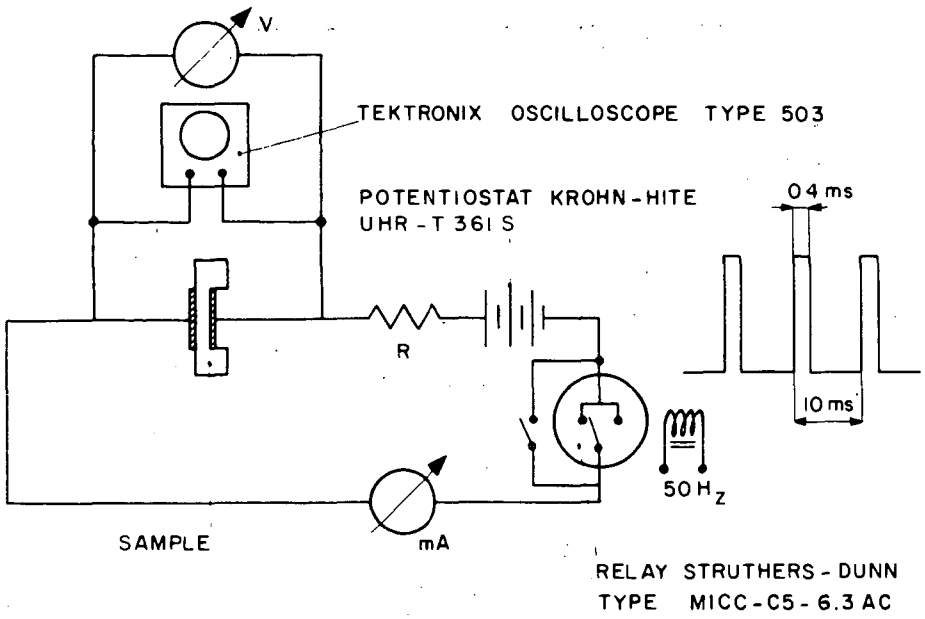

Fig. 3 Electrical measuring circuit

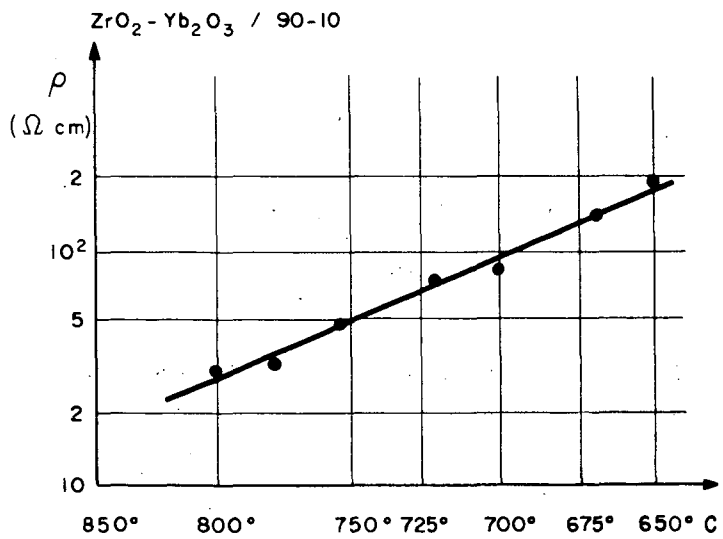

Fig. 4 Resistivity of the electrolyte $(ZrO_2)_{0.9}(Yb_2O_3)_{0.1}$ as a function of temperature

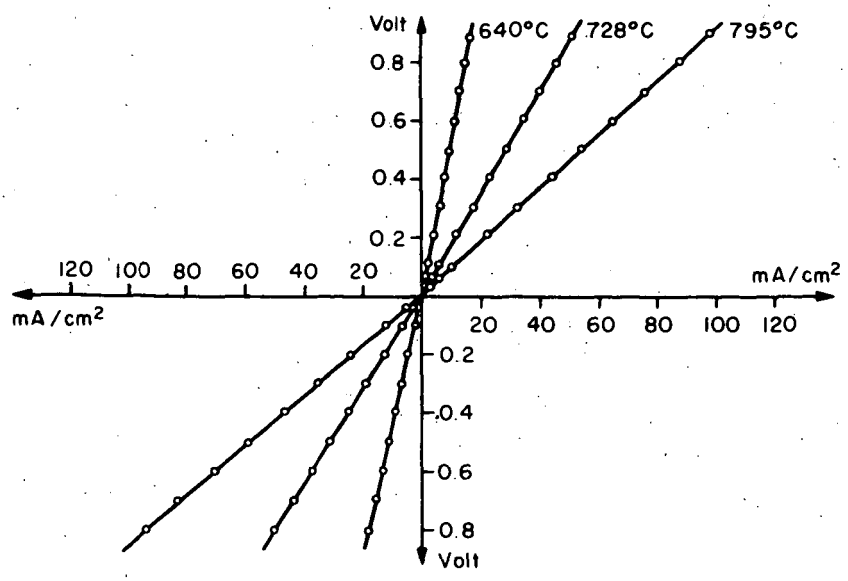

Fig. 5 Characteristics of the cell :
Ag (O_2) / $(ZrO_2)_{0.9}$ $(Yb_2O_3)_{0.1}$ / Ag (O_2)
Electrolyte thickness : 3.65 mm

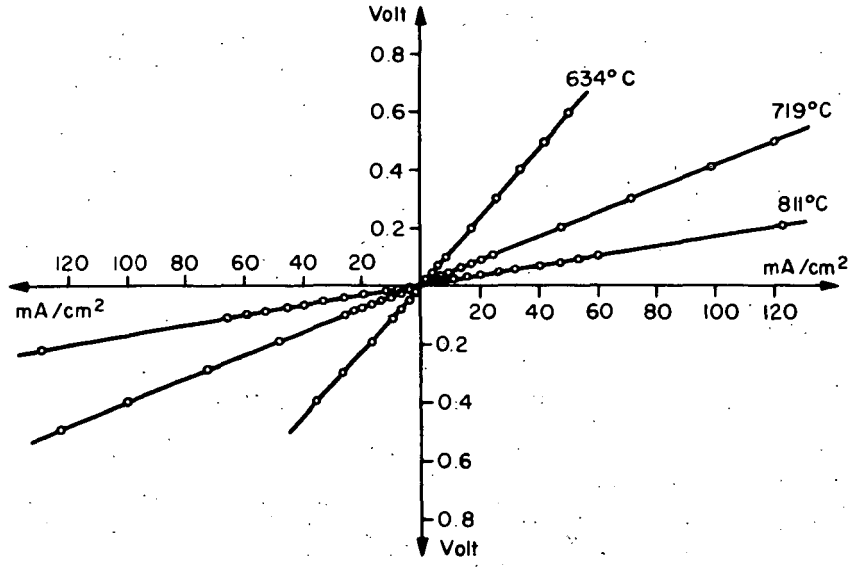

Fig. 6 Characteristics of the cell :
Ag (O_2) / $(ZrO_2)_{0.9}$ $(Yb_2O_3)_{0.1}$ / Ag (O_2)
Electrolyte thickness : 0.38 mm

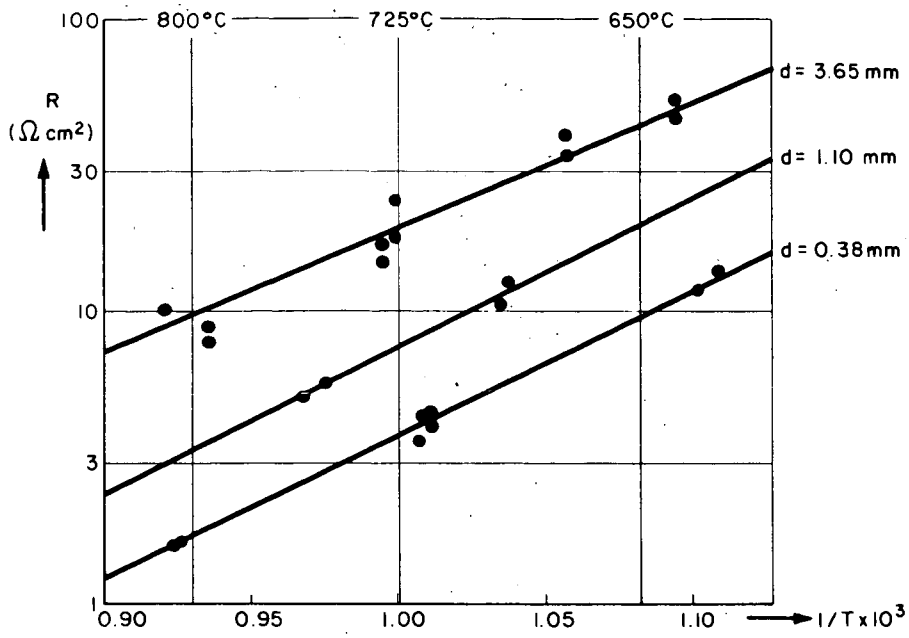

Fig. 7 Total internal cell resistance of three cells with different electrolyte thickness as a function of temperature

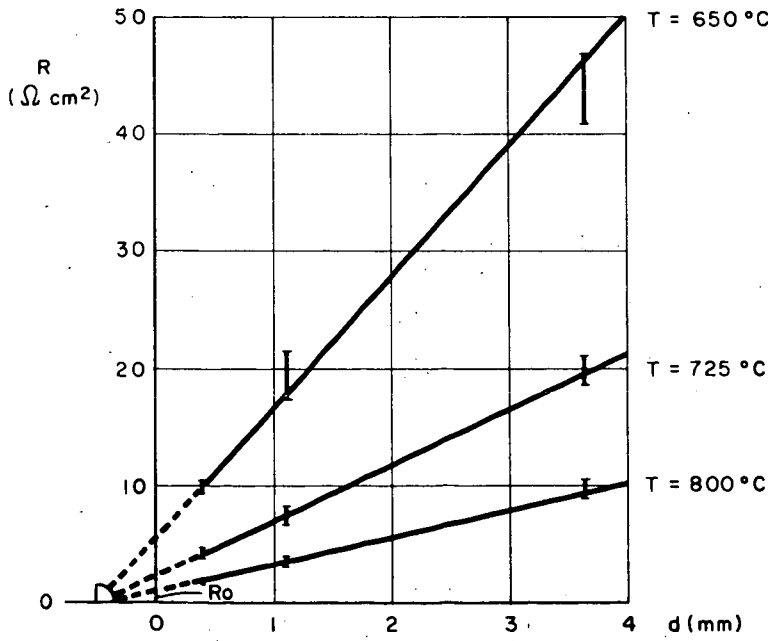

Fig. 8 Total internal cell resistance as a function of electrolyte thickness d at three temperatures

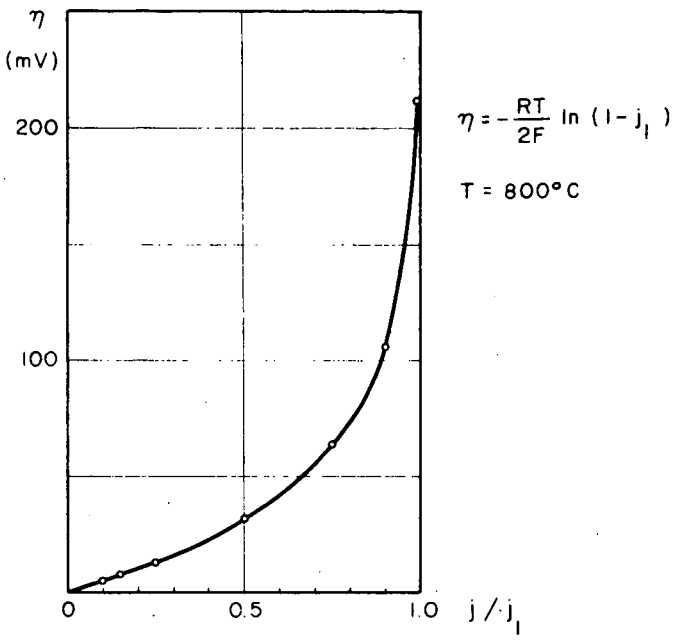

Fig. 9 Concentration polarisation as a function of current density in units of the limiting current density j_l

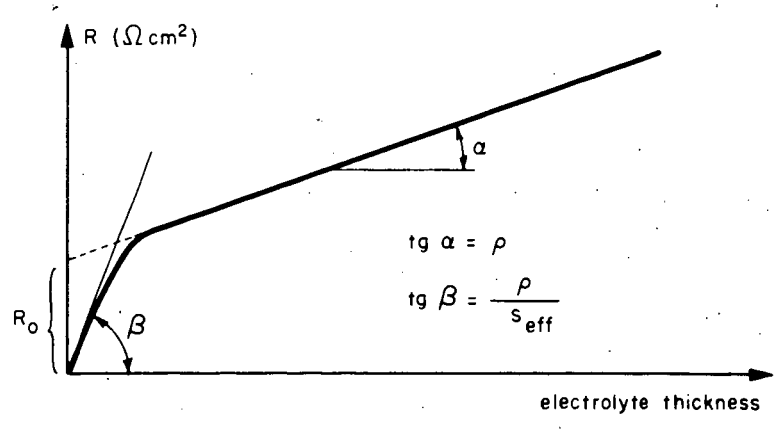

Fig. 10 Total internal cell resistance as a function of electrolyte thickness for a cell having electrodes being active only on isolated spots.

ρ electrolyte resistivity
s_{eff} effective electrode area per cm^2 (Area of the active spots).

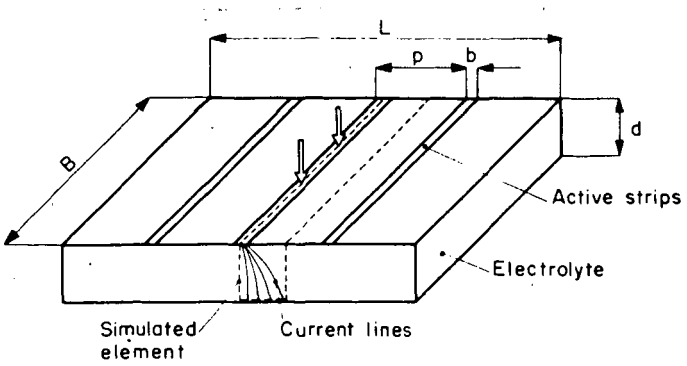

Fig. 11 Model for the simulation of the electrode
L length, B width, d thickness of the electrolyte, p distance between " active strips ", b width of the " active strips "

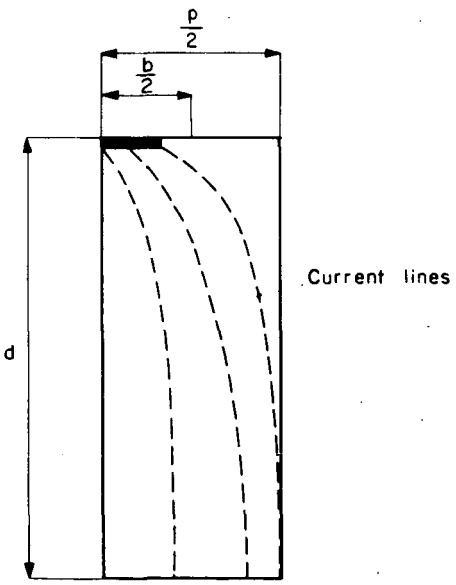

Fig. 12 Simulated single "element"

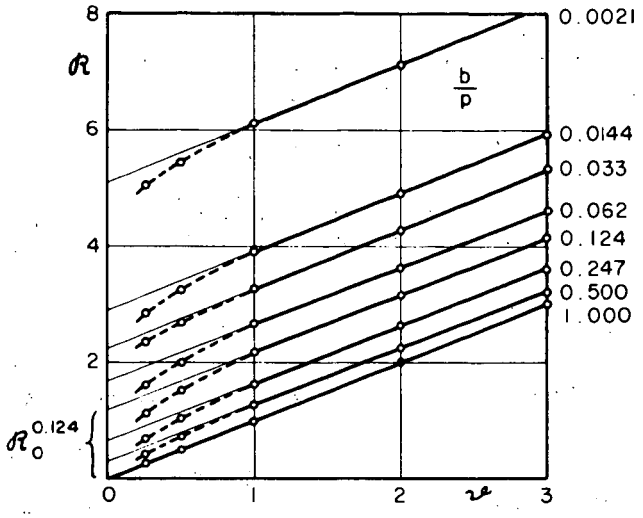

Fig. 13 Resistance $\mathcal{R}$ of the simulated single "element" as a function of the thickness parameter $\nu = \frac{d}{\frac{p}{2}}$ for different values $\frac{b}{p}$ (width of active strips)

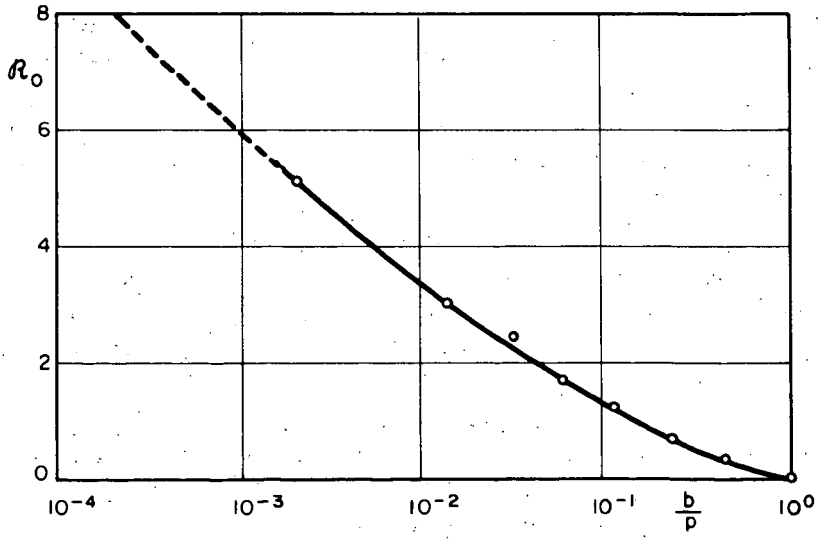

Fig. 14 Residual resistance $\mathcal{R}_0$ as a function of width of active strip $\frac{b}{p}$

THE DESIGN OF A 100-KILOWATT COAL-BURNING FUEL-CELL POWER SYSTEM*

D. H. Archer and R. L. Zahradnik

Westinghouse Research Laboratories
Beulah Road, Churchill Borough
Pittsburgh, Pennsylvania 15235

INTRODUCTION

The development of an economic solid-electrolyte fuel cell system to produce electrical energy from coal and air at an overall efficiency of 60% or greater is the goal of a project at Westinghouse Research. Work reported previously[1,2] has shown that solid-electrolyte batteries can utilize flowing H_2-CO mixtures and air to generate d.c. power with only low losses from resistive and polarization voltage drops at current densities up to 700 amperes/ft.^{2}.

The high operating temperature of solid-electrolyte batteries -- in excess of 1750°F -- allows the heat produced when power is drawn to be effectively utilized in the gasification of coal. Furthermore, the gasification to form H_2-CO fuel can be carried out using hot H_2O-CO_2 combustion products emerging from the batteries. Since both the heat and the medium required for coal gasification are by-products of fuel-cell operation, a high efficiency for an overall system including both the gasifier and the fuel-cell batteires can be achieved.

A conceptual process scheme for incorporating coal-gasification into fuel cell power systems has been introduced and discussed in a previous paper[3]. Essentially, this scheme separates the oxidation of the fuel gases derived from coal into two distinct steps, which take place in two different cell banks as illustrated in Figure 1. The fuel gas stream from the gasification unit is split into two streams -- the first going to a bank of cells in which only a partial oxidation occurs. The second gas stream

---

*The work recorded in this paper has been carried out under the sponsorship of the Office of Coal Research, U. S. Department of the Interior, and Westinghouse Research Laboratories. Mr. George Fumich, Jr., is head of O.C.R.; Neal P. Cochran, Director of Utilization, and Paul Towson have monitored the work for O.C.R.

goes to a second bank of cells where it undergoes essentially complete combustion. The gases emerging from this second cell bank are discharged from the system, while the partially oxidized fuel gases from the first cell bank are recycled back to the reactor, where they gasify the coal.

A thermodynamic analysis[3] of a system similar to that shown in Figure 1 indicates that a maximum system efficiency approaching 100% can theoretically be realized for the coal-burning system. Under normal operation, however, this efficiency is reduced due to irreversibilities which occur within the cell banks and within the coal reactor. Previous analysis has indicated that these irreversibilities are limited so that overall operating efficiencies of 60% or greater are anticipated in full-scale power plants.

A process design for a 100-kw coal-burning solid electrolyte fuel cell power plant has been completed, based on the conceptual scheme of Figure 1. This design incorporates all of the features which now appear necessary to the plant. Details of this design and the predicted operating characteristics of the plant are discussed in this paper.

BASIS FOR SYSTEM DESIGN

The design for the cell banks of the 100-kw fuel cell power system is based on the construction and measured performance of the 100-watt generator shown in Figure 2. This device is the largest solid-electrolyte fuel-cell power system reported to date. The techniques used in fabricating its batteries have been described[1] and the voltage-current curves for the generator have been presented[2]. The device consists of 400 solid-electrolyte cells of the bell-and-spigot design, fabricated into 20 segmented tube batteries, each consisting of 20 individual cell segments. In this generator, platinum was used as electrode material for both the fuel and air electrodes. The battery tubes were held at the 1880°F operating temperature by means of a large, heavily insulated, 3-zone commercial furnace. The tubes were of typical closed-end construction and were mounted in a cold ($<350°F$) metal base plate by means of thick-walled base tubes.

Platinum electrodes are too costly for the fabrication of an economic coal-burning power system, but cheap and plentiful materials are now being developed for both air and fuel electrodes. It is believed that the performance of these materials will meet or exceed that of platinum. For this reason, the performance of the 100-watt unit has been employed as a reasonable basis for the following plant design.

SYSTEM FLOW CHARTS

An overall flow chart for the system is presented in Figure 3. Operating conditions are specified in a simplified version of the chart, Figure 4. Material and energy flow quantities throughout a nominal 100-kw plant are shown in Figure 5; equipment sizes, in Figure 6.

Coal is charged to the reactor unit at the rate of 57 lb/hr. This unit, as indicated in Figure 3, is a complex assembly designed to house in adjoining compartments a fluidized bed of coal and tanks of tubular fuel-cell batteries. The compartments are arranged to facilitate heat transfer from the cell banks operating around 1870°F to the coal-derived solids in the reactor operating around 1750°F. Partially oxidized fuel gases from Cell Bank I pass through the fluidized bed at a superficial velocity of 1.3 ft/sec.; this velocity allows for a gas residence time of about 12 sec -- a time sufficient to gasify the 45 lb. of char per hour produced from the coal feed, to convert the mol ratio $(CO + H_2) / (CO + H_2 + CO_2 + H_2O)$ in the flowing gases from 0.58 at the reactor inlet to 0.81 at the outlet, and to increase the gas flow from 5580 standard $ft.^3/hr.$ at the inlet to 7240 $ft.^3/hr.$ at the outlet.

The gas stream as it leaves the reactor passes through a series of cyclones which remove entrained dust, fly ash, and solid particles and return them to the fluidized bed. The fuel gas, relieved of entrained solids, enters Heat Exchanger I where it is cooled to 970°F. The cooled gas next passes into a series of two fluidized bed absorbers -- each 2 ft. in diameter and 3 ft. high, housed as a single unit. These absorbers contain iron oxide, which acts as a catalyst for the absorption of H_2S and other sulfur containing compounds from the fuel gas stream.

As the absorption of H_2S progresses, the catalyst activity decreases both due to the formation of iron sulfides and to partial reduction of the ore to FeO. In steady state operation, therefore, it is necessary to remove continuously a portion of the catalyst to a second unit into which a stream of air is introduced. Here exothermic roasting of the iron sulfides and reoxidation of the FeO to FE_2O_3 occur at a temperature around 1470°F. The gases emerging from this catalyst regenerator are primarily SO_2 and N_2 -- which can either be discharged to a stack or sent to an acid contact plant. The catalyst regenerated in this unit is recycled to the H_2S absorber, where it contributes some of its sensible heat, which along with that of the fuel gas serves to maintain the absorber at a temperature of 750°F. This sulfur removal process has been developed and successfully used in the treatment of 2-1/2 million ft.^{3}, of coke oven gas per day at the Appleby-Frodingham Steel Company in Great Britain[4].

The fuel gas leaving the H_2S absorber is at a temperature of about 750°F. At this low temperature, the water gas equilibrium constant, K,

$$H_2O + CO \overset{K}{\rightleftharpoons} CO_2 + H_2$$

is quite high. If the water gas equilibrium is catalytically promoted, most of the H_2O in the fuel gas stream can be converted to H_2 -- a fuel which minimizes the polarization voltage losses in the fuel cells. The fuel gas passes, therefore, through a shift converter measuring about 2 ft. in diameter and 6 ft. high containing a commercial shift catalyst such as chromium-promoted Fe_3O_4.

Leaving this unit the gases are at about 600-700°F and have a typical composition as follows: CO, 45%; H_2, 33%; CO_2, 18%; H_2O, 0.5%. At this point in the cycle the gases are introduced to a recirculation pump. A 5-hp drive should be more than adequate to handle any contemplated recycle flow rates.

The gases can, in general, next pass into recycle Heat Exchanger II, in which they receive some heat from the hot exhaust fuel gases. This exchanger is small in size, having an exchange area of less than 10 $ft.^2$.

The gases next enter Heat Exchanger I, where they recover sufficient heat from the high temperature fuel gases just beginning the recycle loop to attain a temperature of about 1550°F. In this instance the total heat generated in operating the cell banks is sufficient to preheat the fuel gases and air, and to supply the heat required for coal gasification in the reactor as indicated in Figure 5.

The fuel gas stream then passes through central core of the fuel cell-reactor unit where it is brought to cell operating temperature by heat exchange with the cell banks. It then enters the cell banks at the bottom of the cell bank-coal reactor unit. Here the stream is split into two unequal portions; about a quarter of the gas is sent to Cell Bank II and three-quarters to Cell Bank I. Upon exiting from Cell Bank I the larger stream, now at 1870°F, is recycled to the coal bed. The smaller stream leaves the second cell bank also at about 1870°F with a mol ratio $(CO+H_2)/(CO+H_2+CO_2+H_2O)$ of less than 0.03.

This stream is then sent to recycle Heat Exchanger II where it gives up a portion of its heat to the recycling gases. In a highly efficient plant, it may be necessary to use this stream not only to heat the recirculating gases, but to preheat the air flow as well. This is accomplished as shown in Figure 3 by having the spent fuel stream, upon its discharge from recycle Heat Exchanger II, pass in countercurrent heat exchange with the incoming air.

Equal amounts of air are fed to each of the cell banks. Internal (to the cell banks) heat exchange between incoming and exiting air streams is sufficient to heat the fresh air -- so that upon its entrance to the active cell region it is about 1470°F. The spent air containing only 3 mol % O_2 discharges to the atmosphere at about 200°F.

DESIGN OF UNIT COMBINING COAL REACTOR AND CELL BANKS

The coal reactor-fuel cell unit consists of a 4 ft. diameter vessel, equally divided by eight spokelike chambers, each 4.25 in. wide and 19 in. long, extending radially from a 10 in. diameter center hub. It is this hub through which the recycle fuel gases flow before they are introduced into the fuel cell banks. The spokelike chambers divide the vessel into 8 pie-shaped slices which extend the height of the vessel -- 16 ft. -- and which contain the fluidized bed of coal.

The cross-sectional area for gas flow through the pulverized coal -- 7.8 $ft.^2$, the volume of the fluidized bed -- 125 $ft.^3$, and the quantity of char contained -- 1200lbs. are ample to provide the fuel gases required to produce 100 kw in the cell banks. Reactor computations have been carried out using data collected on char gasification in this laboratory and information published by other investigators[5].

The 16 faces enclosing the spokes of this wheel design provide ample heat exchange area to transfer heat for the gasifying the coal from cell banks to fuel bed. Heat transfer computations using calculated transfer coefficients between the wall and fluidized-bed have been carried out assuming: 1) that radiation is the sole mechanism for heat transfer from the solid-electrolyte batteries to the walls of the cell banks; and 2) that published empirical formulas[6] are accurate in predicting heat transfer coefficients from the cell bank walls to the fluidized bed. A temperature difference between the cells and coal of less than 60°F is prediced by these computations.

Each of the spoke chambers contains 1250 fuel cell tubes with each tube containing about 40 individual fuel cells. The tubes are mounted horizontally inside the spokes on 3/4 in. equilateral centers, five tubes to a tier. The tubes themselves extend radially into the unit and are attached to 6 in. long base tubes, which extend through about 7 in. of insulation which surrounds the 4 ft. diameter vessel, and are secured in a cold base plate located at the outside shell of the reactor cell bank unit as shown in Figures 7 and 8. Intermittently spaced in the chambers

housing the fuel cell batteries will be four 6 in. high catalyst beds containing chrome-oxide water gas catalyst. These catalyst beds are sufficient to bring the rising gas to water-gas equilibrium according to data gathered in this laboratory. In this way sufficient H_2 is generated for consumption in the fuel cell batteries section of the cell bank immediately above the catalyst.

It should be pointed out that the rising gas is in laminar flow with respect to the cell batteries, so that no separation or wake formation is incurred, and fuel gas is in contact with each postion of the cell fuel electrodes.

Air enters and leaves the system, as shown in Figure 9, by means of an air-exit tube -- which is a 1/8 in. ceramic tube extending along the axis of the battery. Fresh input air flows into the annular space between the battery and the exit tube from an air plenum chamber located in the shell. The battery itself has a closed end[1] so that after traversing the length of the segments and giving up its oxygen to the fuel cell reactions, the now spent air is forced to reverse its direction and flow into the exit tube, where it then flows countercurrent to the incoming air, eventually being discharged to the atmosphere. In the 7 in. insulated region, the counter flow of cold fresh air and hot spent air is sufficient to bring the fresh air up to cell operating temperature. The spent air is thereby cooled, exiting the system at about 200°F.

The design of flowing air inside the cell batteries means that the heated air is only in contact with the ceramic tubes or air electrodes. Nowhere is the hot air in contact with an oxidizable surface. Similarly the metal plates enclosing the fuel cells, the spoke walls, are only contacted by the fuel gas on the cell side and the fuel bed on the reactor side. Thus, the atmosphere surrounding the walls is always reducing, so that the metal of construction of the walls need not be especially oxidation resistant. The electrical performance of the cells in the banks is that predicted from measurements on batteries used in the 100-watt solid-electrolyte fuel-cell generator[2]. The selected operating current for all the cells in both cell banks is 0.44 amperes -- equivalent to a current density of 220 amperes/ft.^{2}.

The average cell voltage at this loading is 0.75 volts in Cell Bank I and 0.65 volts in Cell Bank II -- equivalent to an overall average of 0.7 volts per cell. The calculated power output for 400,000 cells contained in both banks is, therefore, over 120 kw; and the overall efficiency of the plant -- the electrical output of the cells divided by the heat of combustion of the coal -- is 58%. Improvements in solid-electrolyte cell performance have been achieved since the testing of the 100-watt power generator and it now seems likely that an overall efficiency greater than 60% might be obtained from a coal-burning solid-electrolyte fuel-cell power plant.

DISCUSSION

The 100-kw fuel-cell power plant design presented in this paper illustrates several important points:

1. Solid electrolyte cells can be used as the basis of a system to convert coal to electric energy at an overall efficiency approaching 60%.
2. A 100-kw fuel-cell plant based on current fuel-cell and gasification technology is technically feasible; it would not be unreasonable in size or complexity.
3. Sufficient heat is generated in operating the cell banks to provide heat for the endothermic coal gasification process and to maintain the system at the desired operating temperatures.
4. The requisite heat can be transferred from the cells to the coal with a temperature difference of 100°F or less. Gasification can be carried out, therefore, at a reasonably high temperature without exceeding the upper temperature limit of the solid-electrolyte fuel-cells.

The design utilizes only present day technology as far as battery construction and installation are concerned. The current state of this art demands that closed end tubes, fastened in relatively cool base plates form the basic design pattern. This restriction imposes no insurmountable obstacle

in the 100-kw plant, as the technique of mounting the individual cell batteries horizontally allows the cool reactor shell section to serve as a fuel cell base plate. The enclosure of tiers of such batteries into individual chambers allows sufficient heat transfer surface to be built into the unit. However, this design also allows sections of cell batteries to be inserted into or removed from the unit, independent of the remaining batteries. Thus, the assembly can be made up of sections or modules of batteries, each with specific test functions to perform. The ability to test independently fuel-cell batteries incorporating the latest laboratory developments is thus a significant feature of the design.

It should be further pointed out that the volume assigned to the coal reactor is based upon the gasification of 45 lb/hr of a coke or char material. The balance of the 57 lb/hr coal feed is removed from the reactor as ash and carbon associated with the ash. Since the presence of volatile materials in coal will make it considerably more reactive than either coke or char, the design is thus conservative. However, in a pilot plant unit such as the 100-kw plant is intended to be, the conservative design allows for a maximum range of coals, cokes, or chars to be used. This advantage far outweighs any considerations of compact design at this time, and hence the reactor is somewhat oversized. In eventual installations, when fuel-cell performance reaches 0.5 - 1.0 watts/cell and a specific coal is selected as a fuel, it will be possible to produce upwards of 400-kw in a unit the size of the proposed 100-kw assembly.

Another feature of interest in the fuel cell reactor unit is the chrome oxide catalyst beds, housed in the individual spokelike chambers. These beds of catalyst are relatively small, occupying about 9 $ft.^3$ out of a total volume of 200 $ft.^3$; their function is to insure H_2 performance from the fuel-cells by promoting the water gas reaction. Placed in the fuel-cell chambers much in the manner of retractable drawers, these catalyst beds are easily replaceable so that various types and forms of the basic catalyst can be tested in the unit.

A final feature of interest in the unit is the fluidized bed of coal, which has a common bottom from which individual pie-shaped fingers extend upward. The use of the central hub of the unit as a recycle pre-heater solves effectively the problem of longitudinal temperature gradients in the fuel-cell chambers.

The pieces of process equipment in the system flow chart other than the reactor are all standard items, and little difficulty is anticipated in their operation. It might be mentioned, however, that the temperature of operation of the H_2S absorber could possibly be raised above 750°F. This temperature was selected at Appleby-Frodingham as an effective minimum. (It was necessary to heat the input gases.) In the 100-kw plant, the recycle gases to the H_2S absorber are first cooled, the degree of cooling depending upon the desired operating temperature of the unit. If it were possible to raise this operating temperature, then either lower heat losses in the recycle operation or smaller heat exchanger sizes would result.

In summary, therefore, a 100-kw coal-burning, solid-electrolyte fuel-cell, power plant has been designed, scaling up essentially test data from a 100-watt bench-scale unit. The 100-kw plant incorporates a novel combination of fuel-cell batteries and fluidized coal beds into a single fuel cell-reactor unit. This unit together with suitable gas and solids inlets and outlets and certain auxiliary equipment constitute the complete coal-burning system.

Overall efficiency in the proposed system is estimated to be 58%. In order to meet these high efficiency figures, it is necessary to limit the energy losses from the system to those indicated in Figure 5. Furthermore, the net unburned carbon loss from the system must be limited to about 10% of the coal fed. In the design it was assumed that carbon was removed from the bed only in the ash-withdrawal system.

The plant is simple in construction, and its operation involves only the pumping about of various gas streams, the cleaning of these streams, and heat exchange between various of them. This simplicity, together with the great flexibility allowed by the reactor design, make the proposed plant appear as both reasonable and technically feasible.

The economic feasibility of the coal-burning, solid-electrolyte fuel-cell power plant depends on the development of cheap electrode materials and battery fabrication methods. Considerable progress has been made toward producing effective fuel electrodes from non-noble metals and air electrodes from electrically conductive oxides as replacements for costly platinum. Intensive work is now being devoted to the perfection of suitable procedures for high-volume, low-cost production of solid-electrolyte batteries. If these materials and fabrication techniques produce a long-lived battery whose performance equals that measured in the 100-watt power generator, a new means of practical power generation will have been achieved.

REFERENCES

1) Archer, D.H., R.L. Zahradnik, E.F. Sverdrup, W.S. English, L. Elikan, and J.J. Alles "Solid Electrolyte Batteries" Proceedings of the 18th Annaul Power Sources Conference, Max 1964, Atlantic City, N.J.

2) Archer, D.H., L. Elikan, and R.L. Zahradnik "The Performance of Solid-electrolyte Cells and Batteriee on CO-H_2 Mixtures; A 100-Watt Solid-electrolyte Power Supply", Presented at the 150th National Meeting of the A.C.S. in Atlantic City, New Jersey, September 12, 1965. To be published in Hydrocarbon Fuel Cell Technology, Academic Press, New York, 1965.

3) Archer, D.H., E.F. Sverdrup, and R.L. Zahradnik, "Energy from Coal-Burning Fuel-Cell Power Systems", Chem. Eng Prog., 60, : pp. 64-8, June 1964.

4) Reeve, L., "Desulfurization of Coke-Oven Gas at Appleby-Frodingham," J. Inst. Fuel, p 319, July 1958.

5) Jolley, L.J., A. Poll, and J.E. Stanton, "Fluidized Gasification of Non-Caking Coals with Steam in a Small Pilot Plant" Gasification and Liquification of Coal, AIME Publication, New York, 1953.

6) Levenspiel, O., and J.S. Walton, "Bed-Wall Heat Transfer in Fluidized Systems" Chemical Engineering Symposium, Series No. 9, p 1, 1952.

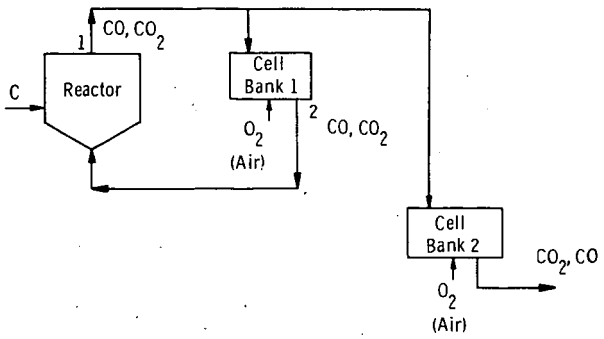

Fig. 1—Simplified coal-burning fuel-cell system

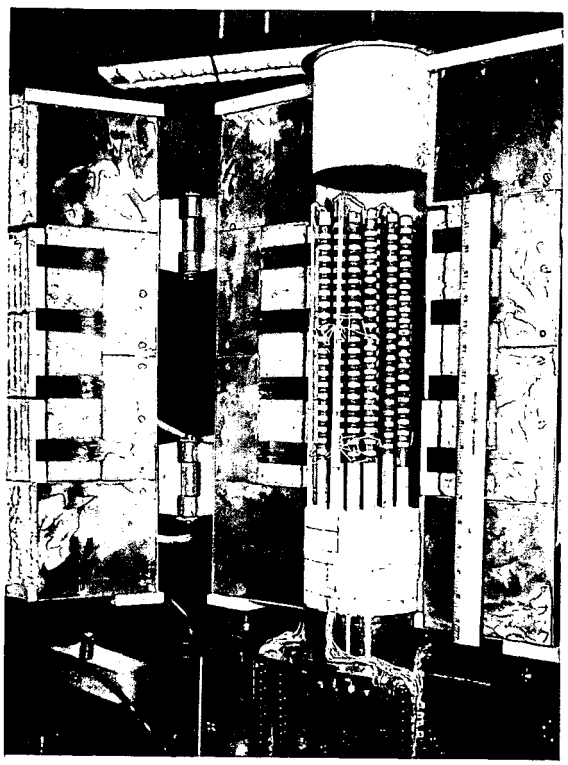

Figure 2 -- 100-watt solid-electrolyte fuel-cell power supply with the furnace door open.

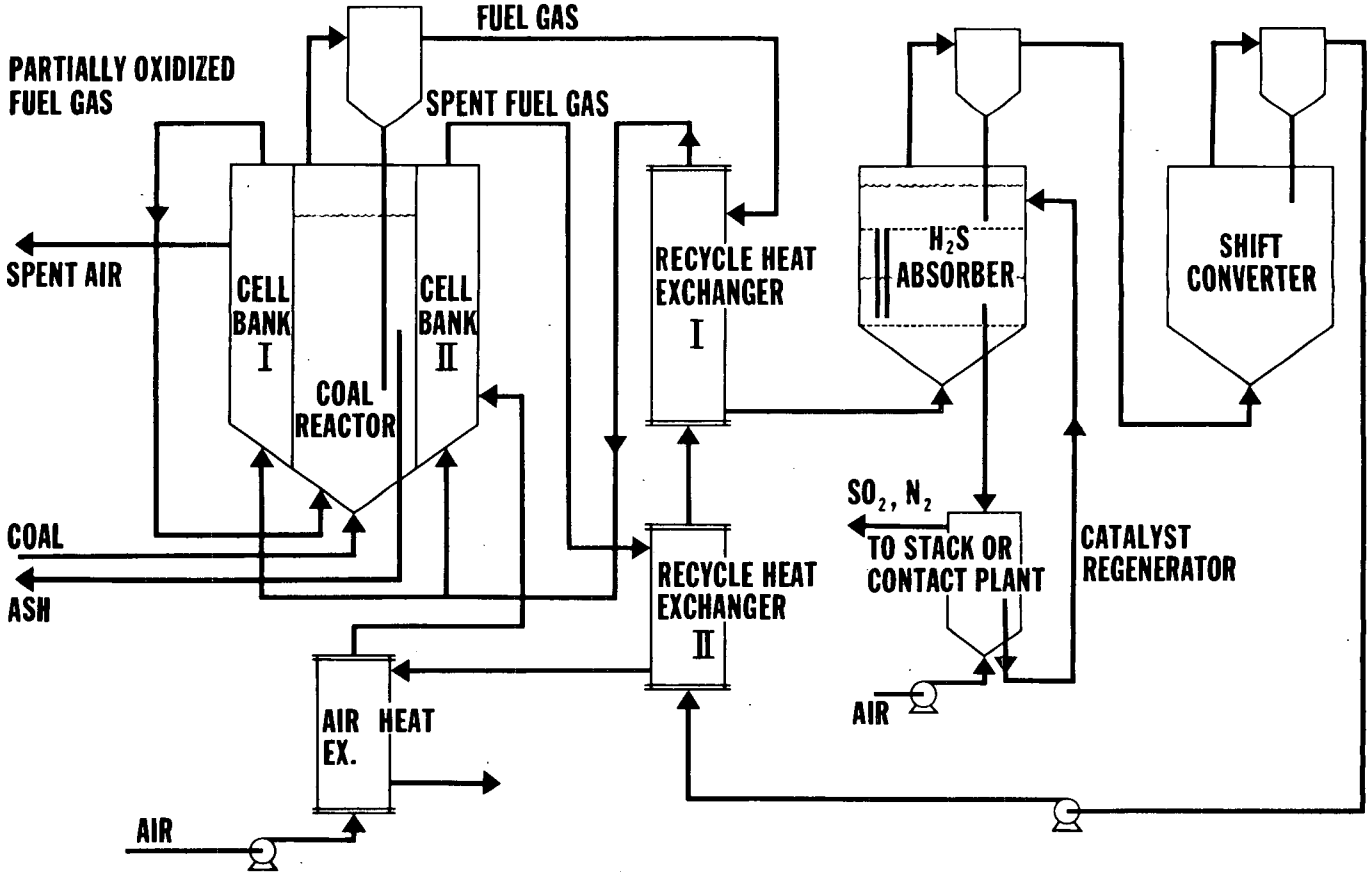

Figure 3 **FLOW CHART FOR 100 kw COAL-BURNING FUEL CELL POWER PLANT**

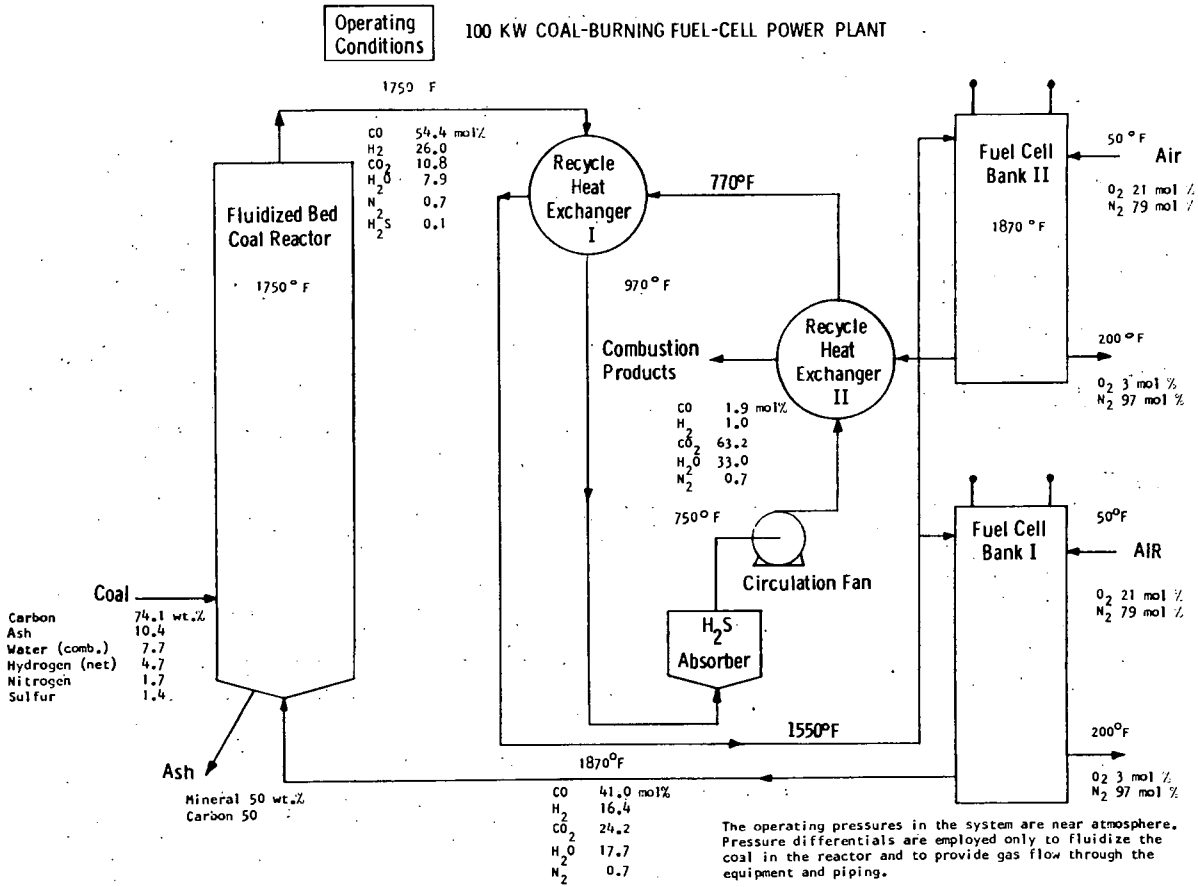

Figure 4 - Operating Conditions for 100-kw Coal-burning Fuel-cell Power Plant

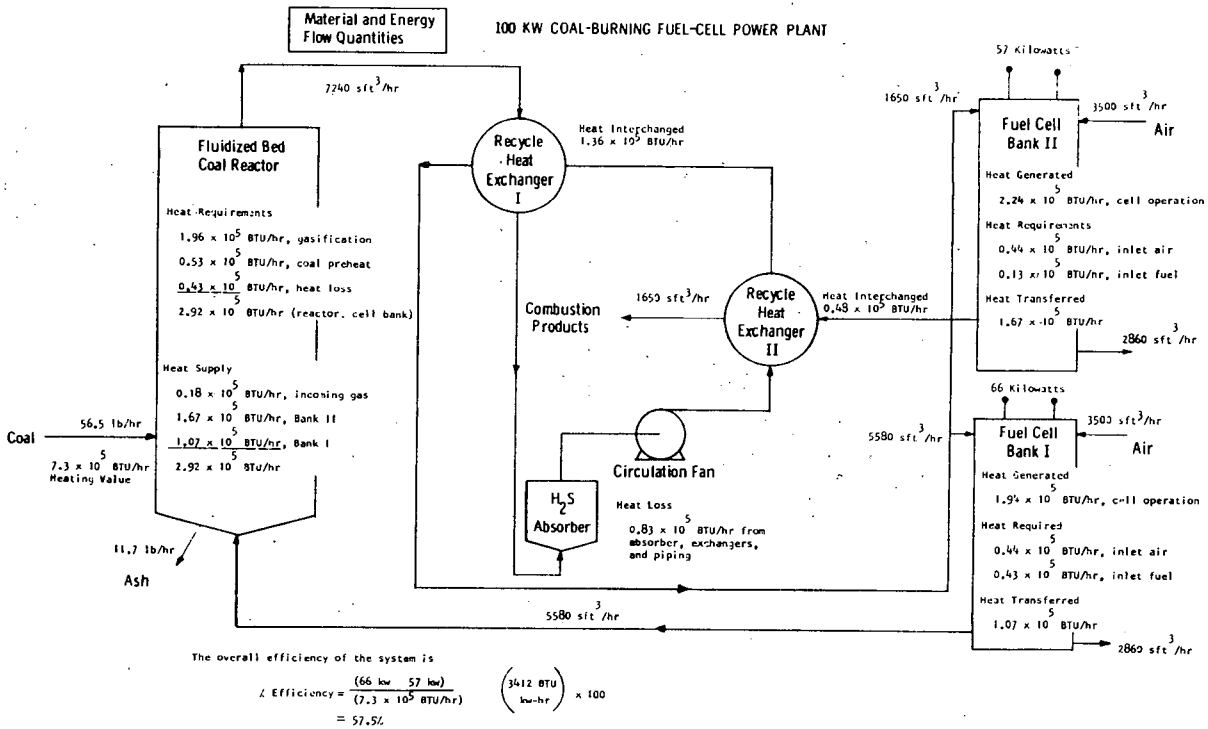

Figure 5 - Material and Energy Flow Quantities for 100-kw Coal-burning Fuel-cell Power Plant

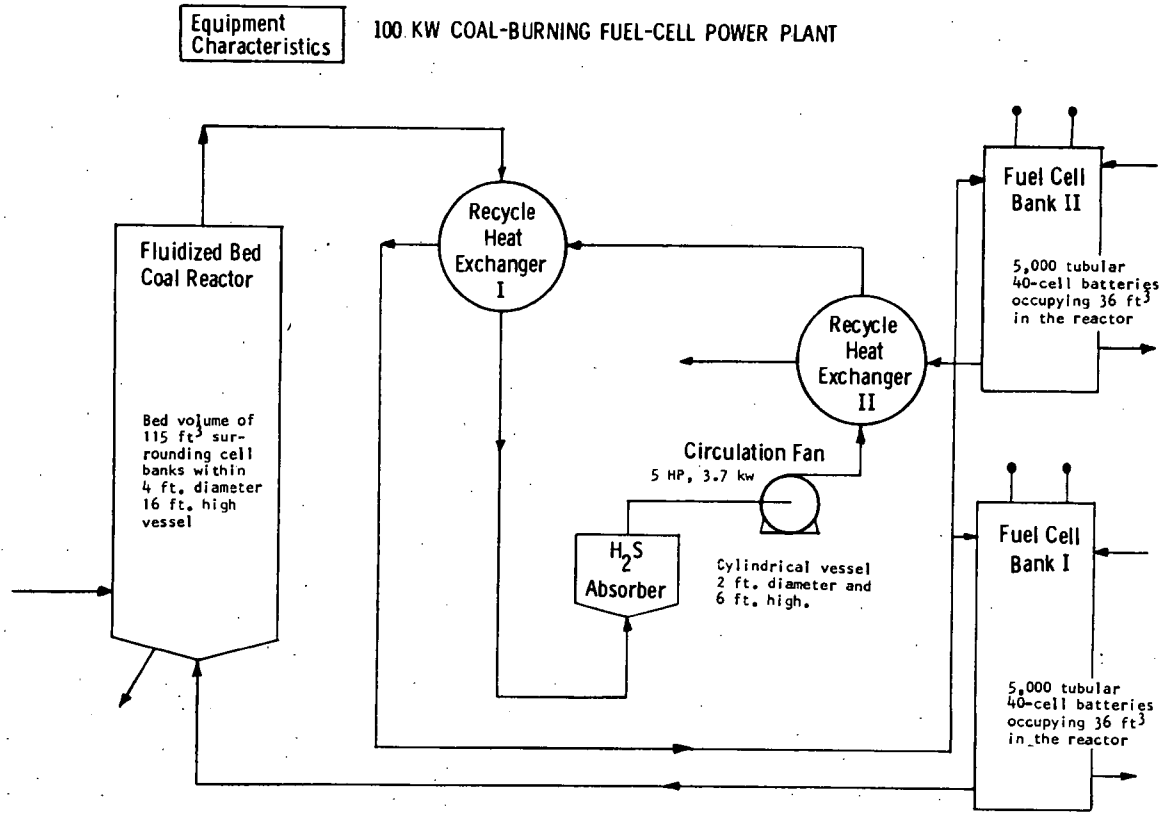

Figure 6 - Equipment Characteristics for 100-kw Coal-burning Fuel-cell Power Plant

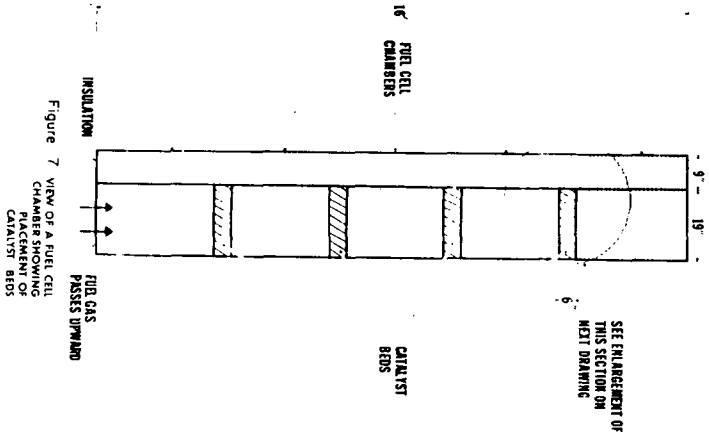

Figure 7 VIEW OF A FUEL CELL CHAMBER SHOWING PLACEMENT OF CATALYST BEDS

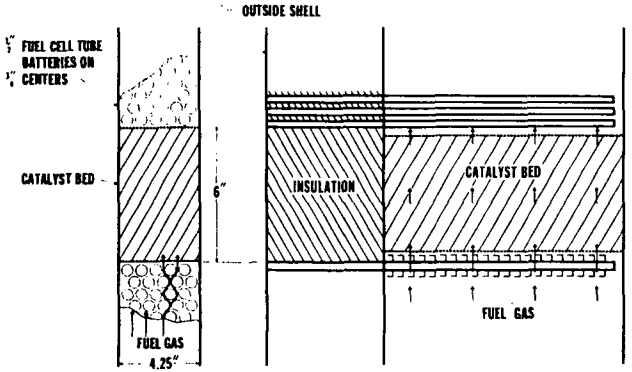

Figure 8 **DETAILED VIEWS OF CATALYST AND FUEL CELL CHAMBERS WITHIN REACTOR SPOKE**

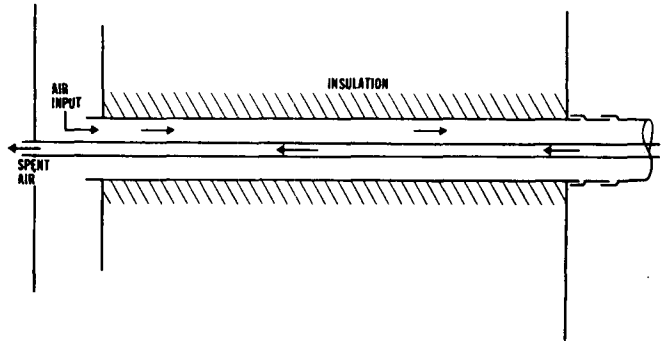

Figure 9 **VIEW OF SINGLE ELECTROLYTE TUBE BATTERY ALONG WITH AIR FEED TUBE**

STANNIC OXIDE AND INDIUM OXIDE FILMS AS AIR ELECTRODES FOR HIGH TEMPERATURE COAL REACTING FUEL CELLS

E. F. Sverdrup, D. H. Archer, A. D. Glasser

Westinghouse Research Laboratories
Pittsburgh, Pa. 15235

Under the Sponsorship of the Office of Coal Research,
U. S. Department of the Interior

I. INTRODUCTION

A high temperature fuel cell using a zirconia ceramic electrolyte is being developed because of its potential for generating electric power with high efficiency by reacting conventional hydrocarbon fuels with oxygen from air. Each cell consists of three layers -- an electronically conducting air electrode -- the electrolyte which at 1000°C is a good oxygen ion conductor and the fuel electrode, another good electronic conductor. Oxygen from the air stream picks up electrons from the air electrode to form oxygen ions. These are conducted through the electrolyte to react with the fuel gases delivering electrons to the fuel electrode. Oxidation of the fuel is controlled by the flow of electrons through the external electrical load connected between the two electrodes.

Electronically conducting oxides are being studied as possible air-electrodes for these fuel cells. A class of oxides has been identified which: (1) display high electronic conductivity, (2) are compatible with the ceramic electrolyte, (3) are stable in air atmospheres at the fuel cell operating temperatures -- 1000°C, and (4) are relatively inexpensive. Coatings of these materials have been applied to electrolyte test samples and the voltage losses (polarization) associated with their operation as air electrodes measured. These tests identify indium oxide, In_2O_3, doped with tin, antimony, or tellurium, and tin dioxide, SnO_2, doped with antimony or tellurium as possible electrode materials. Indium oxide appears especially promising in view of the similarity of its crystal structure and thermal expansion properties to those of the electrolyte.

II. ELECTRICAL CONDUCTIVITY IN TIN AND INDIUM OXIDES

In stannic oxide (SnO_2) the two 5s electrons and the two 5p electrons of the tin are bonded with the 2p electrons of the oxygen. An energy gap of between 3.5 and 4.2 electron volts exists between the valence and conduction band associated with this configuration.[1,2] The intrinsic conductivity of stannic oxide is enhanced by the addition of antimony donor atoms. Measurements by Imai[3] on antimony-doped tin-oxide films have shown that at, and above, liquid nitrogen temperatures each antimony atom is ionized. At antimony concentrations above 1×10^{-3} mole percent, Loch's[4] conductivity versus temperature measurements indicate that the number of intrinsic conduction electrons and electrons contributed from lattice defects can be neglected in comparison to those provided by the antimony donors. The effects of even larger antimony donor concentrations on electrical conductivity have been reported by Mochel.[5] His results (Figure 1) indicate that the conductivity increases with increasing antimony content up to 1 weight percent Sb_2O_3 and then decreases with further antimony additions. Resistivities of 7×10^{-4} ohm-cm were obtained at room temperature with optimum antimony concentration.

In indium oxide (In_2O_3), the 5s and 5p valence electrons of two indium atoms are bonded with the 2p electrons of three oxygen atoms. An energy gap of 3.1 to 3.5 electron volts exists between the valence and conduction bands.[6] Weiher

observes room temperature resistivities of 0.2-3 ohm-centimeters in relatively pure, single crystal samples. Tin, antimony and tellurium will substitute for indium in the indium oxide crystal lattice. These atoms act as donors, contributing electrons to a conduction band at room temperature. Figure 2 shows how the room temperature resistivity depends on the concentration of donor ions in the starting solutions from which these electrode films were prepared. With optimum doping, resistivities were reduced to less than 7×10^{-4} ohm centimeters at room temperature. As in tin oxide, the donor atoms in In_2O_3 are completely ionized at room temperature and the temperature coefficient of resistivity is determined by the predominant electron scattering mechanism.(7) At 1000°C, resistivities of about 10^{-3} ohm-cm were observed with optimum tin doping.

The oxides of indium and tin (In_2O_3 and SnO_2) when appropriately doped display electrical resistivities at fuel cell operating temperatures of the order of 10^{-3} ohm-cm. They can be easily applied in thicknesses up to 10^{-2} cm in the case of indium oxide and 10^{-3} cm in the case of tin oxide. Resistivity/thickness values below one ohm can be achieved with either of these materials. This is low enough to make attractive electrodes.

III. APPLICATION OF TIN OXIDE AND INDIUM OXIDE ELECTRODE FILMS TO ZIRCONIA ELECTROLYTES

These oxide electrode materials are easily applied to zirconia electrolytes by a vapor deposition process. Dilute hydrochloric acid solutions of stannic chloride mixed with appropriate amounts of antimony chloride (or indium trichloride mixed with stannic chloride) are sprayed into a furnace which supplies sufficient heat to vaporize the reactant stream. The vapor stream is then carried into a deposition furnace where, on contacting the heated electrolyte, coatings of tin oxide or indium oxide are deposited. Either an inert gas or air can be used to transport the vapor through the deposition system. Control of the concentrations of the various reactants, of the carrier gas flow rate, and of the heat inputs and temperatures of the various furnaces assures reproducible film characteristics. The following considerations apply to the electrode application process: (1) The vaporization furnace temperature and heat input must be sufficiently high to ensure vaporization of the reactants, it must be kept below a value which will cause the formation of significant quantities of the oxide in the gas stream, i.e., the vapor phase reaction of

$$2\ InCl_3 + 3\ H_2O \rightarrow In_2O_3 + 6\ HCl$$

or

$$SnCl_4 + 2\ H_2O \rightarrow SnO_2 + 4\ HCl$$

must be avoided. For the furnace configuration and reactant concentrations used in our experiments the optimum vaporization temperature for the deposition of tin oxide films was between 325 and 430°C. For the deposition of indium oxide films, vaporization furnace temperatures between 850 and 950°C were used. (2) The deposition furnace temperature must be sufficient to promote the oxidation reactions mentioned above on the substrate but must inhibit appreciable vapor phase reaction. Deposition furnace temperatures of 700-750°C were used in our experiments with SnO_2 and 1000°C in our experiments with In_2O_3. Figure 3 shows the deposition apparatus and Figure 4 the appearance of a typical indium oxide film applied by this process.

IV. STABILITY OF ELECTRODE FILMS IN AIR AT 1000°C

Thermodynamic considerations show that the loss of material from an SnO_2 electrode film in an air atmosphere would most likely occur through gradual decomposition to the gaseous monoxide-SnO.(8) A vapor pressure of 10^{-8} atmosphere of SnO over SnO_2 at 1000°C is indicated. Rough estimates of the rate of material loss

through saturation of the fuel cell air supply with SnO indicate that an electrode life of over five years can be anticipated. Tin oxide appears to be a stable air electrode material.

Experimental determinations of the equilibrium pressures existing over indium oxide (In_2O_3) at 1000°C indicate that a decomposition to the gaseous suboxide (In_2O) is the most likely cause for loss of this electrode material. With an oxygen partial pressure of 2×10^{-8} atmosphere over the In_2O_3 the In_2O vapor pressure is 4×10^{-8} atmospheres.(9) In the presence of an oxygen partial pressure of 0.2 atmosphere corresponding to one atmosphere of air over the electrode, decomposition to In_2O would be inhibited and a vapor pressure of 10^{-15} atm. of In_2O would be expected. In_2O_3 appears to be even more stable that tin oxide and should be suitable for the air electrode.

These considerations do not give any indication of the possible loss of the doping agent from the oxide film. Since loss of the doping agent would cause increases in the resistivity of the film material, tests have been made in which ρ_e/δ_e was measured as a function of time of electrode operation. In test periods of one month there were no measurable changes with either electrode material.

V. STABILITY OF THE ELECTRODE FILM IN CONTACT WITH ZIRCONIA ELECTROLYTE

A. Stannic Oxide (SnO_2) Films

Stannic oxide crystallizes with the tetragonal structure.(10) The material has a coefficient of thermal expansion of 4.5×10^{-6} cm/cm - °C which is roughly one half that of the electrolyte. Films having thicknesses between 10^{-4} and 10^{-3} cm have been successfully applied to the electrolyte by the thermal decomposition of tin-chloride solutions. These films have adhered well and have withstood repeated thermal cycling between room temperature and 1000°C. Films which exceed 3×10^{-3} cm in thickness develop tensile stresses in electrolytes of 0.1 cm thickness which are sufficient to crack the electrolyte when the samples are cooled to room temperature.

Studies of solid state reactions between SnO_2 and ZrO_2 have been made by Stöcker.(11) He finds a solubility of ZrO_2 in SnO_2 of 19 pp 100 moles between 800 and 1300°C and a solubility of SnO_2 in monoclinic ZrO_2 of 9 pp 100 moles at 800°C. Experiments indicated no observable sintering of one-micron tin-oxide powders to electrolyte discs after heating for four hours at 1400°C. At 1600°C, however, the reaction proceeded rapidly and after 20 minutes of exposure the electrolyte material had become frangible. This observation agrees with Stöcker's conclusions that additions of SnO_2 tend to destabilize cubic zirconia. No evidence of alteration of the electrolyte could be seen on photomicrographs of tin oxide coated electrolyte test specimens after 400 hours of electrode operation at 1000°C. It appears that tin oxide electrodes formed from the chlorides are sufficiently stable in contact with the electrolyte to make useful electrode structures.

B. Indium Oxide Films

Indium oxide crystallizes in Tl_2O_3 structure,(10) a deformed cubic fluorite crystal in which three-fourths of the fluorine positions are occupied by oxygen, the remainder remaining vacant. Wyckoff tabulates the lattice parameter as: a_o = 10.118 Å at 26°C. This matches well with the similar spacing in cubic zirconia: $2a_o$ = 2 x 5.10 Å = 10.20 Å. The linear thermal expansion of In_2O_3 single crystal and polycrystalline samples have been measured by Weiher and Ley(12) over the temperature range 0-700°C. Over this range the linear thermal expansion matches that of cubic zirconia (Figure 5). Adherent oxide layers that withstand thermal cycling between room temperature and 1000°C, with or without electrode operation at the high temperature, have been applied to the electrolyte by vapor deposition. Only when

the indium oxide layer exceeded 9 x 10^{-3} cm in thickness was loosening of the electrode film from the electrolyte substrate noted.

To determine whether the electrolyte and indium oxide would interact when held for long times at elevated temperatures, a series of experiments were made in which yttria-stabilized zirconia electrolyte test wafers were imbeded in one micron indium-oxide powder and heated at various temperatures between 1400°C and 1920°C for 20 minutes in an air atmosphere. Below 1500°C no sintering or other evidence of interaction could be detected. Above 1500°C considerable reaction took place. Liquid formation in the vicinity of 1600°C was observed in these tests.

Sintering for twelve hours at 1400°C without detectable interaction make it appear that In_2O_3 electrode films applied by vapor deposition or similar low temperature processes will be stable in contact with the electrolyte under fuel cell operating conditions.

VI. POLARIZATION BEHAVIOR AND ELECTRODE TO ELECTROLYTE CONTACT RESISTANCE LOSSES OF SnO_2 AND OF In_2O_3 ELECTRODES

Vapor deposited tin and indium oxide electrode films were operated as electrodes carrying out the air electrode reaction:

O_2	+ 4e	$\rightarrow 2O^{=}$	
air		electrode	electrolyte

The voltage losses associated with carrying out this process were measured using the electrode tester and monitoring the electrode to electrolyte voltage as a function of electrode current density. The current-interruption technique[13] was used to separate the ohmic losses associated with oxygen ion transport in the electrolyte and the electrode to electrolyte contact resistance from non-ohmic, "polarization", voltage losses.

The electrical behavior of a typical indium oxide electrode film in its "as deposited" condition is shown in Figure 6. Polarization voltage drops increase very rapidly with electrode current. At 100 ma (77 ma/cm^2) the polarization component of the voltage (50 millivolts) agrees very well with the expected ohmic contribution from the electrolyte ionic resistance -- indicating a negligible electrode-to-electrolyte contact resistance. The character of the decay of the polarization voltage drop, as shown by the current-interruption oscillograms, changes when the polarization voltage exceeds approximately 700 millivolts. The volt-ampere curve becomes almost parallel to the ohmic resistance displaced by the 700 millivolt polarization. The time constant of polarization decay is long and depends upon the length of time the electrode has been operated. A partial electrochemical-reduction of the In_2O_3 electrode is apparently responsible. The long decay of the polarization results from the reoxidation of the partially reduced film when current flow is interrupted.

Apparently, the "as deposited" indium oxide films are sufficiently impervious to the passage of oxygen that high polarization voltage drops occur at even low current densities (oxygen demands). The value of the current, at which electrochemical breakdown of the indium oxide film occurs is inversely proportional to the electrode thickness (Figure 7).

Some treatment must be employed to yield electrodes capable of high current densities with low polarization losses. Fortunately, a simple "reverse current" treatment of the electrode film results in greatly improved performance. Reverse current treatment consists simply of applying a voltage across the electrode-electrolyte interface with the indium oxide made positive with respect to the

electrolyte. Under these conditions oxygen is transported through the electrolyte toward the electrolyte-electrode interface. It may be theorized that an oxygen pressure is developed under the electrode film which opens oxygen paths through the previously tight film. When the electrode is operated in the normal direction, polarization voltage losses are greatly reduced. Some increase in the electrode to electrolyte contact resistance may accompany the reverse current treatment.

Figure 8 compares the volt-ampere characteristics of a typical electrode film before and after reverse current treatment. The resistive component of the electrode to electrolyte voltage drop has increased from the calculated value of the electrolyte contribution, 0.48 ohm, to 0.67 ohm while the polarization component has dropped from 730 mv to 150 mv at a current density of 380 ma/cm^2. At a current density of 770 ma/cm^2 the polarization component of the voltage loss is 220 mv.

The polarization characteristics in oxygen of five vapor deposited electrodes after reverse current treatment are shown in Figure 9. The electrodes cover a range of electrode weights from 8 to 37 milligrams per square centimeter of electrolyte coverage. (This corresponds to a range of operating ρ_e/δ_e from 2.6 ohm centimeter per cm to 0.4 ohm cm/cm.) Polarizations are seen to increase from a value between 30-90 mv at 100 ma/cm^2 to between 120-230 mv at 1000 ma/cm^2. A limiting-current type of polarization behavior is displayed suggesting that further efforts to increase the permeability of the electrode film to oxygen may be expected to yield lower polarizations. Tin oxide films performed less satisfactorily. The films tested experimentally displayed electrode resistivity/thickness parameters of three ohms. (Improvements in film application techniques together with optimized doping of the electrode, should make ρ_e/δ_e values less than one ohm attainable.) High values of ρ_e/δ_e in electrode coatings results in a non-uniform current density distribution in the test samples. This complicates the interpretation of polarization losses. The experiments indicated that polarization losses were comparable with those reported for In_2O_3 films (perhaps even somewhat lower due to the tendency of the SnO_2 films to craze under the differential thermal expansion stresses) but that contact resistances between electrode and electrolyte were appreciably higher. It appears that the electrode performance could be significantly improved through the use of better application techniques, optimized doping, and the use of a porous structure.

VII. CONCLUSIONS

Indium sesquioxide, doped with tin, antimony, and/or tellurium, was found to be a promising air electrode for solid electrolyte fuel cells operating at 1000°C. The material is stable in air and in contact with the electrolyte. It can be easily applied in films having a resistivity/thickness parameter as low as 0.2 ohm-cm/cm at the operating temperature. Although polarization voltage losses of the "as deposited" films are high, a simple reverse current treatment reduces polarization losses to 150-250 mv at 1000 ma/cm^2. Increasing the porosity of the In_2O_3 films further reduces the air electrode poalrization. Electrodes of the doped indium oxide have operated for over 1100 hours at a current density of 770 ma/cm^2 with polarization voltage loss of 50 mv, constant electrode resistivity ÷ thickness parameter, and with no measurable contact resistance to the electrolyte (Figure 10).

Tin oxide doped with antimony or tellurium can also be applied to zirconia electrolytes by the thermal decomposition of aqueous solutions of tin and antimony or tellurium chloride. The films are stable at the 1000°C operating temperature of the fuel cell. Despite a lower coefficient of thermal expansion, tin oxide films withstand repeated thermal cycling between room temperature and 1000°C. When operated as electrodes, a weakening of the electrode to electrolyte bond occurs and and the electrode flakes off as it is subsequently cooled through the range 800-600°C. If tin oxide is to be used as an electrode in practical devices, some method must be developed to keep the electrode attached to the electrolyte during cooling.

These materials are suitable as air electrodes. They promise to play an important role in making practical solid electrolyte fuel cell devices.

REFERENCES

1. E. E. Kohnke; J. Phys. Chem. Solids, Vol. 23, pp 1557-1562, 1962.
2. K. Ishiguro, T. Sasaki, T. Arai, & I. Imai; J. Phys. Soc. of Japan 13, pp 296-304, March 1958.
3. I. Imai; J. Phys. Soc. of Japan 15, 937-938, 1960.
4. L. D. Loch; J. Electrochem. Soc. 110 (10), 1081-1083 (1963).
5. J. M. Mochel; U.S. Patent 2,564,706, August 1951.
6. R. L. Weiher; Elec. Properties of Single Crystals of Indium Oxide; J. Appl. Phys. 33,9, '63.
7. E. F. Sverdrup, A. D. Glasser, D. H. Archer, Twenty-Fifth Monthly Progress Report, Office of Coal Research, Contract 14-01-001-303, January 1965.
8. Ibid.
9. R. P. Burns, G. DeMaria, J. Dowart & M. Inghreen; J. Appl. Physics, 38, 1963, pp 1035-36.
10. Wyckoff, R. W. G., Crystal Structures, Interscience, New York, 1951.
11. Stöcker, H. J., A Contribution to the Study of the Properties of Zirconia-Base Refractory Solid Solutions and the Stabilization of Cubic Zirconia, Annales de Chimie, 1960, 1459-1509.
12. Weiher, R. L. and Ley, R. P., J. Appl. Phys., 34, 1963, 1833-34.
13. E. F. Sverdrup, D. H. Archer, J. J. Alles, and A. D. Glasser, Testing Electrodes for High Temperature Solid-Electrolyte Fuel Cells, Hydrocarbon Fuel Cell Technology, Academic Press Inc., New York, 1965, pp 311-333.

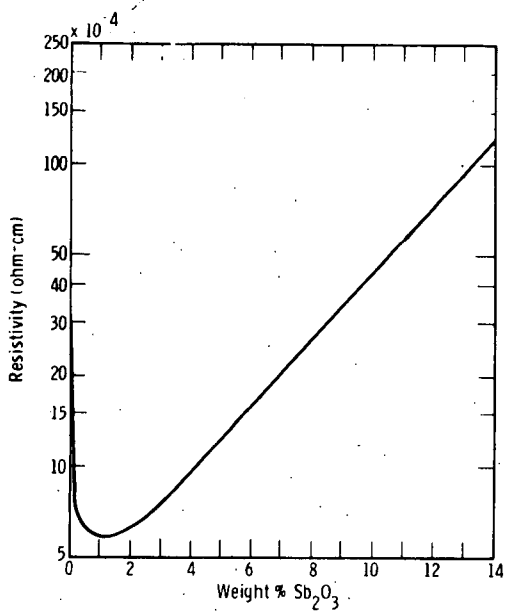

Fig. 1—Effect of antimony doping on the room temperature resistivity of tin oxide (after Mochel, U. S. Patent 2,564,706)

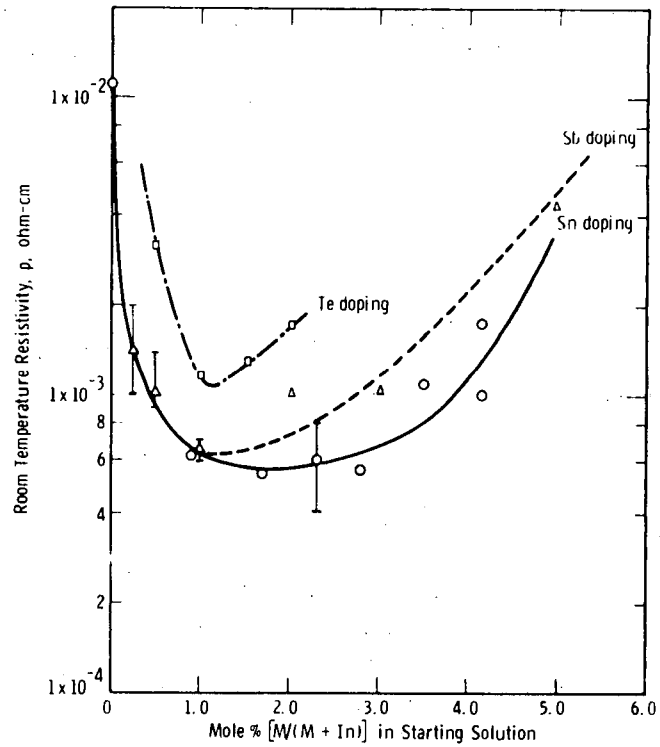

Fig. 2—Effect of doping on the resistivity of Indium Sesquioxide
M = ○ Sn doping
M = △ Sb doping
M = □ Te doping

Figure 3 - Vapor Deposition of Indium Oxide Air Electrodes

Figure 4 - Indium Oxide Air Electrode

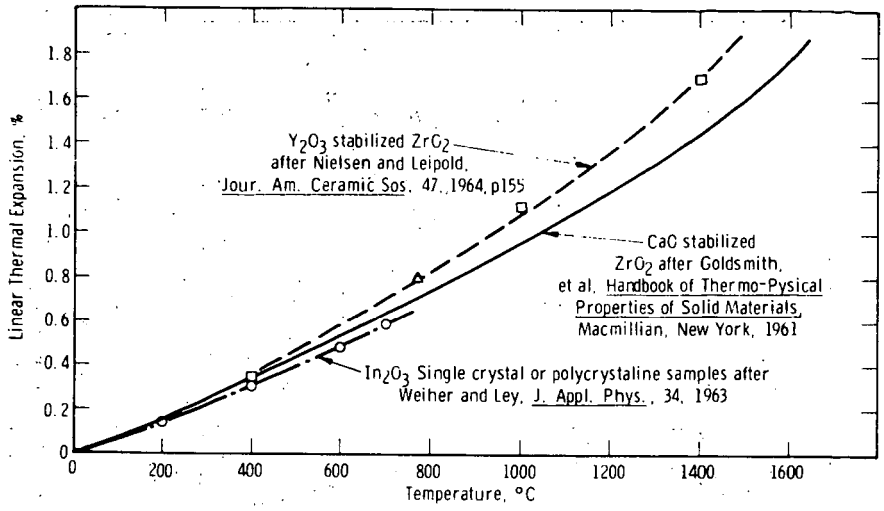

Fig.5—A comparison of the linear thermal expansion characteristics of In_2O_3 and stabilized cubic Zirconia

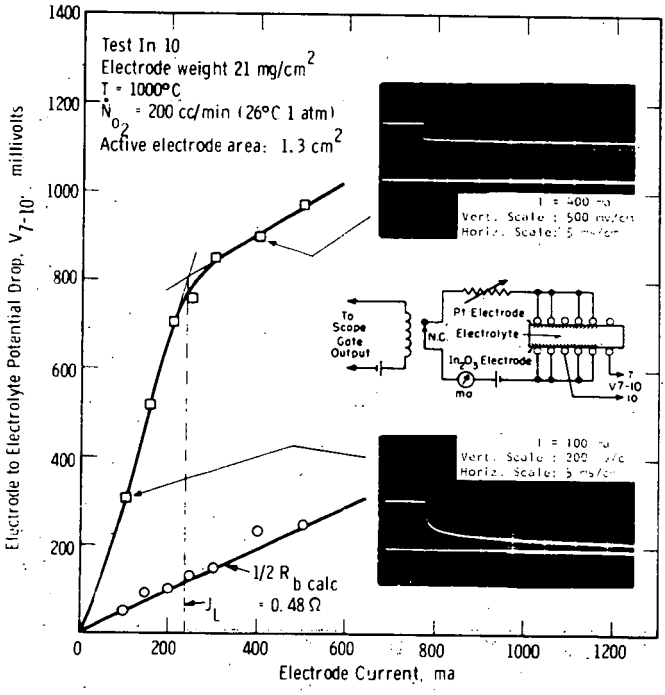

Fig. 6—Volt-ampere characteristic of Indium Sesquioxide air electrode prior to treatment-showing the nature of the polarization

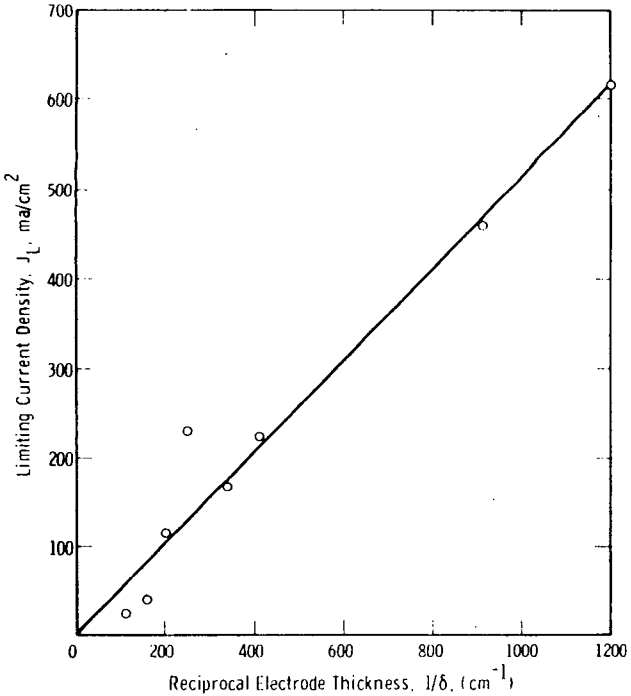

Fig. 7 - The effect of electrode thickness on J_L, the current density at which the break in the voltage-current curve appears (see Fig. 8)

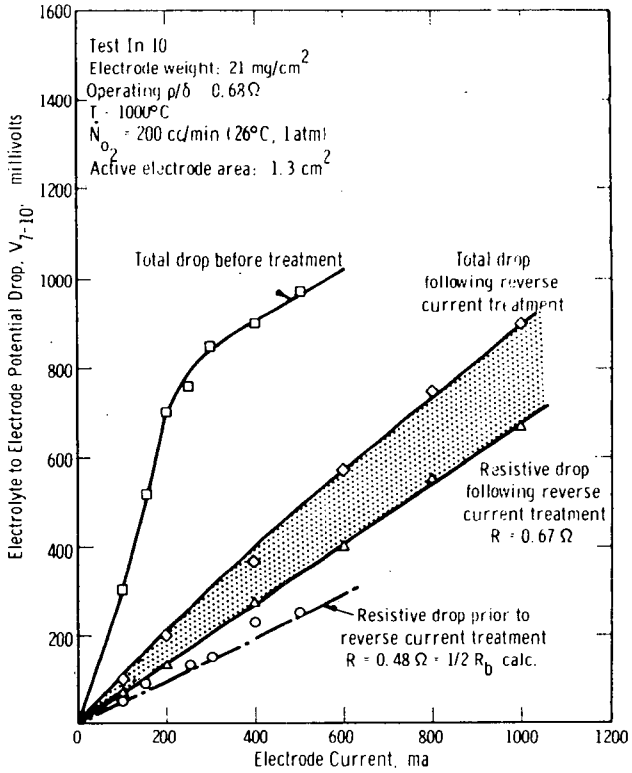

Fig. 8 - Volt-ampere characteristic of Indium Sesquioxide air electrodes before and after "reverse current" treatment

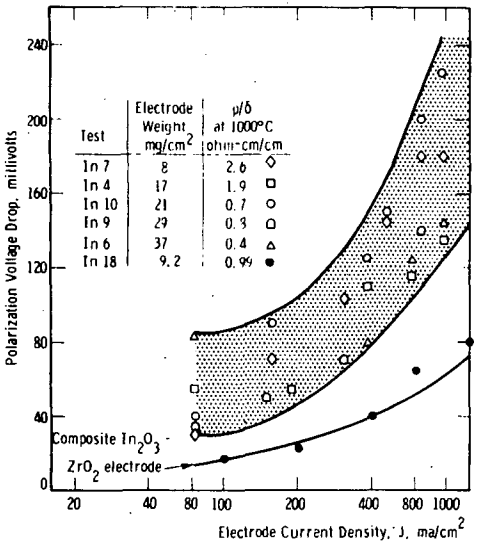

Fig. 9–Indium Sesquioxide electrode polarization following reverse current treatment (1000°C, 1 atm O_2)

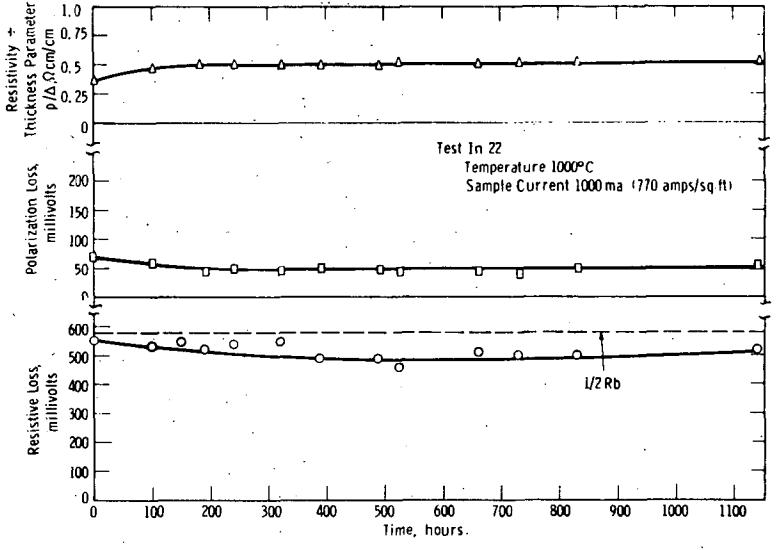

Fig. 10–Life test of a composite In_2O_3 air electrode

(Terminated because of failure of Platinum electrode - loss of In_2O_3 from spots around edges made retesting impossible)

THE USAMECOM-ERDL FUEL CELL ELECTRIC POWER GENERATION PROGRAM

James R. Huff and John C. Orth

Department of the Army
U.S. Army Engineer
Research and Development Laboratories
Fort Belvoir, Virginia 22060

ABSTRACT

Electric power generation in both ground power and vehicular propulsion applications is of major interest to the Army. The goal of the ERDL R & D program is to develop a family of silent power sources in the 1.5 to 15 kw range. The goals for the fuel cell development program have been set on the basis of two generations of developmental models. A systems appraisal of fuel cell technology on the basis of fuels used demonstrates the comparative complexities. The research and engineering accomplishments achieved both under contract and in-house are indicative of the progress being made. The key to obtaining a satisfactory fuel cell is still the electrode. Present fuel cell status may be shown either by considering progress in the oxidation of fuels of increasing complexity or by a consideration of present levels of performance and improvement potential. The overall ERDL approach to achieving the desired family of silent power sources is illustrated by the research program and by tracing the development cycles of special fuel cells and hydrocarbons fuel cells. It is felt that ground power units will provide the enabling technology for many other fuel cell uses.

LOW TEMPERATURE NATURAL GAS FUEL CELL BATTERY

W. J. Conner, B. M. Greenough, G. B. Adams

Materials Sciences Laboratory
Lockheed Palo Alto Research Laboratory
3251 Hanover Street, Palo Alto, California

INTRODUCTION

The Lockheed fuel cell battery is a model power-generating system of the indirect type using reformed natural gas and air. This model, with a gross power output of 430 watts, was constructed as part of a program to develop a reliable, low cost fuel cell system operating on these reactants.

Sulfuric acid is used as an electrolyte to provide compatibility with the carbon dioxide present in both the air and fuel, thus eliminating the need for a carbon dioxide scrubber and a hydrogen purifier. The operating temperature, 60°C, is too low for hydrogen reduction of the electrolyte, but sufficiently high to provide good electrolyte conductivity and a means for product water removal from the waste air. This low operating temperature allows the use of a wider range of construction materials than with higher temperature systems. These advantages, however, are partially offset by the relatively expensive electode materials required for an acid electrolyte system.

A dual-matrix, circulating electrolyte design was selected for this battery because of its reliability and favorable operating characteristics. Electrolyte is circulated between two porous matrices which are contiguous to the operating electrodes. Thus, water balance and temperature control in each cell is simplified, and hazardous cross leakages of reactant gases is prevented; failure of one matrix does not result in a catastrophic reaction between fuel and oxidant. Electrolyte is conditioned thermally and for water balance externally to each cell in a heat exchanger and water feed system to provide a completely controlled cell, regardless of cell load. This conditioning is done automatically and reliably with minimal parasitic power loss.

The battery operates at ambient pressure and employs a novel air feed system. Pressure drops have been minimized with an open manifolding system using low-power blowers to provide adequate air circulation. Reformate is also fed at low pressure to operate the system directly from a three-stage natural gas reformer which draws fuel from a conventional natural gas supply. Gas-liquid differential pressure regulation is achieved by maintaining a siphon action in the pumping of the electrolyte.

System reliability is increased by exclusive use of o-ring seals to eliminate leakage of corrosive electrolyte and hazardous fuel mixture. Battery control is automatically maintained by a safety system which effects system shutdown when triggered by any one of a number of signals indicating abnormal operation. The unit is completely self-contained, requiring only fuel, room air, and water for operation, and an inert purge gas for start-up and emergency shutdowns. A start-up battery is disconnected as soon as electrolyte, fuel, and air are distributed to the cells.

These and other technical advances resulting from Lockheed's fuel cell research and development programs are incorporated as design and operating features. This model provides an effective test bed for studying operational problems and delineating areas for further research and development.

BATTERY CONSTRUCTION AND OPERATION

Cell Reaction. A portion of the free energy of the reaction of hydrogen and oxygen to form water is converted into electrical energy in each cell. Hydrogen for this reaction is supplied as reformate from a three-stage natural gas reformer.* The reformate is approximately 80 percent hydrogen, 19.7 percent carbon dioxide, 0.3 percent methane and 10 parts per million carbon monoxide. Oxygen is supplied to the cell by blowing a stream of air over the oxygen electrode.

Cell Design. A cell is made up of two electrodes, fuel, air, and electrolyte spacer plates, matrix material, and support screens. The active material used for electrodes is designated RA-1 for anodes and AA-2 for cathodes.** Both types are fabricated on expanded tantalum mesh. The electrodes, 145 square centimeters in active area, are stretched flat by a special technique and are spot welded to a thin (2.5 mm) formed tantalum rim. Coarse, expanded-tantalum grids are spot-welded to the rim to provide a supporting structure for the thin electrode material. This rim and screen combination provides a means for current take-off. The anode is carbon monoxide resistant, and operates efficiently over long periods at 60°C in the presence of trace amounts of carbon monoxide.

Spacer plates are made of a corrosion and heat-resistant epoxy resin cast by a closed-mold process. All of the spacers contain o-ring sealed peripheral manifolding for fuel and electrolyte flow. The air spacer is open on two sides to permit blower air to pass uniformly across the cathode surface. Ports for electrolyte and fuel flow are cast into the appropriate plates. Each matrix, with support screen, it held in place in recessed steps cast into the electrolyte spacer. Assembly of the stack is simplified by integral pins on the electrolyte spacer which fit and lock contiguous plates during the stacking operation at assembly. Each fuel spacer is designed to accommodate two anodes and each air spacer, two cathodes. This design feature simplifies gas spacer fabrication and saves weight and volume in the assembled bank. Intercell connections are made externally to each cell with the extended electrode rim.

---

*Institute of Gas Technology, Chicago, Illinois.

**American Cyanamid Company, Wayne, New Jersey.

The electrolyte, 25 weight percent sulfuric acid maintained at 60°C, is circulated through each cell between two sheets of asbestos matrix material* continguous to each electrode. These thin, porous matrices, filled with electrolyte, have a low specific resistance and provide impermeable barriers to the reactant gases. The gas-liquid interface is maintained at each electrode over a wide range of gas-liquid differential pressures. A nominal 10 inches of water gas-over-liquid differential pressure is maintained to prevent electrode flooding.

Module Design. The fuel cell battery consists of three 16-cell modules. One of these modules is shown in different views in Figures 1, 2, and 3. Figure 1 shows the inlet-air side of the module. The open edges of the air spacers and the inter-cell connectors are visible in this view. In Figure 2, the module has been rotated 180 degrees to show the exit-air side of the module. The electrical wiring seen in these figures is used to read individual cell voltages within the module. Series electrical connections are made by connecting extensions of the electrode rims as shown.

Shown in Figure 3 is one of the transparent end-plates through which the fuel spacer for the end cell is visible. The vertical strips inside the space are Viton o-ring stock which serve to direct the fuel flow over the electrode surface and to apply pressure against the electrode to insure good contact between the electrode and its matrix. The o-ring material, because of its resiliency, has a spring-like action which takes up assembly tolerance within the module. Each gas space within the module contains these strips, but in the air spaces they are placed horizontally so as not to obstruct air flow through the module. As the module is shown in Figure 3, electrolyte enters at the bottom of the front end-plate, is manifolded for parallel flow up from the bottom of each electrolyte spacer, and is again manifolded to leave the module at the top of the rear end-plate. With similar manifolding, fuel flows in the reverse direction, entering at the top of the rear end-plate and leaving the module at the bottom corner of the front end-plate.

A low-power, low-pressure fan** provides air flow for each module. The pressure drop which results from blowing air through the module is considerably smaller than the pressure drop for manifolding. As a result of using this air cross-flow technique, a low-power blower is adequate to provide air for the fuel cell reaction and excess air in sufficient quantity to contribute to the cooling of the cell and to remove product water. The air is directed through epoxy-fiberglass ducts into the modules. As it discharges from the module, it passes into a cold-surface chamber on the exit side of each module where product water is condensed from the air stream. In Figure 4, the inlet air duct is shown on the left side of the module; the exit duct with its water-cooled cold surface and exhaust stack is on the right side.

The air filters are shown in Figure 5. The air blowers are mounted inside the ducts directly behind these filters.

---

*Johns Mansville Company, New York City, New York.
**Rotron Manufacturing Company, Woodstock, New York.

Battery Design. The three modules are assembled on a polyester-fiberglass rack measuring 24 × 24 × 40 inches. Total system weight including auxiliaries and controls, but without reformer, is 223 pounds. The auxiliary system is located within this rack and is connected as shown in Figure 6. Figures 4, 5, and 7 illustrate the spatial relationships of the system components.

Materials of Construction. Materials used in the system have been tested for their resistance to the corrosive environment of hot sulfuric acid. Plastics are employed extensively; polypropylene plumbing, epoxy cell parts, polycarbonate reservoirs and module end-plates, epoxy-fiberglass ducts, and polyester-fiberglass system rack. Tantalum is used wherever a metal is required in direct contact with the electrolyte, such as the electrode rims and matrix support screens.

Electrolyte Circulation. The electrolyte circulation system includes a pump, heat exchanger, flow meters, flow control valves, and a liquid reservoir and water balance system.

The centrifugal, magnetically driven pump* is constructed with only polypropylene and Teflon in contact with the hot acid electrolyte. Panel mounted flow meters register the electrolyte flow, and plastic valving controls the flow distribution to the three modules.

Thermal Control. The heat exchanger,** a shell and tube type, is constructed so that the only exposed materials are Teflon and polycarbonate. Depending on the heating or cooling requirements, hot or cold tap water is admitted to the shell side of the heat exchanger. Hot water brings the system up to temperature, after which the hot water valve is interlocked in an off position, and control is maintained by supplying cold water on demand. A thermoswitch in the electrolyte triggers the appropriate heating or cooling water solenoid valve.

Water Balance. The electrolyte reservoir, as shown schematically in Figure 6, consists of a series of cylindrical polycarbonate chambers where electrolyte is returned from the modules and water balance is automatically maintained. Water condensed from the air ducts returns to holding chamber (A) through a filter. Excess condensate is discharged to the drain through an overflow tube. If insufficient water is condensed, a float admits make-up water from an external source by opening the distilled water solenoid valve. All of the spent fuel, laden with water vapor, passes through chamber (B) where water condenses on the walls. The liquid level in this vessel rises until the float valve opens to drop the condensed water into electrolyte compartment (C). A water seal maintained by the float prevents mixing of the spent fuel with air. Electrolyte passes through compartments (C), (D), and (E). The first of these, (C), is a settling chamber which serves to free entrapped gas from the electrolyte. The electrolyte discharges from compartment (C) into (D) which contains a float valve. The initial loading of electrolyte lifts this float valve upwards to the sealed position preventing water from flowing from chamber (A) mounted above. Since

*Micropump Corporation, Concord, California.
**E. I. DuPont De Nemours & Company, Wilmington, Delaware.

excess water is removed from the electrolyte by the air stream, the operation of the cell results in a decrease in electrolyte volume as water is evaporated. This volume change is sensed by the float valve which drops, unseating the valve. Water then flows into this compartment from the air condensate chamber A. When sufficient water has been added to return the float valve and volume to the original level, the valve seals, cutting off water flow. In actual operation, this valve modulates at a point where water is continuously added to make up for the excess that is removed. The reconstituted electrolyte then issues into compartment (E), where a high-low reservoir level sensor detects electrolyte flow irregularities and signals system shutdown if an unsafe condition exists. The electrolyte then is withdrawn by the pump and is circulated through the system.

System Startup. Gas service on the fuel side of the system consists of hydrogen, reformate, and an inert gas, e.g., nitrogen, admitted automatically by solenoid valves. During start-up, the fuel cell system operates on hydrogen and air while the electrolyte is being heated. When the temperature reaches 50°C, the system automatically switches to reformate. This procedure is used to prevent carbon monoxide poisoning of the anode, a reaction which occurs more readily at lower temperatures.

The inert gas is provided as a purge which can be manually operated when the system is to be turned off, but which operates automatically in case of a safety shut-down or whenever the auxiliary power is disconnected.

Safety Features. The automatic safety shut-down is an important feature of the system. It consists of complete system shut-down and inert gas purge in response to a signal from the safety circuit. Low system differential pressure or a significant change in the electrolyte volume due to water imbalance triggers either the high or low level safety circuit in the reservoir. Over-heating of any one of the modules is also sufficient reason for shut-down and is sensed by a thermo-switch in the end fuel spacer of each module. Latching relays in the safety circuit provide control when triggered by any of these signals. These relays are latched into the "safe" position by a manually actuated electrical pulse and then require no electrical power until a safety signal latches the relay in the "unsafe" position actuating system shutdown. In this way, the safety circuit provides control without drawing electrical power.

Parasitic Power Requirements. Except for battery power required for operating auxiliaries during the first few minutes of start-up, the model system is self-sustaining. Figure 8 is a back view of the top section of the front panel showing the location of the electrical control circuits and the auxiliary power inverter. Auxiliary power inversion permits the use of AC motors rather than DC motors with their life-limiting brushes and hazardous brush sparking. The DC to AC inverter operates on fuel cell power, and provides AC power to the air blowers and electrolyte pump. To maintain constant output voltage to the auxiliaries with varying external loads, an automatic voltage selector switch places the required number of cells across the auxiliary power buss to maintain correct voltage within 0.8 volts.

Low-power relays and indicator lights are used to conserve auxiliary power; the maximum auxiliary load at any given time is 58 watts including all power for the blowers, pump, inverter, relays, solenoid valves, and controls. This figure would increase to approximately 70 watts for a 2 kilowatt battery. The front control panel is shown in Figure 9. All of the cell voltages may be measured from the front panel to provide for an easy assessment of cell performance. Various temperatures may be read on the front panel for ready assessment of system operating conditions. The electrical control system is built as a module for easy removal and maintenance.

ELECTROCHEMICAL PERFORMANCE

Initial test work was conducted on cells having an active electrode area of 18 square centimeters. A cell with 90 square centimeters active electrode area was assembled and tested as an intermediate to the final design. Polarization and long-term performance data from these cells provided the scale-up information necessary to design a large cell with 145 square centimeters active electrode area. This cell size was used in the multicell modules.

Long-Term Performance. Long-term performance of the small cells was of particular interest in determining the mode of cell failure, if any. Anode and cathode performance with time was measured versus a hydrogen reference. The results of one 950-hour test are shown in Figure 10. The anode, operating at 60°C on reformate, is quite stable over this long period of operation; the apparent degradation is 10 mV per 1000 hours of operation. The cathode, operating on room air, degrades rapidly in the first 50 hours. This rate then slows and at about 400 hours stabilizes to about 10 mV per 1000 hours. A brief interruption of the load (which occurred at 580 hours) improves the cathode potential (anodic change is negligible). On load again, the cathode degrades rapidly, and after about 48 hours, the cathode potential is the same as it was prior to the interruption. This test cell, representative of a large number of long-term test cells, was operated continuously in an automated test facility.

Figure 11 illustrates a 300 hour performance test conducted on a single large cell similar to those used in the multicell bank. A problem encountered in maintaining the cell temperature in the early portion of this test resulted in unsteady anode performance during this period. At 115 hours, a polarization run (Figure 12) was made, and the temperature control was modified and improved. The latter portion of this test is characteristic.

Cell Voltage-Current Characteristics. The polarization diagram for the large cell is presented in Figure 12. A resistance-free curve is plotted to show the effect of cell resistance on cell performance. Also included is a plot of total power output from the cell. The dashed voltage line illustrates an average cell voltage found in an operating 16-cell module.

In a cell with a carbon monoxide resistant anode, the anodic polarization initially and over long periods of time is low, unless the anode is poisoned by a fuel gas with a high carbon monoxide content or decomposition products from the electrolyte (hydrogen sulfide). This may happen when a cell is operated at too high a temperature or when certain materials of construction not compatible with hot sulfuric acid are used.

The cathode, on the other hand, is rather severely polarized and controls cell voltage at low current densities. As the load is increased, the cathode potential stabilizes and cell resistance then controls cell potential. Even though precautions were taken in the design, fabrication, and assembly of the large cell and modular assembly, the unit cell specific resistance is double that of the small cell. Current development is directed to the definition and further reduction of this increased resistance.

Air-Fuel Flow Rates. A series of tests were conducted with the large cell to define reactant flow rates required to support cell operation at different current densities. Figure 13 illustrates the performance of the anode with reformate. This electrode requires a fuel flow rate only slightly in excess of stoichiometric at all current densities. However, at low current densities with stoichiometric flow, anodic polarization increases slightly due to poor gas flow distribution. The non-reactants in the fuel tend to mask off portions of the anode at low flow rates. At higher current densities with stoichiometric flows, the higher gas flow helps to sweep non-reactants out of the stagnant areas of the anodic gas spacer. Because of this, the anode operates for extended periods at high current densities at the stoichiometric fuel flow rate because of the net purging of the fuel spacer with the carbon dioxide and other non-reactants introduced into the cell as part of the fuel.

The cathode can be operated at stoichiometric rates up to 50 mA/cm^2. At higher current densities, cell performance drops off drastically, but air flow rates three times stoichiometric or greater will support all current densities through (150 mA/cm^2). These data are presented in Figure 14.

An analysis was made of the air flow through a 16-cell module with a fan* which has a free air delivery of 50 cubic feet per minute. The volumetric flow through each air spacer was calculated from velocity probe measurements made at the discharge of each cell spacer. The fan draws air through a polyurethane foam filter and blows air through the module. No distribution device is used in this configuration, and the uneven flow pattern across the face of the module is shown in Figure 15. The lower flow rate through the center cells is caused by zero air flow through the hub of the fan which is located directly in front of cells 7-8 and 9-10. Lines of constant 1 and 10 stoichiometric flow rates are shown in Figure 15 to provide a reference. It can be seen that this fan and distribution configuration is adequate since a minimum three stoichiometric flow requirement is met. The disadvantages of higher air flow rates are the extra load impressed on the air condenser and water balance control system and the lower cell temperature of high-flow-rate cells. If, with the fan used, air flow is decreased further (by restricting the air inflow), the edge-tocenter air flow distribution pattern becomes more distorted. It is therefore imperative that air flow through

*Rotron Sentinel Fan with a 745 motor.

the cells be high enough for good cell performance, but not too high for good water balance control.

The vent stack height used in the multicell system provides sufficient updraft in a module without fan and filter to support the bank at 100 mA/cm^2 at 60°C.

Total System Performance. The assembled, three module, 48 cell battery described in this paper exhibits the performance characteristics shown in Figure 16. The system has been operated under a variety of loads with completely automatic control. The system operates efficiently on reformate and room air to give the power output shows in Figure 16. Little excess fuel is required to maintain a steady load. Sufficient air flow is obtained from 5 watt fans. Work is continuing to define the limiting parameters in the cell performance in order to increase total output from the battery.

FUTURE IMPROVEMENTS

One area for improvement in this system is in the design of a larger, and less costly cell. A larger cell would allow a reduction in the number of cells per module for the same power output. Improvements would include reduced cell resistance, increased ratio of active to inactive area in cell cross section, improved structural integrity, and the development of mass production techniques for cell parts. Electrodes with low catalyst loading would be incorporated in the design to reduce electrode unit costs further.

The cell and module design would also be optimized to maximize performance with respect to minimal weight and volume. This would be achieved with an improved electrode and matrix containment design which would eliminate tantalum at certain points in the cell where it is now used.

Another area for improvement in this system is in further reduction of parasitic power requirements. Thermal control can be achieved by cooling with air instead of water. This can be done with a bypass air cooling system which allows cooling air to flow through or around each cell, regulated by a damper under passive control. Use of a single blower with improved air distribution for larger modules will reduce parasitic power requirements further.

These and additional improvements should establish this system as an efficient, economical power source for future domestic and ground-based military applications.

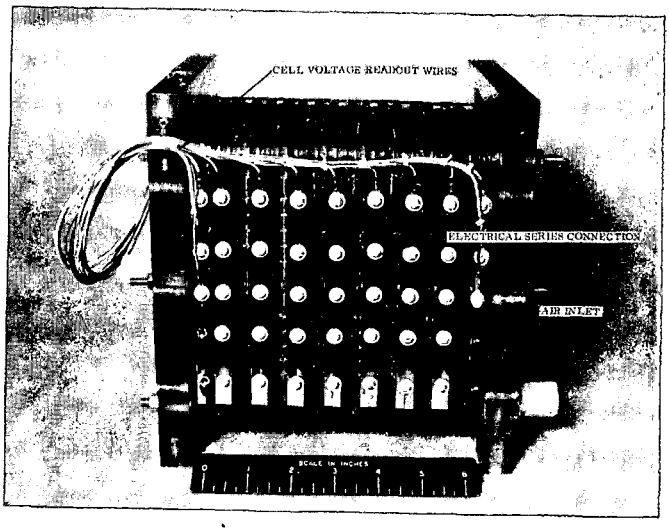

Fig. 1 Sixteen Cell Module – Inlet Air Side

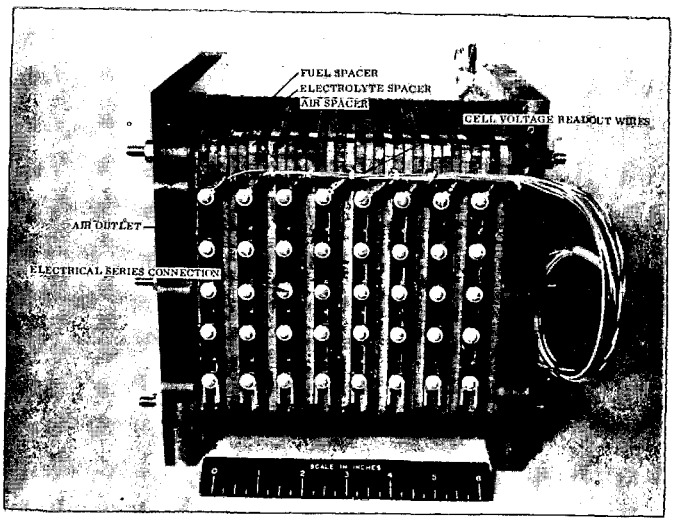

Fig. 2 Sixteen Cell Module – Exit Air Side

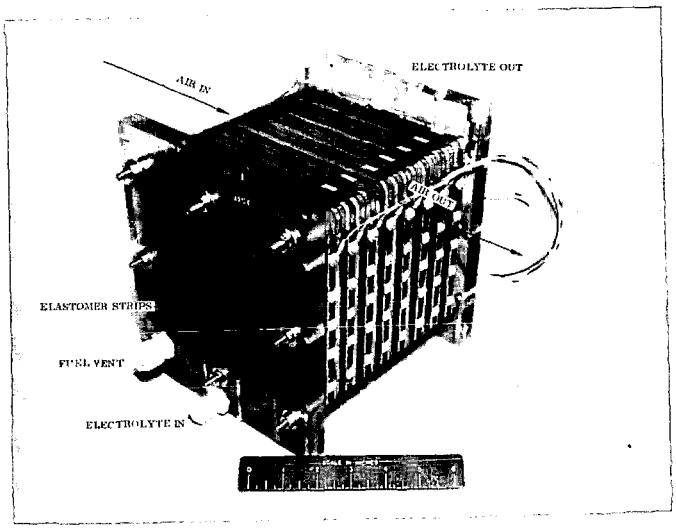

Fig. 3 Sixteen Cell Module

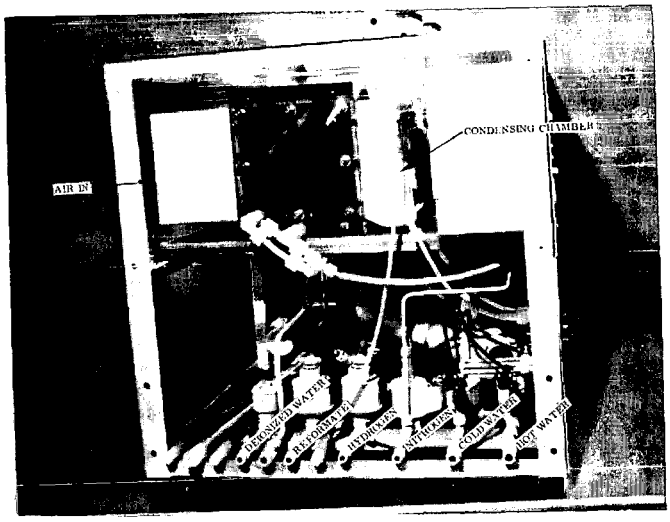

Fig. 4 Fuel Cell System – End View

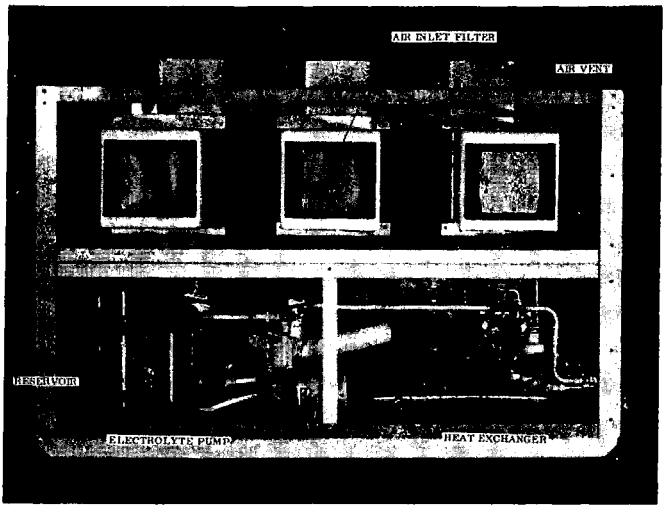

Fig. 5 Fuel Cell System – Rear View

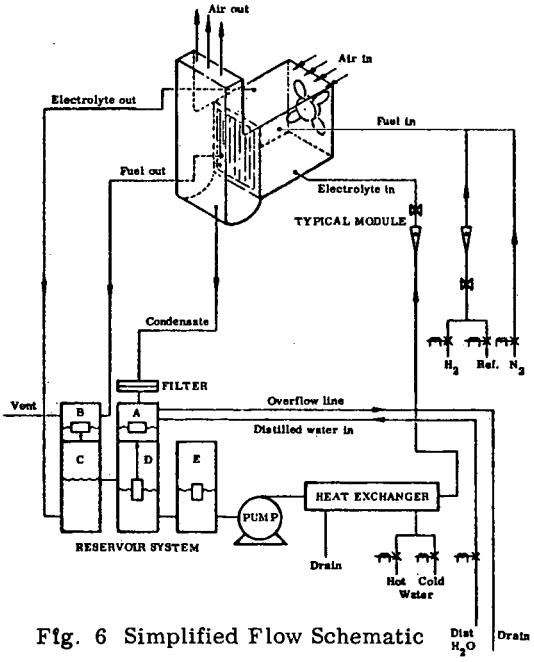

Fig. 6 Simplified Flow Schematic

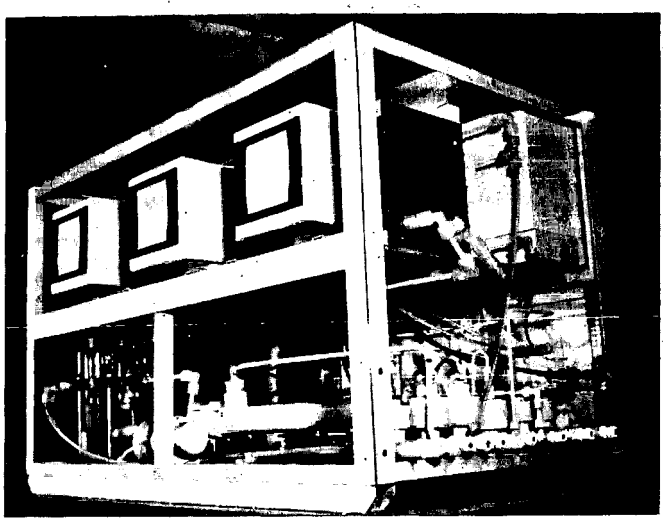

Fig. 7 Fuel Cell System

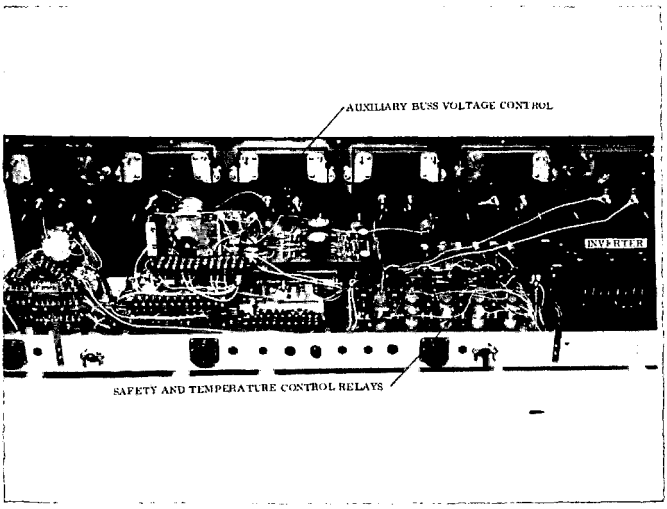

Fig. 8 Electrical Controls

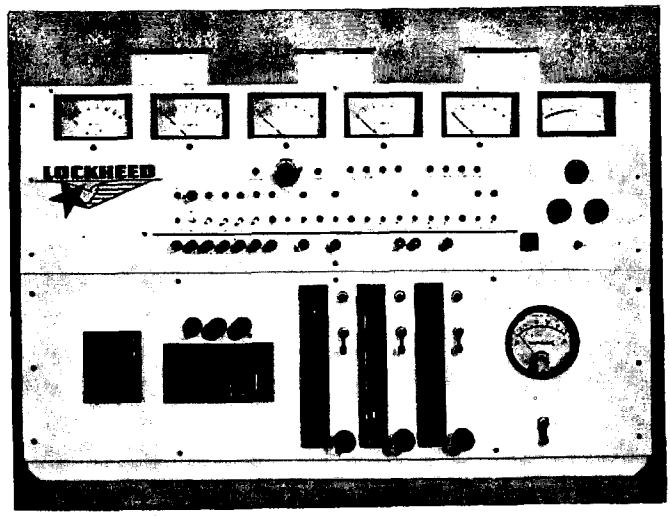

Fig. 9 Fuel Cell System – Front Panel

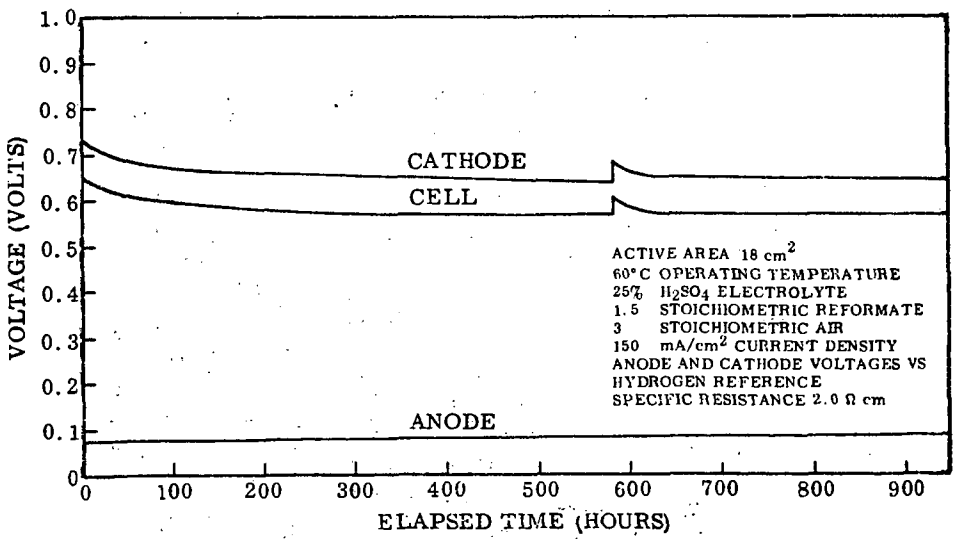

Fig. 10 Long-Term Performance of a Small Cell

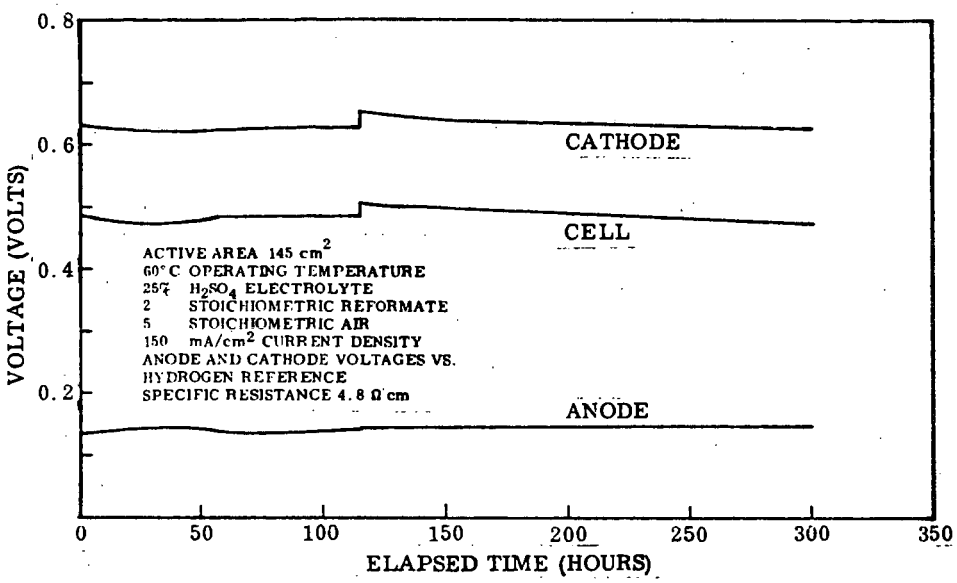

Fig. 11 Long-Term Performance of a Large Cell

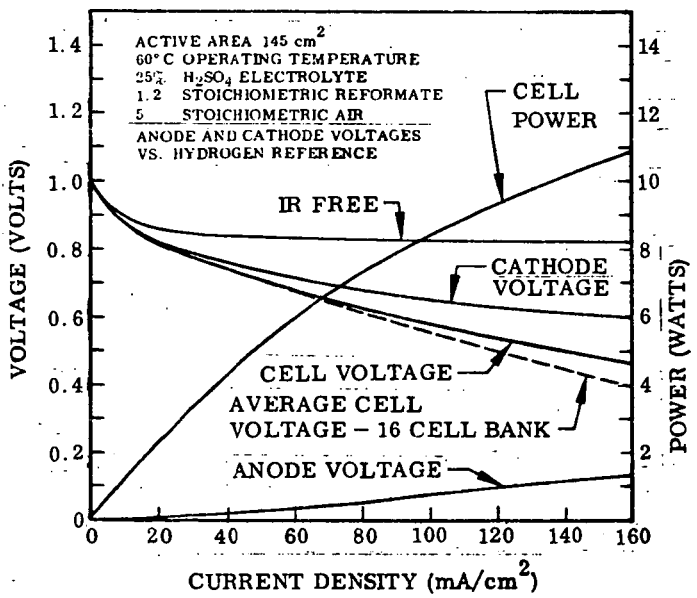

Fig. 12 Performance Characteristics of a Large Cell

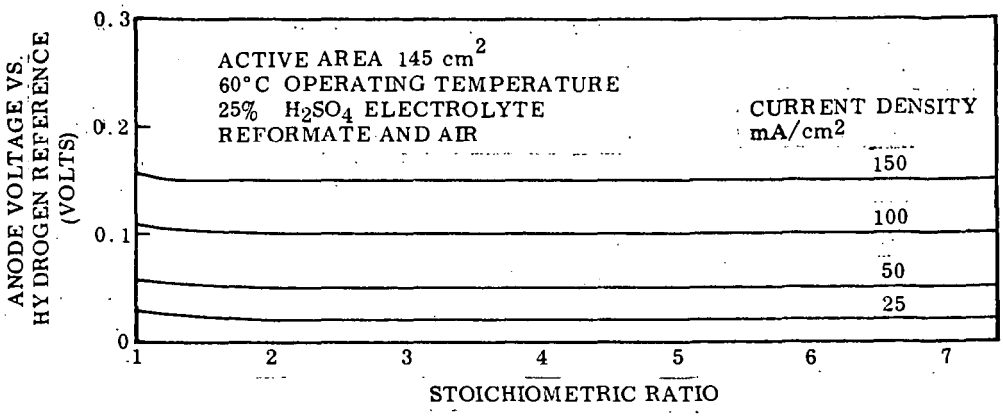

Fig. 13 Variation of Anode Voltage With Fuel Flow Rate

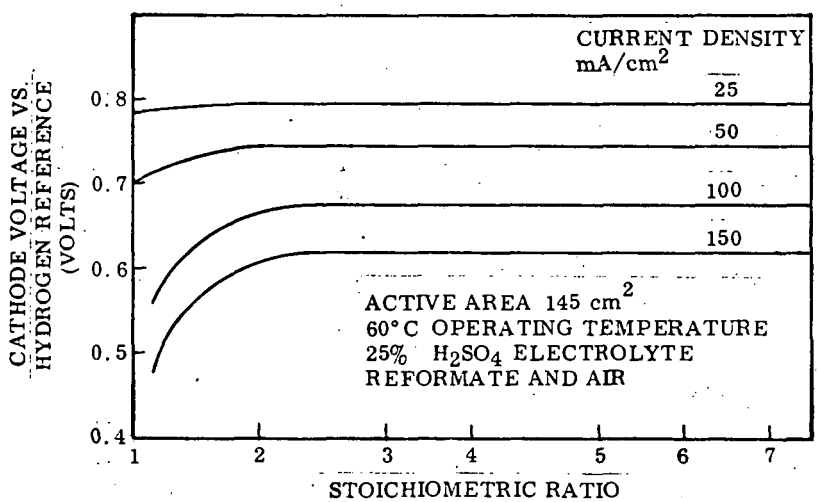

Fig. 14 Variation of Cathode Voltage With Air Flow Rate

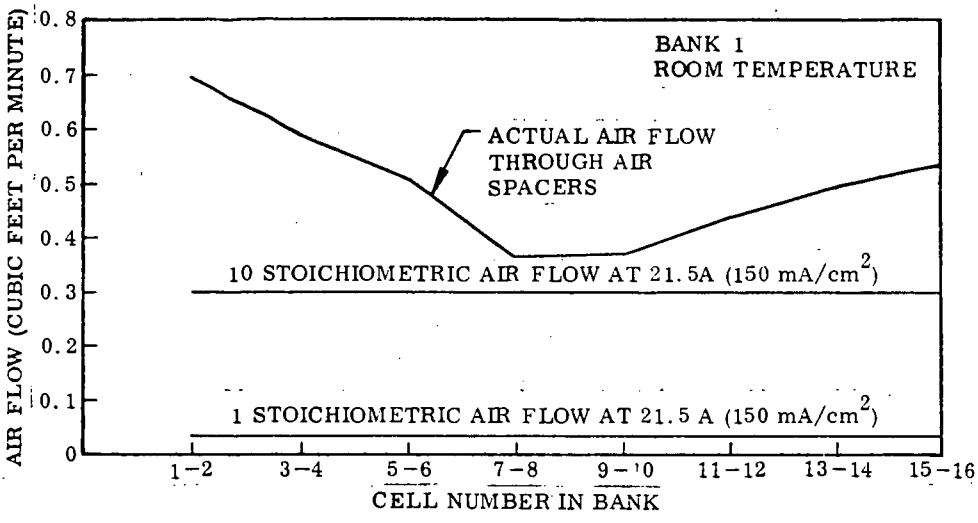

Fig. 15 Variation of Air Flow in Air Spacers of Multi-cell Bank

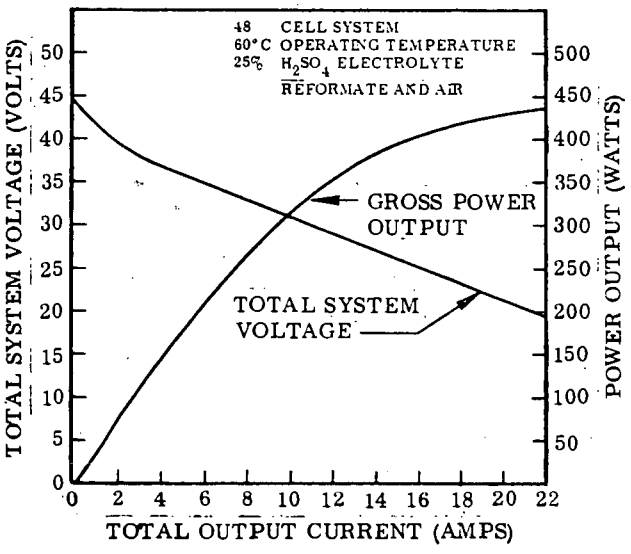

Fig. 16 Performance of a Multi-cell Bank

MILITARY HYDRAZINE-AIR FUEL CELL POWER SUPPLIES

R. E. Salathe
J. O. Smith
J. P. Gallagher
P. L. Terry
J. Kozloff
L. F. Athearn
P. Dantowitz

MONSANTO RESEARCH CORPORATION
BOSTON LABORATORY
Everett, Massachusetts 02149

INTRODUCTION

Monsanto Research Corporation has constructed portable hydrazine-air fuel cells in 60, 300, and 500 watt sizes. The 60-watt units are for the Electronic Command at Fort Monmouth and the 300-watt units for the Army Corps of Engineers at Fort Belvoir.

Hydrazine-air is the electro-chemical energy source chosen for this power range because it can be engineered into reliable, quiet, and simple systems with high watt-hours per pound of over-all weight. This paper presents a number of design considerations in construction of these fuel cells. The basic design of all the units is the same.

Two design questions had to be answered at the outset: first, what is the best combination of components in the single cell to give the desired electrical performance; and, second, how can this cell be packaged to give a battery with optimum characteristics?

THE HYDRAZINE-AIR COUPLE

The single cell that we have chosen operates on 5M KOH in which 0.5 to 1.5 M N_2H_4 is dissolved as the fuel. The anode is a Pd-catalyzed nickel plaque. The separator is asbestos, and the proprietary cathode is a thin, waterproof, porous membrane.

The initial performance of a typical cell and its performance after 1000 hours of operation are shown in Figure 1.

The initial performance curve is fairly flat dropping about 0.1 volt between 10 and 100 ASF. With aging, the voltage drop-off becomes greater, amounting to approximately 0.15 volt between 10 and 100 ASF at 1000 hours. The design operating point for the 60-watt unit is 0.78 volt at 60 ASF. It may be noted that a considerable safety factor has been included in the design performance. The coulombic efficiency at the design point is better than 90%.

The data shown are for operation with four times the stoichiometric amount of air. However, no adverse affects have been noted on operating between two times and sixteen times the stoichiometric amount of air. The cells have been operated on pure air containing no CO_2 and on unscrubbed laboratory air. There appears to be no difference in performance or life. The air is essentially at atmospheric pressure.

Hydrazine concentration is not critical. Good performance is obtained between 0.5 and 1.5M.

Increasing the operating temperature to 194°F gives only slight improvement in performance and shortens the cell life to approximately 200 hours. Decreasing the cell temperature below 140°F leads to some drop-off in performance with no appreciable increase in cell life.

OVERALL DESIGN OF THE UNIT

After a satisfactory hydrazine air couple had been obtained, the second major task was to incorporate it in a functional hardware system. The system had to (1) maintain heat and mass balance and (2) furnish a regulated voltage output. The schematic of the system is shown in Figure 2.

The electrolyte, which, as stated earlier, is 5M KOH containing from 0.5 to 1.5 M N_2H_4 is pumped into the fuel cell module where the N_2H_4 reacts with hydroxyl ions to give nitrogen, water, and electrons. The mixture then goes to the separator where the nitrogen is removed and eventually vented. Although the N_2H_4 concentration is not critical it is maintained approximately constant by a hydrazine concentration sensor which actuates a solenoid valve allowing hydrazine to flow from its tank into the electrolyte.

The chemical air, which is the air used to oxidize the hydrazine, is furnished by a fan. Since the air electrode operates at atmospheric pressure, only sufficient pressure (several tenths of an inch of water) is needed to force the air through the module and maintain approximately even flow distribution among the various cells.

MASS BALANCE CONTROL

Optimum life and performance characteristics of MRC hydrazine fuel cells are realized when they are operated with potassium hydroxide electrolyte maintained at 3 to 5 molar concentration. A mass balance control system achieving this degree of control consists of an electronic level detector geometrically located in the electrolyte tank so as to be insensitive to the attitude of the tank, a speed-controlled chemical air blower; and an electronic circuit to drive the blower providing stoichiometric air flow ratios of approximately 2.5 at no load parasitic conditions, to 3.5 at rated load output. In all modes of operation and environment, control of the stoichiometric air flow ratio is such as to produce an anolyte dilution condition. As the anolyte dilution level increases in the reservoir tank, the level detector causes a signal to be produced. This signal is transmitted through a control circuit to the chemical air blower, causing increased blower speed and delivery rate, regardless of load level, thus affording increased evaporative capacity and causing a mass removal condition to prevail. The maximum air blower capacity necessary to provide drying conditions at all specified environmental air conditions is about 10 times stoichiometric. This blower rate will prevail when the level detector is completely covered. As the liquid level in the anolyte reservoir decreases, the level detector will be uncovered and the override signal will be removed, causing the chemical air blower to revert to a normal mode of delivery, i.e., between 2.5 and 3.5 times stoichiometric from "no load" to rated output.

In actual operation it has been found that such a system will hunt, causing anolyte level regulation and thus concentration control to exist

within a tight band of approximately ± 0.25 molar. Mass balance control systems employing the above-mentioned techniques have been quite successfully operated. Typically, a 300-watt unit was operated under various loads ranging from zero load to 400 watts for a period of approximately 75 hours with an electrolyte molarity variation of only ± 0.3 molar. It is anticipated that the incorporation of this type of mass balance control in conjunction with Monsanto Research Corporation electrodes will permit operation for 250 to 300 hours on a single charge of electrolyte.

HEAT CONTROL

Heat is removed from the hydrazine fuel cell system mainly through (1) the air-cooled heat exchanger, (2) evaporation of water in the stack at the air cathode, (3) evaporation of water by the nitrogen produced by oxidation of N_2H_4, and (4) warming of reaction air in passing through the stack. The incorporation of a mass balance system dependent on control reaction air flow rates permits the utilization of a basically simple single-temperature heat removal system. Such a system having adequate heat removal capacity consists of an air-to-anolyte heat exchanger with suitable blower and thermostat controls. Positive control of electrolyte temperature and thus of cell and stack operating temperatures are maintained at approximately 135°F regardless of mass balance considerations. For operation at low ambient temperatures a thermostatically controlled immersion heater is incorporated within the electrolyte tank to permit fast start up.

FUEL CONTROL

Since hydrazine is consumed not only to produce power but also by a number of parasitic processes, it is desirable to have a means of directly sensing and controlling hydrazine concentration. In our case this has been accomplished by use of a diffusion controlled sensor.

Concentration determination by hydrazine diffusion limitation depends upon the difference in voltage levels required for the electrolysis of N_2H_4 and H_2O. It is well known that the electro-chemical dissociation of hydrazine into hydrogen and nitrogen occurs, even at high current densities, at well below 1 volt, while dissociation of water occurs at considerable above 1.23 volts. This voltage difference is put to use in the operation of a fuel feed control and detection system. It has been found that the shift from hydrazine electrolysis (hydrogen and nitrogen production) to water electrolysis (hydrogen and oxygen production) occurs virtually instantaneously at a current density corresponding to the concentration of hydrazine in solution. A typical curve illustrating this fact is shown in Figure 3. This then permits a current density to be selected that corresponds to a specific hydrazine concentration. When the concentration falls below this value, the voltage will shift upward to support the water electrolysis; as the solution becomes enriched due to fuel addition, the voltage falls sharply. There is, in effect, a "forbidden" voltage region that is never reached. Thus, a convenient signal is developed at each current density to trigger the fuel feeding mechanisms. Mechanization of this system is straightforward. It consists of a detector element inserted at the discharge side of the anolyte pump; a controller consisting of a constant current power supply, detector signal amplification, output signal gate control; and a solenoid valve employed to control on-off introduction of fuel. Gain control of this system is conveniently provided by "On" time control of the solenoid, pulse repetition frequency imposed on the concentration detector, and

signal level imposed on the concentration detector. Excellent fuel utilization efficiencies have been obtained employing this system. As an example, a 60-watt fuel cell operated at 85 ASF yielded 311 watt-hours per pound of fuel while producing 60-watts of useful output when a load-sensing fuel feed control was employed. The identical unit operated with a concentration detection fuel feed system at approximately 0.7 molar hydrazine for the same load yielded 410 watt-hours per pound of fuel. Figure 4 depicts the control of hydrazine concentration actually achieved on a 300-watt system.

VOLTAGE CONTROL

Four types of voltage regulators were considered: (1) the cell tapping relay, (2) the shunt type, (3) the dc-ac-dc type, and the series type. At the present state of the art, the optimum choice appeared to be the series type.

A functional diagram of the regulator is shown in Figure 5.

The output voltage of the series transistor switches are monitored with the voltage detector. When this voltage exceeds a pre-set limit, the detector, through a converter circuit, will in effect cause the series transistor to operate at a higher resistance.

PHYSICAL AND OPERATING CHARACTERISTICS

A picture of the present 60-watt unit is shown in Figure 6. Its specifications are given in Table I.

CONCLUSIONS

Utilizing the hydrazine-air electrochemical couple and employing system design techniques as enumerated above, rugged, reliable, high watt-hour-per-pound fuel cell power supplies can be produced for military applications.

ACKNOWLEDGMENT

This work was done under contract DA28-043-AMC-01460(E) with the U. S. Army Electronics Command, Fort Monmouth, N.J., and contract DAAK02-67-C-0117 with the U. S. Army Engineers Research and Development Laboratories, Fort Belvoir, Virginia.

Table I

CHARACTERISTICS OF 60 WATT
EXPLORATORY MODEL

Weight (+ fuel + electrolyte)	14.5 lbs.
Volume	0.35 ft^3
Power Output	60 watts
Operating Life	450 hrs.
Voltage Regulation (28V, 14V, 7V)	$\pm$ 10%
Watt-hr/Fuel Charge	390
Fuel Charge	1.15 lbs
Low Temp. Start	+14°F
High Temp. Run	+ 115°F

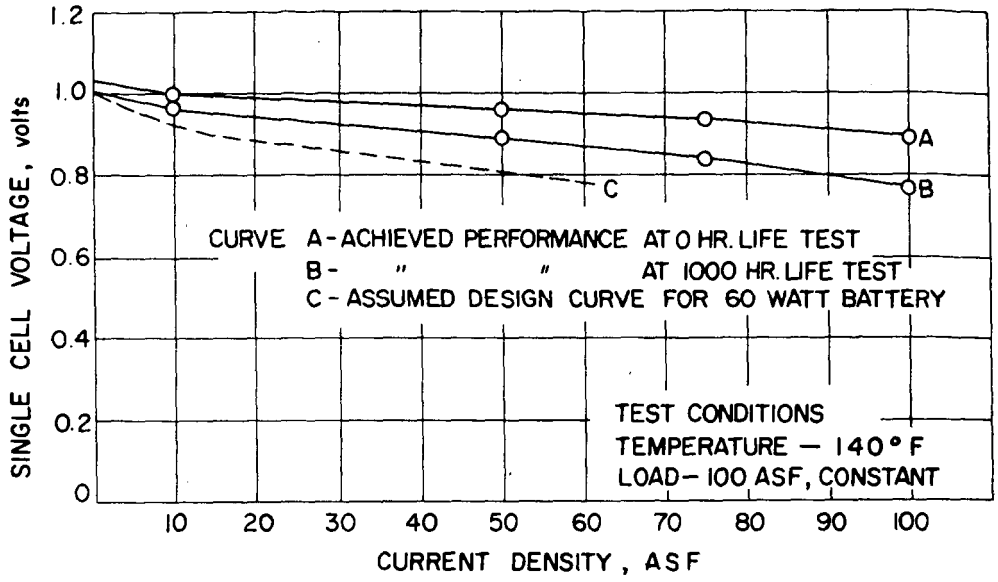

PERFORMANCE CURVES FOR HYDRAZINE-AIR FUEL CELL

FIGURE 1

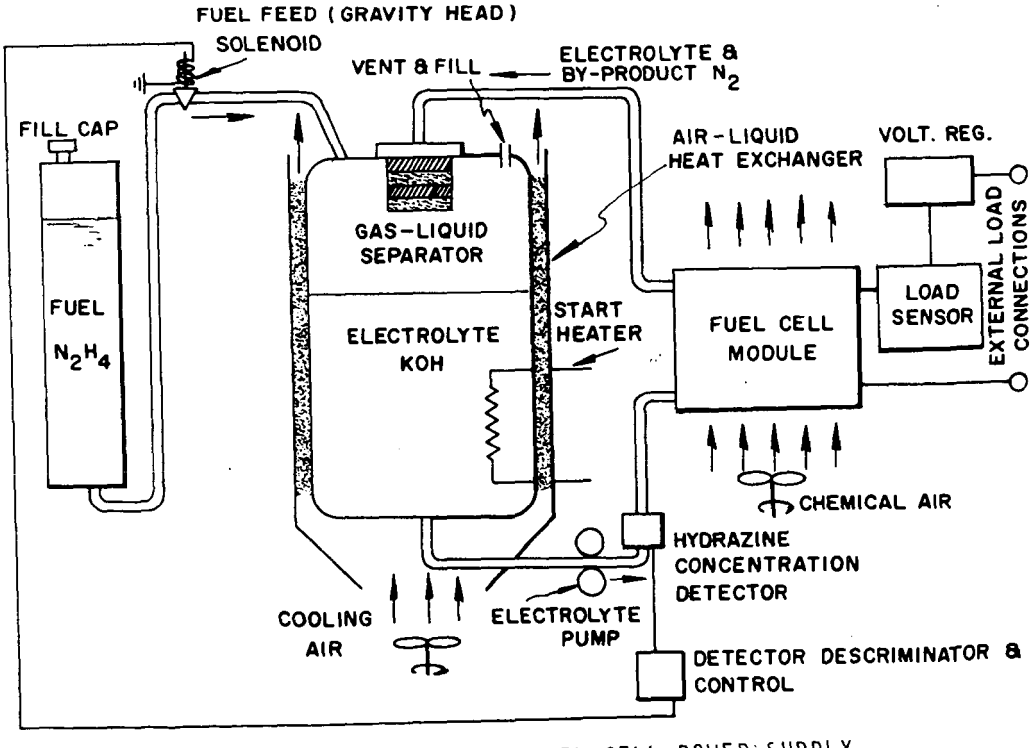

TYPICAL HYDRAZINE-AIR FUEL CELL POWER SUPPLY

FIGURE 2

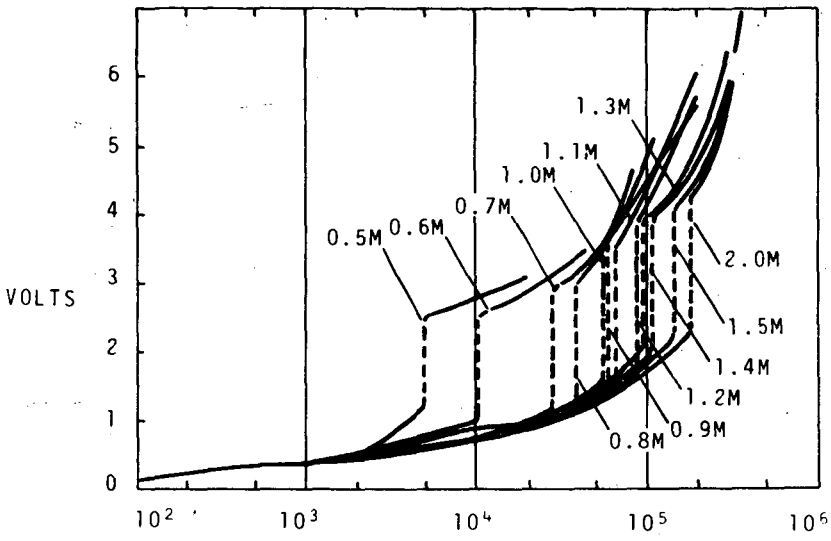

PRINCIPLE OF OPERATION FOR IONIC STRENGTH DETECTION METHOD

FIGURE 3

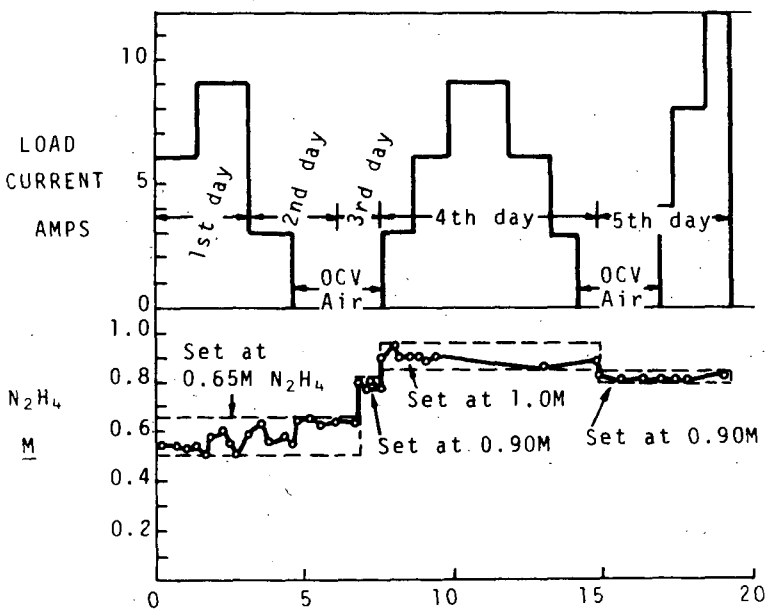

PERFORMANCE OF 300-WATT HYDRAZINE/AIR FUEL CELL
WITH
DIFFUSION-CONTROLLED FUEL FEED

FIGURE 4

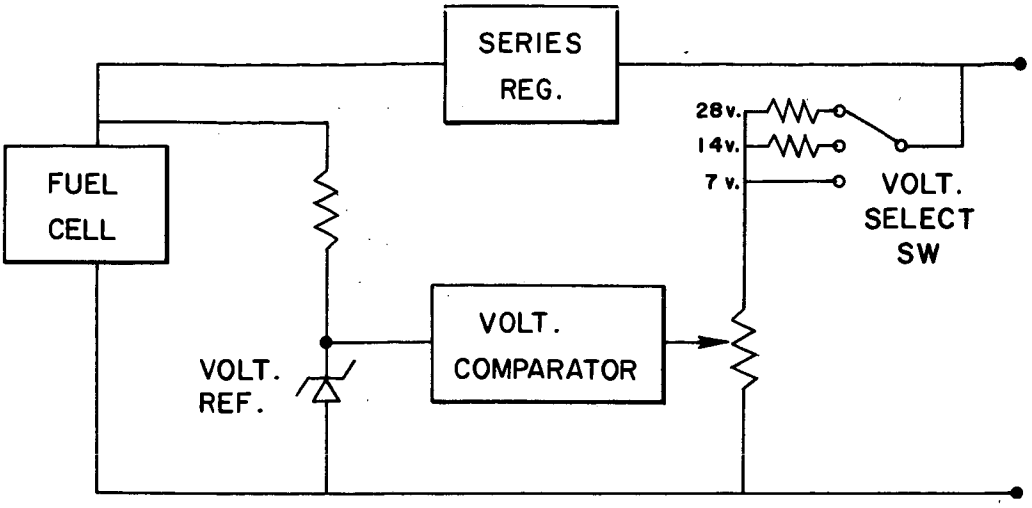

60 W UNIT OUTPUT REGULATION SYSTEM

FIGURE 5

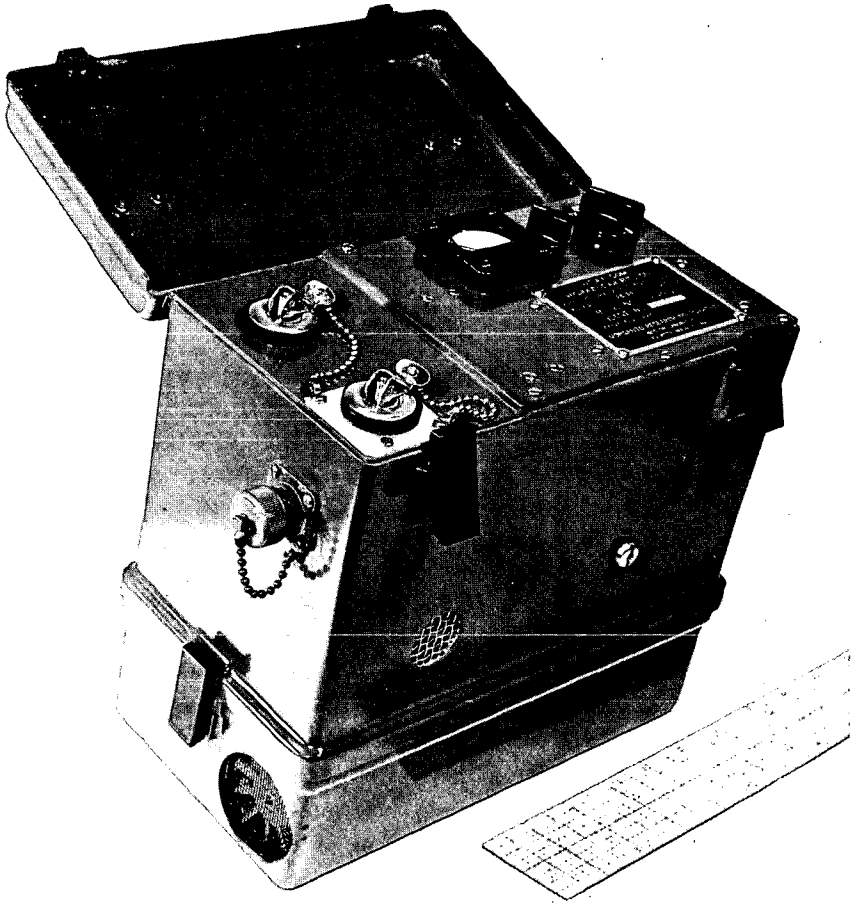

PHOTOGRAPH OF THE 60-WATT UNIT

FIGURE 6

A LIQUID HYDROCARBON FUEL CELL BATTERY

E. H. Okrent and C. E. Heath

Esso Research and Engineering Company
Linden, New Jersey

Introduction

Several types of fuel cell systems are currently under study to meet the wide range of anticipated power, weight and duty cycle requirements. However, commercial (non-military) fuel cell power systems will ultimately have to consume the more economical hydrocarbon fuels in order to compete with existing power systems. This can be accomplished in a number of ways. The hydrocarbon fuel can be fed directly to the fuel cell or it can be converted by reforming or partial oxidation to hydrogen for subsequent electrochemical oxidation. Direct hydrocarbon-air systems are generally simpler but they require acidic carbon dioxide rejecting electrolytes, thus necessitating acid resistant (noble metal) catalysts. Indirect systems can in principle use non-noble catalysts at the expense of system complexity, and in the case of the reformer-air system an expensive palladium diffusor is required.

The development of a direct liquid hydrocarbon-air fuel cell battery is being actively pursued in our laboratory. Liquid hydrocarbon fuels are particularly suitable because they are inexpensive, readily available materials with no transportation or handling problems. Furthermore, operation with liquid fuels results in a simplified carbon dioxide separation problem with no heat duty for hydrocarbon vaporization. Unfortunately, the electrochemical reactivity is inherently lower for liquid hydrocarbons relative to that of propane[1] or butane[2][3]. As a result, highly active electrode structures are required.

The development of high performance anodes (1964-65) and active cathodes has provided a tool for the evaluation of the engineering feasibility of direct hydrocarbon-air fuel cell batteries. This is particularly important since these active anodes all exhibit fuel transport into the interelectrode space. Fuel transport and carbon dioxide rejection in the interelectrode space could dictate system design and operation criteria.

Consequently, a liquid hydrocarbon (decane)-air fuel cell system was developed to assess program assumptions (interface maintaining electrodes, thermal cycling damage, 150°C operation, etc) and illustrate potential obstacles to the use of these novel electrodes in high power density batteries. Liquid decane was selected as the representative fuel because it is typical of a commercial saturated hydrocarbon fuel. Major emphasis was placed on examining the electrolyte space, flow and venting required to prevent decane transport to the cathode. This fuel transport presents a potential explosion hazard and can result in cathode poisoning. In addition, a fuel recovery scheme is required to maintain coulombic efficiency. The five cell assembly to be discussed was intended as a research tool. Therefore, no attempt was made to size or package the system into a compact low weight assembly. Rather ease of control and modification were the key consideration.

Influence of Electrode Structure on Cell Design

Electrode preparation variables can have a profound affect on cell design. Aside from their obvious role in cell output, the extent to which the control and maintain the interface between reactant streams (fuel-electrolyte, electrolyte-air)

is especially important to cell design since at the temperatures (150 to 250°C) required for effective hydrocarbon oxidation auxiliary interface control materials (membranes, matrices, etc) are almost non-existant. Thus, an effective hydrocarbon or air electrode for this system must perform a dual function. It must establish and control the reactant-catalyst-electrolyte three phase contact inside the electrode while maintaining bulk separation of the reactant and electrolyte phases to prevent gross leakage.

Anode Structure

When porous sintered platinum-Teflon gas electrodes are used in liquid hydrocarbon cells their performance is quite poor, despite the fact that they give significant activity on vaporized fuel of the same carbon number. Research with liquid decane indicated that progressive fuel flooding was responsible for this poor liquid hydrocarbon performance(2). Furthermore, it was found that this problem could be eliminated by altering the platinum-Teflon dispersion techniques and changing sintering conditions to re-establish the desired wetproofing. This is illustrated in Figure 1. Using these techniques excellent liquid hydrocarbon electrodes can be prepared. Early structure of this type gave limiting currents in excell of 140 ma/cm^2 with 150°C liquid decane. In addition, further performance improvements could be obtained by incorporating a porous Teflon barrier on the fuel side of the electrode. This improved performance could not be attributed to a flow restriction phenomena, since it was found to be independent of barrier thickness between 3 and 350 mils. However, it does appear to be due to a capillary effect which controls the rate of release of the liquid fuel to the active electrode surface. This effect is not fully understood. Unfortunately, these active structures show a significant amount of fuel transport through the pores of the hydrophobic electrode. This phenomena was first reported by Shropshire, et al(3) in 1965, and attributed to either internal gasification (boiling) in the hydrophobic matrix or diffusive flow (atmolysis) akin to that observed with gaseous reactants. This diffusive flow was discussed by Katan and Allen(4). It appears that a combination of both these effects are responsible for the liquid fuel transport observed. Recent studies indicate that fuel transport rate is independent of electrode activity (for the active systems) thus suggesting that the transport rates can be reduced while still retaining good activity. However, efforts to reduce the atmolysis rate have not met with success as yet.

Tests in small (10 cm^2) total cells indicated that electrode checking and cracking occurred after repeated thermal cycling of the electrode. In addition, anode barrier separation was found to reduce electrode activity by a factor of two. Both these deficiencies were corrected by laminating a 3.5 mil fuel barrier to the preformed anode structure to produce an integral electrode structure. As indicated in Figure 1, the laminated electrode gave about the same performance as the conventional separate barrier system (within fabrication repeatability) and this laminated structure was selected as the standard for the multicell assembly. Current structures attain 200 ma/cm^2 at 0.45 volt polarized with limiting currents of up to 300 ma/cm^2.

Cathode Structure

Operation in intermediate (150-250°C) temperature electrolytes imposes more stringent cathode structure requirements than normally encountered in low temperature fuel cells. Cathodes designed for this service must maintain positive interface control after repeated temperature cycling due to start-up and shut-down sequences. This is especially important in the liquid hydrocarbon-air fuel cell systems since oxygen transport into the electrolyte space cannot be tolerated in view of the significant decane transport previously discussed.

Preliminary experiments indicated that a thin porous Teflon film (10 micron pores) applied to the air side of the cathode could provide the required interface control without loss in electrode performance. However, oxygen transport was observed with a commercial porous Teflon laminated electrode structure. Consequently, tests were conducted to determine the effect of cladding pore diameter on cathode performance and oxygen transport using Teflon films with pores ranging from 5 to 100 microns. This study indicated that pore diameter is an important parameter. Optimum oxygen and air performance was obtained when ten micron pore Teflon films were laminated to the cathode, and no oxygen transport was observed at this pore diameter.

As a result of these studies, three potential cathode systems have been developed for the hydrocarbon-air total cell system. These include a (1) 50 mg Pt/cm^2 sintered platinum Teflon electrode laminated to a 3.5 mil (10 micron pore) porous Teflon film, (similar to the anode structure) (2) a 10 mg Pt/cm^2 Cyanamid AA-1 electrode bonded to a porous Teflon film and (3) a 2.5 mg Pt/cm^2 sintered carbon Teflon structure. The air performance of these potential candidate systems are summarized in Figure 2. As expected, the cathode with the highest platinum loading gave the best performance. However, a five-fold reduction in catalyst loading was obtained with the bonded Cyanamid AA-1 electrode at the expense of only 70 mv debit. The carbon cathode was rejected because of its rather poor open circuit and load reponse and its high decane sensitivity.

Maintenance of cathode integrity has found to be the key to successful total cell operation. Therefore, a series of single and multicell tests were conducted varying cathode configuration while holding the anode configuration fixed. These tests used a 10 cm^2 (1.5 inch diameter) cell to eliminate scale-up problems and minimize hydrocarbon hold-up in the event of cathode failures. Analysis of these data indicates that the initial performance of both the clad Cyanamid AA-1 electrode and the laminated sintered platinum-Teflon studies are quite comparable despite the five-fold variation in platinum content. The average cell performance obtained in these single and multicell tests are shown in Figure 3. The five assemblies tested fell essentially on a single curve with an average peak power capability of 17 mw/cm^2 on oxygen and 14 mw/cm^2 on air. However, the best three cell stack gave 21 mw/cm^2 on oxygen and 17 mw/cm^2 on air. This compares quite well with performance projections based on half cell measurements (22 and 19 mw/cm^2 on oxygen and air respectively including cell resistance loss). Thus, both these electrodes would be suitable for total cell systems. However, the Cyanamid AA-1 structure was found to be quite sensitive to decane "poisoning" which could occur in the event of system upsets. The 10 cm^2 cell was particularly sensitive to this because of inadequate venting and decane residence space. In fact, this decane sensitivity increased with decreasing platinum loading; the 2.5 mg Pt/cm^2 carbon electrode was the most sensitive and the 50 mg Pt/cm^2 laminated cathode least sensitive. Consequently, the 50 mg/cm^2 laminated cathode was selected for use in the final 4" x 4" five cell assembly to minimize performance losses resulting from control system upsets.

Liquid Decane-Air System Description

Liquid hydrocarbon (decane) transport through the cathode cannot be ignored in cell design especially when oxygen or air transport through the cathode structure is even a remote possibility. Impingement of liquid hydrocarbon on the active cathode could result in a severe performance debit and if oxygen atmolysis occurs, and detonation is possible. In addition, the combined effect of fuel transport and carbon dioxide rejection in the interelectrode space can result in excessive cell internal resistance losses if adequate residence and venting space is not provided. The liquid decane-air five cell battery was expressly designed to mitigate some of these problems even at the expense of some stack power output.

A schematic of the 4" x 4" unit cell (80 cm^2 effective area) used in this battery is shown in Figure 4. It consists of three chambers, a central electrolyte chamber (3), inserted between the fuel (2) and the air (4) chambers. The cell separator (1) also serves as an electrode support partition to maintain a small interference fit to insure good electrical contact between the electrode and the current collector. Air is fed to the top of the cathode chamber and exhausted at the bottom, removing product water. Liquid decane is pumped in at the bottom of the fuel chamber--it then percolates through the porous Teflon barrier to the anode where part of the fuel is consumed electrochemically and the remainder is transported into the electrolyte space. Phosphoric acid (14.7 M) electrolyte is also fed from entry ports at the bottom of the cell. The electrolyte level is controlled by an exit weir located well above the active electrode zone. This provides a decane residence space above the electrodes to prevent cathode contact. The electrolyte flow rate and chamber thickness were selected to sweep the transported fuel from the cell without cathode contact. The fuel and electrolyte are separated in the electrolyte tank (using overflow weirs) and the recovered fuel is percolated through a silica gel column prior to its return to the fuel tank for re-use. This is illustrated in a simplified system flow diagram, Figure 5. In addition, both fuel and electrolyte chambers are fitted with gas vent chambers to facilitate carbon dioxide rejection. As a safety precaution a nitrogen purge is supplied to these vents when operating with oxygen at the cathode.

Figure 6 shows the individual components of the unit cell. The plastic frame sections were fabricated from a low distortion silica filled Teflon due to creep and thermal stress problems encountered with unfilled Teflon in small cell tests. The individual cell frames serve to form the various inlet, vent and exhaust manifolds for all the reactant streams. The electrolyte chamber thickness was set at 110 mils to insure that the 3 cm^3/min/cell electrolyte flow could sweep the transported decane into the decane residence space before it contacted the cathode. The decane residence-vent space and exit weir (shown in the back view of the electrolyte chamber) was also provided to help control the decane inventory. The resulting unit cell requires 0.45 inches. However, a 0.25 inch cell could be developed for use in high power systems. The assembled five cell battery illustrated in Figure 7 is series connected using external current collection bus bars on both sides of the collector to reduce "bus bar" resistance losses in the cell current collector. This series arrangement minimizes the effect of short time voltage oscillations encountered with liquid hydrocarbon fuels at high current densities. These oscillations can be quite large (up to 0.4 volts/cell) depending on electrode structure, start-up history and current density. The overall dimensions of the stack are 6-1/4" x 6-3/4" x 4-1/2" including end plates and Belville spring closure (five cells require only 2-1/4 inches) required as a result of differential expansion on start-up and shut-down. Older closures failed to maintain stack integrity for more than one start-up shut-down cycle.

Fuel Cell System Evaluation

The liquid decane-air fuel cell battery described in the preceding section was used to determine if there is any engineering obstacle to the development of a direct liquid decane-air fuel cell battery. Towards this end, tests were conducted to study the effects of system scale-up on cell operation and electrode life. Three individual assemblies were prepared, two were used in our laboratory for systems studies, while the third was delivered to U.S.A. Electronics Command (Fort Monmouth) as a battery demonstrator.

The initial performance obtained with assemblies 1 and 3 are summarized in Figure 8. Average values were used since only three assemblies were prepared and fabricated repeatability could not be established. The oxygen performance was in fairly good agreement with the results obtained in the 1.5 inch diameter cell,

although a 200 mv (40 mv/cell) debit was observed at 5 amps. A similar response was noted on air, however, 3.5 amps was the maximum current possible without dropping below 0.2 volts/cell (a safety cut-off point). This poor air performance is probably due to some decane transport across the electrolyte chamber to the cathode since in the initial tests (Assembly 1) the performance of the individual cells proved to be sensitive to electrolyte flow distribution. This was subsequently corrected by opening an electrolyte balance pressure line to both end plate electrolyte distribution manifolds. Despite this loss the second (#3) five cell assembly produced 6 watts on oxygen and 3.5 to 3.7 watts on air.

Next the use of wide boiling range fuels was briefly examined to assess problems introduced by a realistic fuel. A special low sulfur isoparaffinic turbofuel (OTF-90, boiling range 195-290°C) was silica gel percolated and fed to the cell through the normal fuel feed system. The results shown in Figure 9 indicate a threefold reduction in power capability with this isoparafinic fuel. Inspection of the operating system indicated that this was due to increased fuel transport through the anode with a resultant increased cathode debit. Indeed, significant quantities of fuel were recovered from the exit air stream. However, no performance loss was noted upon returning to the n-decane fuel. Therefore, it appears that a reduction in fuel transport should also improve performance on wide boiling range isoparaffinic fuels.

The decane-air performance history of assembly 3 is summarized in Figure 10, which is a plot of stack power (at 1-1.5 amps) versus time at 150°C ($\sim$40% of this under load). Notice that stack power drops markedly during the first 100 hours and then tends to stabilize at about 50% of its original value. As indicated in the figure, the battery was shut down three times during this program to assess the affect of thermal expansion damage on cathode performance. After the second shutdown, cathode leakage was noted which became worse after the 400 hour shut down. Thus, it appears that hydrocarbon-air batteries will have to remain at their operating temperature during their service life.

At 400 hours, some petroleum derived decane (containing alkyl aromatics) was inadvertently fed to the stack. Operation on this contaminated fuel resulted in an immediate performance loss which was not fully recovered at 560 hours when the test was terminated. This is in direct contrast to the reversible response observed with the OTF-90 fuel. A further indication that the poor performance of the wide boiling range fuel was not due to anode poisoning. From the foregoing, it appears that operation with commercial fuels is not a significant problem per se. However, some fuel purification will be required to remove sulfur, surfactants, and alkyl aromatics.

Conclusions

The development of this five cell direct liquid decane-air battery has demonstrated that operation with fuel transport is feasible. However, decane transport to the cathode can impair cell performance if the electrolyte chamber does not contain adequate decane residence and vent space. In addition, a fuel recovery system is required to maintain coulombic efficiency. Despite these problems, the five cell stack was capable of delivering 6 watts on decane-oxygen and 3.7 watts on decane air feeds. However, improved electrode structures are required since significant performance losses were noted in extended tests. These can amount to up to 50% of the initial performance especially if numerous cold shut downs are required.

Tests with a wide boiling commercial fuel (OTF-90) indicates that these fuels would present no new engineering problems, but performance is impaired due to increased fuel transport which results in an increased cathode debit. In addition, some fuel purification will be required to remove potential catalyst poisons; this problem is currently under study.

Thus, this study has established that there do not appear to be any engineering obstacles to the development of a high power density driect liquid hydrocarbon-air fuel cell battery. Unfortunately, only platinum electrodes have shown suitable electrochemical activity and the quantities required preclude any extensive commercial applications. Thus, a direct liquid hydrocarbon-air fuel cell battery is feasible provided that the noble metal catalyst requirements can be substantially reduced through improved utilization or replacement with non-noble systems. Work in both these areas appears quite promising and ten-fold improvements in platinum utilization have already been demonstrated with experimental electrodes indicating that further improvements may be possible.

Acknowledgment

The work reported in this paper was made possible by the support of the Advanced Research Projects Agency under Order No. 247 through the U.S. Army Electronics Command, Contract No. DA-36-039 AMC-03743(E).

References

(1) W. T. Grubb and C. J. Michalski, Proc. 18th Annual Power Sources Conference, Atlantic City, New Jersey (May, 1964).

(2) W. R. Epperly, Proc. 19th Annual Power Sources Conference, Atlantic City, New Jersey (May, 1965).

(3) J. A. Shropshire, E. H. Okrent and H. H. Horowitz, Hydrocarbon Fuel Cell Technology (B. Baker, ed.) Academic Press, 1965, p. 539.

(4) T. Katan and G. W. Allen, To be published.

Figure 1

Electrode Fabrication Procedure Critical to Liquid Hydrocarbon Performance

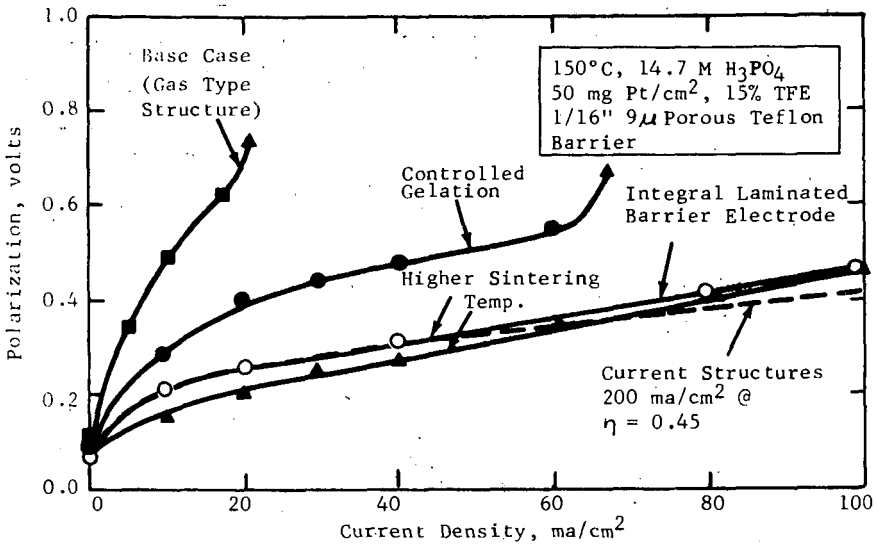

Figure 2

Air Performance of Candidate Cathodes for Hydrocarbon-Air Cell

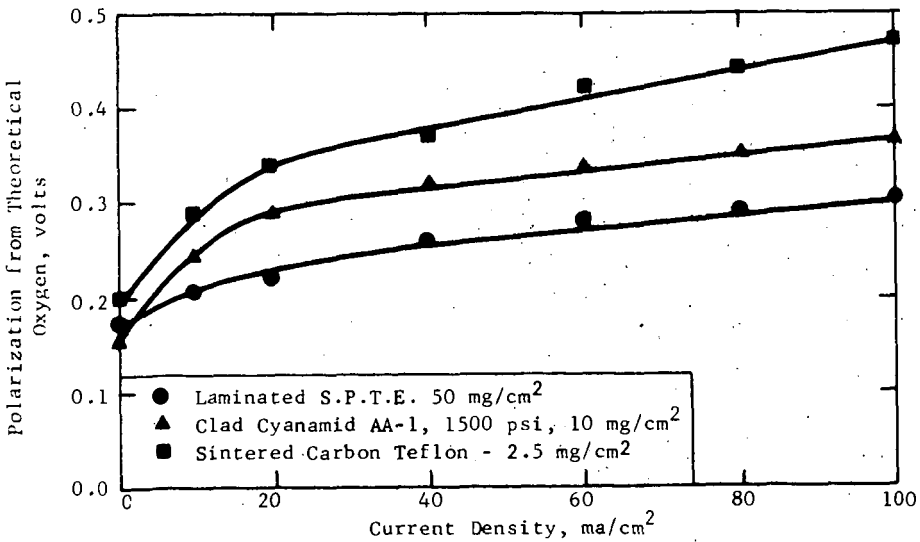

Figure 3

Initial Performance Data Decane Fuel Cells

(10 cm^2 Cells)

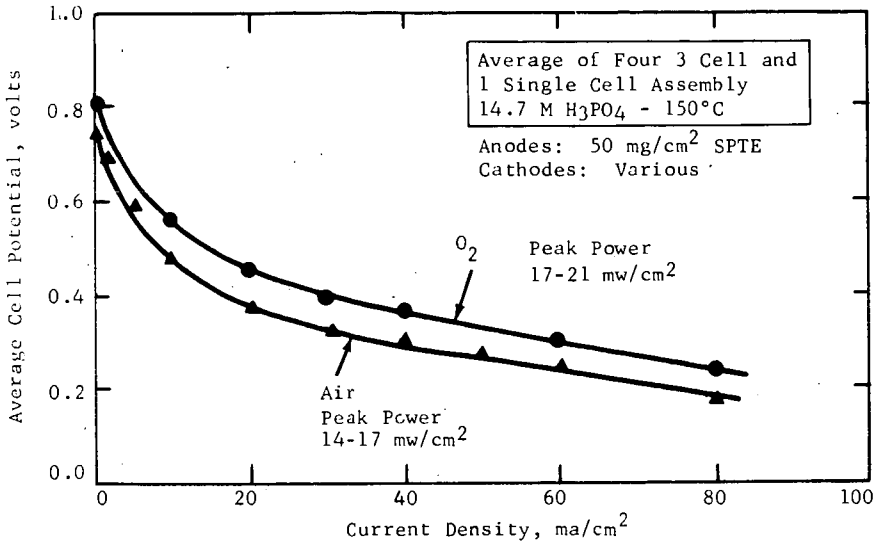

Figure 4

Diagram of Individual Cell Unit

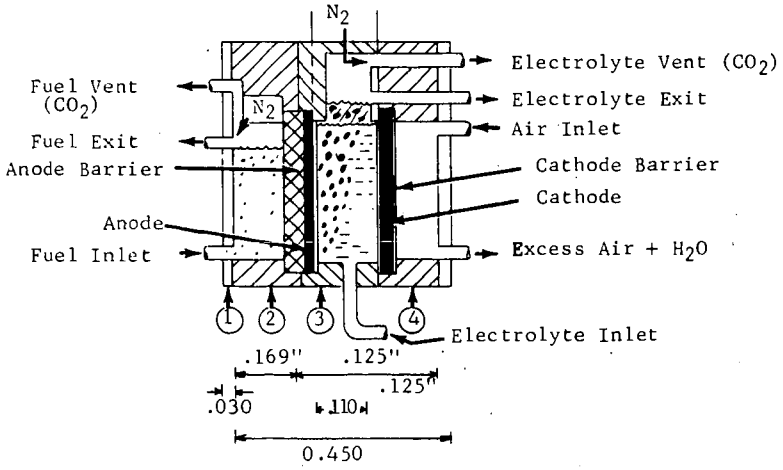

Figure 5

Simplified Decane Air Fuel Cell Battery Schematic

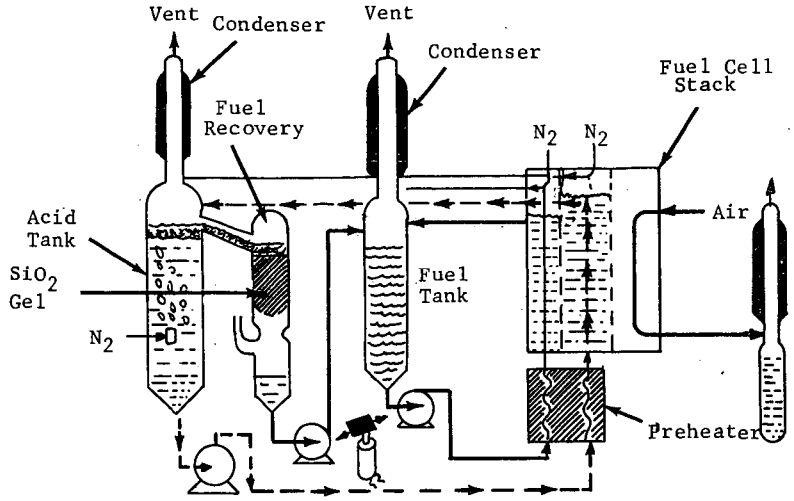

Figure 6

COMPONENTS OF DECANE-AIR UNIT CELL
(SILICA FILLED TFE)

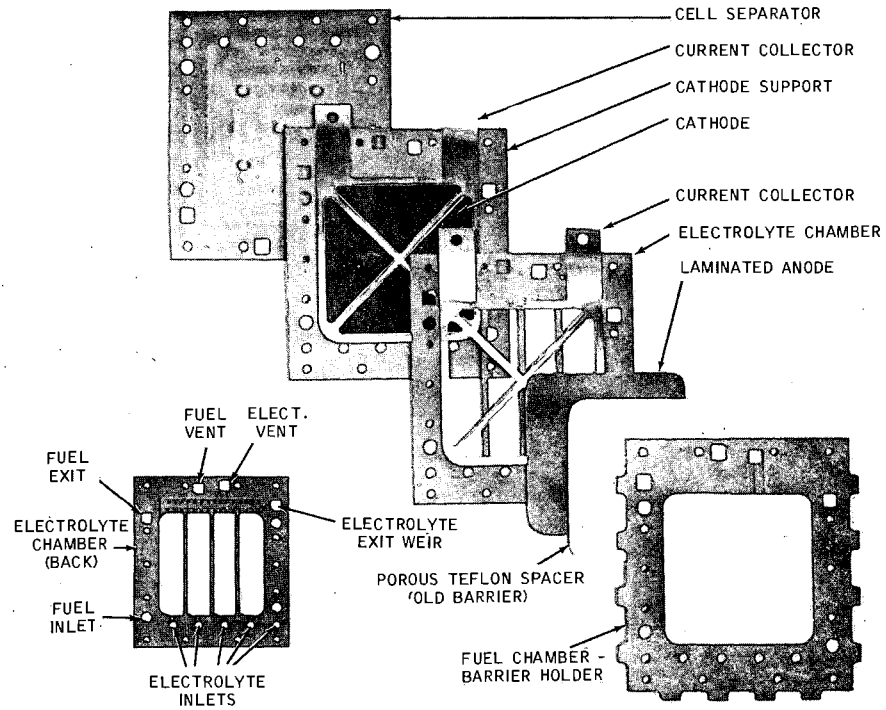

Figure 7

LIQUID DECANE-AIR FUEL CELL
FIVE CELL BATTERY

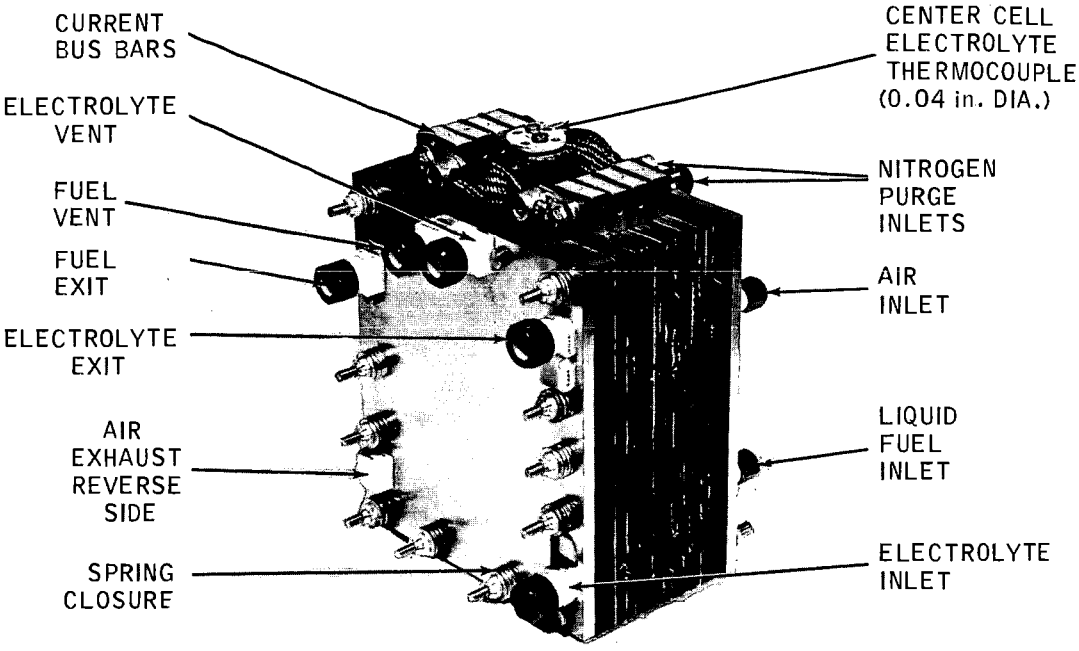

Figure 8

Initial Performance 4" x 4" Decane Fuel Cell Assembly

(Average of Assemblies 1 and 3)

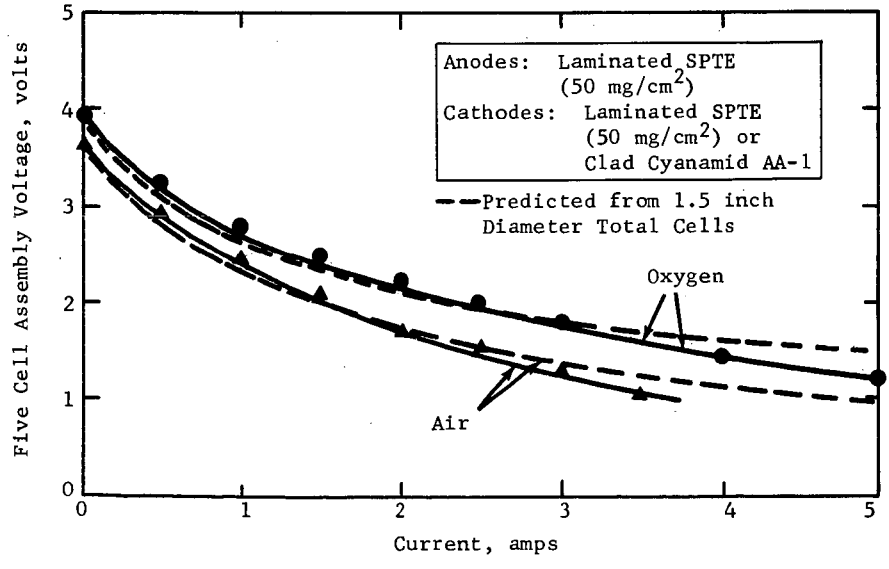

Figure 9

Effect of Wide Boiling Range Fuel

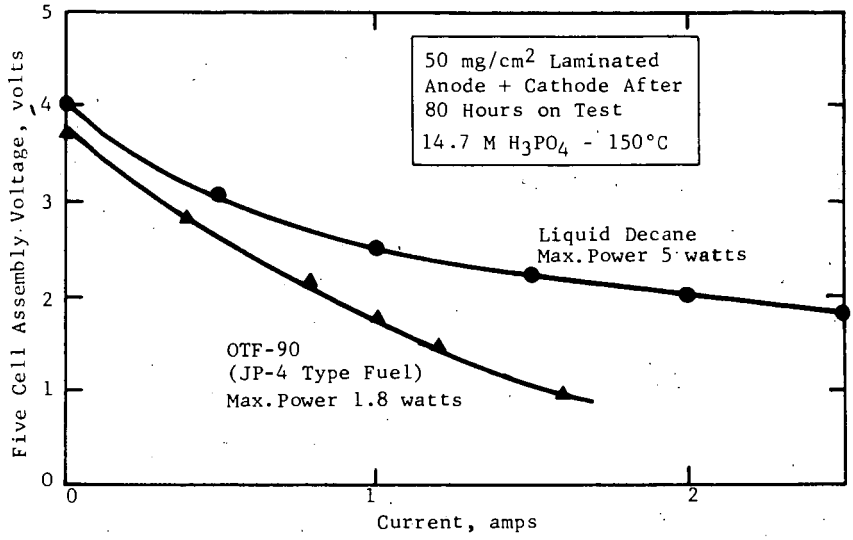

Figure 10

Life Test of Five Cell Decane-Air
Battery Indicates Performance Losses

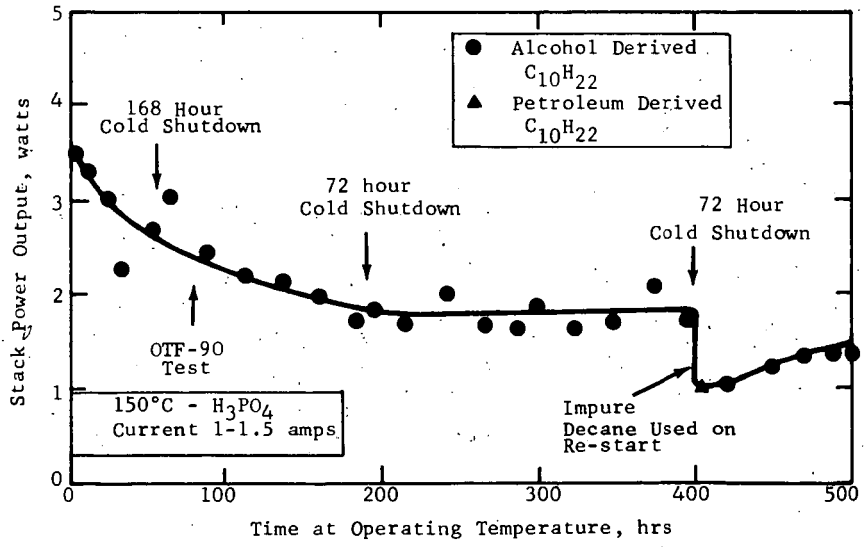

SMALL SIZE LIQUID FUEL AIR AND ZINC AIR PRIMARY CELLS

W. Vielstich and U. Vogel

Institut für Physikalische Chemie der Universität Bonn

Introduction

A special feature of liquid fuels is the high A-h-capacity per unit volume and per unit weight. As an exemple one has 5.000 A-h per liter methanol and a capacity as high as 1.000 A-h per liter in a 6.2 M methanol solution. This compact form of stored energy offers the possibility to use such liquid fuels not only in continuouly operating fuel cells but in primary type cells also. Convenient is the practice to combine a fuel electrode with a hydrophobic air electrode operating at ambient temperature and pressure. The A-h-capacity of such a cell is given by the volume of the added fuel electrolyte mixture. In opposite to commercial primary cells liquid fuel air cells can be reactivated after discharge by renewing the fuel electrolyte mixture (1, 2).

Cells of this type have already been constructed and field tested for several practical applications. 60 W methanol air batteries have been used to power flashing bouys. With 400 liters fuel electrolyte mixture a signal device was sucessfully operated for more than one year (2). Another 40 W battery has been used in actual service to power a TV relay station in Switzerland. This station was positioned in 7.000 ft. altitude where the outside temperature dropped below - 22°F during winter time. At these extreme working conditions also the rated 40 W could be obtained because of the selected methanol/formate fuel mixture (3, 4, 5).

For the above mentioned applications current densities of several mA/cm^2 are feasable. In the meantime, the performance of the hydrophobic carbon diffusion electrode used so far has been increased by more than one order of magnitude in current density. With this new air electrode an extended field of application was discovered. Small cells, e.g. in form of a D-size cell, can now be constructed on the basis of methanol/air or formate/air. In comparison to commercial cells these new electrical power sources have a higher A-h-rate and can be recharged several times. In the following a description of these cells and experimental data are given. Possible low power applications, especially for transistorized equipment are discussed.

Cell Construction

The basic construction scheme of a liquid fuel air cell is shown in fig. 1. The D-size cell has a metal housing (stainless steel). The fuel electrode is pressed against the wall of the housing by a perforated nickel screen. The fuel electrode consists of a sintered nickel foil with a platinum metal catalysts. 1-5 mg/cm^2 are electro-plated from a standard commercial solution of platinum/palladium. The noble metals are deposited in a ratio of Pd:Pt = 4:1 up to 9:1 (compare ref. 5). The carbon oxygen electrode is fixed in the cap of the cell. The carbon rod has a channel in the center to favour the oxygen diffusion to and the nitrogen transfer from the reaction zone. The active carbon

material is bounded by polyethylen which serves as hydrophobic agent also. The content of polyethylen ranges from 10 to 20 %, depending on the character of the solution, e.g. content of methanol. A silver plated nickel grid around the carbon rod serves as current collector. The electrical connections are given by the spring contact on the plastic cap (positive pole) and the metal housing (negative pole).

The cell can be filled with 20 - 24 cm^3 fuel electrolyte mixture through two openings in the cap. The A-h-capacity of the cell depends on the fuel concentration and on the fuel mixture used: 7.5 M KOH + 5 M formate ..... 5.5 - 6.5 A-h
9 M KOH + 4 M methanol ..... 13 - 15.5 A-h

In the alkaline electrolyte, methanol and formate are both converted completely to carbonate ions. In the reaction with methanol 2 OH^- ions are consumed and 6 electrons are delivered per molecule. In the case of formate only one OH^- ion is used for the conversion and two electrons are delivered.

For a D-size dry cell ampere-hour values of about 3 are obtained at low current densities. We have also built cells with a plastic housing. In this construction the negative pole is situated at the bottom of the housing. Fig. 2 shows two types of the D-size alcohol/air element and a plastic spare tube for refill.

The principle of a free liquid electrolyte and a carbon air diffusion electrode can be used in combination with a consumable metal electrode as negative pole also. The liquid fuel and the fuel electrode than are replaced by a zinc or cadmium anode (in form of a foil or a powder). Such a metal air cell has the advantage of a higher operating voltage (1.0 to 1.2 volts). Current loads of 100 - 300 mA easily can be obtained. The A-h-capacity depends to a large extent on the concentration and on the volume of the electrolyte. To avoid heavy corrosion effects at the anode ZnO has to be added to the electrolyte of the zinc air cells. In opposite to commercial dry cells such a zinc air cell can be reused. This can be done by renewing the electrolyte. The number of cycles is determined by the weight of the zinc electrode and the current efficiency.

Experimental Results

In fig. 3 the discharge curves of formate and zinc/air cells are compared with that of a commercial dry cell. In the first part of the curve the dry cell shows a relatively high operating voltage. But the output is decreasing almost linearly with time. By the use of zinc and formate air cells very constant terminal voltages are obtained over the whole discharge period. Forthermore the A-h-capacity of the new air cells obviously exceeds that of the dry cell, weight and volume being almost the same.

At low temperatures (- 15°C) a small decrease in performance only is observed for all cells investigated (fig. 4). The cells with liquid electrolyte again show a much better voltage time behaviour. Current efficiencies of 90 - 97 % for formate and 80 - 90 % for methanol have been obtained. The A-h-efficiency depends of course on the load and on the temperature.

For some applications it is advisable to use methanol/formate mixtures as it has been done in a battery set for signal devices (3, 4, 5). Such a mixture offers a heavy load performance (due to the added formate) combined with a big A-h-capacity (depending on the methanol content).

Discussion of Applications

The simple construction and the maintenance-free operation of liquid fuel air cells clearly suggest a similar field of application as in the case of dry cells. The features of the new battery are: easy reactivation, constant discharge voltage, unlimited storage, and high A-h-capacity. Therefore, many applications are possible in spite of the relatively low terminal voltage.

The operating voltage can be increased by use of an DC-DC-converter. By suitable adjustment of the converter elements it is possible to operate even with input voltages of 0.5 - 0.7 volts. We have built DC-DC-converters of 0.6 to 6 volts with current outputs of 10 - 30 mA which have more than 60 % efficiency. The converter can be placed in the battery housing, e.g. in the cap. Weight and volume of a power set are diminished by such a combination of primary cell and converter. In some cases it will be advantageous to connect two cells in series in order to obtain better converter efficiencies.

According to the specific qualities described the new power source can find the following applications:

(i) portable transistor radios, tape recorders, walkie-talkie-sets
(ii) equipments which require a constant discharge voltage, e.g. electric clocks
(iii) everywhere, if an unlimited storage is required. In this case the cell could be stored without electrolyte.

Literature

1. W. Vielstich, "Brennstoffelemente - Moderne Verfahren zur elektrochemischen Energiegewinnung", Verlag Chemie, Weinheim, 1965
2. W. Vielstich, "Alcohol-Air Fuel Cells - Development and Applications", in B.S. Baker, Hydrocarbon Fuel Cell Technology, Acad. Press Inc., New York, 1965, p. 79
3. Funkschau 38, 138, 1966
4. H.G. Plust, Brown, Boveri, Mitt. 53, 5, 1966
5. H. Schmidt und W. Vielstich, Z. anal. Chem. 224, 84, 1967

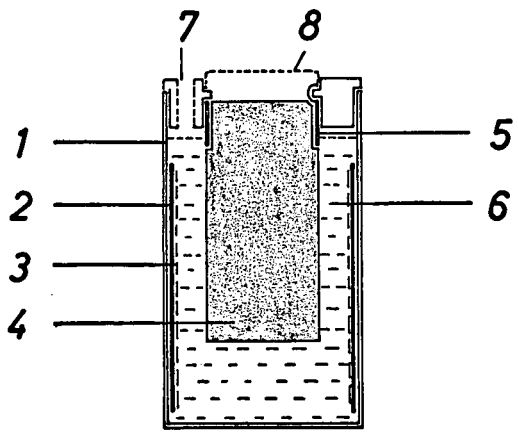

Fig. 1 Liquid fuel air cell cross section
(1) metal housing
(2) fuel electrode
(3) perforated nickel screen
(4) carbon air electrode
(5) silver plated nickel grid
(6) electrolyte
(7) opening
(8) positive terminal

Fig. 2 View of two liquid fuel air cells and of a D-size dry cell
left: plastic housing,
right: metal housing
in front: plastic spare tube with 20 cm^3 fuel/electrolyte mixture

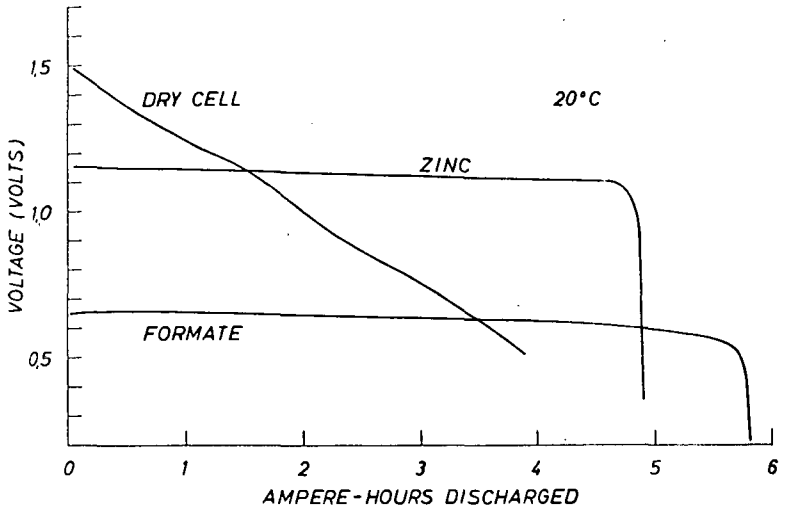

Fig. 3 Discharge voltages of different cells at 20°C;
dry cell: 1,5 V IEC R 20 current 150 mA,
zinc: commercial zinc sheet/carbon air
10 M KOH + 36 g ZnO per litre current 150 mA,
formate: formate/carbon air fuel cell
7.5 M KOH + 5 M HCOOK third charge current 75 mA

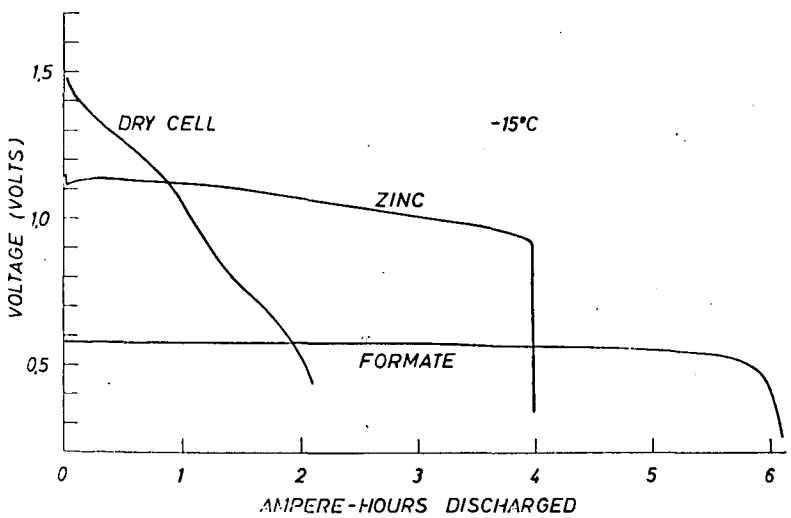

Fig. 4 Discharge voltages as in fig. 3, but - 15°C and 100 mA (dry cell and zinc), 25 mA (formate)

REFORMED NATURAL GAS, ACID MATRIX FUEL CELL BATTERIES

D. Y. C. Ng and D. K. Fleming

Institute of Gas Technology
3424 South State Street
Chicago, Illinois 60616

INTRODUCTION

This paper is a condensed report on the first 4 years of the low-temperature acid electrolyte fuel cell program sponsored at the Institute of Gas Technology by a group of gas utilities. The purpose of the program is to develop an economical, air-breathing fuel cell powered by natural gas.

Because methane is relatively unreactive electrochemically, this program emphasized steam reforming of the natural gas to a hydrogen-rich fuel for the cell. The fuel cell was adapted from the hydrogen-oxygen cell to make it operate on dilute (and poisoning) reformed natural gas and air. Acid electrolyte was required because it is compatible with the carbon dioxide that is present in the fuel.

The program was subdivided into three related technical categories:

1. Conditioning of the natural gas fuel
2. Electrode catalyst reduction and life evaluation
3. Fuel cell stack design and engineering

These technical areas are discussed below, along with another major point – overall fuel cell cost.

HYDROGEN GENERATOR DEVELOPMENT

A novel three-stage process was developed for conversion of low-pressure natural gas into a hydrogen-rich fuel suitable for use in acid fuel cells. The process was translated into efficient, integrated, prototype hydrogen generators which produced a fuel containing less than 20 ppm of carbon monoxide. The process and equipment has been described in detail in earlier papers.[5,6]

Development of the hydrogen generator has been temporarily suspended. Using better anode catalysts, other investigators have successfully operated acid fuel cells with feeds containing as much as 10% carbon monoxide at 300°F with little poisoning effect.[2] However, the hydrogen generation process will probably still be desirable for the operation of fuel cells at the more moderate temperatures that minimize corrosion and with electrodes that have a lower platinum content.

ELECTRODE EVALUATION

The primary goal of the program was the development of economical fuel cells operating on reformed natural gas and air. The noble metal content of the electrode was the primary cost in the acid fuel cell at the beginning of the program. Figure 1 presents the reduction of the noble metal content during the 4 years. At the start of the program, available electrodes contained 80 mg Pt/sq cm – a catalyst utilization of 250 troy oz/kw at obtainable power levels on hydrogen and oxygen.

At the end of 1966, utilization had improved to less than 1 troy oz/kw while operating on reformed natural gas and air.

American Cyanamid Company's introduction of thin-screen electrodes at this meeting in 1963[3] and its recent work on lower loading electrodes are apparent in Figure 1. The intermediate performance improvements reflect better test cell design, improved operating conditions, and higher power densities.

These electrodes have been long-lived. Figure 2 shows the lifetime of one of our first immobilized phosphoric acid, capillary matrix cells operating at 90°C. The performance of this cell was relatively constant if matrix deterioration is discounted. Both electrodes in this test were American Cyanamid Type AA-1 containing 9 mg Pt/sq cm and operating at a 40 ma/sq cm current density.

Table 1 lists the lifetimes and performances of representative small-cell tests. Reduced anode loadings do not cause appreciable power loss with 20-ppm carbon monoxide in the dilute fuel, but the tolerance to higher carbon monoxide dosages is not yet known. The reduced catalyst content at the cathode, however, does cause a noticeable power reduction.

Some of the tests listed in Table 1 were short-term (3 months or less) because the electrodes could not be recovered after dismantling the cell. Some of the low-loading electrodes do not separate readily from deteriorated matrices.

Moisture management and matrix degradation were the two major problems with the small-cell tests. The most common mode of failure for these small tests was electrolyte leaching caused by insufficient moisture removal. With a good cell design and temperature control, the moisture balance is more easily maintained.

The glass-fiber matrix is slowly attacked by phosphoric acid, changing to a gel and losing its wet strength. The effect of replacing a deteriorated matrix is evident in Figure 2. Several other matrix materials have been tested without significant success. We see no clear solution to the matrix problem at the present time.

BATTERY ENGINEERING

The third phase of the low-temperature fuel cell program was the engineering and operation of multicell battery stacks. This section of the program involved the study of heat and moisture management, proper distribution of dilute fuel and oxidant, and other problems of battery operation. Studies with dual ion-exchange membrane batteries were presented earlier.[4] These efforts were abandoned in favor of immobilized electrolyte, capillary matrix batteries, which appear to hold greater promise for ultimate cost reduction. However, the heat and moisture balances are more critical with the matrix battery because of the reduced electrolyte inventory.

Figure 1 includes a line for the catalyst reduction achieved with battery operation. Because all stacks operated since 1964 contained American Cyanamid Type AA-1 electrodes (18 mg Pt/sq cm total), the improved catalyst utilization reflects improvements in power density only. The power densities obtained were 48 w/sq ft with the membrane batteries, 73.2 w/sq ft with 0.25-sq-ft matrix batteries, and 82.5 w/sq ft with larger matrix batteries. The electrode cost of the batteries lags behind that of the test cells by approximately 1 to 1-1/2 years because of electrode availability and the need for preliminary evaluation. The battery electrode costs will probably be similar to those of the present small-cell electrode costs when the low-noble-metal-content electrodes are operated in multicell stacks.

Table 1. REPRESENTATIVE SMALL-CELL (4 sq in.) TESTS

Anode Noble Metal Content, ma/sq cm	Cathode Noble Metal Content, ma/sq cm	Max. Power Density on RNG/Air, mw/sq cm	Noble Metal Utilization at Max. Power, troy oz/kw	Operating Conditions (RNG/O_2) Current Density, ma/sq cm	Potential, mv	Lifetime, days	Matrix Changes	Comments
9	9	68	8.5	40	680	600 †	2	Older cell design
9	9	75	7.7	100	720	135 †	2	Improved cell gas distribution and IR
9	2.5	58	6.4	40	720	239 †	1	Older cell design
9	1	50	6.4	40	700	32 †	1	High air polarization
1	9	72	4.5	40	700	55	0	Anode not recoverable
0.5	9	70	4.4	40	720	58	0	Anode not recoverable
0.25	2.5	64	1.4	40	700	78	0	Very stable
0.25	1	(50)	0.8					Estimated from above tests

†Determined from other tests with these electrodes.
‡Test continuing on January 1, 1967.

The basic matrix fuel cell unit is similar in all of the sizes tested in this program. Figure 3 shows an exploded view of the cell design. The electrolyte is absorbed in Whatman GF-82 glass-fiber paper that is 25 mils thick. The edges of this glass-fiber matrix are impregnated with Kel-F to minimize electrolyte leakage through the exposed edges of the cell. The fuel compartment is enclosed by an ethylene-propylene-terpolymer gasket and has interfaces at the anode, which is adjacent to the matrix, and at the bipolar plate, which it shares with the next cell. Fuel flows into the cell from manifold ports in the top edge and over the face of the cell. Spent fuel is exhausted through a single outlet at the bottom. The cathode compartment is similar.

Matrix cells of this construction are stacked into a battery. The bipolar plate acts as a gas separator and an electrical connector between the adjacent cells. The resulting battery is electrically connected in series. The overall size of a 0.25-sq-ft cell is 5.5 x 9.6 x 0.100 in. with a 4.7 x 7.7 in. active area. The larger cell size is 12 x 13 x 0.100 in. with a 9.5-in.-square active area. Based on the maximum power obtained from the larger cells, exclusive of end plates and fittings, the unit weight of the stack is about 15 lb/kw and the unit volume is about 0.18 cu ft/kw. At design power levels of 55 w/sq ft, the specific weight and volume increase to 22 lb/kw and 0.26 cu ft/kw. Figure 4 is a photograph of the components of a single cell.

The heat and moisture balances within the cell were studied by computer analysis. Partial differential equations modeling the heat and mass flows were solved by the finite difference technique. For the geometry and operating conditions used, the calculations indicated that the gas flow required to remove the heat generated in the cell was an order of magnitude greater than that required to remove the product water. Therefore, the excess heat must be removed by a separate mechanism.

Ethylene glycol circulating through the hollow end plates of five-cell modules cools the stack, as illustrated schematically in Figure 5. At 100 amp/sq ft current density, the temperature variation from the center cell to the end cell of a module is 45°F. Based on published correlations for heat transfer in a fuel cell battery,[1] the effective thermal conductivity in the direction of current flow is only about 0.11 Btu/hr-ft-°F for this geometry. The tortuous path for heat removal probably causes the low conductivity. Each cell in the module operates at the acid concentration which is in equilibrium, at the individual cell temperature, with the gas flows.

Cell modules are connected electrically in series to produce the desired output. Figure 6 illustrates a three-module 500-watt battery which was successfully operated near the end of the reporting period. The output of this battery was 7.6 volts at 70 amp of gross current.

A typical polarization curve for a five-cell module is shown in Figure 7. The stack voltage at 100 amp/sq ft current density was 3.3 volts or 0.66 volt per cell. The maximum power output of this stack was 243 watts at 90 amp (144 amp/sq ft). At 70-amp current, the maximum cell-to-cell deviation was 2.5%, although the deviation was greater at higher current densities. Maldistribution was evident at these conditions, as indicated by the nonlinearity of Figure 7.

The flow distribution across the face of the cell was checked by assemblying a dummy cell without electrodes. The matrix was soaked with lead acetate, the desired flow rate was established, and a small quantity of hydrogen sulfide was injected into the inlet line. The hydrogen sulfide reacts with the lead acetate until the hydrogen sulfide is consumed, leaving a dark pattern which indicates the flow regime over the face of the cell.

Gas distribution can also be determined by fuel utilization efficiency curves such as those shown in Figure 8. In this graph, the flow rate is expressed in multiples of the stoichiometric fuel requirements. Figure 8 indicates that fuel utilizations greater

than 50% may be expected from this cell design at higher current densities without excessive penalty. However, the design should be improved to displace the knee of these utilization curves closer to the stoichiometric fuel requirements.

FUEL CELL COSTS

The basic raw material costs of fuel cell batteries and test cells operated in this program are tabulated below as a function of date.

Table 2. BASIC MATERIAL COSTS OF IGT LOW-TEMPERATURE FUEL CELLS AND BATTERIES

Component	Jan. 1963[a]	March 1964[b]	April 1965[c]	March 1966[d]	Dec. 1966[e]
	$/kw				
Precious Metal (catalyst)	23,000	2,800	1,520	775	80
Electrode Screen	23,000	141	79	40	57
Bipolar Plates	1,140	230	128	65	93
Membranes	385	360	220	--	--
Gaskets, etc.	53	50	28	10	14

[a]Original IEM battery, 18.7 w/sq ft with 72 g/sq ft electrodes on Pt gauze.

[b]Improved IEM battery, 20 w/sq ft with American Cyanamid AA-1 electrodes.

[c]13-cell, 0.25-sq-ft IEM battery with American Cyanamid AA-1 electrodes at 35.5 w/sq ft.

[d]5-cell, 0.25-sq-ft matrix battery with American Cyanamid AA-1 electrodes at 72 w/sq ft.

[e]4-sq-in. matrix cell using an American Cyanamid BA-1/4 anode and BA-2C cathode at 50 w/sq ft(estimated).

Table 2 lists basic material costs only and does not include the value added by manufacture. The reduction in catalyst cost, in line with Figure 1, has been significant. At the present state of development, the value of the other metallic components of this cell is greater than that of the catalyst. If these subsidiary costs can be reduced, the fuel cell should soon become an economic reality.

The fuel cell catalyst costs do not require further reduction. The range of $100/kw is probably less than required for an economic fuel cell because the platinum catalyst is not destroyed in the cell operation. Since the catalyst values may be recovered for a nominal charge (similar to current practice with petroleum refinery catalysts), the platinum is essentially nondepreciable. In addition, the platinum is a highly fluid asset and may be used as collateral for low-interest bonds. Under gas industry economics, the annual costs for this catalyst should be about 7%. Figure 9 presents the annual charge, including platinum recovery, for several electrode combinations. The assumption has been made that the peak power density currently obtainable with these platinum loadings will be the future design basis.

Figure 9 illustrates that the true annual cost of the catalyst is low and that higher catalyst loadings may be possible, depending on the overall economics of the system.

ACKNOWLEDGMENTS

The authors wish to thank Southern California Gas Company, Southern Counties Gas Company, and Consolidated Natural Gas Service Company, Inc., sponsors of this investigation, for permission to publish these results.

LITERATURE CITED

1. Gidaspow, D., Baker, B. S., Jee, B. C. and Oliva, F., "Heat Transfer in a Fuel Cell Battery – Maximum Battery Temperatures." Paper No. C-213 presented at the 17th Meeting of the International Committee of Electrochemical Thermodynamics and Kinetics, CITCE, Tokyo, September 5-13, 1966.

2. Haldeman, R. G., "Electrode-Matrix Materials." Paper presented at the 21st Annual Power Sources Conference, Atlantic City, N.J., May 16-18, 1967.

3. Haldeman, R. G., Colman, W. P., Langer, S. H. and Barber, W. A., "Thin Fuel Cell Electrodes," in Young, G. J. and Linden, H. R., Eds., Fuel Cell Systems, Advances in Chemistry Series No. 47, 106-15. Washington, D. C.: American Chemical Society, 1965.

4. Leitz, F. B., Glass, W. and Fleming, D. K., "Performance of a Reformed Natural Gas-Acid Fuel Cell System. Part II – Fuel Cell Battery," in Baker, B. S., Ed., Hydrocarbon Fuel Cell Technology, 37-50. New York: Academic Press, 1965.

5. Meek, J. and Baker, B. S., "Hydrogen From Natural Gas for Fuel Cells," in Young, G. J. and Linden, H. R., Eds., Fuel Cell Systems, Advances in Chemistry Series No. 47, 221-31. Washington, D. C.: American Chemical Society, 1965.

6. Meek, J., Baker, B. S. and Allen, A. C., "Performance of a Reformed Natural Gas-Acid Fuel Cell System. Part I – Hydrogen Generator Design," in Baker, B. S., Ed., Hydrocarbon Fuel Cell Technology, 25-35. New York: Academic Press, 1965.

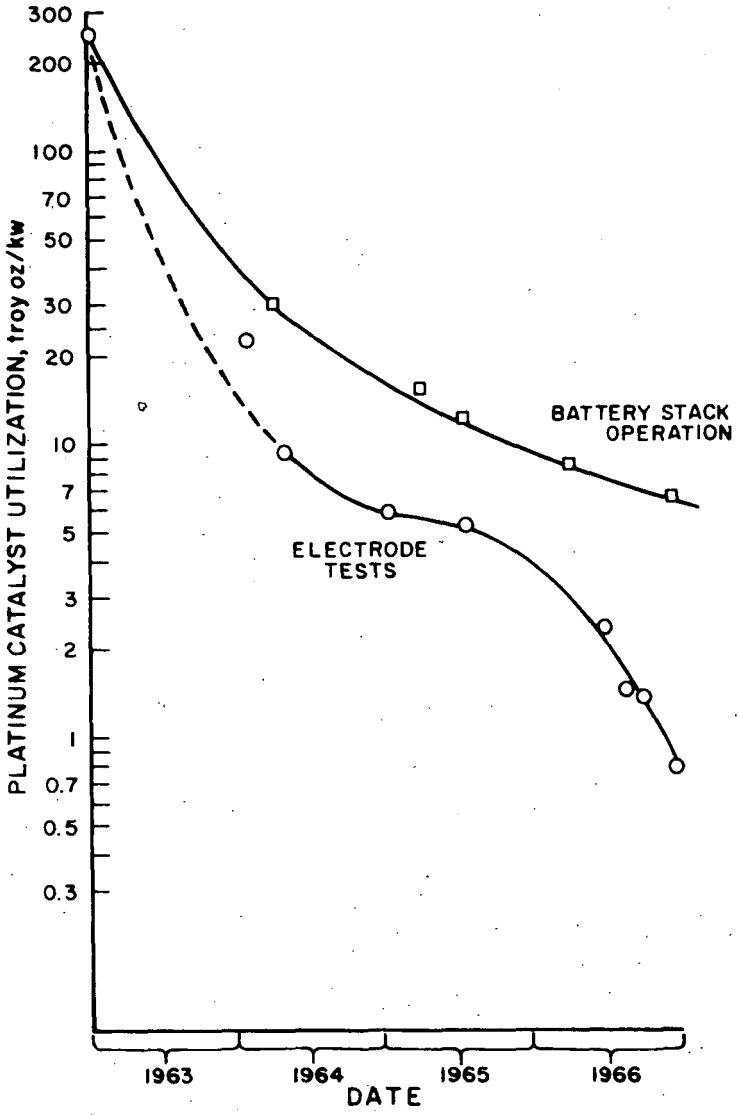

Figure 1. IMPROVEMENT IN CATALYST UTILIZATION

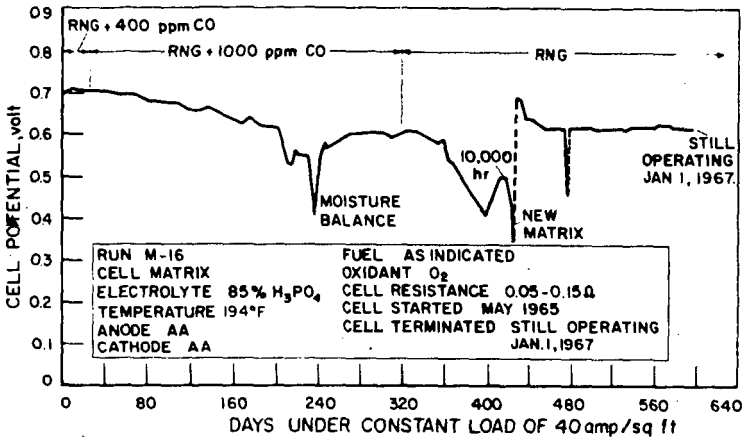

Figure 2. LIFETIME PERFORMANCE OF TEST CELL M-16 (AA-1 Electrodes, Low Current Density)

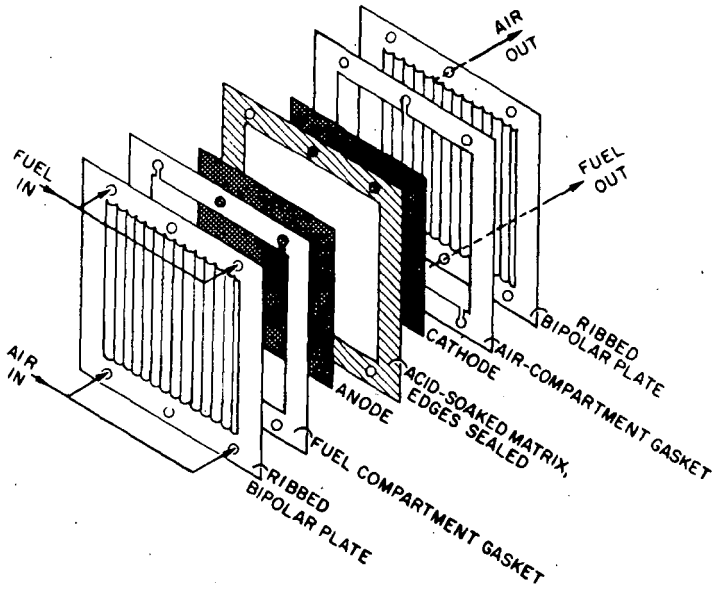

Figure 3. EXPLODED VIEW OF A SINGLE CELL

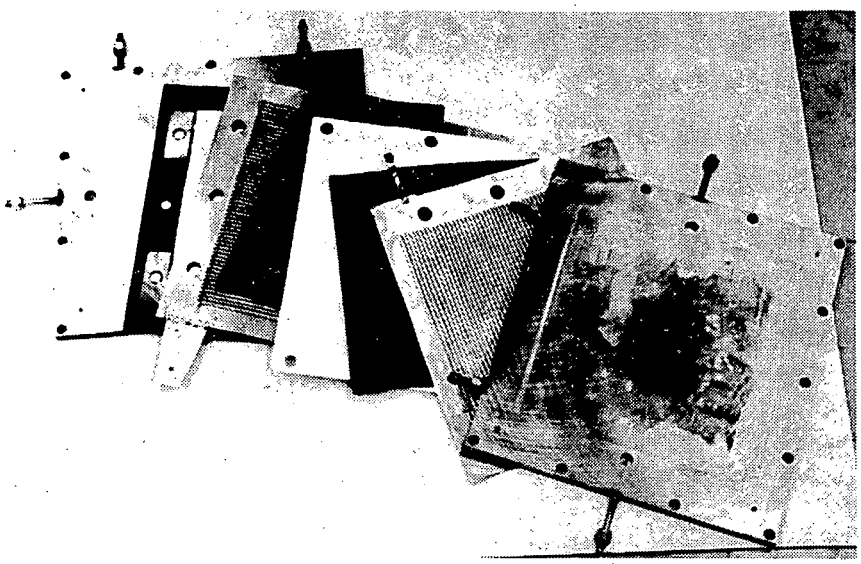

Figure 4. VIEW OF 0.63-sq-ft CELL COMPONENTS

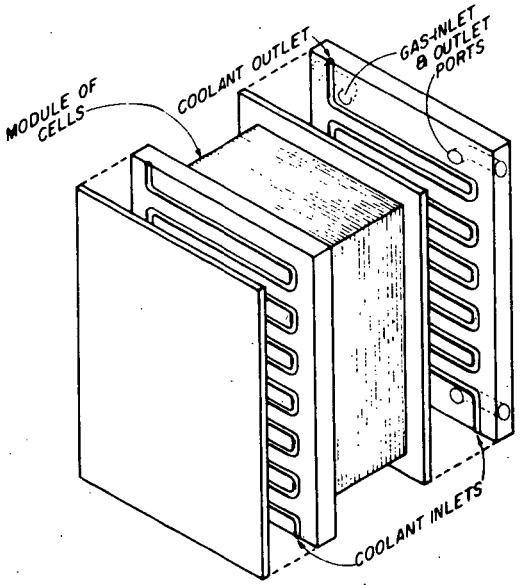

Figure 5. SCHEMATIC REPRESENTATION OF MODULAR CELL COOLING

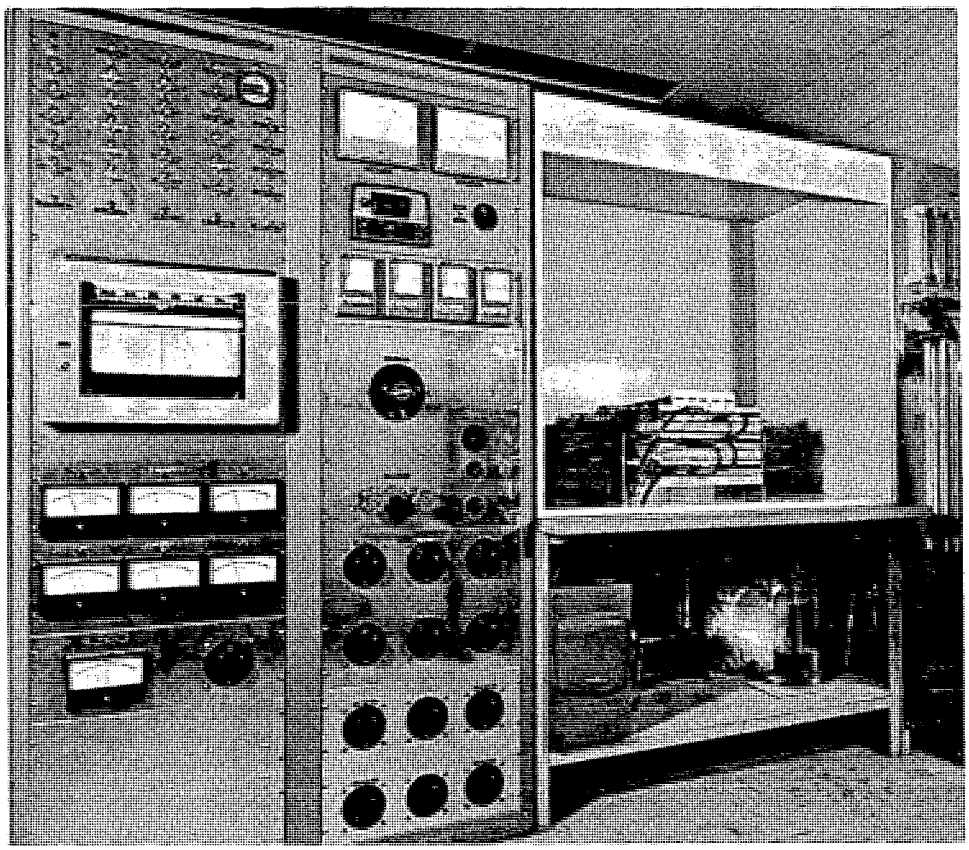

Figure 6. TEST STATION WITH 500-WATT MATRIX FUEL CELL BATTERY

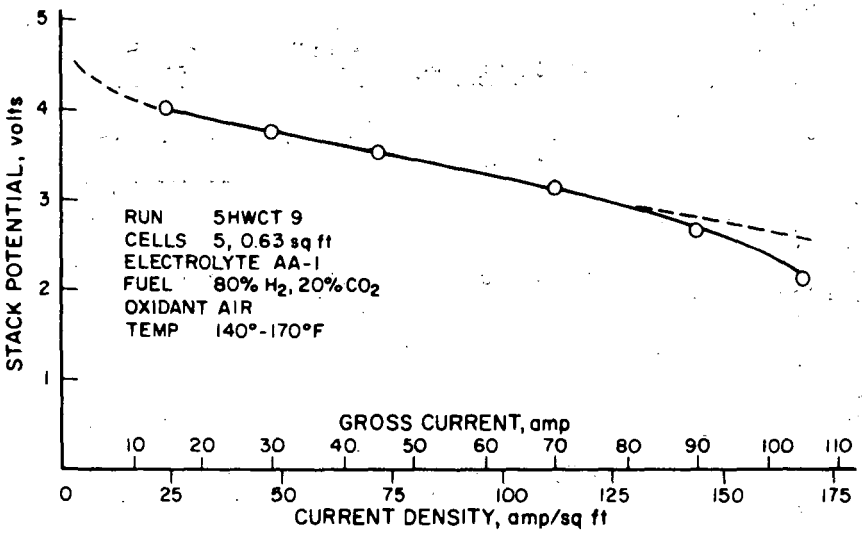

Figure 7. POLARIZATION CURVE FOR LARGE-CELL STACK

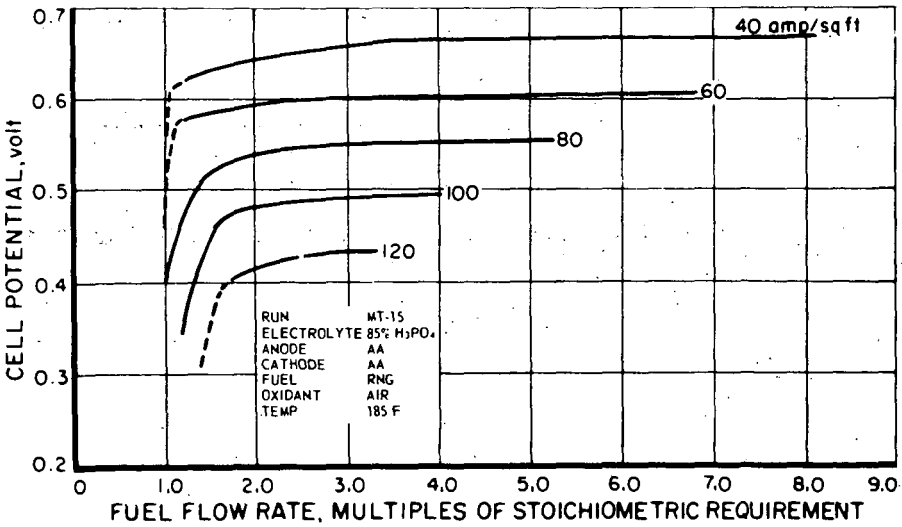

Figure 8. FUEL UTILIZATION

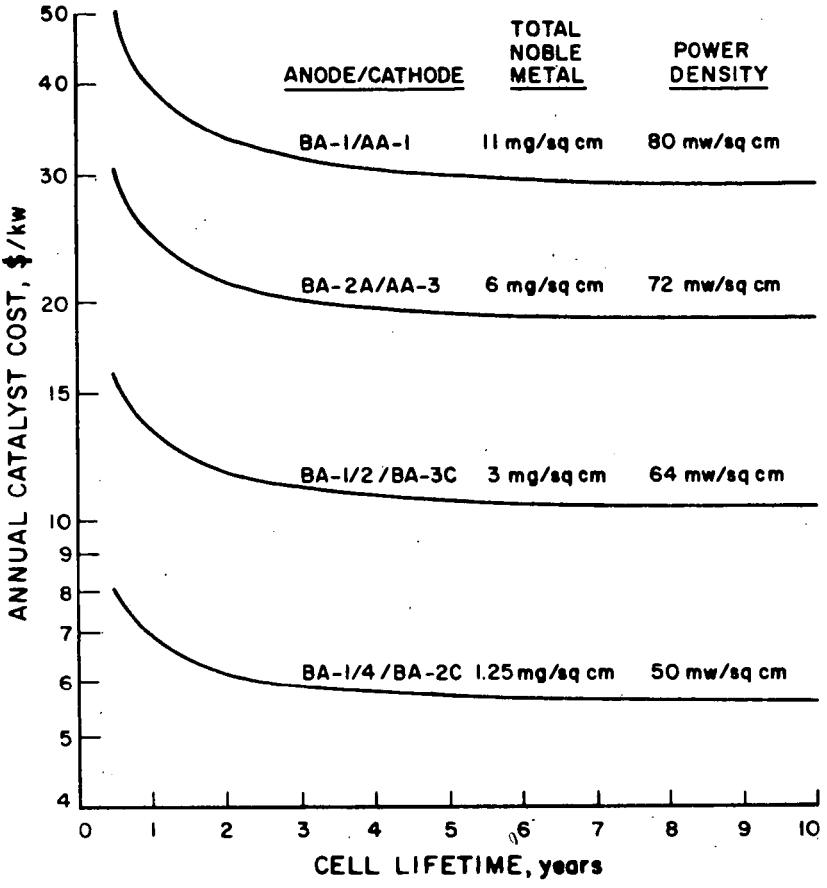

Figure 9. ANNUAL CATALYST COST FOR ELECTRODE CONDITIONS:
Platinum at $90/troy oz
Rhodium at $180/troy oz
Capital at 7%
Noble-Metal Recovery at $1/troy oz

SIMPLIFIED FUEL CELL SYSTEMS FOR ARMY APPLICATIONS

G. R. Frysinger

Power Sources Division
Electronic Components Laboratory
U.S. Army Electronics Command
Fort Monmouth, New Jersey 07703

ABSTRACT

Fuel cells using a variety of fuels and air as oxident have been built in technically feasible prototypes. Before they can gain acceptance for commercial or military markets many refinements must be made to provide extended, low maintenance, customer operation and to greatly reduce fabrication and materials costs. System redesign and simplification to use a minimum of components to perform the minimum required functions is the key to this objective. The Army has found use for those fuel cells which use air and solid or liquid chemical forms of the active hydrogen fuel. Highly simplified configurations of lithium hydride, hydrazine and hydrocarbon fueled fuel cells are being developed. Use of batteries in hybrid battery-fuel cell systems and sensitive fuel feed controllers have eliminated the need for costly and heavy electronic power conditioning, has reduced the number of moving parts, and greatly reduced the size and power required for special startup systems. The system "simplicity" of a 30 watt metal-hydride-air, a 60 watt hydrazine-air and a 500 watt hydrocarbon-air system will be examined in detail.

SOME PROBLEMS IN THE USE OF HYDROCARBONS IN FUEL CELL POWER SYSTEMS

K.R. Williams and A.G. Dixon

"Shell" Research Ltd., Thornton Research Centre, P.O. Box 1, Chester, England

INTRODUCTION

Because of the difficulty of making hydrocarbons react directly in low temperature fuel cell systems, there is considerable interest in hydrocarbon-reforming systems that produce hydrogen for fuel cell power plants. However, most of the technology for the steam-reforming of hydrocarbons has been concerned with large plants for which the throughput of hydrogen has been measured in millions of cubic feet per hour rather than in the hundreds of cubic feet per hour which are of more concern to the fuel cell power system designer concerned with the production of a few kilowatts of electrical power. This means that complexities in plant that can be tolerated in a hydrogen-production plant intended for the chemical industry are often quite unacceptable in a simple power unit that must be operated by unskilled personnel. In constructing a fuel cell power system one has the opportunity to modify the design of both the hydrocarbon-reforming system and also the fuel cell itself in order to achieve a satisfactory compromise between cost, simplicity and reliability. The particular compromise arrived at in any given circumstance will depend considerably on the conditions under which the power system is called upon to operate. In this paper some of the variables at the disposal of the designer will be considered and suggestions made regarding the most fruitful approaches to certain of the problems.

As far as the hydrocarbon-reforming unit is concerned, the most important factors facing the designer are the degree of purity of fuel that is acceptable to the reforming unit and the degree of purity of hydrogen that is acceptable to the fuel cell. Whereas most low temperature fuel cells made to date have used alkaline electrolytes, those with acid electrolytes have received attention recently, and this trend obviously has a strong influence on the purity of the gas required by the fuel cell. Initially, low temperature fuel cells with alkaline electrolytes were the easier to develop and they required pure hydrogen. The advent of the palladium/silver diffuser capable of giving ultra-pure hydrogen from a source supplying impure hydrogen encouraged the development of hydrogen generators suited to the limitations of the alkaline fuel cell. However, it is now possible to contemplate the operation of fuel cells with acid electrolytes and a number of examples have been given in recent years of electrodes that will tolerate various impurities in the feed gas. Use of this type of electrode is considered in this paper and the generation of hydrogen is considered from both aspects, viz. that of producing an ultra-pure product and that of producing a less pure one for use with the electrodes developed more recently.

The first section of this paper will be concerned with some of the problems encountered in the design of the hydrocarbon-reforming system and the second section will deal with electrodes for use on impure hydrogen.

HYDROCARBON REFORMING SYSTEMS

In obtaining hydrogen from hydrocarbons one has the choice of using a steam hydrocarbon-reforming reaction,

$$C_nH_{2n+2} + 2_nH_2O \longrightarrow (3n + 1)H_2 + nCO_2 \quad .....(1)$$

an oxidative reaction,

$$C_nH_{2n+2} + \frac{(3n + 1)}{2} O_2 \longrightarrow nCO_2 + (n + 1)H_2O \quad .....(2)$$

which is highly exothermic and is followed by

$$C_nH_{2n+2} + nH_2O \longrightarrow nCO + (2n + 1)H_2 \quad .....(3)$$

$$C_nH_{2n+2} + nCO_2 \longrightarrow 2nCO + (n + 1)H_2 \quad .....(4)$$

or a cracking reaction,

$$C_nH_{2n+2} \longrightarrow C_n + (n + 1)H_2 \quad .....(5)$$

Generally speaking, a fuel cell power system will be developed because of its attractively high efficiency compared with that of the alternatives. Therefore it would seem desirable to make hydrogen generation as highly efficient as possible. Thus, while there may be special occasions when the simple cracking reaction is attractive, generally this will not be so because the resultant hydrogen contains only a small proportion of the total energy of the fuel entering the system. Although oxidative reactions, such as the Shell gasification processes for heavy oil, can be used successfully on a large scale, their success requires the availability of pure oxygen and for this reason such processes are not normally attractive for use in small power sources. It is possible to operate this type of reaction on air with added steam, to give a gas which contains about 40% hydrogen. This is rather dilute for application in fuel cell systems. However, a major disadvantage of the oxidative process is that, since it involves combustion, particles of elementary carbon are produced which are almost impossible to eliminate from the system without extensive treatment. Such particles vary in size from several microns down to a few Ångstroms in diameter, and are extremely difficult to filter from the gas stream. Fine carbon particles would be expected to give trouble over long periods as they would accummulate at points where the gas flow is subjected to a sharp change in direction such as one can expect to find in the passages that occur in fuel batteries. On the other hand, the steam-reforming reaction can give hydrogen concentrations of the order of 70% on a dry basis, the gas being free from particulate contamination. If a hydrocarbon which is low in sulphur content is available and acceptable to the user, then this process is extremely attractive. In normal commercial practice, when customers wish to purchase a fuel for the generation of hydrogen by the steam-reforming process, fuel of extremely low sulphur content is usually specified since its use simplifies the overall process. Correspondingly, it seems reasonable to adopt this practice for small fuel cells where the small scale of the system reinforces the need for simplicity.

It is useful, in the first instance, to consider the equilibria involved in the generation of hydrogen-rich gases from the hydrocarbon, via the straightforward steam reforming reaction,

$$C_nH_{2n+2} + nH_2O \longrightarrow (2n + 1)H_2 + nCO$$

followed by the water gas reaction

$$H_2O + CO \rightleftharpoons CO_2 + H_2$$

and the methanation reaction

$$CO + 2H_2 \rightleftharpoons CH_4 + H_2O$$

With the availability of computer programs the overall effect of these equilibria in given circumstances can readily be calculated. In Table 1 are given typical equilibria for a mixture of a hydrocarbon and water. The ratio chosen of three molecules of water to each molecule of carbon in the feed stock can with modern catalysts give reliable operation on a variety of hydrocarbons up to and including kerosines with a significant aromatic content. Covered by Table 1 are the effects of pressure and of the removal of water from the feed after it has been through the catalyst stage. Results are given for two operating temperatures, 527°C and 827°C.

Inspection of these columns immediately indicates the embarrassment of choices facing designers. The lower operating temperature is attractive because it limits the possibility of carbon deposition on the catalyst and the consequent reduction of catalyst life. Additionally the efficiency of the system is likely to be greater since less heat exchange will be necessary. Finally, if operation under pressure is contemplated, then the selection of alloys suitable for use under pressure at 500°C is much easier than for use at 750°C. A lower operating temperature implies the possibility of a more rapid start-up of the power system, and this is sometimes of importance. If one wishes to purify the hydrogen by means of a palladium/silver diffuser, operation under pressure is necessary in order to limit the area of diffuser required. Whereas at 500°C and 20 atmospheres a considerable proportion of methane is generated, at 750°C the gas has a high carbon monoxide content. However, this carbon monoxide content can be reduced by the injection of further water and use of a low temperature shift catalyst; under suitable conditions this will reduce the carbon monoxide content to a few tenths of a percent and increase the hydrogen concentration accordingly. Without the additional injection of water for this purpose, the hydrogen content of the gas from the reformer before water has been "knocked-out" is only about 42%. This means that either one must use a large area of diffuser to obtain a satisfactory yield of hydrogen, and this brings with it problems of weight, volume and expense, or, alternatively, some arrangement must be made to remove water from the system. This latter involves reducing the temperature to the point at which condensation occurs (at 20 atmospheres this is about 180°C) and then reheating the gas to 350°C, a temperature suitable for operation of the palladium/silver diffuser. In the two systems so far developed of which the authors are aware, namely that developed by Engelhardt Industries for the U.S. Army Signal Corps and that developed by the Pratt and Whitney Company for the U.S. Army Electronics Command, water knock-out does not appear to have been used and the disadvantages of a large area of diffuser appear to have been accepted. Because of the cost and complexity of high pressure operation it is clear that operation at low pressure is preferable in the interests of simplicity and the low cost of the reformer unit.

If an impure gas is fed to the fuel cell there are certain attractions in passing all the gas through to the fuel cell and then burning the effluent from the fuel cell to supply process heat. In this case it is, of course, essential to ensure that the effluent from the fuel cell is a combustible gas. When the course of using an impure gas is adopted, then the advantages of operating at the lower

feed temperature of 500°C for the steam-reforming catalyst become evident. Whereas for operation at 750°C it is often necessary to specify a fuel which is not far removed from a mixture of straight hydrocarbons, fuels containing up to at least 15%w of aromatic compound are acceptable with suitable reforming catalysts operating at 500°C or below.

Since nickel-containing catalysts are normally used for steam-reforming of hydrocarbons and these catalysts are sensitive to sulphur, the sulphur-content of the fuel has a dominant role in performance. In Figure 1 is shown the time to "kerosine breakthrough" for a typical steam-reforming catalyst when fuels of similar composition but varying sulphur content were used. These were in fact made by blending a fuel of low sulphur content with one of high sulphur content, so that the sulphur compounds are representative of those likely to be encountered in practical fuels. Whereas with a fuel sulphur content of 20 parts per million the life of a catalyst was in excess of 1200 hours, at 1500 parts per million sulphur life had fallen to a mere eight hours. While it is possible to use additional catalyst as a "sulphur guard" this is a very expensive way of desulphurizing fuel and normally one would prefer to specify a fuel of low sulphur content to simplify the operation of the fuel cell. This seems a small price to pay for the high efficiency of the fuel cell.

ELECTRODES FOR USE WITH IMPURE HYDROGEN

Whereas operation on pure hydrogen is a relatively straightforward matter and electrodes are available that operate satisfactorily for thousands of hours, the situation is more complicated when one wishes to operate on gas taken directly from the reformer. Even if the carbon monoxide is reduced to a very low concentration by a suitable catalyst for the methanation reaction (3) as was done by Meek & Baker[1] problems can still arise from the presence of carbon dioxide. In Figure 2 are shown results indicating that at 25°C slow poisoning of a platinum electrode occurs with the mixture of 80%v hydrogen/20%v carbon dioxide. This presumably occurs by the "reduced carbon dioxide" mechanism of Giner[2]. However, this can be overcome by the use of alloy catalysts, as is also shown in Figure 2 by the example of the platinum/ruthenium catalyst. If on the other hand the feed contains appreciable amounts of carbon dioxide together with carbon monoxide, then extremely rapid poisoning of platinum occurs and it becomes essential to use an alloy catalyst. It is also advantageous to operate at as high an electrolyte temperature as possible. The effect of gas composition in terms of hydrogen and carbon monoxide contents is shown in Figure 3 and it will be noted that there are marked advantages in operating with as low a carbon monoxide content as possible. If it is borne in mind that it is the effluent from the last fuel cell of a battery that will determine the operating conditions of the battery itself there would seem to be a strong argument in favour of reducing the carbon monoxide content as much as possible by use of a suitable shift catalyst. In Table 2 are examples that illustrate the advantage which can be obtained from a shift catalyst without any further addition of steam to the feed. If one were aiming at a reformer efficiency of about 60% then the effluent from the fuel cell would contain about 40% of the total input heat necessary for use as process heat. This would imply that if the inlet hydrocarbon contained about 0.6% carbon monoxide the outlet from the cell would contain 1.4% carbon monoxide and the electrode characteristics would be better than those shown for 2% carbon monoxide in the diagram. It should be emphasized that these characteristics are not the optimum that can be achieved but are representative of the advantages of using alloy catalysts in these circumstances to obtain a higher performance. The catalyst loading could be increased by a factor of three, from the twelve milligrams per square centimeter used to 36 milligrams per square centimeter, but whether the increase in performance obtained would be worthwhile would depend upon individual circumstances. It may be noted in passing that whereas hydrogen containing carbon monoxide fed to an electrode with a simple platinum catalyst causes a steady drift

in potential towards that of the oxygen electrode, a completely steady output is obtained with alloy catalysts. This difference would appear to exist as direct oxidation of carbon monoxide takes place on the alloy catalyst electrode leaving vacant sites for the further oxidation of hydrogen. An alternative is to use a pure platinum catalyst and operate at 150°C where oxidation of carbon monoxide on the platinum occurs at a satisfactory rate. However, operation at this higher temperature involves the use of a phosphoric acid electrolyte giving higher internal resistance, slower starting of the cell and additional corrosion problems.

SUMMARY AND CONCLUSIONS

Since low temperature fuel cell power systems that utilize hydrocarbon fuels are likely to be expensive, most applications for which they are chosen will demand long unattended periods of operation because it is only under these conditions that fuel cells are likely to show to economic advantage. In order to achieve the necessary reliability for this type of operation, it is essential to keep the number of moving parts in the system to a minimum and to use electrodes with as long a life as possible. All the evidence suggests that the lower the operating temperature of electrodes, the longer the life. For example, "Shell" Research electrodes have operated unchanged at 30°C for periods of 15,000 hours on hydrogen and oxygen, and this figure relates to a 17-cell battery and so is not a freak performance of an individual electrode. On the other hand, if one goes to temperatures of 150°C or more, then electrode life can be something of a problem. As has been shown, operation at pressure involves complications in addition to the expense of the diffuser required for the production of ultra-pure hydrogen and therefore the impure hydrogen system has much to commend its use. The data presented in the preceeding section of this paper suggest that it is well worthwhile to use an alloy catalyst on the electrode, and to "shift" the carbon monoxide content to as low a level as convenient. To some extent this will be determined by the power level required and the cost of the electrode system.

Bearing in mind the necessity to operate efficiently under part-load conditions when losses in the battery will be at a minimum it will probably be desirable for the battery to be fairly compact in order to minimize heat loss and maintain a reasonably high equilibrium temperature. Consequently the narrow passages of the cell are likely to require a pump or blower to move air through the battery. From the point of view of silence and reliability there is much to commend the use of a centrifugal blower and, for the small quantities of air likely to be involved with most power systems, the arguments in favour of the electrodes which will operate at a minimum pressure are strong.

With the electrodes and reforming catalysts now available there seems to be no problem in assembling reliable fuel cell power generators to use impure hydrogen. As will have become clear from the previous section of the paper the authors are strongly in favour of using fuels of minimum sulphur content. As in all work with low temperature fuel cells, the outstanding problem is of course the cost and availability of platinum catalysts and it will be most interesting to see how successfully they can be eliminated or at least reduced in quantity in practical power systems.

A substantial amount of the work discussed in this paper has been carried out under Ministry of Defence contracts and acknowledgement is accordingly made for permission to publish the information so obtained.

REFERENCES

1. J. Meek and B.S. Baker. "Fuel Cell Systems" - Advances in Chemistry, Series 47, American Chemical Society 1965, p.221.

2. J. Giner. Electrochemica Acta, 8, 857, 1963.

Table 1

Steam-hydrocarbon reaction equilibria

Feed composition, %v

	$C_nH_{2n+2} + 3nH_2O$				$C_nH_{2n+2} + 3nH_2O$ after water "knockout"			
	1 atmosphere		20 atmospheres		1 atmosphere		20 atmospheres	
	527°C	827°C	527°C	827°C	527°C	827°C	527°C	827°C
H_2	34.7	47.9	12.1	42.4	59.8	70.5	31.1	66.8
CO	2.5	12.0	0.4	9.9	4.3	17.7	1.0	15.6
CO_2	12.6	8.0	9.4	8.4	21.7	11.8	24.2	13.2
CH_4	8.2	0.01	17.0	2.8	14.2	0.015	43.7	4.4
H_2O	42	32.1	61.1	36.5	-	-	-	-

Table 2

Effect of shift catalyst on gas composition from reformed kerosine

Feed $C_nH_{2n+2} + 3nH_2O$

	Composition, %v, wet basis	
	From reformer at 527°C	After shift at 227°C
H_2	34.7	37.02
CH_4	8.2	8.2
CO_2	12.6	14.92
CO	2.5	0.18
H_2O	42.0	39.68

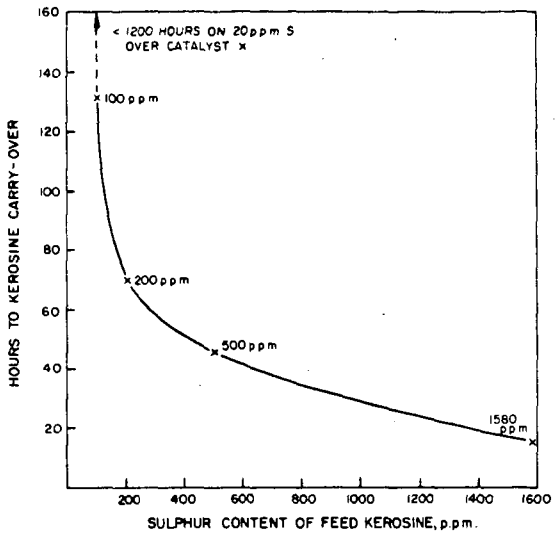

FIG. 1 — Effect of sulphur content of kerosine on time token for kerosine carry-over to be observed when steam-reforming over catalyst x

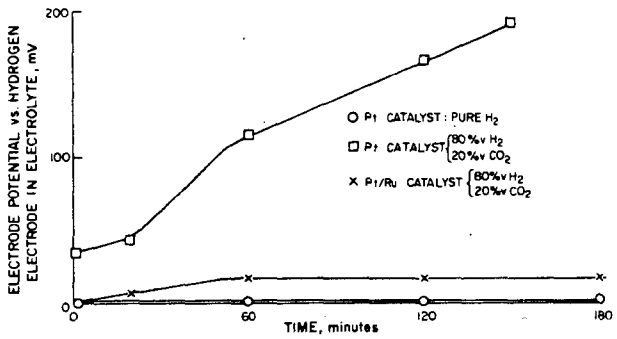

FIG. 2 — Effect of carbon dioxide on electrode performance: 175 mA/sq.cm, 25°C

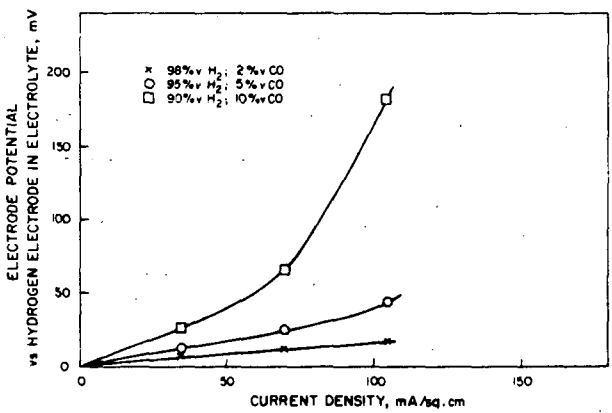

FIG. 3 — Effect of carbon monoxide on alloy hydrogen electrode performance: electrolyte 6N H_2SO_4, 70°C

THE TARGET* PROJECT

M. V. Burlingame

Natural Gas Pipeline Company of America

The TARGET project is a cooperative undertaking of almost thirty gas companies who are financing massive research to try to develop an economical natural gas fuel cell to provide a competitive answer to the all-electric home. The objective is a power plant of a size and capability that will service not only a single family dwelling but also multi-family units, such as apartments and town house groupings, shopping centers, commercial establishments, and light industry facilities.

The sponsoring gas companies are providing up to $5 million annually in this venture with Pratt & Whitney Aircraft Division of United Aircraft Corporation, which in turn is using, as a subcontractor, the Institute of Gas Technology, the gas industry's research facility in Chicago. Pratt & Whitney is contributing another $2 million annually to the effort. With three years of study involved in Phase I of the program, a $21 million effort is scheduled, without question the largest single research effort ever undertaken by the gas industry.

While the fuel cell principle has been known for more than a century--Sir William Grove probably invented the first true fuel cell about 1840--it was confined to the laboratory until The Space Age. The fuel cell became a household word with the successful Gemini space probes which depended for electrical energy on a highly improved Grove-type fuel cell. In this cell, pure hydrogen is the fuel and pure oxygen the oxidant using an electrode catalyzed with platinum.

Natural gas is a good source of hydrogen, and air is a good source of oxygen. The problem and challenge is the right combination of these source materials to produce an economic unit not requiring an expensive catalyst. This, then, together with a detailed market analysis, constitutes the substance of the TARGET project.

In addition to the cell itself, complete systems will have to be investigated. Reformers to produce hydrogen from natural gas, methods of conditioning the air, or means of using either as is--or either substance only slightly modified--must be researched. Inverters are also being studied to determine the most efficient, the most economical, and the most long-lived type or types. Progress has been made on these approaches, but much more is necessary. This is a major part of the research program.

---

* Team to Advance Research for Gas Energy Transformation, Inc.

Our research program is looking at three general groups of cells, fueled with natural gas and air, to determine which may have the best capability for success. These types may be referred to as:

1. Low temperature cells - 140°-300° F.

   a. Acid electrolytes, i.e., sulphuric or phosphoric

   b. Alkali electrolytes, i.e., sodium or potassium hydroxide

   Each of these has pros and cons. The acid cell seems unaffected by the CO_2 in the air and it appears that there is less chance of electrode pollution with insoluble carbonates. The alkaline cell appears a more efficient air electrode with less corrosion complications than the acid cell.

   Both now use rather expensive catalysts, such as platinum or silver palladium, and poison sensitivity (CO_2-H_2S) of the catalyst may be a problem.

   Here research will be directed towards the development of inexpensive catalysts with tolerance for impurities in the gases.

2. Molten-electrolyte cells

   a. Hydrate of potassium hydroxide (medium temperature - 400° F.)

      Requires reformers to provide hydrogen from the natural gas and equipment to remove CO_2 from the air.

   b. Molten carbonate (high temperature - 900°-1400° F. range)

      (1) Does not require noble metal electrode catalysts

      (2) Provides useful heat, but is sluggish in performance and has corrosion problems.

3. Solid electrolyte cells, using stabilized zirconia as the electrolyte, is the last type of cell under investigation. This is a high temperature cell operating in the 1600°-1900° F. range. Because the solid electrolyte must be thin (0.016 in.), structural problems present themselves. Plusses, however, include (1) usable waste heat, and (2) large tolerance to impurities in the reactant gases.

In our efforts, whole systems, not just the cells, must be considered--such as reformers for fuels and oxidant purification, where necessary, means of overcoming sluggishness to load demands, etc. Solution of these problems is the major effort of the TARGET research program.

Additional aspects of the research will deal with:

1. Market analysis (types of customers to be served)
2. Load characteristics
3. Methods of placing the fuel cell in the hands of the public
4. Other special interests.

This is the TARGET story.

I wish I could promise its resounding success, but in any research venture the possibility of failure always exists, of course. However, we think TARGET is not only a worthwhile business venture but one that must be undertaken if the gas industry is to continue as a leader in the primary energy business. As I said at the start, almost thirty major gas companies have laid their money on the line--not only in hope of success but to express their faith in the future.

Figure 1

CELL REQUIREMENTS

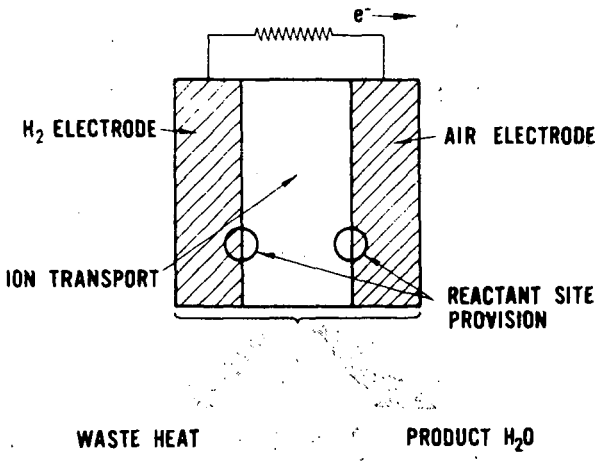

Figure 2

THE PROGRAM

OBJECTIVES

- DEVELOPMENT OF COMPETITIVE SYSTEM
- MANUFACTURING FACILITY
- TRAINED ORGANIZATIONS

ULTIMATE BENEFITS TO GAS INDUSTRY

- NEW LOADS
- LOAD LEVELER THROUGH BASE LOAD SENDOUT INCREASE
- COMPETITIVE ANSWER TO THE ALL ELECTRIC HOME

Figure 3

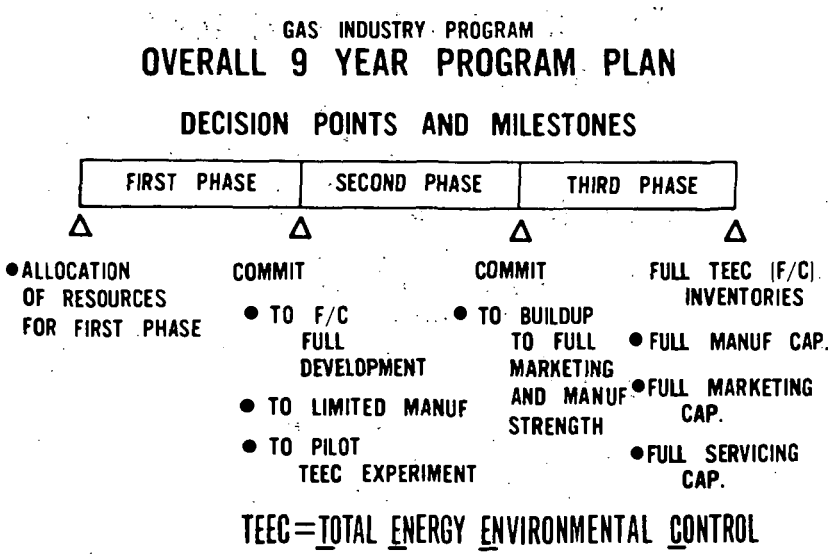

Figure 4

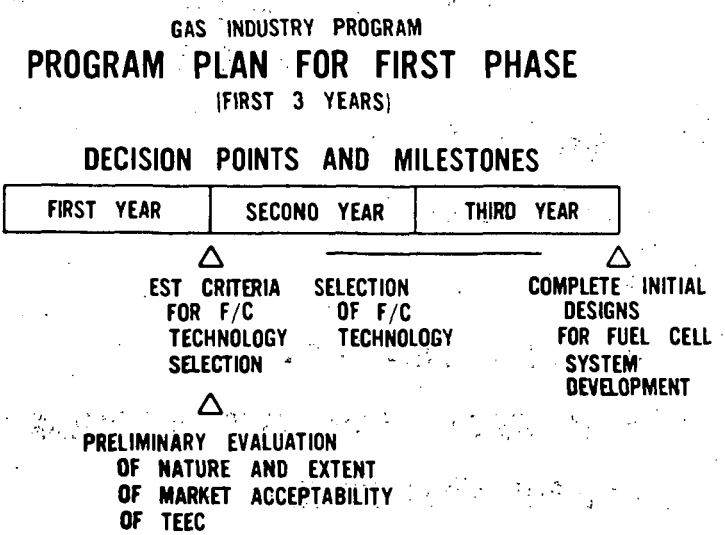

Figure 5

FUEL CELL POWERPLANT FEATURES

PERFORMANCE

- GOOD FUEL ECONOMY
- NO SIZE EFFECT ON CELL EFFICIENCY
- HIGH EFFICIENCY AT PARTLOAD

MODULAR PACKAGING

- MINIMUM OF DISSIMILAR PARTS
- SIMPLIFIED MAINTENANCE
- DEPENDABILITY
- INSTALLATION FLEXIBILITY

OPERATION

- SILENT & VIBRATION FREE
- CLEAN EXHAUST
- HEAT UTILIZATION
- FAST RESPONSE

Figure 6

GAS INDUSTRY PROGRAM

PROGRAM ELEMENTS

- MARKET ANALYSIS
- APPLICATIONS ANALYSIS
- SYSTEM ANALYSIS
- SYSTEM ENGINEERING
- TECHNOLOGY (BASIC AND POWERPLANT)
- APPLICATIONS TESTING

Figure 7

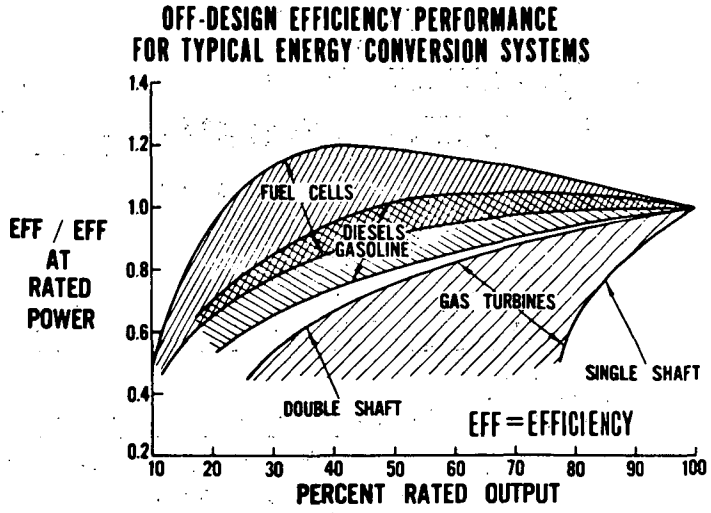

Figure 8

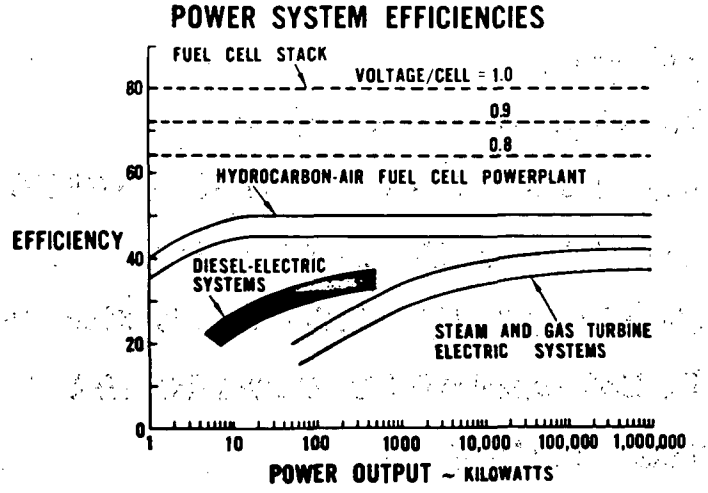

Figure 9

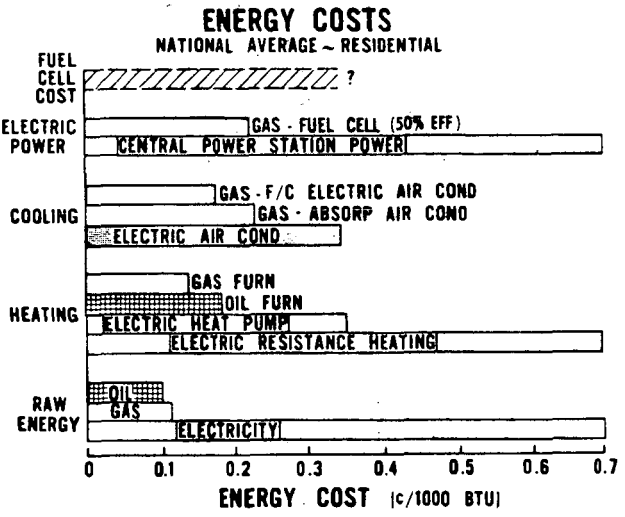

Figure 10

FUEL CELL – TOTAL ENERGY APPLICATIONS

- INDUSTRIAL
- MERCANTILE AND OFFICE BLDGS
- LARGE URBAN RESIDENTIAL (HI-RISE APARTMENT BLDG)
- LARGE HOTEL, HOSPITAL, DORMITORY
- SUBURBAN CONNECTED RESIDENTIAL (GARDEN APARTMENT)
- SUBURBAN DISCONNECTED RESIDENTIAL (TRACT)
- SINGLE RESIDENTIAL

FUEL CELL EXPERIENCES AND IMPRESSIONS

S. Orlofsky
Columbia Gas System Service Corporation

In July, 1961, Columbia entered into an agreement with the Pratt and Whitney Aircraft Division of United Aircraft Corporation for the joint development and field testing of a 500 watt prototype hydrox fuel cell powerplant. So promising was this initial venture that a second agreement for the development of a 3.75 KW/natural gas-air fuel cell powerplant was negotiated in September, 1963. In February, 1967, a group of 27 natural gas industry companies formed TARGET, "Team to Advance Research for Gas Energy Transformation, Inc.", to sponsor and guide a multi-million dollar research program for the development of a marketable fuel cell powerplant operating on natural gas. Pratt and Whitney Aircraft is prime contractor for the TARGET program with the Institute of Gas Technology as subcontractor.

Columbia has one primary reason for participating in fuel cell R & D programs: to sell more natural gas! We know that a fuel cell consuming methanol, or hydrazine, or hexamethyl chickenfat is basically unsuited for our requirements. Since natural gas, which is predominantly methane with lesser amounts of the heavier paraffin hydrocarbons, is quite unreactive electrochemically, we had followed some devious routes in building prototype demonstration hardware. We are interested in any fuel cell type, acid, alkaline, high temperature, or what-have-you that economically utilizes natural gas to produce electricity.

Economical Energy Transmission

It is the high efficiency with which the chemical energy of a fuel is converted to more valuable electrical energy that attracts our interest. The most modern multi-megawatt central generating stations operate at about 40 percent efficiency. And, transmission of energy as electricity introduces other inefficiency. Line losses represent a significant portion of the power produced as it is wired from the central plant to the ultimate consumer.

Fortunately for the gas industry, it is a simple engineering and economic fact that the electrical industry cannot supply energy units as inexpensively as the gas industry. The electric industry has to convert chemical energy to electrical energy in central power stations and then transport the energy through wires to the point of consumption. The cost of doing this is far greater than the cost of transporting natural gas energy to the consumer. The result is that throughout the United States, regardless of the class of customer, electricity costs 3 - 10 times more than natural gas at the meter for an equivalent amount of energy. Although a utilization efficiency correction factor must be applied to gas costs, it does not significantly affect the basic cost relationship.

Conventional central power stations are very well known contributors to air pollution. A typical coal consuming central station will produce 7.7 pounds of solid exhaust emissions per million Btu. Very substantial quantities of sulfur dioxide are also released to the atmosphere. The natural gas fuel cell produces none of these.

500 Watt Hydrox Powercel

Columbia's first, and the free world's first industrial fuel cell engine, was developed by Pratt and Whitney Aircraft Division of United Aircraft Corporation. This 500 watt, hydrogen-oxygen Bacon-type unit was delivered to us in December, 1962, where it was installed at our Stanton, Kentucky, transmission compressor station--located in the hills of southeastern Kentucky.

The 28 cu. ft. engine package consisted of 17 cells arranged electrically in series, chemically in parallel. Each folded can cell contained four dual-porosity nickel electrodes, each 5 inches in diameter, and fuel and oxidant chambers separated by a space for the 85 percent potassium hydroxide electrolyte. The Powercel PC5A1 operated at 450°F cell-electrolyte temperature and atmospheric pressure. The correct operating temperature and electrolyte water concentration were maintained by circulating an excess quantity of fuel through the cells. This fuel, carrying the heat and water, was pumped out of the cells and circulated through a heat exchanger-condenser system.

Open circuit voltage of the powerplant was 20 VDC corresponding to 1.2 VDC per cell. At full load, the output voltage dropped to 15 VDC of 0.88 VDC per cell. Actual hydrogen consumption rate was 0.056 lb/hr. at maximum power corresponding to an overall fuel to DC buss efficiency of 49 percent. Parasitic power requirement was 60 watts to operate the hydrogen circulating pumps.

Predictably, there were some unique problems associated with startup and operation of the prototype powerplant. One of our first problems was holding a small positive pressure on the cells anytime the unit was hot to prevent flooding. Flooding

can occur as a result of loss of reactant pressure within the cells at operating temperature, or inadequate removal of the excess water. Ultimately, these problems were traced to plugging at the hydrogen inlet lines.

The fuel cell was operated at partial load first on P&WA hydrogen containing 8 ppm CO_2 and then on Stanton hydrogen containing 195 ppm CO_2. A water column manometer was connected across the modul hydrogen system. During the test with P&WA hydrogen, no increase in pressure drop was observed during the course of the 12-hour run, but performance gradually decayed. Water content of some cells increased from the normal 15 percent to 27 percent at the conclusion of this test. A subsequent test using the Stanton hydrogen terminated after 30 minutes due to cell plugging.

One cell was split open to recover a plug deposit sample for analysis. The plugs occur at the point of maximum hydrogen velocity where the inlet hydrogen impinges on the coarse por sinter. The analysis by X-ray diffraction indicated potassium carbonate.

Clearances on the hydrogen inlets to the cells can be extremely close. Cell X-ray photos indicate clearance ranging from 0.067 inches maximum to less than 0.020 inches between the hydrogen line in the outer shell and the sinter. Turrets were installed at a lower position on the cells where clearance is greatest. The turrets also serve to lower the inlet hydrogen velocity. Use of the turrets necessitates redesign of the internal module heaters.

In view of the definite existence of carbonate plugs and the apparent relation to fuel carbon dioxide level but the complete absence of potassium hydroxide or carbonate in the circulating control system, visualizing the source of KOH for the plug buildup caused a problem. However, P&WA's physical chemists have experimentally established that at least a monomolecular layer of KOH exists at the coarse pore-fuel interface. The KOH migrates from the electrolyte through the adjacent fine pore and through the coarse pore to the external coarse pore surface which forms one face of the hydrogen inlet chamber. This KOH acts as a natural CO_2 scrubber.

The experience to date is very typical of the difficulties that occur in trying to get an instrument or process from the laboratory into the field. Though there had been many problems found in the shakedown of this system, they have been of a simple and troublesome nature rather than deep-rooted.

3.75 KW Natural Gas-Air Powercel

Our second working prototype powerplant was delivered in July, 1966. This unit was also built by P&WA. It is installed at Columbia's Marble Cliff, Ohio, research laboratories where it provides the power requirements for a simulated homw.

The 43 cu. ft. engine package is a completely self-contained demand-responsive powerplant, providing 3.75 KW at the buss bar. Parasitic power consumption is 300 watts to supply an air pump, a cooling oil pump, water pump and electronic controls. The Powercel generates electricity at a nominal 28 VDC at full load consuming 0.645 SCFM of natural gas for an overall efficiency of 38 percent.

Desulfurized natural gas and demineralized water are fed through a boiler into the reformer. To achieve maximum hydrogen production, the primary reactor product gas stream is cooled somewhat and passed to a secondary carbon monoxide shift reactor. In this process, the carbon monoxide formed during the previous processes reacts chemically with water to form additional hydrogen and carbon dioxide. Hydrogen is removed from the reformate by diffusion through palladium--silver diffusers.

This ultra-pure hydrogen is piped to the cell stacks. Separator waste gases are burned external to the reformer to provide heat for the endothermic gas steam reaction. Excess steam is provided in the reactor to prevent carbon deposition.

The hydrogen generator is designed to operate over a wide range of hydrogen production flows, depending on the fuel cell requirements. A surge tank located downstream of the hydrogen purifier unit supplies hydrogen to the fuel cells on demand and allows the generator to adjust to a new steady state load level.

Process air supply serves the dual purpose of providing oxygen for the fuel cell reaction and removing water produced by the electrochemical reaction. Since this is an alkaline electrolyte system, process air is conditioned to remove carbon dioxide. Electrolyte water concentration is maintained by recycling a portion of the oxygen-depleted moist air.

Two stacks of 36 cells each, arranged electrically in parallel provide the net 3.75 KW output. The compact hydrogen-air fuel cells used in this system have an active area of 7.5 inches by 7.5 inches. Each cell contains two catalyzed porous electrodes

separated by an asbestos matrix containing an aqueous solution of potassium hydroxide. The individual cells are separated by metal cooling plates with integral cooling flow passages. The cooling plates also serve as gas distribution housing, current collector, and cell mechanical structure. The entire cell including electrodes, electrolyte, gas housing and cooling plate is about 0.17 inches wide, or a pitch of about six cells per inch.

The PC-10 operates at a gross power density of 150 watt/sq. ft.

Extensive monitoring instrumentation was provided at this Powercel installation so that we could observe fuel cell system performance under conditions of rapidly changing load. The fuel cell would sustain transient overloads of 100 per cent, limited more by protection devices within the unit than by process considerations. However, the solid state static inverter used to convert the 28 VDC fuel cell output to 120 VAC would not sustain an overload, even instantaneously.

Why is this short term overload capability important? In an effort to simulate a normal domestic power requirement, we have loaded the fuel cell with some standard AC home appliances--clothes washer, gas clothes dryer, refrigerator, toaster, electric iron, coffee maker, vacuum sweeper, and some not-so-standard DC appliances--a DC air conditioner. Electric motors characteristically require a tremendous current surge to start: the starting current can be five times the normal run current, but lasts for less than one second. As an example, a popular brand washer comes equipped with a $\frac{1}{2}$ horsepower split-phase

motor--this unit draws almost 50 amps to start but runs at 8 amps. For this program, a capacitance start motor was substituted which drew 22 amps to start and 7 amps run current.

The homeowner just doesn't concern himself with these problems because he does not pay a demand charge on his domestic electric bill. And, the electric company is not concerned because the transformer on the pole in the backyard serves eight to ten houses: the odds on two housewives creating a simultaneous surge is small. But, starting surges are important considerations in designing a system to provide all domestic energy requirements.

Reason for Columbia's Interest in Fuel Cells

Columbia is chartered to sell energy--energy in the form of the premium fuel natural gas. We have captured 92 per cent of the residential and commercial heating markets within our operating areas. Direct industrial sales account for about a quarter of Columbia's total annual natural gas sales, which are in excess of a trillion cubic feet--and this market is growing. Columbia is actively seeking new markets.

A vast market potential exists for natural gas in on-site power generation. Columbia already has installations where gas provides all of the energy requirements, including electricity, of industrial plants, shopping centers, high-rise apartments, hospitals, and hotels. These installations use gas engines or gas turbines and loads are above 50 KW. For small commercial establishments, apartments, and homes where the total power requirement is less than 50 KW, gas engines and gas turbines are not economical.

However, the fuel cell does appear economically feasible for these applications. Projections indicate that by the year 1980 nearly 200,000 new homes will be built each year in Columbia's service area. Assuming that only half of these are truly all-gas homes, they would generate approximately $24 million in new gas sales annually.

With the fuel cell, we will introduce an entirely new concept in home comfort conditioning. The homeowner will be able to purchase or lease one package which will heat and air condition the home, clean and humidify the air in the home, cook the food, heat the water, and supply all electricity using one economical dependable source of fuel, natural gas.

Surprisingly little is known about patterns of electrical energy requirements for the American homeowner. The 1965 average residential power consumption was 4,933 KWH according to Electrical World. Now this consumption figure works out to a steady requirement of less than 500 watts over the year, yet the electrical service connected to the home is commonly 100 amperes at 240 VAC with power companies constantly pushing for 200 ampere installations. The mismatch is apparent when one considers that the transformer on the pole in the backyard has 25 KVA capacity and serves 8 to 10 homes. It is apparent that the power company has sized the transformer on the generally valid assumption that all homeowners served will not require maximum demand simultaneously. However, in the single home on-site fuel cell system, no such diversity exists: the system must be capable of handling any power requirement on demand.

Design of the fuel cell system necessitates information on exact power requirements with an accuracy that is not available. To this end, Columbia has instrumented several homes with rapid response wattmeters and fast response recorders to define and document present consumer power consumption patters.

TARGET--Why an Industry-Wide Joint Venture

Fuel cell technology has advanced to the point where an aggressive, greatly expanded program which has as its goal the production and sale of competitive natural gas fuel cell systems is justified. The Institute of Gas Technology has operated high temperature molten carbonate single cells continuously for over a year. Pratt and Whitney has engineered a self-contained demand-responsive prototype natural gas-air fuel cell system. But, technology has reached that stage of sophistication where little more can be accomplished through continued low cost laboratory type experimentation. Through the American Gas Association and industry, the gas industry has put significant funds into fuel cell research at IGT. The transition to high expenditure, semi-manufacturing scale, prototype hardware is the essential next step in the development of natural gas consuming fuel cell power systems.

Appraisal of the state of fuel cell technology indicates that a properly supported and staffed program could force the entry of the fuel cell into the market by 1975. However, our cost studies project a need for $20 million to finance the first three-year phase of the program. For an individual company to undertake a

major program of such sweeping significance to an industry would not be practical. So, 27 natural gas utilities have joined in the formation of TARGET, Inc.--Team to Advance Research for Gas Energy Transformation.

The benefits to the gas industry from the development of competitive natural gas fuel cell systems for residential, commercial, and industrial application are threefold. These benefits are that:

1. New loads will be obtained.
2. Base load sendout will be increased.
3. The gas industry will gain a competitive answer to the all-electric concept.

The goal of TARGET is the development of a complete comfort package for homes, apartments, and businesses which will be better than any of the methods presently used for environmental conditioning. This package will provide for complete control of temperature and humidity year-around along with generation of electricity for all needs on-site, using safe, dependable natural gas. Reduction of air pollution is a corollary benefit.

The exact target at which our industry effort is aiming is the development and marketing of fuel cells specifically designed to operate on natural gas and air. Present plans call for development of marketing, economic, and technological information necessary to establish the competitive position and usefulness of fuel cell total energy and environmental conditioning packages of various sizes by Pratt and Whitney Aircraft under the supervision of TARGET.

The first phase of the development program is an extensive market evaluation.

FUEL CELLS FOR CENTRAL STATION POWER

N. P. Cochran

U.S. Department of the Interior
Office of Coal Research
Washington, D.C. 20240

ABSTRACT

Fuel Cells can be engineered for use of hydrocarbon fuels. High efficiency and low capital cost of such cells in the range of 100,000 and 2 million kilowatts is described. How such cell systems can be used to generate power from fossil fuels is included. The paper includes a judgment on near term commercial applications of such cells and projects future power-plant costs.

RECENT ADVANCES IN FUEL CELLS AND THEIR APPLICATION TO NEW HYBRID SYSTEMS

E. J. Cairns and H. Shimotake

Argonne National Laboratory
9700 S. Cass Avenue
Argonne, Illinois

INTRODUCTION

In our rapidly-advancing technological society, there is an increasing need for versatile sources of electrical energy. Some of the desired characteristics of these power sources are:

1. High specific energy (watt-hours/lb)
2. High specific power (watts/lb)
3. Fast refuel (or recharge)
4. Fast response to load changes
5. Cleanliness (no pollution)
6. Low cost
7. Silence

Some fuel cells have some of the desired characteristics, and some secondary cells have others; no known power source possesses all of them. One possible solution is to take advantage of the desirable characteristics of both fuel cells and secondary cells by using a composite power source containing both of these devices. In considering the characteristics of fuel cells, it becomes clear that some fuel cell systems can provide high specific energy (greater than 500 watt-hours/lb for cells operating on air), none can provide very high specific power (all fuel cell systems are below 30 watts/lb), most can be refueled quickly, some will respond quickly to load changes (systems using reformers respond slowly), most can be made to operate at a very low level of emission of pollutants, none are low-cost yet, and many are quiet. Some of the shortcomings of fuel cells can be compensated for by an appropriate secondary cell having a reasonable specific energy (greater than 40 watt-hours/lb), a high specific power (greater than 150 watts/lb), and fast charge acceptance (15 minutes for full charge). In their present state of development, neither fuel cells nor high specific power, fast-recharge secondary cells are low-cost devices. In applications where the other characteristics are essential, however, a price-premium is justified as for remote power and military and space applications.

The recent advances in fuel-cell development will be summarized below, in order to include the best performance, endurance, and cost estimates in considering some applications. Because fused-salt secondary cells show the most promise for high specific power and high specific energy applications requiring fast charge acceptance, the secondary cells considered will be of this type. Specifically, the Li-Te and Li-Se cells, with which the authors have the most experience, will serve as the basis for the calculations.

RECENT ADVANCES IN FUEL CELLS

In considering the areas where improvement in fuel cells is needed, the three most prominent are: a) Electrocatalysts, primarily as they affect cost and performance, b) Electrode structure, as it affects cost, endurance and weight, and c) Engineering, as it affects endurance, weight, and volume. Of course, improvements in these three areas are desired while maintaining at least the present level of performance.

The fuel cells which are expected to find the most widespread application are those operating on air. For this reason, only cells with air cathodes will be discussed here. In addition, because of the trouble and expense involved in storing hydrogen, either as a liquid or as a gas, only fuel cell systems using fuels normally

stored as liquids will be considered. These fuel cell systems can be classified as indirect (those using a reactor to produce hydrogen which is then consumed in the fuel cell), and direct (those in which the unaltered fuel is fed directly to the cell).

Indirect Fuel Cells

Indirect fuel cell systems can be arranged so that: a) only very pure hydrogen is fed to the anode (most expensive), or, b) hydrogen of almost any degree of purity (including the untreated reformer exit gas) is fed to the anode. Some of the indirect fuel cell systems which have been investigated are diagramed in Figure 1. The indirect systems which use very pure hydrogen at the anode (parts a and b of Figure 1) are the most well-developed and make use of high-performance fuel cells. Furthermore, because of the high reactivity of hydrogen and the absence of chemical and electrochemical complications due to impurities, a great deal of progress toward the elimination of expensive platinoid-element electrocatalysts has been made for these cells.

The amount of platinoid element electrocatalysts necessary in hydrogen fuel cells has been reduced from 35-50 mg/cm^2 a few years ago[1,2,3] through intermediate loadings[4,5] to values as low as 0.5-2 mg/cm^2(on each electrode) in low- temperature alkaline systems[4,5] and 0.5-4 mg/cm^2 (on each electrode) in low-temperature acid systems.[8,9,10] This decrease in the amount of platinum required has been made possible largely by the use of electrocatalyst supports such as high-area carbon,[6,7,8,9,10] resulting in very small platinum crystallites having a high specific area.

It is not only possible to minimize the amount of platinum in hydrogen anodes, but for alkaline-electrolyte cells, the platinum can be eliminated by using nickel (high-area,[11,12] or Raney form[13,14]) or nickel boride.[15,16] High area nickel has disadvantages, however, such as the irreversible loss of activity after being used at too high a potential (oxidation of the nickel occurs). Nickel boride, formed in various ways,[15,16] seems to be less sensitive to overvoltage excursions than nickel, and may be an acceptable hydrogen anode electrocatalyst for operation near 80°C at a modest performance penalty.[15]

It is also possible to eliminate platinoid elements from air cathodes for alkaline electrolyte systems. Some of these cathodes use silver[7,17,18] or spinels such as $CoOAl_2O_3$,[7] or phthalocyanines such as cobalt phthalocyanine[19] instead of platinum, providing an additional saving. It should be noted, however, that the advantage of the more flexible electrocatalyst requirement for the alkaline electrolyte cell is at least partially offset by the need for CO_2 removal from the air (or periodic electrolyte replacement).

Almost as important as the advances in electrocatalyst use are the improvements in electrode structure, particularly at the air cathode. In the last few years, the trend has been towards very thin electrodes (0.006 to 0.03")[1,2,6] with relatively high porosity[4,9] providing for limiting current densities of several hundred ma/cm^2 on air at only moderate air flow rates[4,8,9] (1.5-3 times stoichiometric). Thin, highly porous electrodes are also essential in those systems which remove product water by evaporation through the porous electrodes.

The requirement of minimum cell internal resistance has led to the use of thin, porous, absorbent matrices to hold the electrolyte, resulting in inter-electrode distances of 0.010" to 0.030". The use of thin electrodes (about 0.020" each) and thin absorbent electrolyte matrices (0.020") allows the construction of relatively compact fuel batteries, with cell stacks of about seven cells per inch.[20] This stacking factor corresponds to stack power densities in the range 7-8 kw/ft^3 for 160 w/ft^2 cells. The density of the stacks is estimated to be about 140 lb/ft^3, corresponding to 18 lb/kw for future fuel cell stacks. The weights and volumes should be increased by 10 to 20 percent for cells with liquid electrolytes.

The present state of fuel cell engineering can be appreciated by consulting the papers describing the design, development and operation of the GM Electrovan[21,22] which is powered by Union Carbide hydrogen-oxygen cells.[23] This is a

remarkable achievement, especially when one considers the relatively sophisticated control system[24] and the high performance of the vehicle. The most notable disadvantage of this fuel-cell powered vehicle is the excessive weight of the fuel cells (3,380 lb!) made necessary by the peak power requirement (160 kw) of five times the nominal rating (32 kw). This weight penalty could be minimized by use of a fast charge, high specific power secondary cell. This point will be discussed in more detail below. Despite the disadvantages, the Electrovan proves that fuel cell engineering has progressed to the point that vehicles can be powered by hydrogen fuel cells and can retain reasonable performance and range.

The combined effect of improved use of electrocatalysts, thinner, high-porosity electrode structures, and small interelectrode distances yields the performances shown in Figure 2. The upper curves correspond to alkaline electrolyte cells, using thin matrices and moderate catalyst loadings (9-10 mg Pt/cm^2) on thin, PTFE-bonded electrodes.[3,5,20] Replacement of the Pt at the anode with Ni_2B[15] yields slightly lower voltages as shown. The next lower curve corresponds to the substitution of H_2SO_4 for KOH as the electrolyte. The poorer performance of oxygen cathodes in acid electrolytes is responsible for this decrease in cell voltage. The next lower set of curves with the somewhat higher slopes corresponds to the use of liquid electrolytes, with larger interelectrode distances and consequently a higher internal resistance.[1,6,10] The lowest curve of Figure 2 corresponds to the use of dual ion exchange membranes.[25] The higher internal resistance of this arrangement is evident.

Based on the results shown in Figure 2, it seems reasonable to adopt the uppermost curves for design purposes, assuming a catalyst loading of 1 mg Pt/cm^2 (or its cost equivalent of Ni_2B and Ag or $CoOAl_2O_3$) on each electrode. Only a small performance penalty would be paid if the platinum in the cathode were replaced by silver or $CoOAl_2O_3$,[7] and the platinum in the anode by nickel boride.[15,16] This performance is what would be expected from the cell in any indirect system supplying pure hydrogen (or hydrogen with non-adsorbing inerts, such as N_2) to the anode.

A five-kilowatt indirect system using a KOH electrolyte and an air scrubber has been constructed by Englehard (reformer) and Allis-Chalmers (fuel battery) and has been tested at Fort Belvoir.[26,27] This system operates on a sulfur-free hydrocarbon fuel (JP 150, a Udex raffinate),[27] and uses a silver-palladium alloy diffuser to purify the hydrogen (an expensive method). The operating point was 0.83 V at 135 ma/cm^2. A second 5 kw indirect system using a silver-palladium diffuser, but methanol as the fuel to the reformer, was constructed by Shell Research, Ltd.[28]

For indirect systems involving the use of unpurified gases (H_2, CO, CO_2, CH_4, H_2O), as in case c of Figure 1, acid electrolytes must be used if the anode is porous, in order to reject the CO and CO_2. The strong adsorption of CO on platinum, and the low rate of electrochemical oxidation of the CO make platinum an unsuitable anode electrocatalyst at temperatures below about 130°C, as shown by the lowest curve in Figure 3. At higher temperatures, with H_3PO_4 as the electrolyte, Pt will provide adequate performance as shown by the upper curve of Figure 3. At 150°C, about 110 ma/cm^2 can be obtained at 0.75 V using 90% H_2 and 10% CO with an anode containing 2.8 mg Pt/cm^2, supported on boron carbide.[3] At 85°C, Pt-Ru alloys show moderate activity with CO-containing reformer gases and H_2SO_4 as the electrolyte, as indicated in Figure 3, but the electrocatalyst loadings used (34 mg Pt-Ru/cm^2)[29] must be considered to be about an order of magnitude too high to be practical. For the present, it appears that the oxidation of reformer gases containing more than a few ppm of CO requires the use of acid electrolytes at temperatures near 150°C. The improvements in CO tolerance shown by Pt-Ru alloys are encouraging, however, and it is expected that alloy catalysts will be improved further, making the use of unpurified reformer gases practical at temperatures below 100°C.

The same thin, highly porous electrode structures found to be useful with hydrogen/air cells are also useful in reformer gas/air cells. The lower performance

obtained from the latter cells is primarily related to electrocatalytic problems at both electrodes, and not electrode structure problems.

Engineering work resulting in the construction of fuel batteries or complete fuel cell systems operating on reformer gas is just beginning. Several systems are probably being built, and only one low-temperature battery has been reported.[25] Significant performance losses were observed, with only 20 ppm of CO in the feed to the fuel battery, which used 9 mg Pt/cm^2 electrodes and H_2SO_4 electrolyte at 65°C (see Figure 3). It is likely that the indirect systems built in the near future will use fuel cells which operate at temperatures above 100°C, and will have performances like that shown by the uppermost curve in Figure 3.

The molten carbonate cell, operating at temperatures in the range 600 - 750°C is capable of consuming reformer gases containing relatively large amounts of CO (10-20%) with excellent performance. At an operating temperature of 750°C, it is conceivable that the cell and reformer might be integrated in such a manner that the reject fuel cell heat is used by the endothermic reforming reaction, increasing the overall system efficiency. Furthermore, the carbonate cell employs relatively inexpensive electrocatalysts such as nickel at the anode and copper oxide (or silver) at the cathode,[30-34] making this an economically attractive system. During the last few years, considerable improvements in performance[31] and operating life[30,34] have been made, bringing this system to the point where it is ready for an increased engineering effort. A reasonable design point for a molten carbonate system would be 200 ma/cm^2 at 0.75 V, as shown in Figure 4. The life expectancy for a single cell is now more than six months,[30] and 36-cell modules operate for about 1000 hours.[35]

An interesting recent approach to the indirect fuel cell is the integration of the fuel cell and the reformer, placing the reforming catalyst in the fuel compartment of the cell[36] (case d of Figure 1). This is best done when the anode is a non-porous hydrogen diffusion electrode (Ag-Pd activated with Pd black on both sides).[36-38] These electrodes are expensive, their materials costs being equivalent to that of about 20 mg Pt/cm^2 for a 0.001" thick electrode activated on both sides.

Because of the fact that the fuel battery and integrated reformer operate at the same temperature (200-250° C, 85% KOH electrolyte), the reject heat from the fuel battery can supply the endothermic heat for the reforming reaction. In addition, since the fuel cell reaction extracts hydrogen directly from the reforming zone, the response of the reformer to the demands of the fuel cell is relatively rapid. Start-up is not very fast, however, and external heating energy must be supplied.

The best-performing integrated system is that operating on methanol,[36,38] the performance of which is given in Figure 5. The corresponding indirect hydrocarbon cells show poorer performance and short catalyst lifetimes, even at the higher temperature of 250°C,[36,39] as shown in Figure 5. These systems, especially the methanol system, could gain popularity during the interim period before direct methanol or hydrocarbon cells show high performances at capital costs comparable to those for present hydrogen-air cells.

In choosing among the various indirect systems, the operating requirements of the application will probably dictate the optimum combination of reformer, hydrogen purifier (if any) and fuel battery. For fast start-up, a low-temperature fuel battery is desirable. This may require the use of pure hydrogen (as from a silver-palladium diffuser), but it is possible that a cell using a Pt-Ru anode electrocatalyst could be started quickly from room temperature on unpurified reformer gases. Where steady operation without shut-down is needed, the molten carbonate system probably offers the lowest capital cost and highest efficiency. A reasonable compromise system with medium start-up time and medium cost, using no scrubbers or purifiers would be a cell with 2-3 mg Pt/cm^2 at the anode, H_3PO_4

electrolyte, and 3-4 mg Pt/cm^2 at the cathode.[3] This seems to be the simplest system in concept, and could be the simplest in practice.

Direct Fuel Cells

The direct fuel cell which shows the highest performance on a liquid fuel is the hydrazine cell. This cell has received more engineering attention than any other except for hydrogen-oxygen.[40,41] Typical performance curves for hydrazine-air cells are shown in Figure 6. Both platinoid element electrocatalysts[40,42] (Pt and Pd) and nickel-based electrocatalysts[42] (high-area nickel and nickel boride) have been used successfully with hydrazine hydrate as the fuel. Because hydrazine reacts with acids, an alkaline electrolyte is necessary. This means that the CO_2 must be removed from the air fed to the cathode. As in the hydrogen cells, thin, porous electrodes are used, and the electrolyte is usually held in a matrix.

Several complete hydrazine fuel cell systems have been built for vehicle applications, including a 20 kw system for an Army M-37 truck.[41] Because nickel boride can be used at the anode and silver or a spinel at the cathode, the hydrazine cell looks promising from a capital cost viewpoint, but the high cost of hydrazine will probably restrict this cell to special applications. Strong points are the admirable performance obtained with relatively simple systems and the use of non-platinoid electrocatalysts.

All other non-hydrogen direct fuel cells show poorer performance than hydrazine cells, and require unreasonably large amounts of precious-metal electrocatalysts. These other systems must still be considered to be in the research stage and should not be included in any designs involving cost as an important criterion for the near-term future.

Several advances in the direct use of carbonaceous fuels are notable, however. A few years ago, large amounts of platinum ($\sim$ 50 mg/cm^2) were necessary in order to obtain current densities near 100 ma/cm^2 from propane at cell potentials of 0.2 to 0.3 volt.[43-48] It has been reported recently that electrocatalyst loadings as low as 5 to 10 mg Pt/cm^2 can be used with propane, while still obtaining current densities of 100 ma/cm^2 at cell potentials of 0.4 volt.[49,50,51] Some of the recent data are summarized in Figure 7. The liquid hydrocarbons which yield the highest performance are propane and butane; the higher molecular weight fuels give decreasing performance with increasing molecular weight.[44,47-49,54] Some of the problems which remain to be solved are the cycling behavior of the anode reaction rate when phosphoric acid is used as the electrolyte,[55] and the conservation of water, in addition to the obvious problems of electrocatalysis and corrosion.

No presently-known hydrocarbon cells will start up from room temperature, so external heat for start-up must be provided. No appreciable amount of fuel battery or systems work has been done yet, but the time is approaching when this will be appropriate.

The direct methanol cell has not shown the progress that might have been expected of it a few years ago. This cell still requires electrocatalyst loadings of 20 to 40 mg/cm^2 of platinoid electrocatalysts[56,57] at the anode. Even with these loadings, the performance is still relatively modest, as shown in Figure 8. In spite of this disadvantage, some engineering work has been completed, resulting in a battery delivering 300 watts[59], and a compact system delivering about 100 watts at a regulated voltage.[60]

Summary of Fuel Cell Performance

The present state of affairs, with respect to cell choices, reflecting all of the recent advances discussed above incorporating new, low electrocatalyst loadings, and improved performances on air (in some cases estimated by the authors)* is

* All asterisks in the figures identify those current density-voltage curves which have been converted from oxygen performance to air performance by the authors, based on published data.

summarized in Table I. The performance values for the indicated electrocatalyst loadings may be slightly optimistic. The systems which are expected to have the lowest capital cost are the molten carbonate (indirect) and the hydrazine (direct), followed by the reformer gas (indirect) and the integrated methanol reformer-fuel cell. The hydrazine system is the most well-developed, followed by reformer gas (indirect), the other direct cells being farther behind. Direct hydrocarbon and direct methanol cells still contain too much expensive electrocatalyst and require a great deal more engineering work before they can compete with the other systems.

The current status of the systems just discussed is also presented in Table I, together with the authors' estimates of the specific power of the fuel cell stacks and systems (including reformers and plumbing but not fuel and tank) which could be constructed using the present research and engineering results. The specific power values for some of the systems of Table I, together with the specific energy values (watt-hr/lb) of the fuel plus tank allow the direct calculation of specific power (watts/lb) versus specific energy (watt-hr/lb) curves for fuel cell systems containing various weight fractions of fuel cell and fuel. These results are summarized in Figure 9. This figure is particularly useful in selecting fuel cell systems which must meet specific power and energy requirements. This will be discussed in more detail below.

SECONDARY CELLS WITH FUSED-SALT ELECTROLYTES

In order to augment the characteristics of fuel cells to form a high-performance hybrid system, it is necessary that the secondary cell have the ability to deliver large amounts of power per unit weight, on a repeated basis, with no damage to the cell. Specific power values above 100 watts per pound are necessary for many applications, and values as high as 500 watts per pound are desirable. Furthermore, it is necessary that the secondary cell have the ability to accept charge very rapidly without detrimental effects. This feature is important in vehicle propulsion and other applications where fast recharge is essential. A full charge should be achievable in 15 minutes or less for some applications.

The lithium-tellurium and lithium-selenium cells possess both of the characteristics discussed above.[66,67] These cells are still in the early stages of development, but laboratory-model cells have indicated that these systems have the required fast charge-discharge characteristics and high specific powers.[61,62]

The lithium-tellurium cell makes use of molten lithium as the anode (negative electrode), fused lithium halides as the electrolyte, and molten tellurium as the cathode (positive electrode). The minimum operating temperature is set by the melting point of the tellurium (449.8°C),[68] hence thermal insulation must be provided to prevent excessive heat loss. Under normal operating conditions, the internal heat generation will be sufficient to maintain operating temperature, while on stand-by, the cell temperature may be maintained by means of a small heater.

The overall cell reaction is the electrochemical transfer of lithium through the electrolyte into the tellurium, resulting in the formation of a lithium-tellurium alloy at the cathode. On recharge, the lithium is electrochemically extracted from the cathode alloy and returned to the anode compartment. The electrode reactions on discharge are:

$$Li \rightarrow Li^+ + e^- \quad (1)$$

$$Li^+ + e^- + Te \text{ (excess)} \rightarrow Li \text{ (in Te)} \quad (2)$$

Typical steady-state current density-voltage curves for two Li-Te cells operating at 470°C are shown in Figure 10. The open circuit voltage of 1.7-1.8 volts is in good agreement with the values reported by Foster and Liu.[69] Current densities in excess of 7 amp/cm^2 were obtained on both charge and discharge. Because of the fact that the open circuit voltages of the cell are in good agreement with the published reversible emf values, and because the voltage-current density data lie

on straight lines, it is concluded that there are no significant activation or concentration overvoltages present. Furthermore, since the slopes of the voltage-current density curves agree with the measured cell resistance, the only appreciable irreversibilities in the operation of the Li-Te cell at current densities up to 8 amps/cm^2 are those associated with ohmic losses. The ohmic losses arise from the electrolyte resistance and the resistances associated with current collection from the electrodes, primarily the tellurium electrode.

The maximum power density obtained from the cells, whose results are shown in Figure 10, was 3.5 watts/cm^2, indicating that high power densities can be obtained. The use of charging current densities up to 7 amp/cm^2 shows that fast recharge rates can be used. In addition, operation at even higher power densities can be achieved for short periods of time. Figure 11 shows the cell performance for short discharge times (within one minute after start of discharge from the fully-charged condition), corresponding to a cathode composition of about 5 a/o Li in Te. The peak power here was 5 watts/cm^2; the short-circuit current density was 12.7 amp/cm^2.

The Li-Te cells were charged and discharged repeatedly over periods of up to 300 hours at temperatures of 450 to 500°C with no signs of degradation. The charge-discharge coulombic efficiencies at the 1-hour and 45-minute rates were 85 to 91 percent.

A lithium-selenium cell was also operated using the same cell parts as for the lithium-tellurium cell. The operating temperature was reduced to 350°C, since the melting point of Se is only 217°C. The current density-voltage curve for this cell is shown in Figure 12.

Based on the voltage-current density curves of Figure 10, secondary batteries can be designed. The designs include bipolar current collectors and rigid paste electrolyte[70] of minimal thickness ($\sim$ 1 mm). A realistic design, allowing for 5 cells per inch corresponds to a specific energy of 80-100 watt-hr/lb for the Li-Te battery at a 1.5-hr discharge rate, and a specific power of 300 watts/lb at the 1/5 hour rate. The curve of specific power vs specific energy on which these points lie is shown in Figure 9, together with several other curves corresponding to various cell spacings. The method used for calculating the Li-Te battery curves in Figure 9 is explained in detail elsewhere.[66] These curves and those for the fuel cell systems are used in preliminary design calculations. The important features of Figure 9 are the high specific power values obtainable at reasonably high specific energies, since high-performance hybrid systems depend upon the secondary cell for high peak-power capability.

FUEL CELL-SECONDARY CELL HYBRID SYSTEMS

As can be seen by inspection of Figure 9, fuel cell systems have the ability to deliver low to moderate specific powers for long periods of time, but are not able to provide specific powers in the range of 100 watts/lb or higher. In fact, sustained power densities in excess of 30-35 watts/lb are not possible with present-day air-breathing fuel cell systems. Furthermore, air electrodes in general cannot support heavy overloads for even a few minutes because of oxygen diffusion limitations. This situation results in the necessity of designing fuel cell systems around the peak power requirements of the anticipated application. The disadvantage of this practice is that the fuel cell system then is very heavy and bulky, and has a significantly higher capital cost than would be required if the design were for the average power demand.

By combining a fuel cell system with a high specific power secondary cell, a hybrid system is obtained. The hybrid system is designed to take advantage of the high specific power secondary cell to supply the peak load requirements, while the fuel cell system is designed to meet only the time-average power requirements. This results in a total system which is lighter than either a fuel cell system or a secondary battery designed to do the job alone. In vehicle applications of the

hybrid system, it is possible to take advantage of the fast-recharge characteristics of the secondary cell by using regenerative braking. This practice can recover a large fraction of the energy expended in acceleration, providing an extended vehicle range. Thus, fuel cell-secondary cell hybrid systems provide the following features:

1) The high energy:weight ratio of fuel cells.
2) The high power:weight ratio of bimetallic cells.
3) The high charge-discharge rate of bimetallic cells.

These features permit the design of compact portable power sources, particularly well-suited for applications where power profiles having high peak to average power ratios are encountered. These points will be illustrated in the following section by means of practical designs relating to applications in automobiles, homes, and submarines.

Automobile Power Sources

The electric propulsion of automobiles has been viewed as a potential means for reducing air pollution and other urban irritants.[71] However, because of range limitations due to the low specific energy of present batteries[66], it is unlikely that an economically competitive electric automobile with a range of more than 40 miles powered by presently-available secondary cells will be available in the near future.

Fuel cells have also been proposed for automobile propulsion, but the severe limitation of a low overload capability requires that the fuel cell system be sized according to peak power requirements, resulting in a heavy, bulky system.

The hybrid design provides a combination of the high specific power capability of secondary cells and the high specific energy of fuel cells. This will be illustrated by the following calculations for an automobile suited for urban driving where an air pollution problem exists and where the fuel cell fails to meet the requirements of the frequent stops and starts in the driving pattern which require a high specific power. For this driving pattern, a light automobile, like the Volkswagen (1960) was chosen. Pertinent data for the Volkswagen (1960)[72] are listed below:

Unladen car weight*	1,600 lb
Laden car weight (passengers inclusive)*	2,000 lb
Engine brake horsepower	36 hp at 3,700 rpm
Engine weight* (transmission inclusive)	250 lb

*Numbers have been rounded off.

As a design specification for the electrically-powered automobile, the weight of the power source was set at 400 lb or 25% of the unladen car weight, including fuel and tank.

The traction required to drive the automobile consists of tire resistance F_f, air resistance F_a, gravity resistance Mg sin α, where M is the mass of the car and sin α is grade, and acceleration $M\frac{dv}{dt}$, where v is the car velocity and t is time. The total traction required is therefore:

$$F_t = F_f + F_a + Mg \sin \alpha + M \frac{dv}{dt} \tag{3}$$

The power requirement is obtained by multiplying each term by the car velocity:

$$P_t = P_f + P_a + Mgv \sin \alpha + Mv \frac{dv}{dt} \tag{4}$$

The tire resistance for passenger-car tires, with various percentages of synthetic rubbers lie in the range 1.2 to 1.4% of the load carried, and increases to 1.6-2.0% at 70 mph.[73] The air resistance varies with the square of the car velocity and may

be expressed by

$$F_a = C_D \cdot A_f \cdot \rho \frac{v^2}{2g} \qquad (5)$$

where C_D is the drag coefficient of the car (0.6 for a Volkswagen), A_f is the frontal area of the car (20 ft^2 for a Volkswagen) and ρ is the air density (2.38×10^{-3} $lbs\text{-}sec^2/ft^4$). From the above equations, it follows that for a Volkswagen at 30 mph on a 1% grade, having a typical acceleration of 15 to 30 mph in 4 seconds requires 26.6 hp, 20.9 hp of which is required for acceleration.

The traction requirements at various speeds calculated from Equation 3 are plotted together with the performance of the Volkswagen (1960) using four standard gear ratios in Figure 14, illustrating the power requirements for this automobile.

The simplified urban driving profile presented in Figure 13a has been adopted for the present design purposes.

The power profile calculated from this figure and Equation 4 is shown in Figure 13b. This power profile shows that in typical urban driving, the power requirement at the wheels consists of

continuous power:	5 hp	(3.75 kw)
pulse power:	25 hp	(18.8 kw)

By providing a 25 hp electric motor, the design will essentially produce the performance of the Volkswagen as can be seen from the curve labeled as 25 hp in Figure 14. Table II summarizes the design specifications for the urban auto which will perform according to the driving profile of Figure 13a.

The design calculations for the urban automobile powered by the hydrazine/air fuel cell - Li-Te secondary cell hybrid system are summarized in Table III. The weight, energy, and power capabilities of this hybrid system are compared to those for other power sources in Table IV. Note that no fuel cell system used alone could meet the specific power requirement of 58 watt/lb. However, if the car is redesigned to allow more weight for the fuel cell, it is possible to build an automobile powered solely by fuel cells as shown in column 3 of Table IV and demonstrated by the Electrovan. The lead-acid battery may be the least expensive power source at present, however, no lead-acid batteries can meet the specific energy required for a practical range (column 4, Table IV). The silver-zinc and lithium-tellurium systems are both very attractive with respect to the power-to-weight ratio. In particular, the fast charge-acceptance capability of the lithium-tellurium cell presents interesting possibilities including regenerative braking,[74] which is not practical for cells unable to accept charge very rapidly. In the present analysis Ag-Zn batteries show only a marginal range. In summary, Table IV clearly illustrates the superior features of the hybrid system over the other systems.

Power Source for the Home

In many areas, the largest component of the consumer's cost of electricity is the cost of transmission from the power generating station. For the home owner purchasing power from a large utility, this cost is approximately 50% of the consumer price for the electricity. While this cost seems to be a large fraction of the total, it is still acceptable when the economics of central power generation are considered. At present, or in the near future, it is unlikely that any type of fuel cell will be economical enough to be used for supplying electrical power to homes, replacing available power lines. However, because of the very rapid progress made in the last few years, some fuel cells, particularly molten carbonate cells, are becoming attractive in special situations such as areas which are not already serviced by power lines. Under these conditions, fuel cells and hybrid systems may be suitable and economically attractive, with the advantage that the transmission of a fuel such as natural gas is much more economical than transmission of electricity.

The energy and power requirements for a home exhibit a cyclic profile, as shown in Figure 15. Four peaks appear, corresponding to breakfast time, lunch time, afternoon work, and the evening hours. A detailed listing of the power and energy demands,[75] is shown in Table V. Because of the high ratio of peak power to average power shown in Figure 15, it is to be expected that a hybrid system will have an advantage over a fuel cell system. It is seen from Table VI that the hybrid system weighs less than half that of the fuel cell system. A lower system weight means in general a lower initial investment and a lower maintenance expense. In addition, one may take advantage of the high flue temperature of the molten carbonate cell in the hybrid system by using it to maintain the operating temperature of the Li-Te cell. The heat balance shown in Figure 16 indicates that under the given conditions assuming 30% fuel cell efficiency,[31] and using an after-burner to combust the residual hydrogen in the flue, the flue gas from the after-burner will have a thermal energy of approximatel 12,000 BTU/hr. This energy can be used to operate an ammonia absorption refrigeration unit to produce approximately 6000 BTU/hr refrigeration, which is more than enough to run several refrigerators and dehumidifiers but not sufficient to provide central air conditioning (which requires 36,000 BTU/hr refrigeration for an average home). The additional energy for central air conditioning and heating would be supplied by direct combustion of natural gas, and would be independent of the hybrid system.

Submarine Power Source

The use of fuel cells for propulsion of combat submarines is rather unlikely in view of the almost unlimited submergence capability of nuclear-powered submarines. However, many unique features of fuel cells make them attractive for special-purpose submarines. Some of the attractive features are: low fuel and oxidant weight requirements resulting in smaller displacement vehicles with greater depth capability, quiet operation, and simplicity. From the point of view of buoyancy and weight-displacement ratio, the high energy density of fuel-cell systems makes them very attractive in applications where weight-to-energy and volume-to-energy ratios are critical. Although secondary cells are superior from the standpoint of power-to-weight ratio, they are only suited for missions of a few hours' duration. As the mission length increases to days or weeks, the weight of the battery pack increases much more rapidly than that of fuel cell systems.

A power source for a small submarine requiring 10^3 kw of power for propulsion and 10^4 kw as pulse power for sonar can make good use of the fast-charge fast-discharge capabilities of the Li-Te cell, as shown by the results in Table VII.

Other Applications

As illustrated in the preceding three examples, the hybrid system surpasses the other energy and power sources, including the system with a fuel cell alone or storage batteries alone in applications where periodic high peak energy demands exist. Since the bimetallic battery is capable of being charged and discharged at high rates, it can be combined with a regenerative braking system which recovers a part of the energy which would otherwise be wasted. These unique features of the hybrid system make many possible applications for the fuel cell much more attractive. For example, industrial trucks, commuter buses, commuter trains, passenger boats, speed boats, submarines, hydrofoil boats, portable communication units, and electrolytic machining equipment are all potential applications of fuel cell-high rate secondary cell hybrid systems.

CONCLUSIONS

The recent advances in fuel cells have placed them in a much more competitive position than they were just a few years ago. The previous requirements for large amounts of platinoid metal electrocatalyst have been drastically reduced to the point where platinoid elements can be eliminated from hydrogen-air cells using alkaline electrolytes, and only 1-4 mg/cm^2 of platinoid elements are required when acid electrolytes are used in hydrogen-air cells. The direct use of unpurified reformer gases (containing more than about 20 ppm CO) is presently only

feasible with low-loading (< 5 mg platinoid metal/cm^2) electrodes at temperatures above 130°C. The direct use of hydrocarbon fuels is not yet practical, although very encouraging progress has been made, reducing the electrocatalyst loadings by a factor of about 10 from the original requirements of a few years ago. Molten carbonate cells have improved significantly in both performance and endurance, to the point where they can compete with other fuel cells on a performance basis, and are most attractive from an economic viewpoint.

The choices among the most advanced fuel cells are governed by the specific requirements of each application. For simplicity and high power density, direct hydrazine cells are attractive; for use with conventional carbonaceous fuels, indirect systems operating either on pure or impure hydrogen appear to be the best at present. In choosing between acid and alkaline electrolytes, the gain in system weight due to the necessary air scrubber for the alkaline electrolyte is counterbalanced by the lower performance of the air electrode in the acid system, so that the choice should be based on system simplicity (acid) or system cost (alkaline).

Since fuel cells are still relatively low specific power devices (maximum of 30 watt/lb for a system), the specific power requirements of many applications cannot be satisfied by fuel cell systems, unless a method is available for providing the peak power. Design calculations indicate that a fuel cell-high rate secondary cell hybrid system should provide the ability to meet the demands of high peak-to-average power profile with a system weight lower than that available using either fuel cells or secondary cells alone. These hybrid systems provide an attractive opportunity for the early use of fuel cells in high specific power applications.

Work performed under the auspices of the U. S. Atomic Energy Commission, operated by the University of Chicago under Contract No. W-31-109-eng-38.

ACKNOWLEDGMENTS

We thank Mr. G. L. Rogers for his help in performing the experiments. The encouragement and support of Drs. A. D. Tevebaugh and R. C. Vogel are appreciated. Mr. B. S. Baker of the Institute of Gas Technology kindly provided some of the information relating to power demands for homes.

References

1. L. W. Niedrach and H. R. Alford, J. Electrochem. Soc., 112, 117 (1965).

2. W. P. Colman, D. Gershberg, J. DiPalma, and R. G. Haldeman, in Proc. 19th Ann. Power Sources Conf., PSC Publications Committee, Red Bank, N. J., (1965).

3. G. R. Frysinger, in 20th Ann. Power Sources Conf., PSC Publications Committee, Red Bank, N. J. (1966).

4. H. I. Zeliger, J. Electrochem. Soc., 114, 236 (1967).

5. R. G. Haldeman, W. P. Colman, S. H. Langer, and W. A. Barber, in "Fuel Cell Systems", Adv. in Chem. Ser. 47, R. F. Gould, Ed., American Chemical Society, Washington, D. C. (1965).

6. M. B. Clark, W. G. Darland, and K. V. Kordesch, Electrochem. Tech., 3, 166 (1965).

7. K. V. Kordesch, in "Hydrocarbon Fuel Cell Technology", B. S. Baker, Ed., Academic Press, New York (1965).

8. E. J. Cairns and E. J. McInerney, in "Technical Summary Report No. 9, ARPA Order No. 247, Contract No. DA-44-009-AMC-479(T), to USAERDL, Jan. 1 - June 30, 1966, AD 640, 521.

9. W. T. Grubb and L. H. King, in "Technical Summary Report No. 9", ARPA Order No. 247, Contract No. DA-44-009-AMC-479 (T), to USAERDL, Jan. 1 - June 30, 1966, AD 640, 521.

10. M. A. Christopher, in Proc. 20th Ann. Power Sources Conf., PSC Publications Committee, Red Bank, N. J., (1966).

11. A. M. Adams, F. T. Bacon, and R. G. H. Watson, in "Fuel Cells", W. Mitchell, Jr., Ed., Academic Press, New York (1963).

12. R. A. Wynveen and T. G. Kirkland, in Proc. 16th Ann. Power Sources Conf., PSC Publications Committee, Red Bank, N. J. (1962).

13. E. W. Justi, Proc. IEEE, 51, 784 (1963).

14. E. W. Justi and A. W. Winsel, "Cold Combustion Fuel Cells", Franz Steiner, Publisher, Wiesbaden (1962).

15. R. Jasinski, in Proc. 18th Ann. Power Sources Conf., PSC Publications Committee, Red Bank, N. J., (1964).

16. I. Lindholm, in Proc. International Meeting on The Study of Fuel Cells, SERAI, Brussels, June 21-24, 1965.

17. J. Platner, D. Ghere, and P. Hess, in Proc. 19th Ann. Power Sources Conf., PSC Publications Committee, Red Bank, N. J. (1965).

18. H. M. Dittman, E. W. Justi, and A. W. Winsel, in "Fuel Cells", Vol. 2, G. J. Young, Ed., Reinhold, New York (1963).

19. R. Jasinski, J. Electrochem. Soc., 112, 526 (1965).

20. R. F. Buswell, in Proc. 19th Ann. Power Sources Conf., PSC Publications Committee, Red Bank, N. J. (1965).

21. C. Marks, E. A. Rishavy and F. A. Wyczalek, Presented at Automotive Eng'g Congress and Exposition, Detroit, Jan. 9-13, 1967, SAE Paper No. 670176.

22. F. A. Wyczalek, D. L. Frank and G. E. Smith, Presented at Automotive Eng'g Congress and Exposition, Detroit, Jan. 9-13, 1967, SAE Paper No. 670181.

23. C. E. Winters and W. L. Morgan, Presented at Automotive Eng'g Congress and Exposition, Detroit, Jan. 9-13, 1967, SAE Paper No. 670182.

24. P. D. Agarwal and I. M. Levy, Presented at Automotive Eng'g Congress and Exposition, Detroit, Jan. 9-13, 1967, SAE Paper No. 670178.

25. F. B. Leitz, W. Glass and D. K. Fleming, in "Hydrocarbon Fuel Cell Technology", B. S. Baker, Ed., Academic Press, New York (1965).

26. T. G. Kirkland and W. G. Smoke, Jr., in Proc. 19th Ann. Power Sources Conf., PSC Publications Committee, Red Bank, N. J. (1965).

27. T. G. Kirkland, in Proc. 20th Ann. Power Sources Conf., PSC Publications Committee, Red Bank, N. J. (1966).

28. K. R. Williams, Ed., "An Introduction to Fuel Cells", Elsevier, New York (1966).

29. L. W. Niedrach, D. W. McKee, J. Paynter, and I. F. Danzig, Presented at Electrochem. Soc. Meeting, Philadelphia, Oct. 1966, Abstr. No. 14; See also Extended Abstracts of The Battery Div., 11, 32 (1966).

30. G. H. J. Broers and M. Schenke, in "Hydrocarbon Fuel Cell Technology", B. S. Baker, Ed., Academic Press (1965).

31. B. S. Baker, L. G. Marianowski, J. Zimmer and G. Price in "Hydrocarbon Fuel Cell Technology", B. S. Baker, Ed., Academic Press, New York (1965).

32. A. D. S. Tantram, A. C. C. Tseung, and B. S. Harris, in "Hydrocarbon Fuel Cell Technology", B. S. Baker, Ed., Academic Press, New York (1965).

33. J. Millet and R. Buvet., in Proc. Journées Internationales d'Etude Des Piles À Combustible, SERAI, Brussels, June, 1965.

34. I. Trachtenberg, in "Hydrocarbon Fuel Cell Technology", B. S. Baker, Ed., Academic Press, New York (1965).

35. J. Truitt, in Proc. Journées Internationales d'Etude Des Piles À Combustible, SERAI, Brussels, June, 1965.

36. M. A. Vertes and A. J. Hartner, in Proc. Journées Internationales d'Etude Des Piles A Combustible, SERAI, Brussels, June, 1965.

37. S. M. Chodosh, N. I. Palmer, and H. G. Oswin, in "Hydrocarbon Fuel Cell Technology", B. S. Baker, Ed., Academic Press, New York (1965).

38. A. J. Hartner and M. A. Vertes, in Preprints of the AIChE-IChem.E Joint Meeting, London, June 13-17, 1965, Paper 5.3.

39. D. P. Gregory and H. Heilbronner, in "Hydrocarbon Fuel Cell Technology", B. S. Baker, Ed., Academic Press, New York (1965).

40. P. Terry, J. Galagher, R. Salathe, and J. O. Smith, in Proc. 20th Power Sources Conf., PSC Publications Committee, Red Bank, N.J. (1966).

41. E. A. Gillis, in Proc. 20th Ann. Power Sources Conf., PSC Publications Committee, Red Bank, N. J. (1966).

42. R. Jasinski, Electrochem. Tech. 3, 130 (1965).

43. H. Binder, A. Kohling, H. Krupp, K. Richter, and G. Sandstede, J. Electrochem. Soc., 112, 355 (1965).

44. W. T. Grubb and C. J. Michalske, in Proc. 18th Ann. Power Sources Conf., PSC Publications Committee, Red Bank, N. J. (1964).

45. E. J. Cairns, Nature, 210, 161 (1966).

46. E. J. Cairns, in "Hydrocarbon Fuel Cell Technology", B. S. Baker, Ed., Academic Press, N. Y. (1965).

47. E. J. Cairns, Presented at San Francisco Meeting of the Electrochemical Society, May, 1965, Abstract No. 140; See also Extended Abstracts of the Electro-Organic Division, 2, 6 (1965); J. Electrochem. Soc., 113, 1200 (1966).

48. E. J. Cairns, and G. J. Holm, Presented at Washington, D. C. Meeting of the Electrochem. Soc., Oct. 1964, Abstract No. 30; See also Extended Abstr. of the Battery Div., 9, 75 (1964).

49. E. J. Cairns and E. J. McInerney, J. Electrochem. Soc., Submitted; See also Extended Abstracts of the Industrial Electrolytics Div., 2, 1 (1966).

50. E. J. Cairns and E. J. McInerney, Presented at Electrochem. Soc. Meeting, Philadelphia, Oct. 9-14, 1966, Abstract No. 8; See also Extended Abstracts of the Battery Div., 11, 19 (1966).

51. O. J. Adlhart and A. J. Hartner, in Proc. 20th Ann. Power Sources Conf., PSC Publications Committee, Red Bank, N. J. (1966).

52. W. R. Epperly, in Proc. 19th Ann. Power Sources Conf., PSC Publications Committee, Red Bank, N. J. (1965).

53. G. R. Frysinger, in Proc. 19th Ann. Power Sources Conf., PSC Publications Committee, Red Bank, N. J. (1965).

54. E. J. Cairns, Science, 155, 1245 (1967).

55. E. R. White and H. J. R. Maget, in Proc. 19th Ann. Power Sources Conf., PSC Publications Committee, Red Bank, N. J. (1965).

56. E. J. Cairns and D. C. Bartosik, J. Electrochem. Soc., 111, 1205 (1964).

57. B. L. Tarmy, in Proc. 19th Ann. Power Sources Conf., PSC Publications Committee. Red Bank, N. J. (1965).

58. O. J. Adlhart, in Proc. 19th Ann. Power Sources Conf., PSC Publications Committee, Red Bank, N. J. (1965).

59. K. R. Williams, M. R. Andrew, and F. Jones, in "Hydrocarbon Fuel Cell Technology", B. S. Baker, Ed., Academic Press, New York (1965).

60. G. Ciprios, in Proc. Intersociety Energy Conversion Engineering Conf., Amer. Inst. Aeronautics and Astronautics, New York (1966).

61. G. E. Evans, in Extended Abstracts of the Symp. on Power Systems for Electric Vehicles, Columbia Univ., N. Y., April, 1967.

62. A. Levy, "Final Tech. Report", Contract No. DA-44-009-AMC-747(T), to USAERDL, July 27, 1964 - July 27, 1965, AD 473143L.

63. L. W. Niedrach and I. B. Weinstock, Electrochem. Tech., 3, 270 (1965).

64. N. I. Palmer, B. Lieberman and M. A. Vertes, in "Hydrocarbon Fuel Cell Technology", B. S. Baker, Ed., Academic Press, New York (1965).

65. H. Binder, A. Köhling and G. Sandstede, in "Hydrocarbon Fuel Cell Technology", B. S. Baker, Ed., Academic Press, New York (1965).

66. H. Shimotake and E. J. Cairns, Presented at the Intersociety Energy Conversion Engineering Conf., Miami Beach, August, 1967.

67. H. Shimotake, G. L. Rogers and E. J. Cairns, Presented at Electrochem. Soc. Meeting, Chicago, October, 1967.

68. A. D. Tevebaugh and E. J. Cairns, J. Chem. Eng. Data, 9, 172 (1964).

69. M. S. Foster and C. C. Liu, J. Phys. Chem., 70, 950 (1966).

70. G. H. J. Broers, in "Fuel Cells", A CEP Technical Manual, Amer. Inst. of Chem. Engrs., New York (1963).

71. Bureau of Power, Federal Power Commission "Development of Electrically Powered Vehicles" (February 1967).

72. Volkswagenwerk Ag., "Instruction Manual Sedan and Convertible" (1959).

73. N. MacCoull, in "Mechanical Engineer's Handbook", T. Baumeister, Ed., 6th ed., McGraw-Hill, New York (1958), p. 11-5.

74. W. G. Hudson, in "Mechanical Engineer's Handbook" , T. Baumeister, Ed., 6th ed., McGraw-Hill, New York (1958), p. 10-4.

75. F. R. Innes, in "Standard Handbook for Electrical Engineers", A. E. Knowlton, Ed., 9th ed., McGraw-Hill, New York (1957) p. 17-622.

76. Am. Soc. Heating, Refrig. and Air-Cond. Engrs., "ASHRAE Guide and Data Book Fundamentals and Equipment for 1965 and 1966", p. 486.

TABLE I

Estimated Performances for Some Fuel Cell Systems

System	Anode*	mg/cm² *	Electrolyte	Cathode	mg/cm² *	Operating point T °C	E, volt	i, ma/cm²	Stack Life, Hr	Specific† Power w/lb Stack	Specific† Power w/lb System	Remarks	References
Indirect													
HC Fuel/Reformate/H_2/Air	Pt/C	1	KOH, Matrix	Pt/C	1	80	0.80	200	10^3	55	25	Air scrubber; Ag-Pd diffuser.	3,6,7,17,20,22,23, 26,27
HC Fuel/Reformate/H_2/Air	Ni_2B	10	KOH, Matrix	Ag/C	1	80	0.80	140	10^3	38	20	Air scrubber; Ag-Pd diffuser.	6,7,12,15-20
HC Fuel/Reformate/H_2/Air	Pt/C	1	H_2SO_4,Matrix	Pt/C	2-3	80	0.70	150	10^3	36	23	Ag-Pd diffuser.	3,4,8,9,10,25,29
NH_3/N_2+H_2/Air	Pt/C	1	KOH, Matrix	Pt/C	1	80	0.80	200	10^3	55	30	Air scrubber.	3,6,7,17,20-23, 26,27,62
HC Fuel/Reformate/Air	Pt/C	2-3	H_3PO_4	Pt/C	2-3	150	0.70	150	10^3	36	23		3,51
HC Fuel/Reformate/Air	Pt-Ru	34	H_2SO_4	Pt/C	2-3	85	0.60	150	?	31	21	High catalyst loading.	29,63
HC Fuel/Reformate/Air	Ni	20	$(LiNaK)_2CO_3$	CuO	20	650	0.80	150	10^3	12	10	Inexpensive, but heavy.	30-35
CH_3OH/Integrated Reformer/Air	Pd	5	KOH	NiO/Ni	100	200	0.70	190	10^3	21**	16	Ag-Pd anode; air scrubber.	36-38, 64
HC/Integrated Reformer/Air	Pd	5	KOH	NiO/Ni	100	250	0.75	80	2×10^2	9.6**	8	Ag-Pd anode; air scrubber.	36,39
Direct													
N_2H_4/Air	Ni_2B	10	KOH, Matrix	Ag/C	2	80	0.80	150	2×10^3	42	30	Air scrubber.	40-42
CH_3OH/Air	Pt-Ru	20-40	H_2SO_4	Pt/C	10	70	0.40	50	10^3	7	6	Too much Pt; low power.	57-60
CH_3OH/Air	Pt-Ru	20-40	Cs_2CO_3	Ag/C	2-3	125	0.40	50	$>6\times10^2$	7	6	Too much Pt; low power.	7,56,65
LPG/Air	Pt/C	5-10	H_3PO_4	Pt/C	3	150	0.50	60	?	10	8	Too much Pt; low power.	9,44,51-53,55
LPG/Air	Pt/C	5-10	HF	Pt/C	3	105	0.50	60	?	10	8	Too much Pt; low power.	8,45-50

*This is the weight of electrocatically active material only; e.g., Pt, Ni_2B, etc.

†The estimates are for systems of 10-50 kw power output.

**Includes catalyst in reforming anode.

TABLE II

Design Specifications for Power Sources
For a Light Urban Automobile.

Design Requirement	
Unladen car weight	1600 lb
Laden car weight	2000 lb
Maximum speed on level road	60 mph
Acceleration 0 to 30 mph	8 sec
Brake horsepower (pulse)	25 hp
Power source (pulse)	23.2 kw
Brake horsepower (continuous)	5 hp
Power source (continuous)	4.65 kw
Weight allowance for power source*	400 lb
System specific power (peak)	58 watt/lb

* Exclusive of motor, controls and gear train. The motor and controls will weigh 90 lb.[24]

TABLE III

Hybrid System for the Urban Automobile

Fuel Cell	
System $N_2H_4 \cdot H_2O$/Air	
Continuous power required	4.65 kw
Specific power of fuel cell	30 watt/lb (From Table I)
Weight for 4.65 kw	155 lbs
Battery	
System Li-Te	
Power Requirement	23.2 kw - 4.65 kw = 18.55 kw
Design specific power (with 3.6 cell per inch from Fig. 9)	300 watt/lb
Specific energy	58 watt-hr/lb
Weight for 18.55 kw	62 lb
Energy stored	(58)(62) = 3.6 kw-hr
Fuel and Tank	
Weight allowance	400 - 155 - 62 = 183 lb
Energy available	(183)(680.2)* = 125 kw-hr
Total energy availabe	3.6 + 125 = 128.6 kw-hr
System specific energy	$\frac{(128.6)(10)^3}{400}$ = 322 watt-hr/lb
System specific power (peak)	$\frac{(23.2)(10)^3}{400}$ = 58 watt/lb
Range in the typical urban driving (from Figure 13a)	(128.6 kw-hr)(3.75 miles/kw hr) = 481 miles

* Specific energy of fuel and tank for the $N_2H_4 \cdot H_2O$/Air fuel cell is taken as 680.2 watt-hr/lb.

TABLE IV

Comparison of Various Electric Power Sources for an Urban Automobile

System	Hybrid $N_2H_4 \cdot H_2O$/Air and Li-Te	Fuel Cell $N_2H_4 \cdot H_2O$/Air	Lead-Acid	Ag-Zn	Li-Te
Weight					
Fuel cell and fuel, lb	338	970	-	-	-
Battery, lb	62	-	400	400	400
Total, lb	400	970	400	400	400
System Power, kw	23.2	23.2	23.2	23.2	23.2
System Energy, kw-hr	128.6	66	0.96	28	56
Range*, miles	481	246	3.6	105	210
Recharging time	<15 min	<15 min	> 8 hr	>8 hr	<15 min

* Based on a typical urban driving profile shown in Figure 13 a, 3.75 miles/kw-hr is obtained.

TABLE V

Power Requirements for a Home

Continuous Loads	Thermal BTU/Hr	Electric, Watts	Duration, Hr
Heating[76]	80,000	-	24
Home appliances	-	1,000	24
Pulse Loads			
Cooking	10,000	-	2
Household chores	-	2,000	0.5
Clothing dryer	15,000	-	0.5
Home appliances	-	3,000	0.5
TV and Radio	-	600	7
Lights	-	1,000	7

TABLE VI

Designs of Power Sources for a Home

Design Requirements

Electric power and energy requirements:

Continuous power	1 kw
Pulses integrated over 24 hr period	22.5 kwh
Energy of largest pulse	16 kwh
Peak pulse power	6.6 kw

Calculations are made for both hybrid system and fuel cell system.

Hybrid System

Fuel cell system: Molten carbonate cell with a reformer.

Cell operating temperature	650°C
Fuel: Natural gas (methane) from gas supply line	
Average power requirement:	$\frac{24 + 22.5}{24} = 1.95$ kw
Specific power of the fuel cell system (Table I) (reformer inclusive)	10 watt/lb
Weight:	$(1.95)(10)^3/(10) = 195$ lb

Battery system: Li-Te

Peak power requirement	4.65 kw
Energy storage requirement (from Figure 15)	8 kwh

From the definition of specific energy, σ_E and specific power, σ_p [*]

$$\frac{4.65}{\sigma_p} = \frac{8}{\sigma_E} \quad \text{or} \quad \sigma_p = 0.58\,\sigma_E$$

By finding the intersection of the above equation and the Li-Te line in Figure 9, we have the following points for the Li-Te battery with 2.1 cells per inch.

specific energy	136 watt-hr/lb
specific power	68 watt/lb
weight required	$(8)(10)^3/(136) = 59$ lb
combined weight	195 + 59 = 254 lb

Fuel Cell System

Fuel cell:	molten carbonate cell with a reformer
Fuel:	natural gas (methane)
Power requirements:	6.6 kw
Specific power:	= 10 watt/lb (reformer inclusive)
Weight:	$(6.6)(10)^3/(10) = 660$ lb.

[*] σ_E is watt-hr/lb and σ_p is watt/lb.

TABLE VII

Designs of Power Sources for Small Submarines

Design Requirements

Search, rescue, salvage or research missions with sonars

Continuous power requirement:	1,000 kw, 48 hours
Total propulsion energy:	4.8×10^4 kw-hr
Pulse power requirement:	10,000 kw for 10 seconds 1,000 pulses at 100 second intervals
Total pulse energy:	2.78×10^4 kw-hr
Total mission energy requirement:	7.58×10^4 kw-hr

Hybrid System

Battery

System	Li-Te
Power requirement	10,000 kw
Energy requirement for a sonar pulse	27.8 kw-hr
Specific power (for the Li-Te battery with 8.5 cells per inch)	500 watt/lb
Weight for 10,000 kw	20,000 lb
Specific energy (from Figure 9)	20 watt-hr/lb
Energy stored	(20,000)(20) = 400 kw-hr

The stored energy is more than sufficient to produce several pulses without recharge.

Fuel Cell

System	Ammonia (Dissociator)/Air
Energy requirement	7.58×10^4 kw-hr
Power requirement	$\frac{7.58 \times 10^4}{48} = 1{,}580$ kw

From the definition of specific energy and power

$$\frac{7.58 \times 10^4}{\sigma_E} = \frac{0.158 \times 10^4}{\sigma_p} \quad \text{or} \quad \sigma_p = 0.0208\, \sigma_E$$

By drawing the above relation on the coordinates of Figure 9, we find the line intersects with the ammonia (dissociator)/air line at the following points

Specific energy	605 watt-hr/lb
Specific power	12.5 watt/lb

These numbers correspond to the fuel cell system consisting of 43 w/o fuel cell and 57 w/o tank plus fuel

Weight required	$\frac{7.58 \times 10^7}{605} = 1.25 \times 10^5$ lb
Power available	$1.25 \times 10^5 \times 12.5 \times 10^{-3} = 1.56 \times 10^3$ kw

This power is sufficient to meet the mission requirement.

Total system weight $= (0.2 + 1.25)10^5 = 145{,}000$ lb

TABLE VIII

Submarine Power Source Designs

System	Hybrid NH_3/Air and Li-Te	Fuel Cell NH_3/Air	Ag-Zn Ag-Zn	Li-Te Li-Te
Weight				
Fuel cell, lb	125,000	398,000	-	-
Battery, lb	20,000	-	1,080,000	525,000
Total, lb	145,000	398,000	1,080,000	525,000
System Power, Mw	10	10	10	10
System Energy, Mw-hr	75.8	75.8	75.8	75.8

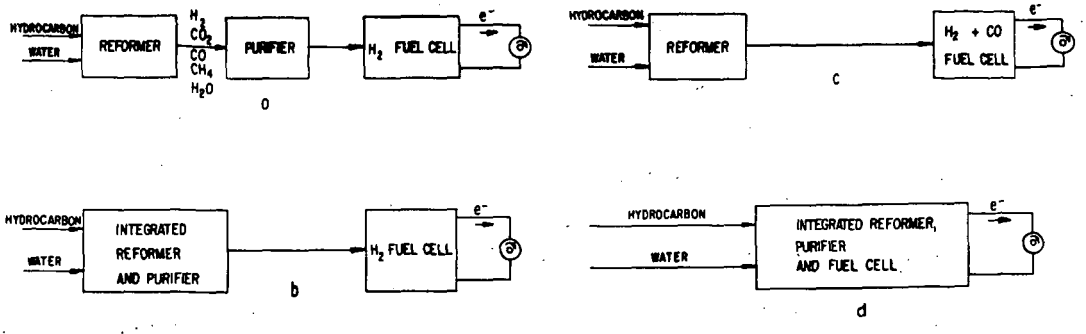

Fig. 1 Some indirect hydrocarbon fuel cell systems.

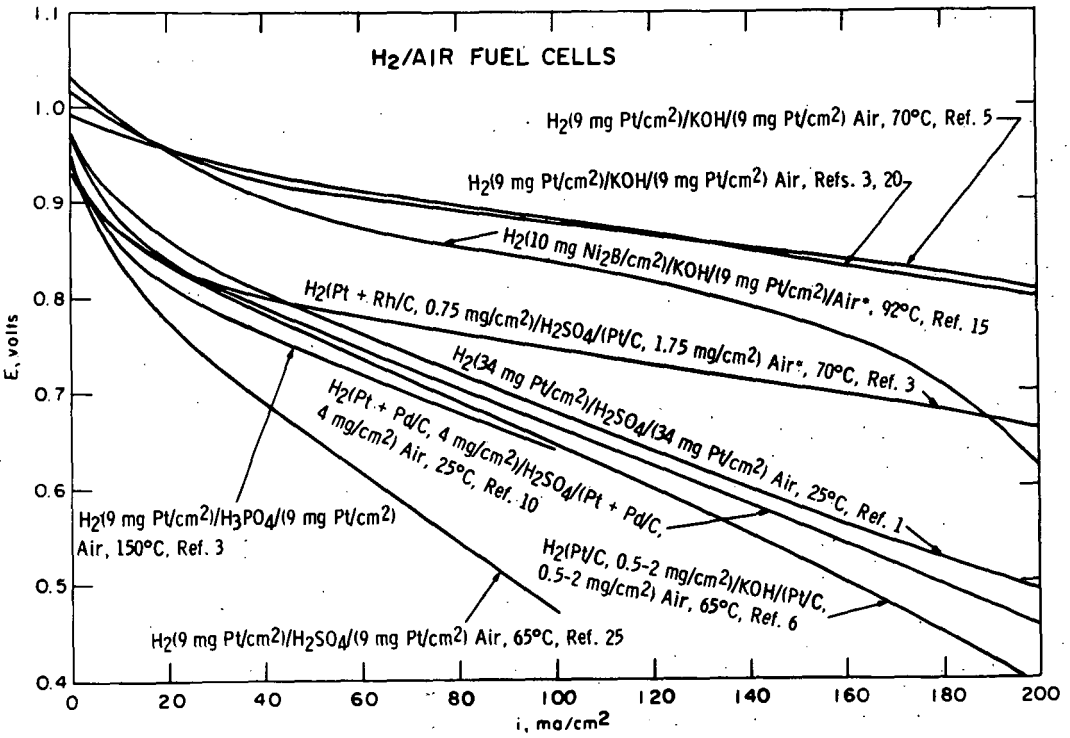

Fig. 2 Voltage-current density curves for hydrogen/air fuel cells.

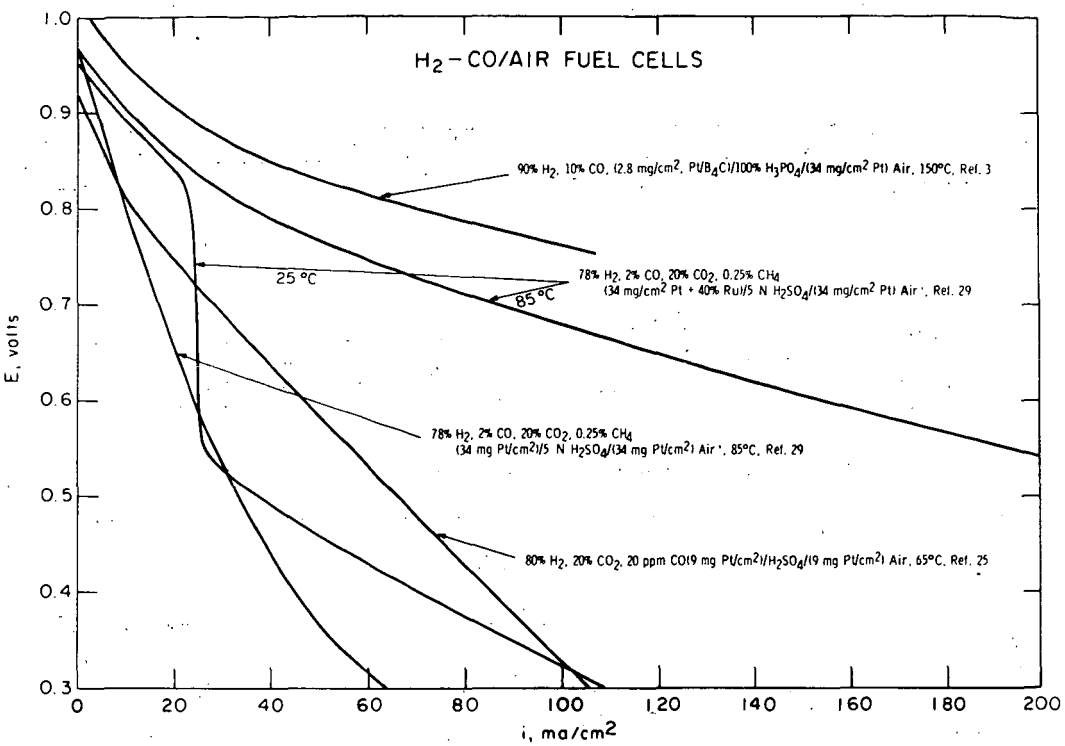

Fig. 3 Voltage-current density curves for H_2-CO/air fuel cells.

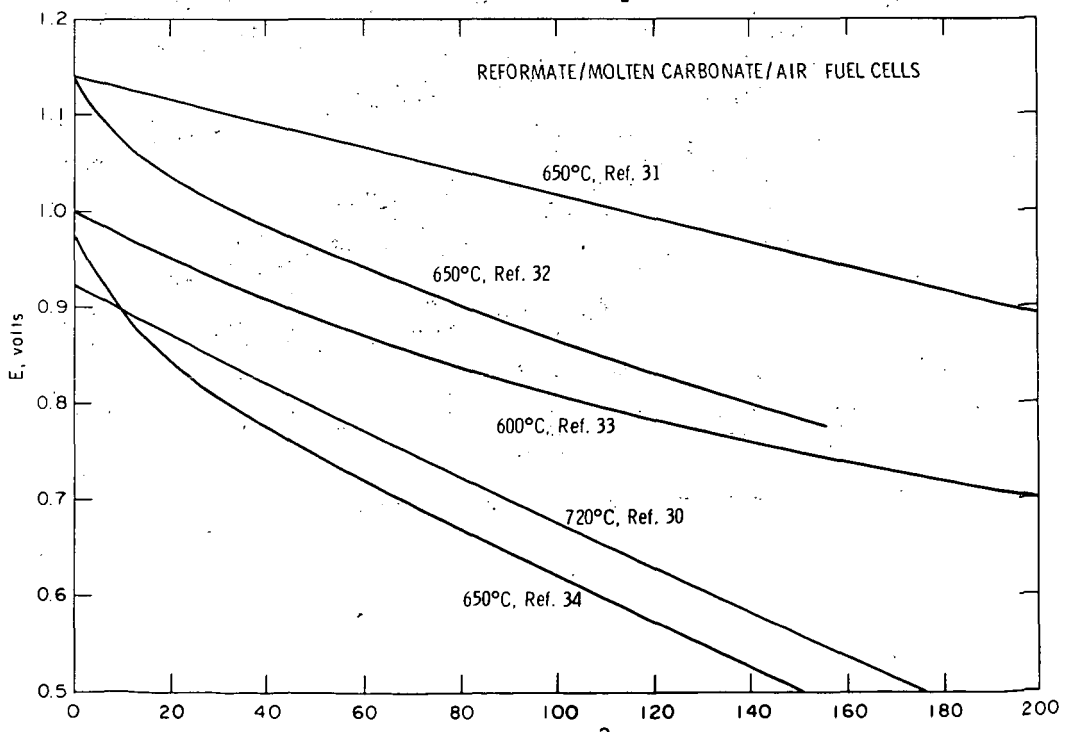

Fig. 4 Voltage-current density curves for molten carbonate cells operating in reformer gases and air.

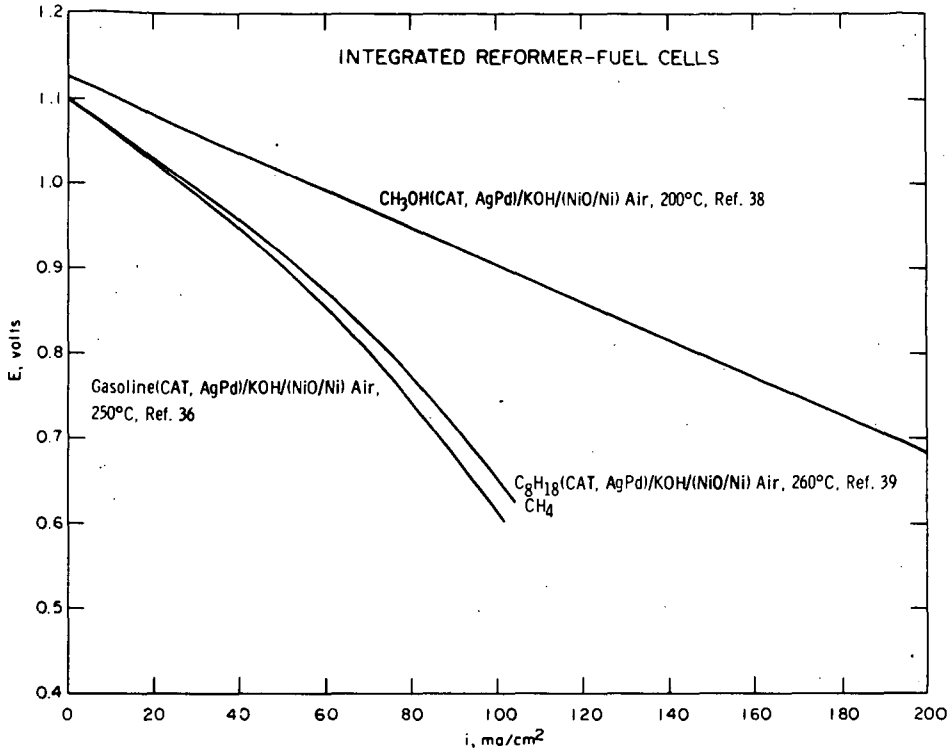

Fig. 5 Voltage-current density curves for integrated reformer/air fuel cells.

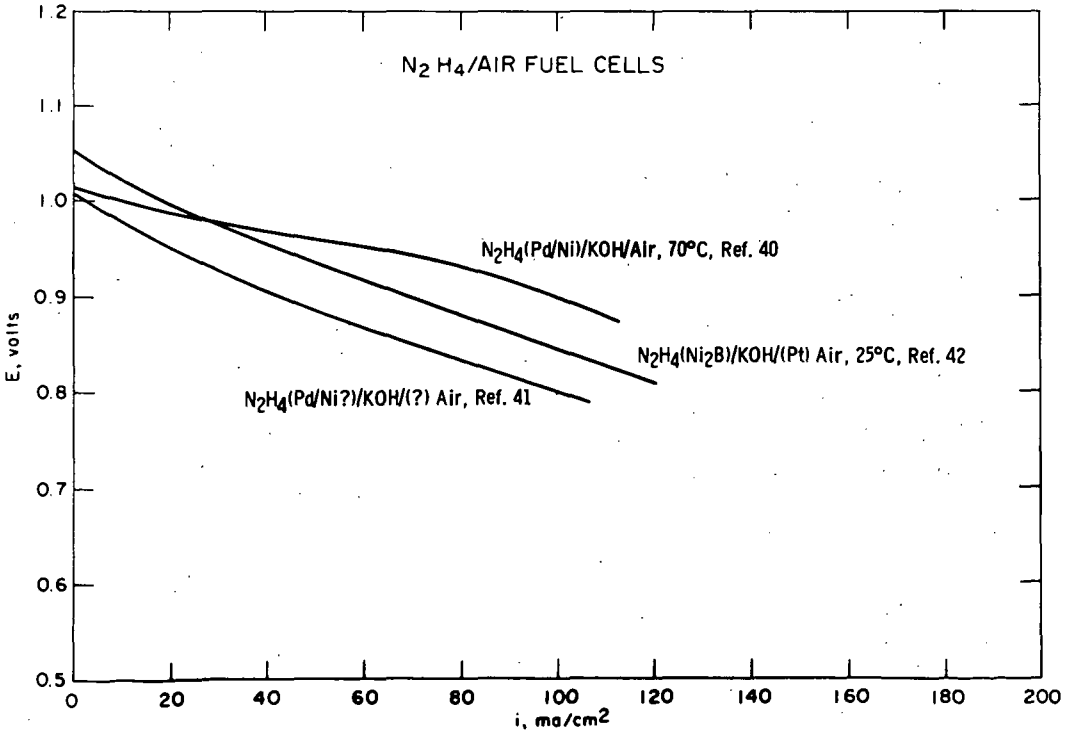

Fig. 6 Voltage-current density curves for direct hydrazine/air fuel cells.

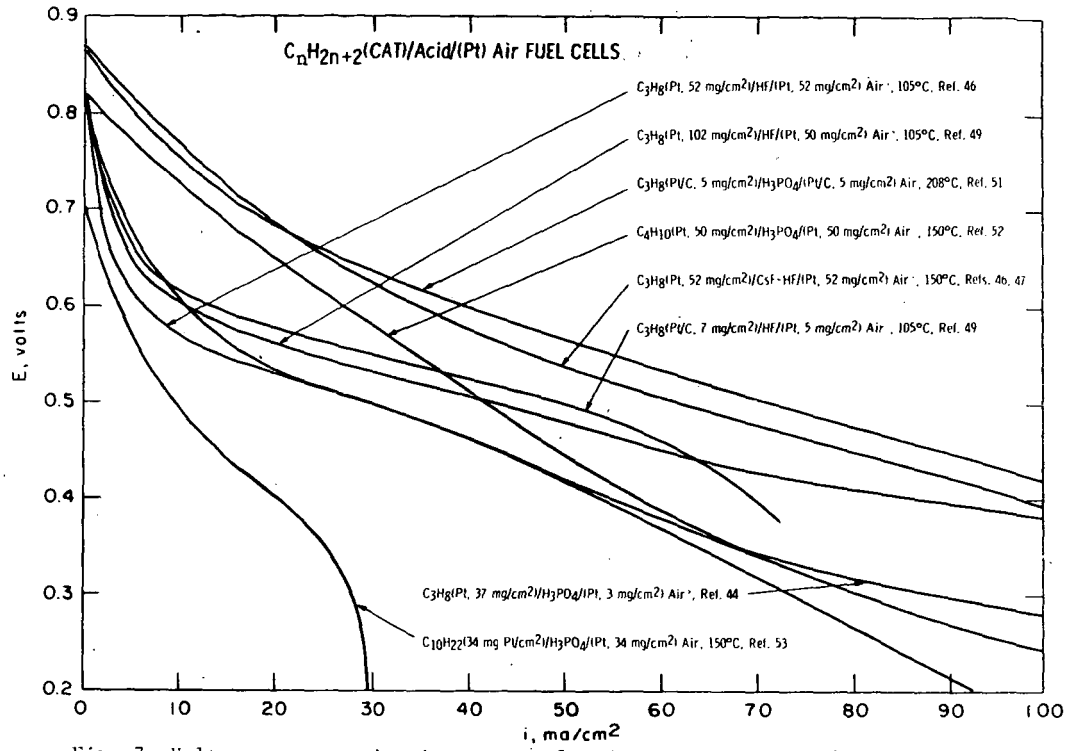

Fig. 7 Voltage-current density curves for direct hydrocarbon/air fuel cells with acid electrolytes.

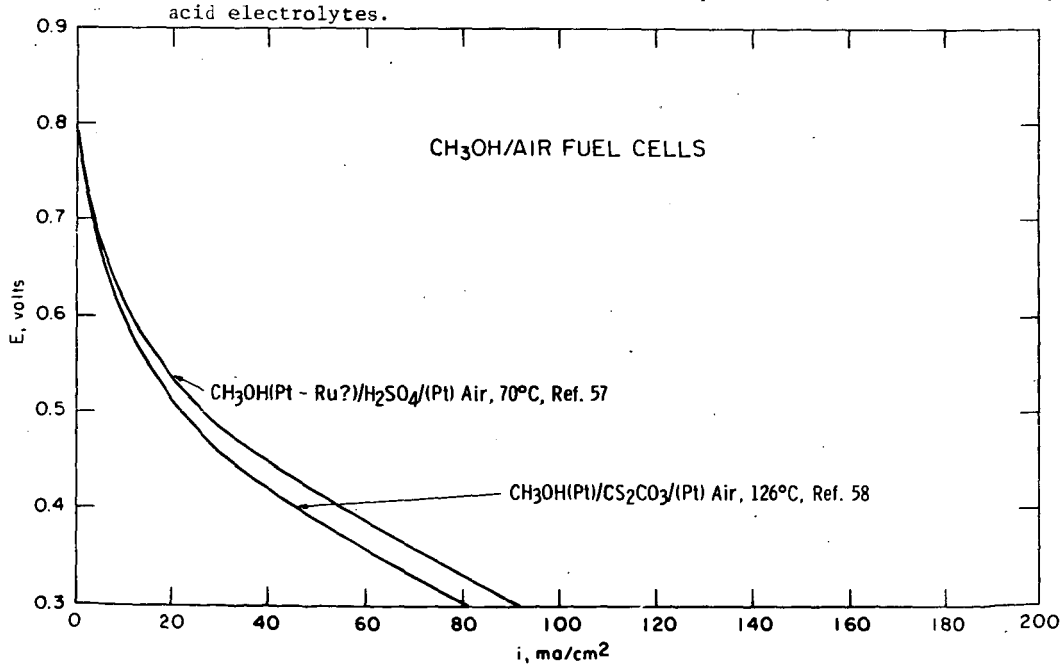

Fig. 8 Voltage-current density curves for direct methanal/air fuel cells.

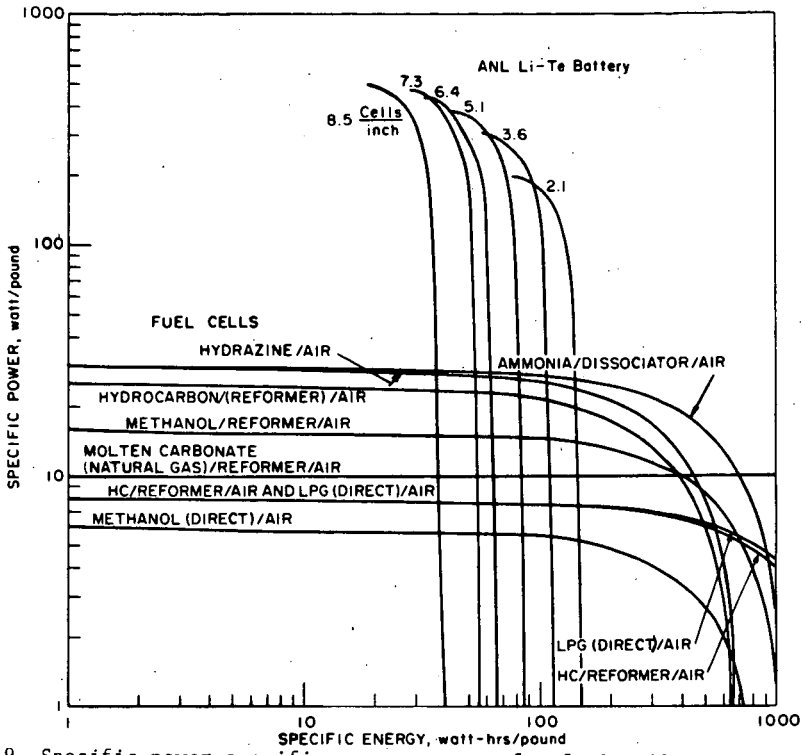

Fig. 9 Specific power-specific energy curves for fuel cell systems and Li-Te batteries.

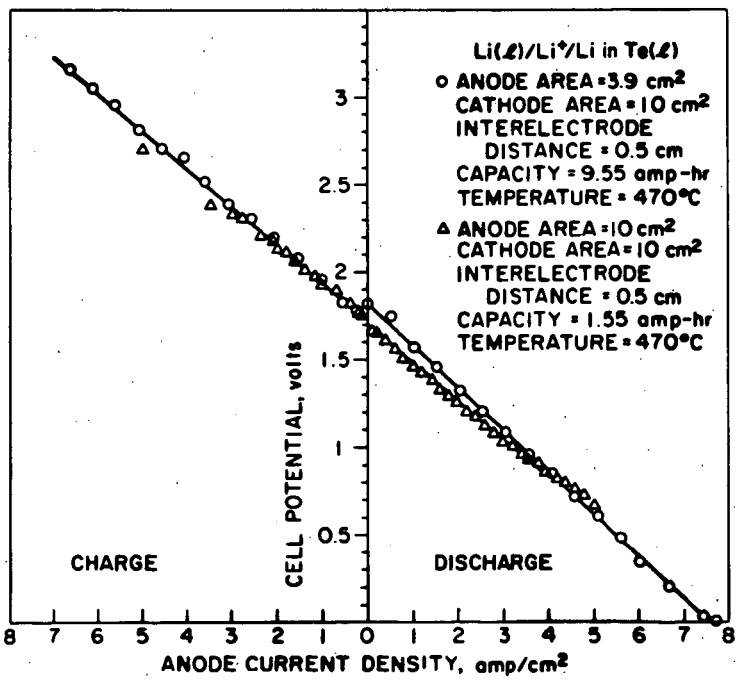

Fig. 10 Steady-state voltage-current density curves for Li/Te cells.

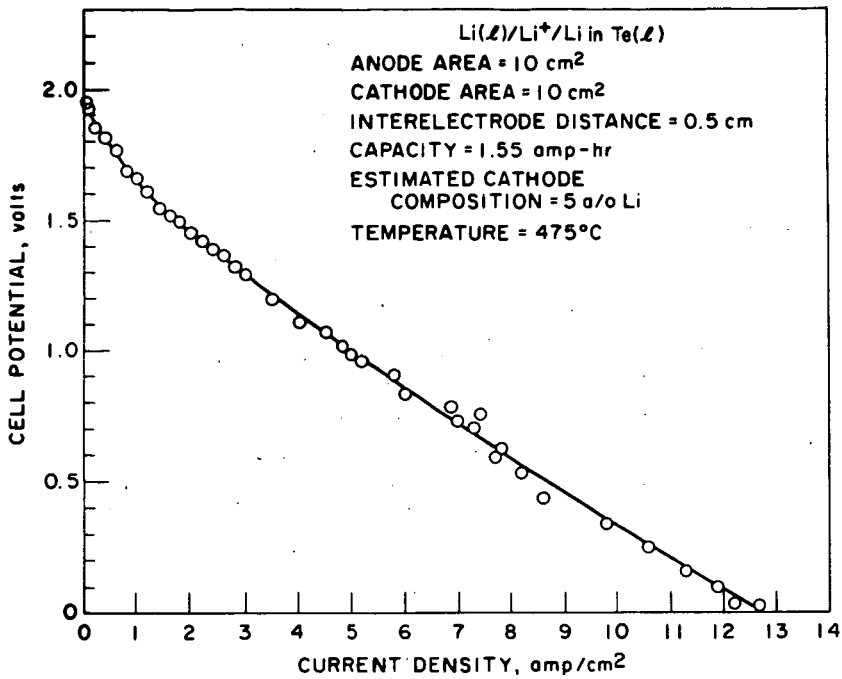

Fig. 11 Short-time voltage-current density curves for a Li/Te cell.

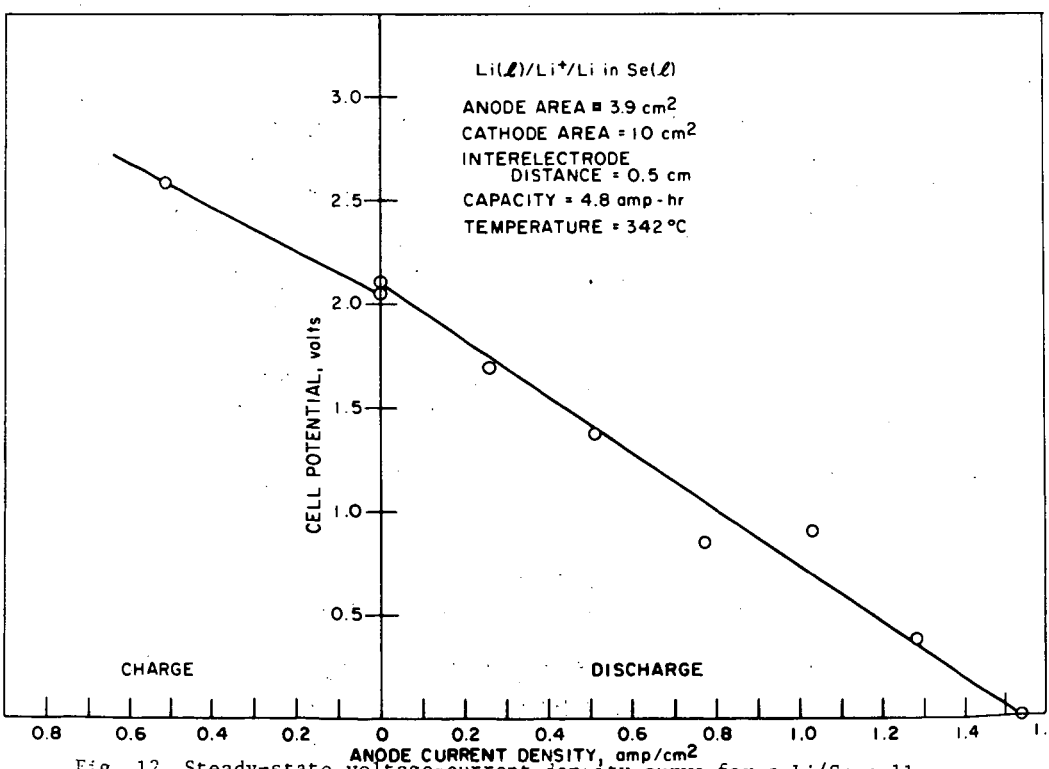

Fig. 12 Steady-state voltage-current density curve for a Li/Se cell.

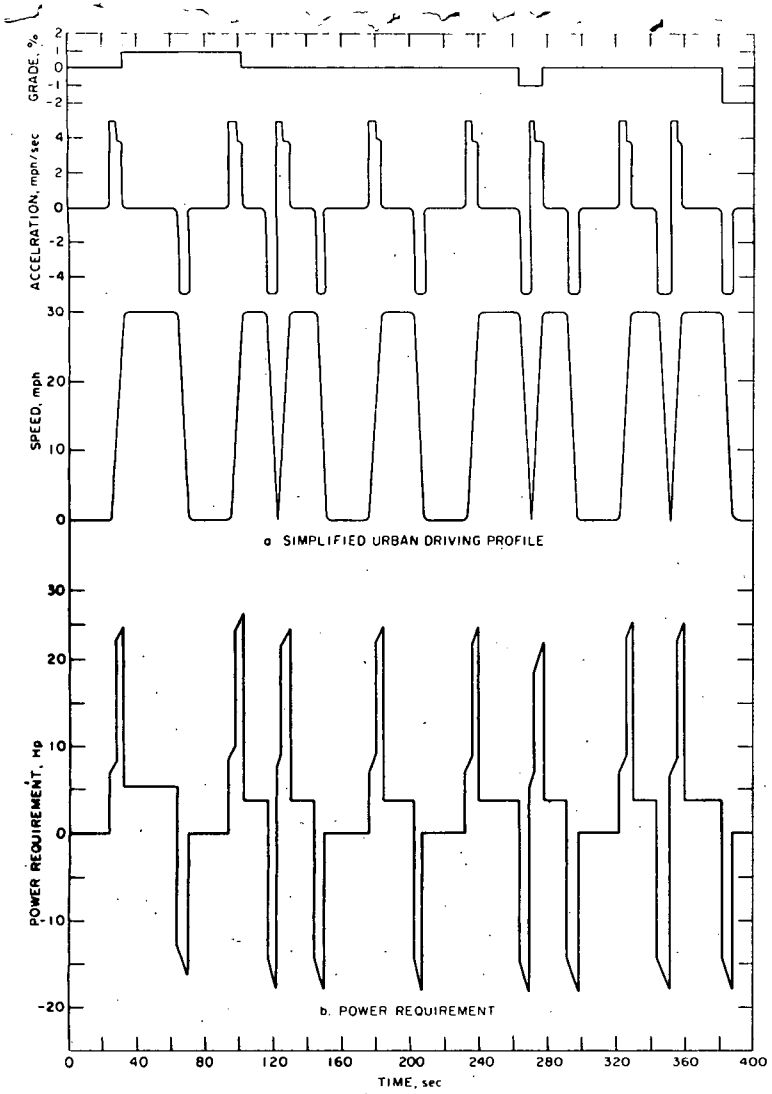

Fig. 13 Driving profile and power requirements for small urban auto.

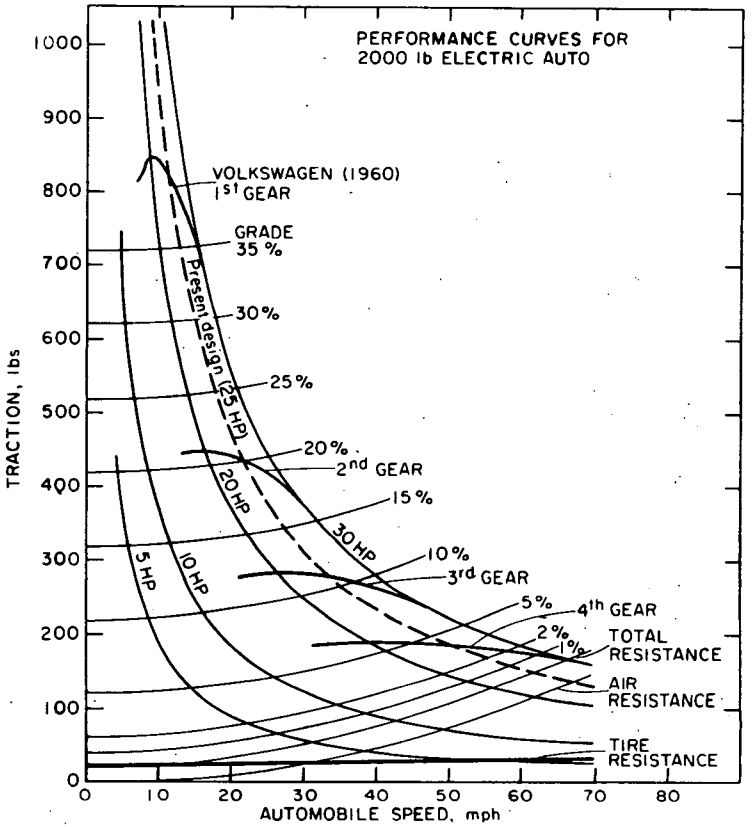

Fig. 14 Performance Curves for 2000 lb. Electric Auto.

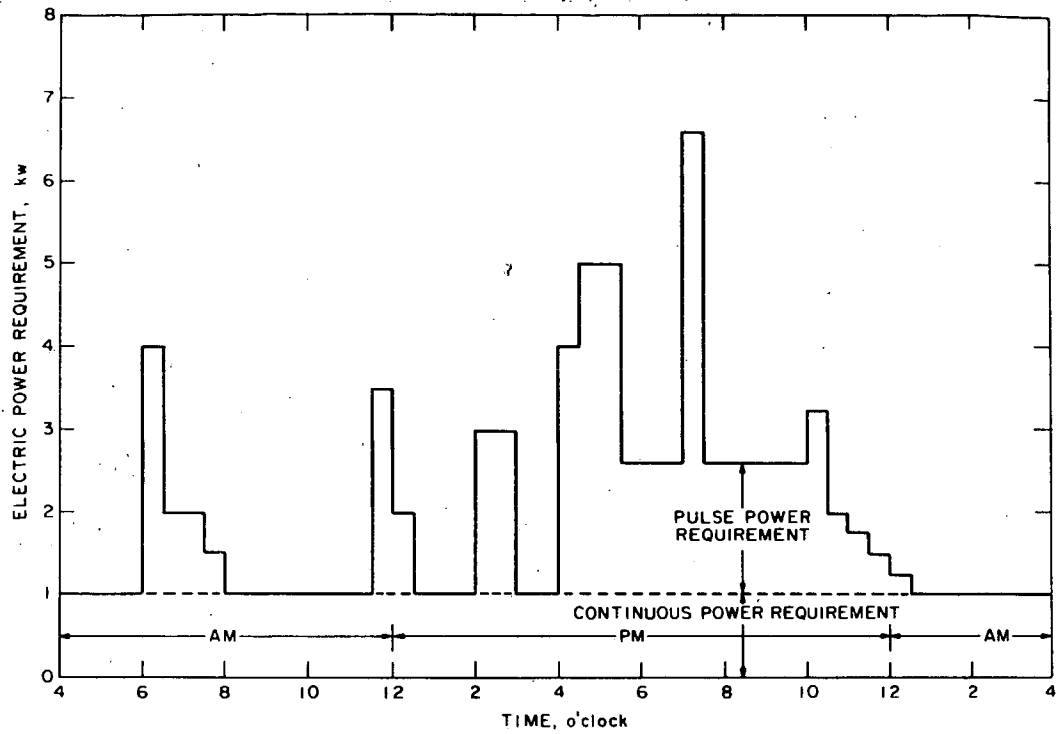

Fig. 15 Electric power requirements for a home.

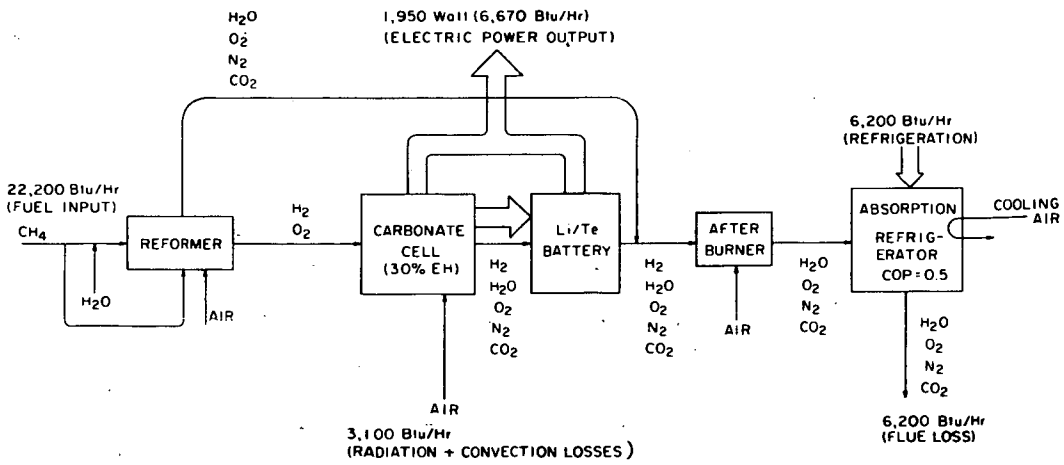

Fig. 16 Schematic diagram of a home hybrid power source.